



UiT The Arctic University of Norway

Faculty of Science and Technology

Department of Chemistry

Towards Enantioselective Carboxylation and Hydrogenation Reactions

Quantum Chemical Modelling of Homogeneous Reactions

Ljiljana Pavlovic

A dissertation for the degree of Philosophiae Doctor, June 2020

Abstract

With the aid of DFT methods, it is possible to get insights into the mechanistic details of homogeneous reactions, the substrate preferences and activities of catalysts. Computational methods can also help to identify the selectivity-determining factors that govern asymmetric reactions. In this thesis, DFT methods are applied in order to study the enantioselective addition of small molecules, such as CO₂ and H₂, to alkenes in order to form saturated carboxylic acids and alkanes.

Both rhodium-mediated hydrocarboxylation and cobalt-mediated hydrogenation reactions were investigated using the popular DFT functionals PBE and B3LYP, including dispersion corrections. First, the nonselective Rh-cyclooctadiene(COD)-catalyzed hydrocarboxylation of alkenes with CO₂ was studied by employing the PBE-D2 functional. Several styrene derivatives and α,β -unsaturated compounds were analyzed. Our computational investigation of Rh-COD-benzyl complexes revealed an unusual TS for the C-CO₂ bond formation step, where CO₂ does not interact with the metal center and the substrate is coordinated to the metal in a η^6 -fashion via a phenyl ring. The study was expanded by analyzing the potential of five chiral ligands, (*S*)-SEGPHOS, (*R,R*)-BDPP, (*R,R*)-tBu-BOX, (*S*)-iPr-PHOX, and (*R*)-StackPhos, to form Rh-based catalysts for asymmetric hydrocarboxylations. Interestingly, the preferred carboxylation TSs with chiral Rh-complexes display a similar substrate binding mode as with the achiral COD ligand and also show a preference for outer sphere CO₂ insertion. However, the results indicate that different CO₂ insertion paths, *frontside* or *backside*, are possible, dependent on the nature of the ligand. For ligands containing an N-heterocyclic ring, it is shown that CO₂ is able to form stacking interactions with the ring, which for several ligands results in a preference for frontside CO₂ insertion.

Second, a detailed mechanistic investigation of Co-catalyzed asymmetric hydrogenation of enamides was performed at the B3LYP-D3 level of theory. The study of enamides with very different molecular structures shows that two mechanistic pathways appear accessible, both a non-redox Co(II) mechanism proceeding through metallacycle intermediates and a more classical redox Co(0)/Co(II) mechanism. The obtained barriers indicate that these mechanisms may be competing. It is also shown that explicit solvent affects the computed barriers significantly and that its inclusion appears to be crucial for the proper estimation of the enantiomeric excesses of Co-catalyzed hydrogenation of enamides.

Table of Contents

Abstract	i
List of papers	v
Acknowledgements	vii
Abbreviations	ix
1. Introduction	1
2. Computational methods	5
2.1 Introduction to computational <i>ab initio</i> methods	5
2.2 Fundamentals of Density Functional Theory	6
2.3 An overview of Density functionals	7
3. Computational protocol	11
3.1 Basis sets	11
3.2 Solvation models	13
3.3 Dispersion	13
3.4 Modelling of reaction mechanisms	14
3.4.1 PES	14
3.4.2 Geometry optimization techniques	16
3.4.3 Optimization methods to locate TSs	17
3.5 Energies	18
3.5.1 Corrections to the energy	19
3.6 Enantioselectivity	20
3.6.1 Chirality	20
3.6.2 Evaluation of enantiomeric excess with DFT	21
3.6.3 The Curtin Hammett principle	22
3.7 Accuracy of DFT on properties we are interested in	24
3.7.1 Prediction of geometries with B3LYP	24
3.7.2 Prediction of geometries with PBE	26
3.7.3 Prediction of atomization, binding and dissociation energies with B3LYP	26
3.7.4 Prediction of reaction barriers with B3LYP	28
3.7.5 Prediction of atomization and reaction energies with PBE	28
3.7.6 Performance of B3LYP for spin-state ordering	31
3.7.7 Prediction of enantioselectivity with B3LYP	32
3.7.8 Prediction of enantioselectivity with PBE	35
3.8 General conclusions	36
4. Hydrocarboxylation	39
4.1 CO ₂ properties	40
4.2 Introduction to metal-catalyzed hydrocarboxylations	40

4.3	Rh-COD-hydrocarboxylation of styrene derivatives and α,β -unsaturated carbonyl compounds with CO ₂ (Paper I&II)	45
4.4	Results and discussion of Rh-catalyzed hydrocarboxylation	46
4.4.1	Substrate preferences	51
4.5	Rh-catalyzed asymmetric hydrocarboxylation with CO ₂ (Paper II&III)	53
4.5.1	Potential of various chiral ligands in asymmetric hydrocarboxylation	53
4.5.2	Asymmetric Rh-(<i>S</i>)-SEGPHOS-catalyzed carboxylation of methyl 2-phenylacrylate. 56	
4.5.3	Asymmetric Rh-(<i>S</i>)-SEGPHOS-catalyzed carboxylation of 4-(tert-butyl)benzyl 2-phenylacrylate.....	59
4.5.4	Asymmetric Rh-(<i>R</i>)-StackPhos-catalyzed carboxylation of methyl 2-phenylacrylate..	60
4.5.5	Asymmetric Rh-(<i>R,R</i>)-tBu-BOX-catalyzed carboxylation of methyl 2-phenylacrylate.	62
4.5.6	Asymmetric Rh-(<i>R,R</i>)-BDPP-catalyzed carboxylation of methyl 2-phenylacrylate.....	64
4.5.7	Asymmetric Rh-(<i>S</i>)-iPr-PHOX-catalyzed carboxylation of methyl 2-phenylacrylate..	65
4.6	General conclusion	66
5.	Hydrogenation	69
5.1	Mechanistic aspects of metal-catalyzed hydrogenations	70
5.2	Introduction to asymmetric metal-catalyzed hydrogenation	71
5.3	Background on Co-mediated asymmetric hydrogenation	73
5.4	Co-catalyzed asymmetric hydrogenation of enamides (Paper IV)	76
5.5	Computed results and discussion for enamide hydrogenation	78
5.5.1	Hydrogenation of methyl 2-acetamidoacrylate	78
5.5.2	Hydrogenation of <i>dehydro</i> -levetiracetam	84
5.6	General conclusion	89
6.	Conclusions	91
	References	93

List of papers

This thesis is based on the following papers:

- I. *Rhodium-Catalyzed Hydrocarboxylation: Mechanistic Analysis Reveals Unusual Transition State for Carbon–Carbon Bond Formation*
Ljiljana Pavlovic, Janakiram Vaitla, Annette Bayer and Kathrin H. Hopmann
Organometallics, **2018**, 37, 941–948.
<https://pubs.acs.org/doi/abs/10.1021/acs.organomet.7b00899>
- II. *To bind or not to bind: Mechanistic insights into C–CO₂ bond formation with late transition metals*
Diego García-López, **Ljiljana Pavlovic** and Kathrin H. Hopmann
Organometallics, **2020**, 39, 8, 1339–1347.
<https://doi.org/10.1021/acs.organomet.0c00090> (open access)
- III. *Computational and experimental insights into asymmetric Rh-catalyzed hydrocarboxylation with CO₂*
Ljiljana Pavlovic, Martin Pettersen, Ashot Gevorgyan, Janakiram Vaitla, Annette Bayer and Kathrin H. Hopmann (*In preparation*)
- IV. *Mechanistic study of asymmetric Co-catalyzed hydrogenation of enamides*
Ljiljana Pavlovic, Hongyu Zhong, Paul J. Chirik and Kathrin H. Hopmann (*In preparation*)

List of other publications:

- V. *Carbon-carbon bonds with CO₂: Insights from computational studies*
Marc Obst¹, **Ljiljana Pavlovic**¹ and Kathrin H. Hopmann
Journal of Organometallic Chemistry, **2018**, 864, 115–127. (Minireview)
¹Shared first authorship
<https://doi.org/10.1016/j.jorganchem.2018.02.020> (open access)

I was responsible for the writing and all calculations presented in the papers **I**, **III**, and **IV**.

I was responsible for the calculations of Rh-COD and Rh-(S)-SEGPLHOS systems in the manuscript **II**.

I was responsible for the literature analysis and for drafting the sections about Pd and Rh complexes in the minireview **V**.

Acknowledgements

The research presented in this thesis was performed in the CHOCO group, at the Hylleraas Centre for Quantum Molecular Sciences at the Department of Chemistry, UiT The Arctic University of Norway.

My PhD journey started in 2016, and it would not have been possible without support and guidance of my supervisor Prof. Kathrin Helen Hopmann. Thank you for being an amazing supervisor and for everything you taught me during these years!

I want to thank the head of our department Prof. Annette Bayer and Prof. Luca Frediani for great collaborations and supervisions. I would also like to express my gratitude to Prof. Timo Repo for a short stay in his laboratory at the University of Helsinki. I am also very grateful for the opportunity to work with Prof. Paul J. Chirik and Hongyu Zhong and for inspired scientific conversations that we had.

Thanks to the CHOCO team and dear colleagues at the Hylleraas Centre and at the Chemistry department. Thanks to Glenn and Diego who helped me a lot during my studies. Special thanks to my darling Aya for support and friendship!

Thanks to all special people from my beloved Belgrade: Draga, Ranka, Ruza, Nata, Caki, Mesi, Lui and Ležaić family! Special thanks to my mom Radmila and my sisters Dana and twin Gaga for love, support and encouragement. (Puno Vas Volim!)

Special thanks to Vojin for his love, support and life full of adventures!

I also acknowledge funding by the Department of Chemistry at UiT, Tromsø Research Foundation, Research Council of Norway, NordForsk and Notur.

Abbreviations

(<i>R</i>)-StackPhos	Imidazole-based biaryl <i>P,N</i> -ligand
(<i>R,R</i>)-BDPP	(2 <i>R,4R</i>)-(+)-2,4-Bis(diphenylphosphino)pentane
(<i>R,R</i>)-iPr-DuPhos	(+)-1,2-bis[(2 <i>R,5R</i>)-2,5-diisopropylphospholano]benzene
(<i>R,R</i>)-Ph-BPE	(+)-1,2-Bis((2 <i>R,5R</i>)-2,5-diphenylphospholano)ethane
(<i>R,R</i>)-tBu-BOX	2,2'-Isopropylidenebis[(4 <i>R</i>)-4-tert-butyl-2-oxazoline]
(<i>S</i>)-iPr-PHOX	(<i>S</i>)-2-[2-(diphenylphosphino)phenyl]-4-isopropyl-4,5-dihydrooxazole
(<i>S</i>)-SEGPPOS	(<i>S</i>)-(-)-5,5'-Bis(diphenylphosphino)-4,4'-bi-1,3-benzodioxole
Aaron	An Automated Reaction Optimizer for New catalysts
B3LYP	Becke 3-parameter (exchange), Lee-Yan-Parr correlation Functional
B3PW91	Becke 3-parameter (exchange), Perdew-Wang correlation functional
B88	Becke exchange functional from 1988
B97D	Becke 97 functional including Grimme's dispersion correction
BIBOP	Bis(trialkylphosphane)
BIDIME	Dihydrobenzooxaphosphole
BINAP	2,2'-Bis(diphenylphosphino)-1,1'-binaphthyl
BP86	General gradient functional developed by Becke 1988
BSSE	Basis set superposition error
CASPT2	Second order perturbation theory-corrected complete active-space self-consistent field
CASSCF	Complete active-space self-consistent field
CC	Coupled Cluster
CCD	Coupled Cluster doubles
cc-pVNZ	Correlation-consistent basis sets by Dunning, N=D,T,Q, etc.
CCSD	Coupled cluster singles and doubles
CCSD(T)	Coupled cluster singles and doubles excitations and perturbative triples correlation
CI	Configuration Interaction
COD	1,5-Cyclooctadiene
def2-SV(P)	Split valence Karlsruhe basis set with polarization functions on heavy atoms (not hydrogen)
def2-TZVP	Split valence triple-zeta polarization basis set
DFT	Density functional theory
DIOP	(2,3- <i>O</i> -isopropylidene- 2,3-dihydroxy-1,4-bis(diphenylphosphino)butane)
DIPAMP	Ethane-1,2-diylbis[(2-methoxyphenyl)phenylphosphane]
DLPNO-CCSD(T)	Domain based local pair natural orbital coupled-cluster method with single and double excitations and the inclusion of perturbative triples correction
DMF	Dimethyl-formaldehyde
Dmpe	1,2-Bis(dimethylphosphino)ethane
Dppe	1,2-Bis(diphenylphosphino)ethane
<i>e.e.</i>	Enantiomeric excess
<i>e.r.</i>	Enantiomeric ratio
ECP	Effective Core Potential
GDIIS	Geometry optimization by direct inversion of the iterative subspace method

GGA	Generalized-gradient approximation
HF	Hartree-Fock
HS	High spin
IEFPCM	Integral equation formalism polarizable continuum model
IRC	Intrinsic reaction coordinate
KS	Kohn-Sham
LANL2DZ	Los Alamos National Laboratory 2-double- ζ
LANL2TZ	Los Alamos National Laboratory 2-triple- ζ
LDA	Local density approximation
L-DOPA	1-3,4-dihydroxyphenylalanine
LS	Low spin
LST	Linear Synchronous Transit
LYP	Lee–Yang–Parr gradient corrected correlation functional
M06-L	Minnesota 06 local functional
M11-L	Minnesota local functional with dual-range DFT exchange
MAA	Methyl 2-acetamidoacrylate
MP2	Second-order many-body perturbation method
MSE	Mean signed error
MUE	Mean unsigned (absolute) error
NHC	N-Heterocyclic Carbene ligands
PBE	Perdew-Burke-Ernzerhof exchange correlation functional
PBE0	Hybrid Perdew-Burke-Ernzerhof (PBE) exchange correlation functional
PBF	Poisson Boltzmann Finite element method, solvation model implemented in Jaguar 7.0
PES	Potential energy surface
PPh ₃	Triphenylphosphine
PW91	Perdew-Wang correlation and exchange functionals
QCISD	Quadratic Configuration Interactions with single and double excitations
QST	Quadratic Synchronous Transit
RMSD	Root mean square deviation
SDD	Stuttgart–Dresden pseudopotential
SMD	Solvation Model based on Density
SORCI	Spectroscopy-oriented configuration interaction method
<i>Sp</i>	Single point
SS	Standard state
Tpm	Tris-(1-pyrazolyl)methane) ligand
TPSS	Exchange functional of Tao, Perdew, Staroverov, and Scuseria
TS	Transition state
VWN	Correlation functional, developed by Vosko, Wilk and Nusair
ω B97XD	Range-separated hybrid functional from Head-Gordon and co-workers, which includes empirical dispersion

1. Introduction

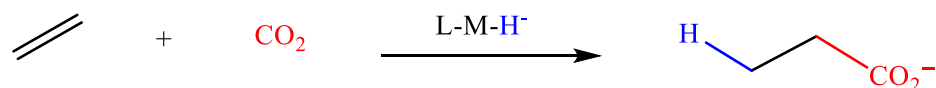
Chirality is an intriguing topic in chemistry as well as in biology. It is well known that many receptors and molecules that control various biological functions are chiral. Chirality implies that two molecules have the same chemical and physical properties but exist as enantiomers, which are not superimposable and which rotate the plane of polarized light in opposite directions. One enantiomer may have biological activity and may be used as a drug, whereas another enantiomer may be completely inactive or even toxic.¹ It is thus desirable to develop approaches for the formation of only one of the possible enantiomers. This may be achieved through enantioselective reactions, which represent good strategies for the formation of chiral fine chemicals, for example in the pharmaceutical industry.²

One possible approach to realize enantioselective reactions is to use chiral metal-complexes as catalysts. Many metals, with very different nature and reactivity, can be used. For example, in enantioselective hydrogenation reactions, well-known examples are rhodium-, iridium- and ruthenium-based catalysts,³⁻¹⁴ but also earth abundant metals such as cobalt and iron receive increasing attention as asymmetric hydrogenation catalysts.¹⁵⁻²³ These *3d* metals are interesting due to the fact that they can show different reactivities than their precious metal counterparts.²⁴ For other reactions, the scope of metals that can be employed may be less explored, and for example for the enantioselective hydrocarboxylation of alkene-type substrates, only one experimental study has been reported, with a rhodium-based catalyst.²⁵

In order to obtain a deeper insight into the possible reaction pathways, the selectivity-determining factors and the substrate preferences of asymmetric reactions, computational methods such as density functional theory (DFT) can be employed.^{26,27} The obvious advantage of DFT is not only its reasonable cost and accuracy but also its ability to deal with large systems. DFT methods are often employed to rationalize experimentally known systems, but can in principle also be used to predict the behaviour of complexes that have not yet been studied experimentally.

In this thesis, DFT methods were employed to study the metal-catalyzed enantioselective addition of small molecules, CO₂ and H₂, to alkenes to form more valuable chiral products. The studied transformations include asymmetric hydrogenation and hydrocarboxylation of alkenes, with the general reactions displayed schematically in Figure 1.1.

General hydrocarboxylation reaction



General hydrogenation reaction

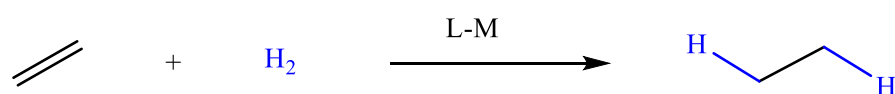


Figure 1.1 Schematic representation of the reactions studied in this thesis. M = Co, Rh, whereas L = COD, *P,P*, *N,N* or *N,P* ligands. If the substrates are prochiral, and L is chiral, chiral products can be formed.

In both hydrogenation and hydrocarboxylation reactions, a large variety of unsaturated substrates can be converted, which may undergo different mechanistic routes.^{15,17,25,28} In the projects described in this thesis, I have used DFT to investigate the reaction mechanisms of Rh-based hydrocarboxylation of different styrene derivatives with CO₂ and the Co-based hydrogenation of different enamides. Besides mechanistic analysis, the goal of my work was also to elucidate the origin of the substrate preferences seen in experiments and the factors that control the observed enantioselectivities. Density functional theory was employed in order to calculate molecular geometries and vibrational frequencies of intermediates and TSs and to obtain reaction energies, activation barriers and enantiomeric excesses. In the hydrocarboxylation study, non-selective CO₂ conversion into carboxylic acids with an achiral Rh-COD catalyst was investigated. Then, the study was expanded to include several chiral ligands to form potential catalysts for the asymmetric Rh-based hydrocarboxylation. In the computational analysis, particular emphasis was put on the intimate mechanistic details of the CO₂ insertion into metal-C bonds. This is important, because CO₂ may insert into metal-ligand bonds through both inner and outer sphere mechanisms,²⁹ which in case of a prochiral substrate may result in different stereochemical configurations at the chiral carbon.

The aim of my work in this thesis can be summarized as follows:

- Investigation of the reactions mechanisms of transition metal-catalyzed H₂ and CO₂ addition to alkenes.
- Analysis of the behaviour of CO₂ during C-CO₂ bond formation and evaluation of the importance of metal-CO₂ interactions.
- Elucidation of the stereoselectivity-determining factors in asymmetric hydrogenation and hydrocarboxylation and evaluation of the ability of DFT and implicit solvent models to reproduce experimental enantioselectivities of complex reactions.
- Design of new hydrocarboxylation catalysts and computational analysis of their performance.

The content of this thesis is divided into six sections. Chapter **II** gives a brief background of the computational methods. In Chapter **III**, I introduced what kind of strategies we used for modelling homogeneous reaction, followed by a description of the DFT methods that have been employed in the current work and their applications. In chapters **IV** and **V**, the obtained results are discussed and finally summarized in chapter **VI**. This is followed by the references and the included papers **I-IV**.

2. Computational methods

Over the past few decades, density functional theory methods have evolved and advanced as the most widely employed computational approaches in different fields of chemistry and physics. These methods are used to calculate and determine electronic structures and to explore various molecular properties. For instance, in organometallic chemistry, molecular properties of interest may be: bond lengths and angles, spin or charge distributions, vibrational frequencies, spectral properties, noncovalent interactions and their strength, etc. In this thesis, our goal was to study the mechanistic details of the conversion of small molecules into more valuable products. Hence, we were particularly interested in the investigation of reaction pathways and in the prediction of barrier heights and enantioselectivities. Below, I will provide a general introduction to computational *ab initio* methods and DFT methods.

2.1 Introduction to computational *ab initio* methods

Ab initio methods are established on the basis of the Schrödinger equation, where the wave function that is used to compute electron distributions, contains all information about the molecule.³⁰ The simplest method is the Hartree-Fock (HF) method, which has been known since 1928. It is worth highlighting that HF theory uses only one Slater determinant to represent the wave function and it does not include electron correlation. Qualitatively speaking, electron correlation is defined as the influence on the motion of a given electron, exerted by the presence of the other electrons. However, HF computes electron-electron interactions only as the interaction of each electron with the overall electronic density of the system and does not take into account instantaneous electron-electron interactions. As such, HF is often called a “mean field” approach. In order to predict more accurately molecular properties, one should use advanced *post*-HF methods (such as Coupled Cluster (CC) and Configuration Interaction (CI)) that include electron correlation. However, these methods are generally time consuming and not accessible for the systems investigated in this thesis, hence they will not be a subject of further discussion. A widely popular computational method that is time and cost efficient is density functional theory³¹ and its fundamentals will be described further below.

2.2 Fundamentals of Density Functional Theory

DFT has been shown to be one of the most efficient and convenient computational methods for studying mechanisms of organometallic reactions. It was introduced by Hohenberg and Kohn in 1964, even though early attempts of this method were known already in the 1920s through the work of Thomas and Fermi.^{32,33} The main idea was to swap the complicated wave function for describing molecular properties of many electron systems with an electron density that is a quantity, which depends only on three spatial variables. According to Hohenberg's and Kohn's first theorem, the energy of the system can be given as a functional of the ground state electron density $\rho_0(r)$:

$$E_0[\rho_0] = E_{Ne}[\rho_0] + F_{HE}[\rho_0] \quad (2.1)$$

where the first term in equation (2.1) represents a potential energy due to nuclei electron attraction ($E_{Ne}[\rho_0] = \int \rho_0(r)V_{Ne} dr$) and the latter term, $F_{HE}[\rho_0]$ is an universal functional, which is however unknown. This term includes the kinetic energy functional $T[\rho]$ and the electron-electron repulsion functional $E_{ee}[\rho]$.

$$F_{HE}[\rho] = T[\rho] + E_{ee}[\rho] \quad (2.2)$$

$$E_{ee}[\rho] = J[\rho] + E_{ncl}[\rho] \quad (2.3)$$

In the second term in the equation (2.2), the piece of information that is known is a classical Coulomb part $J[\rho]$, where the $E_{ncl}[\rho]$ functional (2.3) represents the non-classical (quantum) contribution to the electron-electron interaction that has the following corrections: self-interactions, exchange and correlation. Finding an accurate kinetic energy functional $T[\rho]$ is a very challenging task, which can however be avoided by switching to the Kohn-Sham (KS) method. The KS formulation uses the kinetic energy of a fictitious system of the non-interacting electrons $T_s[\rho]$ and the remaining part of the kinetic energy is then incorporated in the exchange-correlation functional $E_{xc}[\rho]$, which is then defined as:

$$E_{xc}[\rho] = E_{ncl}[\rho] + (T[\rho] - T_s[\rho]) \quad (2.4)$$

The exchange-correlation functional ($E_{xc}[\rho]$) can be separated into two parts: exchange functional, $E_x[\rho]$ and correlation functional $E_c[\rho]$ where each of them are also functionals of the electron density.

The universal functional is then given with the following equation (2.5).

$$F_{HE}[\rho] = T_s[\rho] + J[\rho] + E_{xc}[\rho] \quad (2.5)$$

Because the exchange-correlation functional is unknown,³⁴ a huge effort has been put into finding good approximations to it. Such approximations are developed both by constructing functional with desired mathematical and physical properties and by fitting them to known thermochemical data.

The ability of functionals to reproduce experimental data, in order to predict more reliable molecular properties, should be ideally within 1 kcal/mol, which is referred to as chemical accuracy.³⁵ In order to determine how accurate a specific functional is for the study of a particular property, one needs to perform a benchmark study where the results obtained for a given DFT functional are compared with experimental data or more accurate *ab initio* methods.

A widely used set of accurate experimental data is called the G2 data set and it is employed as a standard for the calibration of numerous methods.³⁶ It contains experimental data on atomization energies, ionization potentials and proton affinities of more than 100 molecular compounds of the first and second rows. Another example is the expanded G3 data set that includes 75 additional molecules.³⁷ During the past few years, many other data sets in benchmark studies have also been reported,³⁸⁻⁴⁰ for example to study a particular property, such as dissociation energies in metal complexes.²⁷

2.3 An overview of Density functionals

The pursuit and development of approximate exchange and correlation functionals is a very attractive area for theoretical chemistry, because the deeper insight obtained might be relevant for the design of more sophisticated functionals that can predict various properties very accurately.

The hierarchy of DFT functionals has been associated with a biblical ladder that leads to heaven.³⁴ This idea was given by Perdew who introduced Jacob`s ladder and separated functionals on several rungs (Figure. 2.1).⁴¹ At the first rung of the ladder are placed local density approximate functionals (LDA)⁴² that assume that the electron density is an uniform electron gas.⁴³ A well-known example is the correlation VWN functional, developed by Vosko, Wilk and Nusair.⁴⁴ However, the electron density is not uniform in molecules. LDA methods are not very accurate for molecular quantum chemistry, because they underestimate bond energies and reaction barriers.³²

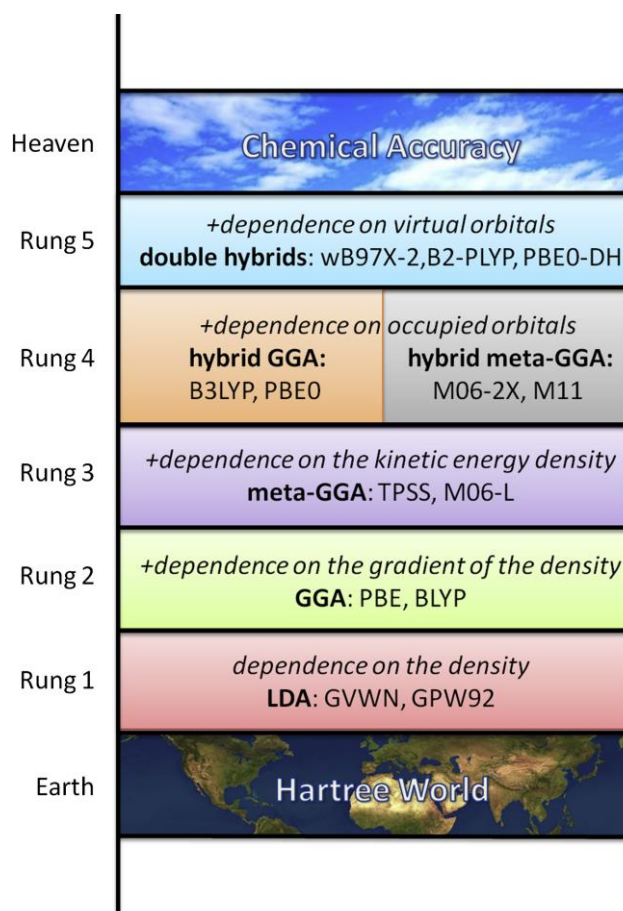


Figure 2.1^a The hierarchy of the DFT exchange-correlation functionals according to their simplicity and accuracy shown as the Jacob`s ladder.⁴¹

Further improvements are the generalized-gradient approximation GGA functionals³² that include the gradient of the density and thus assume that the electron density is not

^a Adapted from [Annual Reports in Computational Chemistry, Vol 11/1574-1400, Joaquín Calbo, Enrique Ortí, Juan C. Sancho-García and Juan Arago, The Nonlocal Correlation Density Functional VV10: A Successful Attempt to Accurately Capture Noncovalent Interactions, Pages 37-102]. Copyright (2015), with permission from Elsevier B.V.

homogeneous. The GGA functionals give better atomization energies⁴⁵ as well as reaction barriers⁴⁶ relative to the LDA functionals, but they are not good enough for accurate descriptions of several properties.⁴⁷ One of the well-known exchange functionals was developed by Becke in 1988, abbreviated as B88.⁴⁵ Several years later, Perdew, Bruke and Ernzerhof developed the exchange PBE functional.⁴⁸ Among the widely used correlation functionals are LYP⁴⁹ and PW91.⁵⁰ As we climb further, the meta-GGA^{51,52} level appears and these functionals contain the kinetic energy density. They showed an improvement regarding to the reproduction of atomization energies and well-known examples are TPSS⁵³ and M06-L.⁵⁴ The hybrid functionals occupy the fourth rung and contain exact HF exchange information.³² The most popular B3LYP^{43,45,49} functional belongs to this group. As we continue to climb further, we approach the so called “heaven of chemical accuracy” that is within 1 kcal/mol. Thus, on the top are the most sophisticated functionals but the use of some of them can be very expensive. From various benchmark studies,^{34,55,56} it is well known that GGA and hybrid functionals are still among the most popular ones. In this thesis, we used two functionals, the hybrid B3LYP and the gradient corrected PBE functional.

Among the hybrid functionals, B3LYP has been known since the 1990s and it is still one of the most featured functionals. One of the reasons for its dominance lies in the fact that it is not heavily parameterized compared to some other functionals, and it is also capable to predict several molecular properties quite accurately.³⁵ It is a common practice in the community of theoretical chemists to assign functionals according to their exchange and correlation terms. Concerning that, in B3LYP, B3 represents the Becke88 3-parameter⁴⁵ exchange term and LYP⁴⁹ (Lee, Yang and Parr) the correlation term. In our study of asymmetric Co-based hydrogenation of enamides (Chapter V, Paper IV), B3LYP was the method of choice, given that the same computational protocol was shown to provide good agreement with experiments in a previous study on a related dppe-Co-(CH₂SiMe₃)₂ system²⁸ and its use allowed direct comparison of previous and current results.

A popular GGA functional is PBE (Perdew-Burke-Ernzerhof).⁵⁷ The PBE functional was our method of choice in the Rh-based hydrocarboxylation with CO₂ study presented here (Chapter IV, Papers I and III). The choice was motivated by the fact that PBE (together with an empirical dispersion correction) was shown to give good results in a benchmark performed by our group on iridium-mediated reactions.²⁶

3. Computational protocol

There are several aspects that have to be taken into account when modelling chemical reactions that take place in solution. Some of them are the chosen molecular model, the description of its geometry and electronic structure, the choice of the basis sets and the description of dispersion and solvation effects. The use of full molecular systems, without any truncations of the catalyst or involved species is mandatory in the study of asymmetric reactions. This is because the enantioselectivity can be quite affected by the presence of small groups on substrates⁵⁸ or ligands.⁵⁹⁻⁶¹

In this Chapter, I will briefly describe basis set concepts, because the choice of basis set can affect the results a lot. In this thesis, only homogeneous reactions were studied, which means that all active species are in the same phase, usually in solution. Therefore, it is important to include a solvation model in order to describe properly the system of interest, and I will introduce briefly the relevant models. One more important thing to consider is a proper description of noncovalent interactions, thus the use of empirical dispersion corrections will be also introduced. After this part, I will introduce modelling of reaction mechanisms, where the emphasis will be put on the potential energy surface concept and on the optimization techniques to locate minima and TSs. Then attention will be given to the two important concepts: energies and enantioselectivities. At the end of this chapter is given a section where the accuracy of DFT functionals to predict properties of interested is outlined.

3.1 Basis sets

Three important concepts in computational chemistry will be discussed here: basis sets, pseudopotentials (ECPs) and basis set superposition errors (BSSEs).

Basis sets are mathematical functions that are used to describe the electron distribution around the nuclei.³⁰ In our calculations, we often use contracted Gaussian functions. Among them the most used are Pople⁶² and Dunning`s⁶³ Correlation Consistent basis sets. A minimal basis set is the smallest number of functions that is used to describe the electron distribution of a simple

atom. A term *split-valence* basis set was introduced later when more functions were taken into account. These basis sets have one function for core atomic orbitals whereas valence orbitals are improved in contrast to minimal basis set, because they have for example, two functions per atomic orbital (double-zeta) or even three functions per atomic orbital (triple-zeta).

In this thesis, for geometry optimizations, we used the Pople split-valence triple-zeta basis set 6-311G(d,p). It involves six primitive Gaussian functions for core orbitals and three Gaussian functions for inner valence orbitals.³⁰ The letters in parentheses indicate that *p* functions are added on hydrogens and *d* functions are added on all other atoms. These basis functions are extra functions added to the basis set to give a better description of chemical bonds and they are often called polarization functions. One more group of functions that are well known are diffuse functions, which are often used to render broad electron distributions that are important in anions. Furthermore, it is common to use polarization and diffuse functions for single point calculations, in order to obtain more accurate electronic energies. Some of the examples are: 6-311+G(d,2p) and 6-311++G(2df,2pd).

An important concept is the Effective Core Potential (ECP).³⁰ All-electron basis sets are expensive to compute, especially for heavier atoms such as metals. The ECP is used to describe the electronic distribution in heavy atoms. Within this approximation core electrons are replaced by a set of frozen functions, because the core electrons are not important for forming bonds between atoms. The use of core potentials also has the advantage that they are parameterized to reproduce relativistic effects. Among the most used pseudopotentials are LANL⁶⁴, abbreviated as Los Alamos National Laboratory ECPs of Hay and Wadt, CEP (Consistent Effective Potential) introduced by Stevens and co-workers³⁰ and Stuttgart–Dresden (SDD)⁶⁵ energy-constant pseudopotentials. In this work, the LANL2DZ pseudopotential was used on Rh and LANL2TZ on Co.

The third basis set-related concept discussed here is the Basis Set Superposition Error (BSSE).³⁰ This process leads to an artificial lowering of the electronic energy, when two separated molecular models are combined into one. The BSSE arises from the fact that one uses a finite basis set, and that fragments that are moved closer together start borrowing basis functions from each other. The BSSE can be corrected with the Counterpoise (CP) correction method. This approach gives an estimate of the intermolecular basis set error. In general, the BSSE error is expected to be small if a large enough basis set is used.

It is worth highlighting that the mentioned concepts may affect the final energies significantly. With the DFT method, it has been shown that reasonable energies can be obtained with polarization split valence double zeta basis sets.⁶⁶

3.2 Solvation models

It is a common approach to include solvent effects in our calculations, if we want to compare results with a reaction in solution.³⁰ The solvent can stabilize charges and thus affect energies and geometries. There are two approaches to include solvent effects in DFT.⁶⁷ The first approach assumes explicit interactions between the solute molecule and the solvent and it is called microsolvation. In DFT models, one can add a single explicit solvent molecule to test if it may affect reactivity or selectivity. This approach has been tested in our Co-hydrogenation study (Paper IV). The second approach, which is implicit, treats the solvent as a continuous dielectric medium where a solute (the molecule of interest) is placed in a cavity.^{68,69} In physics, a dielectric is an electric material that can interact with an external field and in turn it can be polarized. In this thesis, we used an integral equation formalism polarizable continuum model, IEFPCM, developed by Cancés, Mennucci and Tomasi.⁷⁰⁻⁷² IEFPCM was included in all calculations in this thesis, also for microsolvation model.

3.3 Dispersion

Dispersion interactions are weak attractive forces between molecules.⁷³ Although they are weak, their total contribution to the energy of a system can be large. These interactions are important forces in chemistry and biology.⁷⁴ In biological systems, they have a main role in the antigen-antibody recognition. Alongside hydrogen bonding, dispersion interactions are responsible for the specific orientation of aromatic amino acids in proteins as well as for the stability of DNA.⁷³ Based on the molecule's nature, dispersion interactions can be divided into: stacking or π - π interactions, C-H- π , cation- π , anion- π etc.⁷⁵ Over the past twenty years, there are reported numerous computational studies where these interactions were analyzed and described.⁷⁶⁻⁸⁰ In asymmetric catalysis, these weak interactions are often responsible for the stereochemical outcome of a reaction.^{81,82} Hence, the proper description of these interactions is compulsory in the computational study of enantioselective reactions.

For example, a main limitation of the B3LYP functional is a lack of proper description of some long-range weak dispersion interactions, for example π - π interactions.⁸³ In this regard, empirical dispersion effects were introduced later through the work of for example Grimme and

Truhlar.⁸⁴⁻⁸⁷ Truhlar's approach in the so-called Minnesota functionals uses an intrinsic parameterization of the functional to reproduce dispersion.

On the other hand, Grimme's approach⁸⁸ in the so-called D2⁸⁹, D3⁹⁰ and D3B3J⁹¹ corrections, computes the dispersion effect based on the distance between atoms and which in later versions contained functional-dependent parameters. The addition of Grimme type empirical dispersion corrections to DFT to give so-called DFT-D approaches has led to more reliable results,⁹² especially for the accurate prediction of reaction energies and barriers in metal-based reaction, where the errors can be reduced by approximately 20 kcal/mol.^{66,93}

Today, the method DFT-D is widely accepted as a dispersion corrected density functional. In this work, we used dispersion corrected methods: B3LYP-D3 and PBE-D2.

3.4 Modelling of reaction mechanisms

Metal-catalyzed reactions are often multi-step processes, which means that the product formation occurs via several intermediates. Hence, many reaction pathways need to be analyzed. One of the main tasks in the study of reaction mechanisms is to describe, determine and understand the structures of the intermediates and TSs.⁹⁴ The DFT method is often used in order to obtain geometries and energies of molecules, whereas computed Gibbs free energies are used to render energy profiles and thus to investigate various mechanistic possibilities. The energy profile is represented as a plot of the computed energy against the reaction coordinate.

A path from the reactants to the product through intermediates and transition states is described with the help of potential energy surfaces (PES).⁹⁵ Furthermore, one can define it as a path that contains all information about a specific chemical process. Hence, I will briefly describe the potential energy surface concept alongside with optimization techniques to locate intermediates and TS structures.

3.4.1 PES

A potential energy surface (PES) is a link between the energy of the system and its geometry.⁹⁵ In reality, PESs are quite complex and hard to be visualized. Therefore, it is a common procedure to use just a piece of information from these multidimensional surfaces. A simple PES would be a one-dimensional PES for diatomic molecule, where the energy is plotted against specific geometric parameter (r), for example the bond length.

We are often interested in locating minima and first-order saddle points on the PES. In a mathematical expression, at this point the first derivative of the potential energy (the gradient) with respect to each geometric parameter ($dE(r)/dr$); is zero.⁹⁵ The second derivatives of the energy with respect to the geometric parameters (d^2E/dr^2) are referred to as the Hessian or force constant matrix, where the force constant values can help us to identify the nature of the stationary points (Figure 3.1 a). Minima match to reactants, intermediates and products, where all force constants, eigenvalues of the Hessian are positive ($d^2E/dr^2 > 0$).^{30,95} First-order saddle points correspond to transition states and have only one negative eigenvalue of the Hessian, along the reaction coordinate of interest, but in all other directions, eigenvalues are positive.

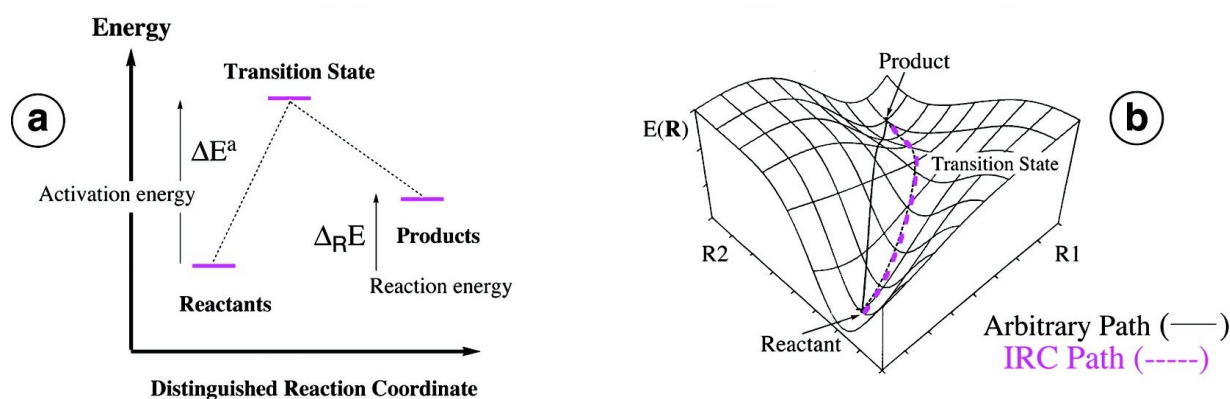


Figure 3.1^b a) Illustration of the stationary points on the PES. b) Illustration of the energy profile along IRC path vs arbitrary path.⁹⁴

It is worth noting that the nature of these stationary points can be tested through calculations of vibrational frequencies. If all vibrational frequencies are real, then the stationary point is a minimum. In contrast to that, the presence of only one imaginary frequency leads to the conclusion that a TS is located. After determination of the stationary points on the PES, the intrinsic reaction coordinate (IRC) calculations are performed in order to confirm that a specific TS is indeed connected with the intermediates, such as reactant and product (Figure. 3.1 b).^{94,96} Equilibrium structures are minima on the PES and their vibrations can be described with the harmonic oscillator approximation.⁹⁶ In a simple macroscopic ball-and-spring model, a diatomic molecule vibrates like two balls on a spring with a potential energy. As the bond between two atoms stretches and compresses, the potential energy of the molecule increases.

^b Adapted with permission from [Kraka, E.; Cremer, D., *Accounts of Chemical Research* **2010**, 43 (5), 591-601] Copyright (2010) American Chemical Society.

In real systems, the harmonic oscillator curve differs when a molecule is distant from its equilibrium structure and this deviation is called anharmonic oscillation. Moreover, molecules always vibrate hence they will be placed on various vibrational levels. In computational chemistry, the vibrational frequencies are typically computed on the basis of the harmonic oscillator approximation, as a second derivative of the energy with respect to nuclear positions. However, in order to obtain more accurate frequencies⁹⁷ one can employ an anharmonic correction, where the higher order derivatives are included.

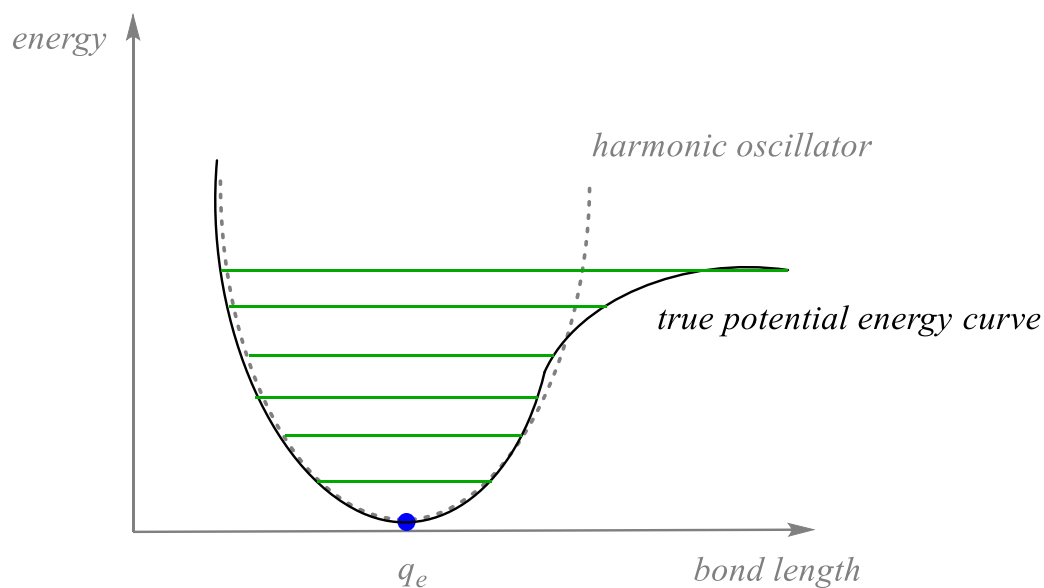


Figure 3.2 A one-dimensional PES of a diatomic molecule where the harmonic approximation is applied. The true potential energy curve (black) differs from the harmonic oscillator (dashed line) when the molecule is away from the equilibrium. Vibrational levels are given with green color, where q_e is the equilibrium structure of a diatomic molecule (adapted from⁹⁵).

3.4.2 Geometry optimization techniques

In the study of reaction mechanisms, it is common to build energy profiles that contain all intermediates and TSs structures. In order to locate these molecular geometries, one can employ several optimization techniques.^{30,98} This section gives a brief overview of the optimization techniques for finding minima, followed by optimization techniques to locate TS structures. The term geometry optimization refers to a process, where atoms are arranged in such a manner that they yield the energetically most stable structures. There are several optimization techniques implemented in different computer programs.^{99,100} The process starts with submitting a geometry, which we have previously built, to a computational algorithm that alters molecular arrangements until it finds a stationary point. These algorithms will converge the geometry to a local minimum on the PES. We can never be certain if we are in global minima,

therefore several different conformers need to be tested. For example, conformers may differ a lot in the energy, due to rotation of some groups around one or more bonds. Thus, in computational chemistry, an extensive conformational search is necessary, in order to obtain reliable conclusions about chemical processes.

There are different types of algorithms for finding minima, where most of them use the first and the second derivatives of the energy with respect to the geometrical parameters.^{30,99} Gradient methods use only the first derivative information and among the widely known ones are conjugate gradient and quasi-Newton methods. For example, quasi-Newton methods are often employed as the algorithm of choice. A simple workflow of this optimization method consists of several steps. First, the energy and the gradient are calculated followed by the minimization step across the line from the current and previous point. Next, the Hessian is updated at each step.

Algorithms that use the second derivative information are Newton-Raphson and GDIIIS (geometry optimization by direct inversion of the iterative subspace) methods.

3.4.3 Optimization methods to locate TSs

One of the biggest challenges in the study of reaction mechanisms for computational chemists is finding a transition state (TS). It is the highest energy point along the reaction pathway. There are several optimization techniques that one can use in order to locate saddle points (TSs).^{30,100} One of the simplest approaches to locate a TS is to start from a structure that looks like the target TS. In general, we select atoms, bonds or angles of interest and fix them at certain values, while other bond lengths and angles are unconstrained and freely optimized. This strategy is based on our chemical intuition. With the help of the linear transit scan method, one can do a constrained stepping, then take the point with the highest energy and proceed to a TS optimization from there.

Some algorithms are only based on the optimized geometries of the reactant and product and these approaches use an interpolation scheme between two minima. These methods locate a point close to the target TS. Among the widely known are Linear Synchronous Transit (LST) and Quadratic Synchronous Transit (QST).³⁰

In the next two sections, two important concepts, energies and enantioselectivity, will be outlined.

3.5 Energies

The PES calculations can provide the electronic energy of a system of interest.⁹⁵ After geometry optimization calculations, we can extract the electronic energy. However, in order to make predictions about chemical systems, we need to obtain the *free* energies. The Gibbs free energy (G), enthalpy (H) and entropy (S) can be obtained after vibrational frequency calculations.³⁰

In the study of chemical transformations, chemists introduced a standard state condition as a reference tool to compare various reactions.¹⁰¹ The standard state is 1 atm for the gas, whereas for some substances in solution, it is 1 M concentration. However, the standard state of solvent is not 1 M, but the pure solvent. For example, for water, the standard state is pure water, which has a molarity of 55 M.

We are often interested in the change of Gibbs free energy (ΔG), thus the sign of ΔG will give us information about the reaction spontaneity. The change of Gibbs free energy (ΔG) is related with the reaction quotient (Q) and the equilibrium constant (K) with the following formula:

$$\Delta G = RT \ln \frac{Q}{K} = RT \ln Q - RT \ln K \quad (3.1)$$

A reaction quotient Q represents concentrations or pressures of all active species during a chemical reaction. On the other hand, K represents these concentrations or pressures at equilibrium. Under standard state conditions of 1 M, the concentrations of reactants and products are assumed to be equal, thus $Q = 1$.¹⁰¹ Now, the standard Gibbs free energy can be written as:

$$\Delta G^\circ = RT \ln 1 - RT \ln K \quad (3.2)$$

Due to fact that $\ln 1 = 0$, the equation above can be rewritten as:

$$\Delta G^\circ = -RT \ln K \quad (3.3)$$

In this manner, one can find the standard Gibbs free energy change of a reaction from its equilibrium constant.

In computational chemistry, these insights may be quite helpful when an evaluation of computed energies take place. The relationship between the experimentally determined Gibbs free energy of reaction ΔG_r , and the standard state free energy ΔG°_{1M} is given below.¹⁰²

$$\Delta G_r = \Delta G^\circ_{1M} + RT \ln \frac{[P]}{[R]} \quad (3.4)$$

In experimental work, under reaction conditions, concentrations of all active species are often unknown. It was already mentioned that the computed energy ΔG°_{1M} assumes that the concentrations of reactants and products are equal under standard state conditions (1 M). When this statement is valid, we can write $\Delta G_r = \Delta G^\circ_{1M}$. This implies that under standard state conditions, the computed energy is actually obtained under stoichiometric conditions instead of catalytic conditions, where the excess of reactant is present. However, in metal-based catalysis, reactions often proceed under catalytic conditions. Therefore, the interpretation of obtained energies should be made with caution, when the concentration effect or pressure play important roles.

The Gibbs free energies reported in this work correspond to the solution standard state (1 M) and were determined as:

$$\Delta G^\circ_{1M} = \Delta G^\circ_{1atm, 298 K, BS1} - \Delta E_{BS1} + \Delta E_{BS2} + T_{corr} + SS_{corr} + BSSE \quad (3.5)$$

where ΔG°_{1atm} is the computed energy that corresponds to 1 atm standard state, BS1 is the basis set that was used for geometry optimizations and BS2 represents a larger basis set, employed during single point (*sp*) calculations to get more accurate energies. Temperature (T), standard state (SS) and BSSE corrections are added to the final energy. The BSSE correction is explained in the Basis set section (Chapter III), whereas the SS and temperature corrections will be outlined in the next section.

3.5.1 Corrections to the energy

The computed Gibbs free energy is by default obtained at 298 K and thus under different temperature conditions, it has to be converted into one that matches to the experiments. In our study, we employed the Gaussian *freqchk* utility to calculate temperature corrections. It is also a common practise to translate the computed free energy at 1atm (ΔG°_{1atm}) into a 1 M solution standard state (ΔG°_{1M}). For this purpose, the following expression can be used:

$$\Delta G^\circ_{1M} = \Delta G^\circ_{1atm} + R_1 T \ln(R_2 T^{\Delta n}) \quad (3.6)$$

where $R_1 = 8.31447 \text{ J K}^{-1} \text{ mol}^{-1}$, $R_2 = 0.08206 \text{ L atm K}^{-1}$; T is the temperature (T) in K and Δn is the change in number of moles. For a simple association reaction $A + B \rightarrow C$, Δn has the

value of -1, due to reduction of 1 mole. Therefore, at 273 K (0°), the above expression is -1.69 kcal/mol and that value was added to the final energy in the hydrocarboxylation study (Papers I, III). The hydrogenation reaction (Paper IV) occurs at 323 K (50°) and the above value is -2.1 kcal/mol. It is important to add that only reactions with unequal number of moles are affected by the standard state conversion and the final energy is corrected for these specific reactions only.

3.6 Enantioselectivity

In asymmetric reactions, a new element of chirality is formed on a prochiral substrate, resulting in unequal enantiomeric product ratio. This thesis considers two asymmetric reactions, given in paper III and IV. Thus, in this section, the attention is first given to several key concepts related to asymmetric catalysis such as chirality, evaluation of enantiomeric excess (*e.e.*) with the aid of DFT and the Curtin Hammett principle.

3.6.1 Chirality

There can be different types of chirality present in a molecule.^{81,103} Chirality may be a consequence of a chiral atom, which is connected with different substituents. A well-known example is a *sp*³-hybridized C atom that has four different groups linked to it. A chiral molecule does not have a plane of symmetry and it is a non-superimposable compound. Enantiomers always have different configurations at the chiral C atoms, whereas diastereoisomers can have the same configuration at one center at the most (Figure 3.3).

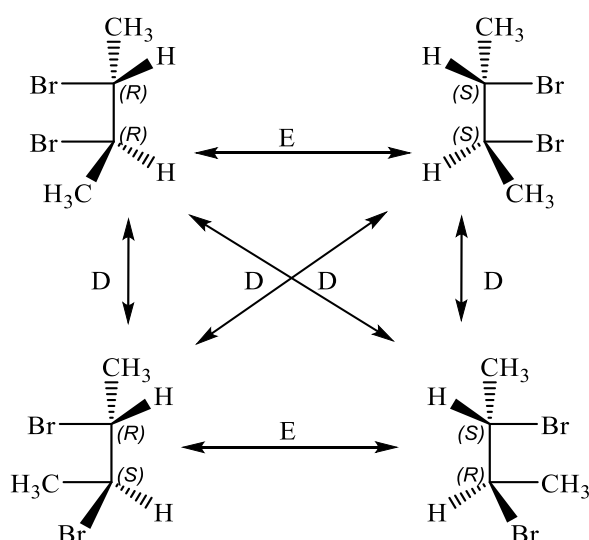


Figure 3.3 Relationship between enantiomers (E) and diastereoisomers (D).

A second type of chirality, referred to as axial chirality, may occur due to constraints that keep four substituents of a molecule in an arrangement that cannot be superimposed on the mirror image. A common example are biaryls, where the rotation around the single bond between the two aromatic rings is constrained.¹⁰⁴ This type of chirality is also called *atropisomerism*, whereas a 6,6'-dinitro-2,2'-diphenylic acid was the first experimentally detected compound where atropisomerism was recognized (Figure 3.4).¹⁰⁵ Axial chirality is very important in asymmetric organometallic catalysis due to the fact that many chiral ligands contain these biaryls components.

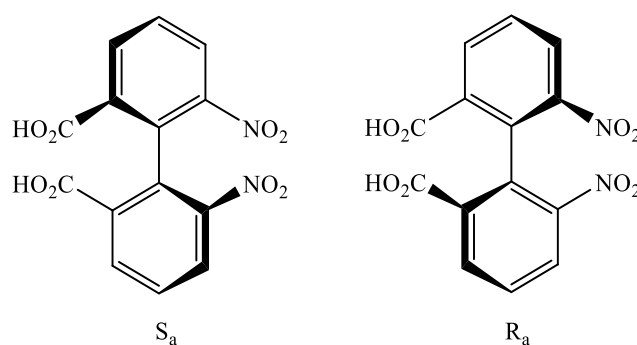


Figure 3.4 Atropisomers of 6,6'-dinitro-2,2'-diphenylic acid.

3.6.2 Evaluation of enantiomeric excess with DFT

In computational chemistry, the energy difference between a pair of diastereomeric TSs can be used for the evaluation of the enantiomeric excess (*e.e.*) of a reaction (eq 3.7).³¹ It is defined as an excess of one enantiomer over another in the mixture of both enantiomers.

If there are more than two TS structures that are energetically close lying, the *e.e.* will be computed as a sum over all these TSs. The barrier of each TS needs to be computed relative to the most stable conformer.

$$ee_{theo} (\%) = \frac{1 - e\left(-\frac{\Delta\Delta G_{R/S}^\ddagger}{RT}\right)}{1 + e\left(-\frac{\Delta\Delta G_{R/S}^\ddagger}{RT}\right)} * 100 \quad (3.7)$$

Additionally, it needs to be kept in mind the exponential dependence between the computed energy difference of the diastereomeric TS structures and the enantiomeric excess. From the graph given below (Figure 3.5), we can also see that the selectivity is temperature dependent. At lower temperature (173.15 K), it can be noted that the curve is much steeper than at higher temperature (298 K). This indicates that an enantiomeric excess of 90 % can already be reached

when the energy difference between two TSs is 1 kcal/mol. Hence, very reliable methods are necessary for the estimation of *e.e.*'s.

In order to compare the computed *e.e.* with the experiments, the common procedure is to estimate the error in kcal/mol. For example, the error is 0.5 kcal/mol if the computed *e.e.* is 25 % and the experimental value is 60 % (at 298.15 K). On the other hand, the error is 1.5 kcal/mol if the computed *e.e.* is 91 % and the experimental value is 99.1 %.

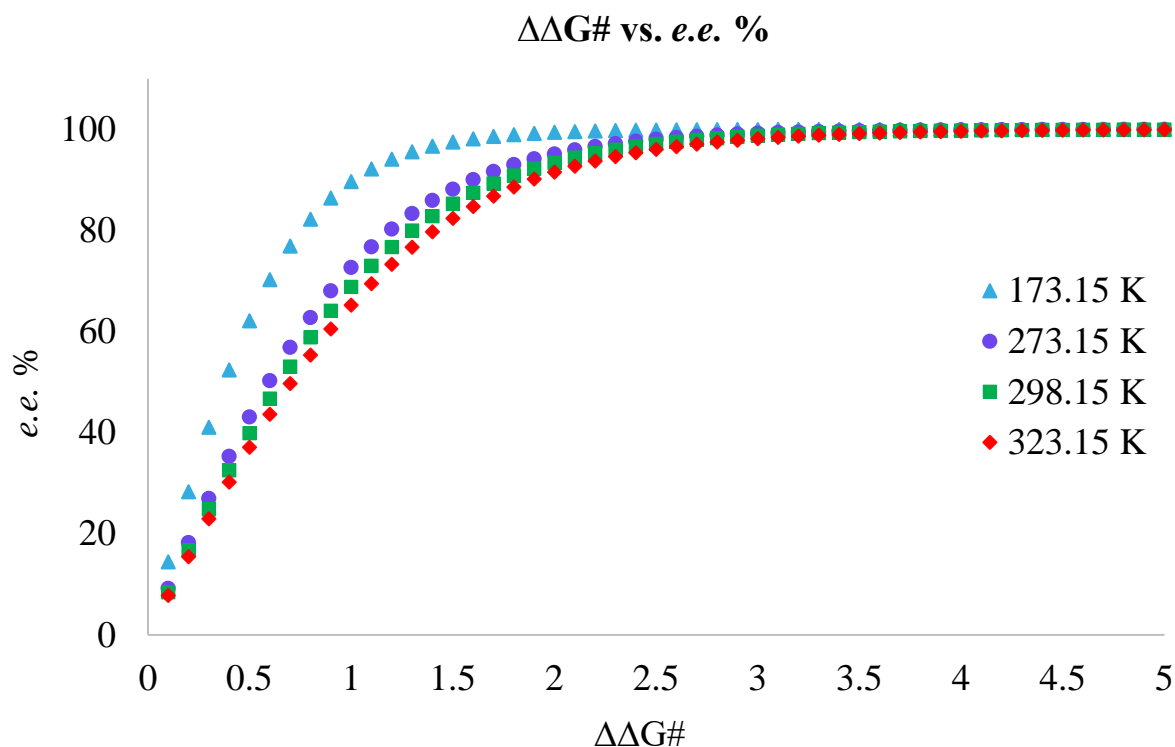


Figure 3.5 The exponential dependence between the *e.e.* and the $\Delta\Delta G^\ddagger$ (kcal/mol) and the temperature dependence of the *e.e.*.

3.6.3 The Curtin Hammett principle

During enantioselective reactions, the prochiral substrate can undergo molecular changes over distinguished reaction pathways to yield two diastereomeric intermediates. It was already mentioned that enantioselectivity is often estimated as an energy difference ($\Delta\Delta G^\ddagger$) between the pro-(*S*) and pro-(*R*) TS pair, whereas the energy difference between diastereomeric intermediates is assumed irrelevant.³¹ Under these conditions, the rate of the interconversion of intermediates needs to be faster than the rates of the two diastereomeric reactions (Figure 3.6).¹⁰⁶ This assumption is known as the Curtin Hammett principle.¹⁰⁷

In this particular example (Figure 3.6), the minor intermediate pro-(*S*)-Int will give the major (*S*)-product, via (*S*)-TS. This scenario is known as the minor/major principle.^{108,109} The opposite situation is also possible, where the more stable isomer yields the major product. This case is known as the lock and key concept.⁵ The process in the middle is an isomerization TS, where pro-(*S*)-Int interconverts into pro-(*R*)-Int or vice versa.

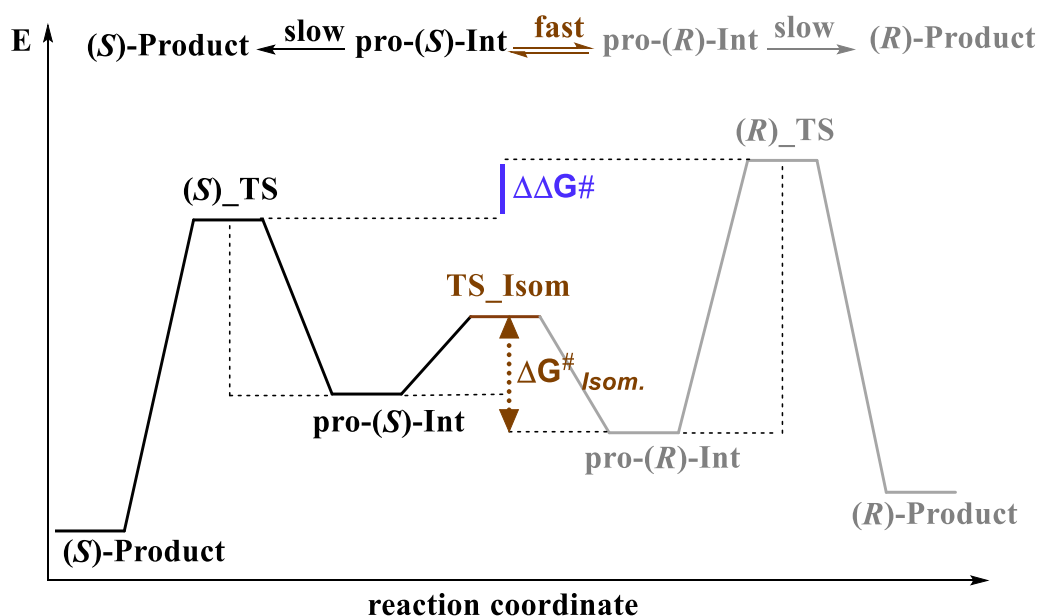


Figure 3.6 Illustration of the Curtin Hammett Principle.

It is worth highlighting that in some cases the Curtin Hammett principle is not valid (Figure 3.7). This scenario is possible when the interconversion barrier of one isomer into another is too high (TS_Isom), thus the rates for the two diastereomeric reactions are faster than the rate of the interconversion of the two intermediates.

An illustrative example is given in Figure 3.7. When all pro-(*R*)-Int is used up, it will not interconvert into pro-(*S*)-Int, due to a high isomerization barrier. This leads to the conclusion that the formation of the major product will be affected by the more stable intermediate. The predominant product will be the (*S*)-product due to fact that pro-(*S*)-Int is energetically lower than pro-(*R*)-Int. Moreover, it is not enough that pro-(*S*)-Int is the energetically preferred intermediate, but the barrier for the formation of this intermediate from the reactant also has to be low.

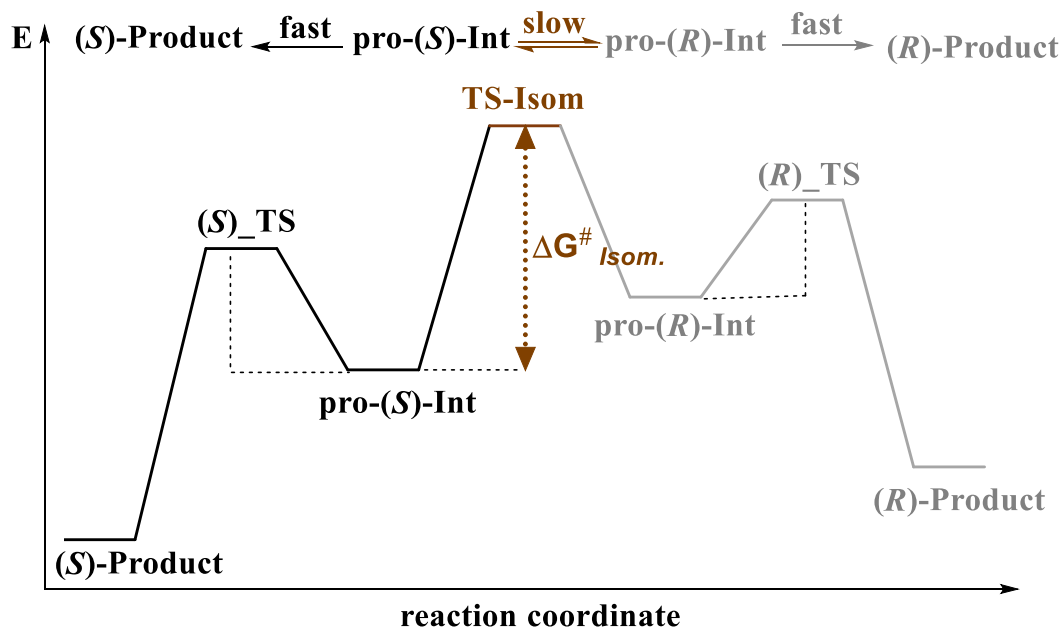


Figure 3.7 A possible non-Curtin Hammett condition.

3.7 Accuracy of DFT on properties we are interested in

In this section, I will discuss the advantages and limitations of using DFT for computing the type of properties we are interested in. The performances of two functionals, B3LYP and PBE, which are used in this work, are given. Properties of interests are geometries, energies, and enantioselectivity.

3.7.1 Prediction of geometries with B3LYP

In 2004, Wilson and Wang studied performances of DFT functionals for the description of several molecular geometries such as O₃, H₂, H₂O, HF, HCN, CO, N₂ etc. by increasing the basis set size.¹¹⁰ The obtained results were compared with experimental data. For example, the experimentally reported bond length of 0.741 Å bond for the H₂ molecule agreed well with the bond length of 0.7429 Å at the B3LYP/cc-pVTZ level of theory. Thus, the deviation relative to the experimental result was only 0.0019 Å. For many tested molecules, the deviation relative to the experimentally determined bond lengths was within 0.015 Å at the B3LYP/cc-pVTZ level.

More than a decade ago, Riley *et al.* reported a broad benchmark study for the prediction of several molecular properties such as bond lengths and angles, ground state vibrational

frequencies, electron affinities and ionization potentials etc.¹¹¹ They tested 37 DFT functionals with eleven basis sets. The obtained results were compared with the second-order many-body perturbation (MP2) method and experimental data from the G2 and G3 data set. A good accuracy was already achieved with the B3LYP/6-31G(d) protocol. For instance, the average unsigned bond length error was within 0.002 Å, whereas the average unsigned bond angles error was within 1.5°.

In 2009, Bühl and Sieffert studied the prediction of the binding enthalpies of a triphenylphosphine (PPh₃) ligand in the Ru(CO)Cl(PPh₃)₃(CH=CHPh) complex by employing DFT methods.⁹³ The bond distances were evaluated and compared with the experimentally determined X-ray structures. The gas-phase geometry optimizations and frequency calculations were performed at the B3LYP/6-311+G(d,p)/SDD level of theory. The B3LYP functional, without dispersion corrections, gave the largest deviation of around 0.24 Å for both, the Ru-P and the Ru-Cl bond lengths. With the dispersion corrected B3LYP-D3 functional, the bond distances were accurately predicted, with a deviation of 0.03 Å relative to the experiments.

In 2012, Jensen and co-workers reported a benchmark study for the accurate prediction of geometries of 18 Ru-based complexes by employing 8 DFT functionals.¹¹² The Ru-based structures were determined by X-ray diffraction experiments.¹¹² Four of the tested functionals (B3LYP, BP86, PBE and TPSS) did not include dispersion corrections. Two of the employed functionals were dispersion corrected B97D and ω B97XD functionals, whereas the remaining two were Minnesota functionals, M06 and M06L, which are designed to account for dispersion interactions. An analysis of all interatomic distances (15 395) in the 18 Ru-complexes showed that all employed functionals without dispersion overestimated the interatomic distances with the mean unsigned errors (MUEs)^c in the range of 0.131-0.166 Å and mean signed errors (MSEs) in the range of 0.131-0.113 Å. With functionals that take into account dispersion, the errors were reduced. For example, the MUEs were in the range 0.101-0.113 Å, whereas the MSEs vanished. The authors reported that the reason for the MSEs vanishing is due to the fact that overestimated distances are exactly compensated by the underestimated distances. In this

^c A mean unsigned (absolute) error (MUE) is computed with the following formula, where N is a number of atoms and R_{ij} is the interatomic distance between atom pair ij.

$$MUE(DFT) = \frac{2}{N(N-1)} \sum_{i=1}^{N-1} \sum_{j>1}^N |R_{ij}(DFT) - R_{ij}(X ray)|$$

study, carbon-carbon and carbon-heteroatom distances were also investigated in Ru complexes. Although the ω B97XD functional was found to be the best choice for the geometry optimization of the Ru-complexes, B3LYP also showed very good performance with the MUE/MSE equal to 0.017 Å/0.015 Å.

3.7.2 Prediction of geometries with PBE

In Jensen's study of Ru-complexes,¹¹² it has been shown that PBE, without dispersion corrections, is able to predict accurately metal ligand bond distances in Ru-complexes.¹¹² Regarding to the ruthenium-ligand bond distances, of all eight tested DFT functionals, the highest accuracy was obtained with PBE, with the MUE/MSE equal to 0.026 Å/0.022 Å.

In 2004, Grimme reported a study of how reliable DFT methods are for the accurate description of various interactions between non-aromatic and aromatic complexes. One of the studied properties was intermolecular distance.¹¹³ The distances were obtained at the PBE-D/cc-pQZV(2df,2pd)//PBE-D/cc-pTZV(2d,2p) level of theory and were compared with the MP2 method. For example, the obtained intermolecular distance of the hydrogen bonded (NH₃)₂ complex of 3.18 Å^d matched perfectly the MP2 reported distance of 3.17 Å. On the other hand, the obtained π - π distance between two benzenes (4.04 Å) was elongated by 0.34 Å relative to the MP2 reported distance of 3.70 Å.

3.7.3 Prediction of atomization, binding and dissociation energies with B3LYP

With regard to the energies, one can be interested in the computation of atomization energies, ionization potentials, heats of formation, hydrogen bond interaction energies, conformational energies, activation barriers etc. In the next sections are outlined examples of B3LYP performances regarding atomization and dissociation energies, followed by predictions of reaction barriers. In chemical reactions, it is quite important to predict activation barriers accurately, in order to gain a deeper insight into the kinetics of a reaction. The computed activation energy then can be used for the determination of reaction rates. Finally, the accuracy of B3LYP to describe the ordering of spin states is also discussed.

^d The reported distances are given in pm. By using conversion factor, distances were converted to Å, where 1pm corresponds to 0.01 Å.

Partridge and Bauschlicher showed that B3LYP/6-31(G) without dispersion corrections performed poorly for prediction of atomization energies of the 55 molecules from the G2 data set.¹¹⁴ The average error was found to be 5.18 kcal/mol. However, the use of the 6-311+G (3df) basis set improved results, with the error reduced to 2.2 kcal/mol.

In Buhl's and Sieffert's study of triphenylphosphine (PPh₃) binding to the five-coordinated Ru(CO)Cl(PPh₃)₃(CH=CHPh) complex, the attention was focused on the binding enthalpies, evaluated at the B3LYP level of theory.⁹³ The experimental binding enthalpy was compared with the computed energies at the B3LYP/6-31G(d,p) level of theory, where the 3-21 G basis set was used on phenyl groups and the Stuttgart-Dresden pseudopotential (SDD) on Ru. The B3LYP functional gave the weakest binding of 2.8 kcal/mol relative to the experimental value of -17.5 ± 2.0 kcal/mol, whereas B3LYP-D led to the largest overbinding of -40 kcal/mol. The results were improved by including an enthalpy correction term^e, a basis set superposition error (BSSE) correction and solvation effects. In this way, the dispersion corrected B3LYP-D method gave the enthalpy value of -21.6 kcal/mol, which was in good agreement with the experimental reference.

In several reported studies, it has been shown that B3LYP underestimates bond strengths dramatically.^{55,93,115} Gilbert and Check showed that B3LYP/6-311++G(d,p) underestimates C-C bond dissociation energies of alkanes with a deviation of 15 kcal/mol relative to experiments and the MP2 method.¹¹⁶ One of the studied example was the C-C bond dissociation energy of ethane. The experimentally reported energy needed to break the C-C bond into two CH₃ fragments was 90 ± 0.2 kcal/mol, yet at the B3LYP/6-311++G(d,p) level of theory it was computed to be 81.5 kcal/mol.

^e The binding enthalpy ΔH (kcal/mol) was computed as:

$$\Delta H = \Delta E + \Delta E_{BSSE} + \Delta E_{solv} + \Delta E_H$$

where ΔE is the total binding energy corrected with BSSE (ΔE_{BSSE}), solvation (ΔE_{solv}) and enthalpy term (ΔE_H). ΔE_{solv} was computed as the energy difference between the reaction energy in continuum ($\Delta E_{CH_2Cl_2}$) and the gas phase ΔE . The enthalpy correction term, ΔE_H (-1.9 kcal/mol) was obtained as the energy difference between the total binding energy ΔE in gas phase (-4.4 kcal/mol) and the binding enthalpy in gas phase (-2.5 kcal/mol, at -70°C).

3.7.4 Prediction of reaction barriers with B3LYP

In 2014, Neese and co-workers studied the Ir-PHOX-catalyzed asymmetric hydrogenation of olefins using DFT methods and a new domain based local pair natural orbital coupled-cluster method with single and double excitations and the inclusion of perturbative triples correction (DLPNO-CCSD(T)).¹¹⁷ The reported results included B3LYP-D/def2-TZVP energies at BLYP/def2-SVP (or def2-TZVP) geometries. An implicit solvation model and Grimme empirical dispersion corrections were also included. A migratory insertion mechanism, which involves Ir^{III}/Ir^V oxidation states, was supported. The B3LYP-D results gave activation barriers which were comparable with the DLPNO-CCSD(T) computed barriers. For the (*E*)-1,2-diphenyl-1-propene substrate, the computed barrier for the C-H bond formation step was 8.9 kcal/mol relative to the barrier of 7.2 kcal/mol obtained at the DLPNO-CCSD(T) level of theory.

One of the very important reactions in biology and chemistry is a proton transfer, which occurs in various enzymatic reactions, acid-based neutralization processes, etc.¹¹⁸ Moreover, proton transfer is one of the elementary steps in the hydrogenation reactions, which are discussed in this thesis (Paper IV). Adamo and co-workers tested 27 DFT functionals in a benchmark study for prediction of proton transfer barriers in various systems, such as: a protonated water dimer, an ammonia dimer, an imidazole dimer, malonaldehyde and formamide.¹¹⁹ Relative to CCSD/cc-pVTZ//CCSD(T)/aug-cc-pVTZ energies, the barriers at the B3LYP-D/6-311+G(3df,3pd)//B3LYP-D/6-311+G(2d,p) level of theory had a mean absolute deviation^f and a root mean square deviation of 0.97 and 1.17 kcal/mol, respectively.

3.7.5 Prediction of atomization and reaction energies with PBE

Regarding to atomization energies, Pederson and co-workers reported a computational study where small molecules and transition metal complexes were investigated with the PBE functional, in the absence of dispersion corrections.¹²⁰ The results were compared with

^f A mean absolute error (*MAE*) can be expressed by the following formula:

$$MAE = \frac{\sum_{i=1}^n |y_i - x_i|}{n}$$

where y_i is a measured value, x_i is a reference or known value, and n is a number of measurements.

experimental data. PBE predicted atomization energies with an average error of 3.9 kcal/mol^g and the root mean square deviation (RMSD)^h of 9.5 kcal/mol.

In 2016, Hopmann reported a detailed study of how reliable DFT is in order to reproduce activation and reaction energies of 11 Ir-based transformations in solution, where four elementary reactions were taken into account: bond formation, isomerization, ligand association and substitution.²⁶ Five DFT functionals were tested, including the hybrid functionals B3LYP and PBE0, the gradient corrected PBE and two Minnesota functionals: M06L and M11L. Alongside with Grimme dispersion corrections, the solvent effect was included. Several approaches were used in order to compare the computed energies with experiments. For example, equilibrium ratios or constants (eq. 3.3) were used for the calculation of the Gibbs free reaction energies.

One of the computationally studied reactions was the isomerization of an imine at a IrH₂[C₆H₃-2,6-(OPt-Bu₂)₂] pincer complex (Figure 3.8).¹²¹

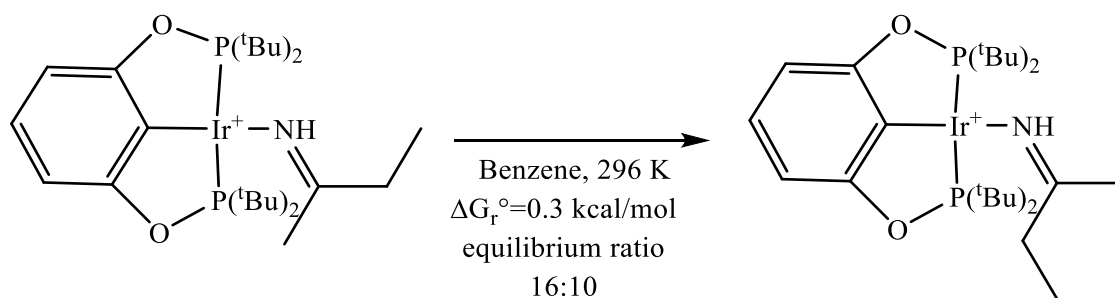


Figure 3.8 The isomerization of a σ -bond imine ligand at a IrH₂[C₆H₃-2,6-(OPt-Bu₂)₂] pincer complex (experimental results by Bernskoetter *et al.*, ref ¹²¹).

The imine ligand can adopt two σ -bond orientations, with NMR experiments showing that two possible forms of this complex exist, with a ratio of 16:10, for (*E*) and (*Z*) isomers, respectively. The energies were computed with DFT-D/6-311+G(2d,2p) at DFT-D/6-311G(d,p) geometries. The pseudopotential and the basis set LANL2DZ, with one *f*-polarization function, was used on Ir, whereas LANL2TZ(f) was employed in single point calculations. Albeit all tested

^g The reported energies are given in eV unit. 1 eV corresponds to 23 kcal/mol.

^h A root mean square deviation (*RMSD*) is defined as a root of the average of the squared errors.

$$RMSD = \sqrt{\frac{\sum_{i=1}^n [y_i - x_i]^2}{n}}$$

functionals were able to predict the preferred isomer (*E*), the PBE-D2 functional was superior with a deviation from the experimental results of 0.8 kcal/mol. When all 11 reactions were considered, it was shown that PBE-D2/PCM provided the most accurate free energies with an average error of 1.2 kcal/mol.

Recently, Shiekh reported a benchmark study on the prediction of reaction energies in six Rh-mediated chemical transformations.¹²² Some of the elementary reactions, such as ligand exchange, hydride elimination, dihydrogen elimination etc. were investigated with 17 DFT functionals. The computed Gibbs free energies were compared with the experimentally reported reaction free energies. The experimental reaction energies were obtained with either NMR or spectrophotometric equilibrium studies, at room temperature. The computed Gibbs free energies were obtained at the PBE/6-31+G(d,p)//PBE/6-31G(d,p) level of theory, with the pseudopotential and the basis LANL2DZ set used on rhodium.

One of the studied reactions was a ligand exchange reaction between N₂ and η²-H₂ at an Rh-(I)-PCP complex,¹²³ where PBE and PBE-D3 performed poorly. The deviation of the computed reaction free energies from the experimental value (-0.71 ± 0.03 kcal/mol) was 4.77 kcal/mol and 6.68 kcal/mol, for PBE and PBE-D3, respectively. The second studied reaction was a H₂ elimination reaction, which occurs at a *cis*-[(H)₂Rh(dmpe)₂]⁺ complex (Figure 3.9).¹²⁴

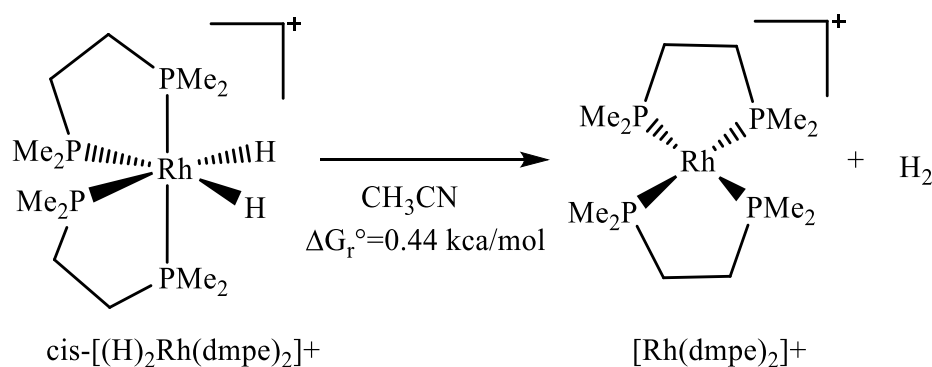


Figure 3.9 The hydrogen elimination reaction at a *cis*-[(H)₂Rh(dmpe)₂]⁺ complex (results by Wilson *et al.*, ref ¹²⁴).

Here, the highest accuracy was achieved with the PBE-D3 functional, alongside with the hybrid PBE0-D3 functional. The deviation from the experimental value was only -0.35 kcal/mol, at the PBE-D3 level of theory. The fact that the PBE-D3 functional failed to correctly predict the reaction energy in the ligand-exchange reaction yet it was superior for the elimination reaction

indicates that there is no general rule about the performances of some functionals, highlighting the need for benchmark studies for individual properties.

3.7.6 Performance of B3LYP for spin-state ordering

In this thesis, in the Co-based hydrogenation study (Paper IV), a low spin $S = 1/2$ ground state was employed in our computations, as determined experimentally for the (*R,R*)-Ph-BPE-Co complex.¹⁷ However, due to the possibility of Co-complexes to access other spin states, I also evaluated the quartet state ($S = 3/2$) but it was higher in energy. Concerning this topic, it is important to introduce one more term *spin-state ordering* and the performance of B3LYP to describe this phenomenon accurately. The spin state ordering is here considered as a static property - the energy difference between different spin states for a given complex.

When we look at the periodic system, there are many transition metals with unfilled *d* orbitals. Metals can differ a lot regarding to their nature and reactivity. A metal in a certain oxidation state with certain ligands and at a certain temperature and reaction condition will have a preference for certain spin states. Open-shell complexes, which have number of unpaired electrons in *d* orbitals, may cause various difficulties in the proper computational description of a catalytic cycle. Nowadays, it is well known that these complexes can give different energetically close lying electronic states.^{125,126} Hence, if one does not take into the account the proper spin state of a metal, the wrong conclusion about the barriers and overall reaction flow may be taken. It is therefore important to see how reliable DFT is in describing the spin state ordering in metal-complexes.

In 2004, Neese and co-workers studied the energy differences between high spin (HS) and low (LS) spin states of the hexaquoferrous cations $[\text{Fe}(\text{H}_2\text{O})_6]^{2+}$ with B3LYP.¹²⁷ The comparisons were made to *ab initio* methods, such as the complete active-space self-consistent field (CASSCF), the second order perturbation theory-corrected complete active-space self-consistent field (CASPT2) and the spectroscopy-oriented configuration interaction (SORCI) methods. It was found that B3LYP overestimates a HS-LS energy difference by 1000 cm^{-1} (2.8 kcal/mol).

Generally, hybrid functionals favour high spin states, whereas the pure functionals favour low spin states. Trautwein and co-workers showed that B3LYP stabilized the HS state for substituted and unsubstituted di[tris-(1-pyrazolyl)methane] ferrous cation $[\text{Fe}(\text{tpm})_2]^{2+}$.¹²⁸ Hess and co-workers noticed the same trend in the HS-LS splitting study of Fe(II) spin crossover

complexes with sulphur. It is worth highlighting that if more HF exchange is present in hybrid functionals the more HS states are stabilized. Therefore, Hesse and co-workers introduced the B3LYP* functional which has reduced amount of HF exchange ($a_0 = 0.15$) and thus provided more accurate HS-LS energy differences, comparable with experiments.¹²⁹

In 2009, Harvey and co-workers studied different spin states in Fe-tetracarbonyl complexes.¹²⁵ A coordination of ethylene to the triplet $\text{Fe}(\text{CO})_3$ complex was studied at the B3PW91**/TZVⁱ level of theory and with *post*-Hartree Fock methods. Previously, it was reported that $\text{Fe}(\text{CO})_3(\text{C}_2\text{H}_4)$ has a triplet ground state with the BP86 functional¹³⁰ yet with the B3PW91** functional the singlet was lower in energy by 0.6 kcal/mol. In order to understand this outcome, the authors did calculations with the B3LYP, B3PW91 and B3PW91* functionals. The B3LYP, B3PW91 and B3PW91* functionals favoured a triplet as the ground state, with an energy splitting of 8.3 kcal/mol, 4.6 kcal/mol and 1.9 kcal/mol, respectively. However, based on the CCSD(T) results, the singlet was preferred. Therefore, the performance of B3LYP was poor relative to CCSD(T).

In 2012, Hauser and co-workers studied prediction of HS-LS energy differences in $[\text{Co}(\text{NCH})_6]^{2+}$ and $[\text{Fe}(\text{NCH})_6]^{2+}$ complexes, with DFT and more accurate couple cluster methods (CCSD(T)).¹³¹ The B3LYP functional performed superior for $[\text{Fe}(\text{NCH})_6]^{2+}$ but not for $[\text{Co}(\text{NCH})_6]^{2+}$ complex.

Based on these examples, one cannot make general conclusion about the reliability of B3LYP to describe spin-state ordering accurately. This area is still a challenging topic for DFT methods and requires further investigations.

3.7.7 Prediction of enantioselectivity with B3LYP

Enantioselectivity is based on small energy differences, and an important question is if DFT is able to accurately model enantioselective processes. In Neese's computational study of the asymmetric Ir-PHOX based hydrogenation of olefins, one of the goals was to study the enantioselectivities.¹¹⁷ The *e.e.*'s were computed for five unsaturated substrates and then the obtained results were compared to experiments. For example, it has been shown that PHOX ligands give high *e.e.* in the Ir-based hydrogenation of (*E*)-1,2-diphenyl-1-propene. Andersson

ⁱ B3PW91** functional contains 10 % of the HF exchange. B3PW91* and B3PW91 contain 15 % and 20 %, respectively.

and co-workers reported an experimentally obtained *e.e.* in the range of 89-91 %, with a (*S*)-tBu-PHOX ligand (Figure 3.10).¹³² Neese and co-workers obtained a computed *e.e.* using the energy barriers of four energetically close-lying TSs. At room temperature, the computed *e.e.* was 93 %. Thus, a good agreement with the experiments was achieved.

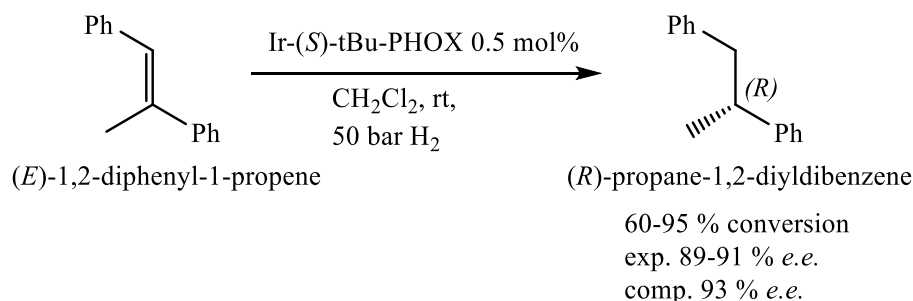


Figure 3.10 The Ir-(*S*)-tBu-PHOX-catalyzed asymmetric hydrogenation of (*E*)-1,2-diphenyl-1-propene (experimental results by Brandt *et al.*, ref ¹³², computed results by Sparta *et al.*, ref ¹¹⁷).

In 2008, Bolm and co-workers studied the hydrogenation of α,β unsaturated ketones using Ir-*P,N* complexes as catalysts (Figure 3.11).¹² Later, the same group reported the computational study of this reaction, in order to get deeper insight into the mechanistic details.¹³

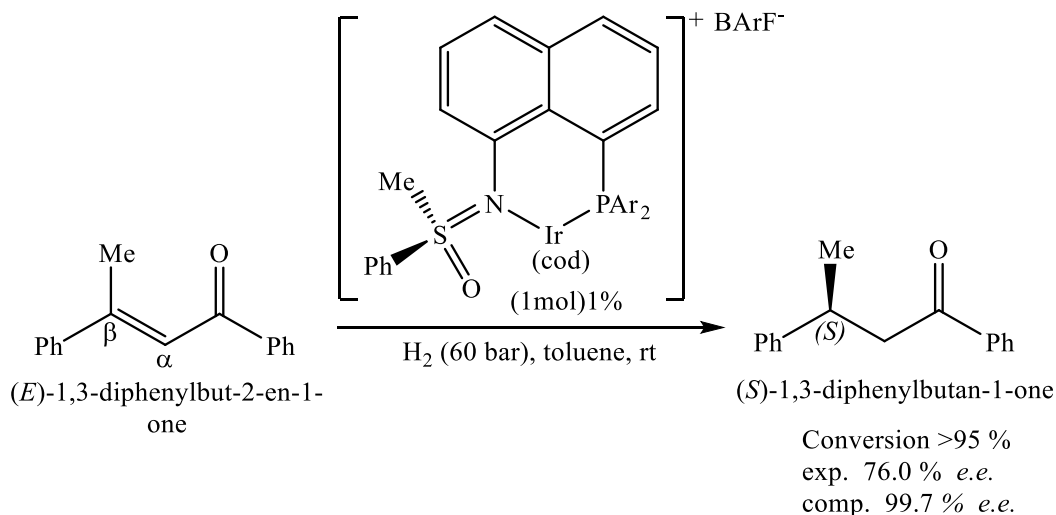


Figure 3.11 Enantioselective Ir-catalyzed hydrogenation of (*E*)-1,3-diphenylbut-2-en-1-one (experimental results by Lu *et al.*, ref ¹², computed results by Engel *et al.*, ref ¹³).

The computed energies were obtained at the B3LYP-D3/6-31G(d)//B3LYP-D3/6-311++G(d,p)//IEFPCM level of theory. The pseudopotential and the basis LANL2DZ was used on Ir, whereas LANL2DZ(f) was employed in single point calculations. Several mechanistic possibilities were investigated including Ir^{III}/Ir^{IV} and Ir^I/Ir^{III} reaction routes. It was proposed a

mechanism where Ir has a +3 oxidation state during the whole catalytic cycle. A substrate (*E*)-1,3-diphenylbut-2-en-1-one was employed in computations. The rate-limiting step was found to be hydride transfer to the C- β atom, with barriers of 10.0 kcal/mol and 13.8 kcal/mol, for pro-(*S*) and pro-(*R*) TSs, respectively. The experimentally reported *e.e.* was 76 % (at 298K), whereas the computed *e.e.* was 99.7 %. The calculations provided the same major product as in experiment, albeit with a somewhat larger computed *e.e.*.

Houk and Lam employed the B3LYP-D3(BJ) method in the study of the intermolecular condensation of 4-substituted heptene-2,6-dioans into chiral cyclohexenones, catalyzed by cinchona alkaloid (Figure 3.12).¹³³ The computed energies were obtained at the B3LYP-D3(BJ)/def2-TZVPP-IEFPCM//B3LYP/6-31G(d)-IEFPCM level of theory. For the 4-methylheptene-2,6-dioan substrate, the computed selectivity of 91.5 % *e.e.* (at 268 K) matched the experimentally reported *e.e.* of 92 %.¹³⁴

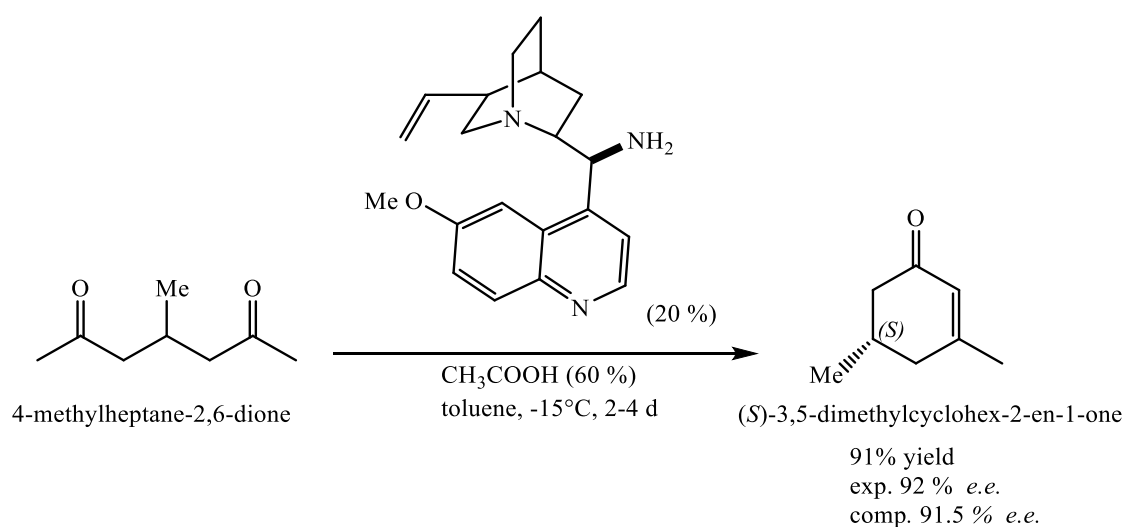


Figure 3.12 Enantioselective intermolecular condensation of 4-methylheptene-2,6-dioan catalyzed by the given cinchona alkaloid (experimental results by Zhou *et al.*, ref¹³⁴, computed results by Lam *et al.*, ref¹³³).

Friesner and co-workers reported a broad benchmark study for the prediction of the enantiomeric excesses for a large data set, including various dioxirane-catalyzed asymmetric epoxidations of olefins (Figure 3.13).¹³⁵ The computed *e.e.*'s were compared with the experimentally known ones. The computed energies were reported at the spin unrestricted B3LYP/6-311+G(d,p)/PBF//B3LYP/6-31G(d)/PBF^j level of theory, without dispersion cor-

^j PBF is abbreviated as Poisson Boltzmann Finite element method, which is a solvation model implemented in the Jaguar 7.0 program.

reactions. I will below describe two examples of the 46 reported possible substrate-catalyst combinations.

A good agreement with experiments was achieved for the asymmetric epoxidation of 1,2-dihydronaphthalene, with a dioxirane-based catalyst **I** (Figure 3.13), at room temperature. The experimentally reported *e.e.*¹³⁶ of 18 % matched the computed *e.e.* of 26 % so the error was within 0.2 kcal/mol. The second illustrative example is the asymmetric epoxidation of (*E*)-1,2-diphenylethene with the Catalyst **II**. The computed *e.e.* of 99.7 % (at 263 K) was overestimated relative to the experimentally reported of 97 %. The error of the computed *e.e.* was 1.2 kcal/mol, however, the the correct major product was predicted. The mean unsigned error (MUE) was 0.73 kcal/mol.

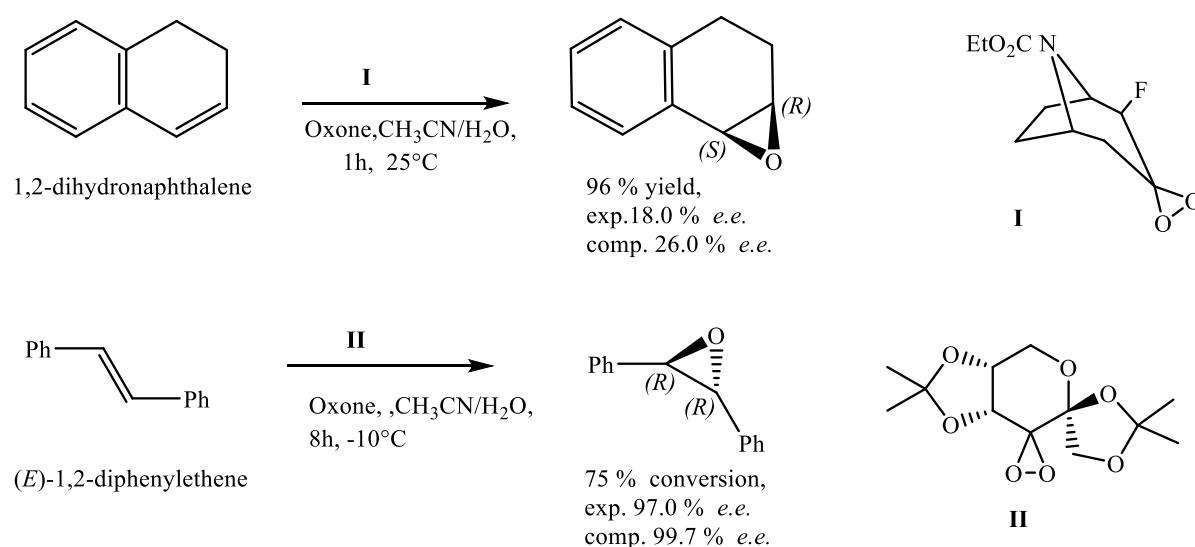


Figure 3.13 Dioxirane-catalyzed asymmetric epoxidations of 1,2-dihydronaphthalene (results by Armstrong *et al.*, ref¹³⁶) and (*E*)-1,2-diphenylethene substrates (results by Wang *et al.*, ref¹³⁷). Computational results for both substrates are from Schneebeli *et al.*¹³⁵

3.7.8 Prediction of enantioselectivity with PBE

An example, where the dispersion corrected PBE-D2 method was the method of choice, has been reported recently by Senanayake and co-workers.¹³⁸ The asymmetric Ir-based hydrogenation of 1,4 benzodioxines was studied both experimentally and computationally (Figure 3.14). With the [Ir(cod)Cl]₂-BIDIME-dimer catalyst system, very high yields and enantioselectivities were achieved in experiments. The computations were performed with a truncated version of the ligand (Ph-BIBOP) and the energies were obtained at the PBE-D2/6-311+G(d,p)-IEFPCM-MeOH//PBE/6-31G(d) level of theory. The pseudopotential and the basis set

LANL2DZ was used on Ir, whereas LANL2DZ(f) was employed in single point calculations. Only two substrates, methyl and methoxycarbonyl substituted benzodioxines were analyzed computationally.

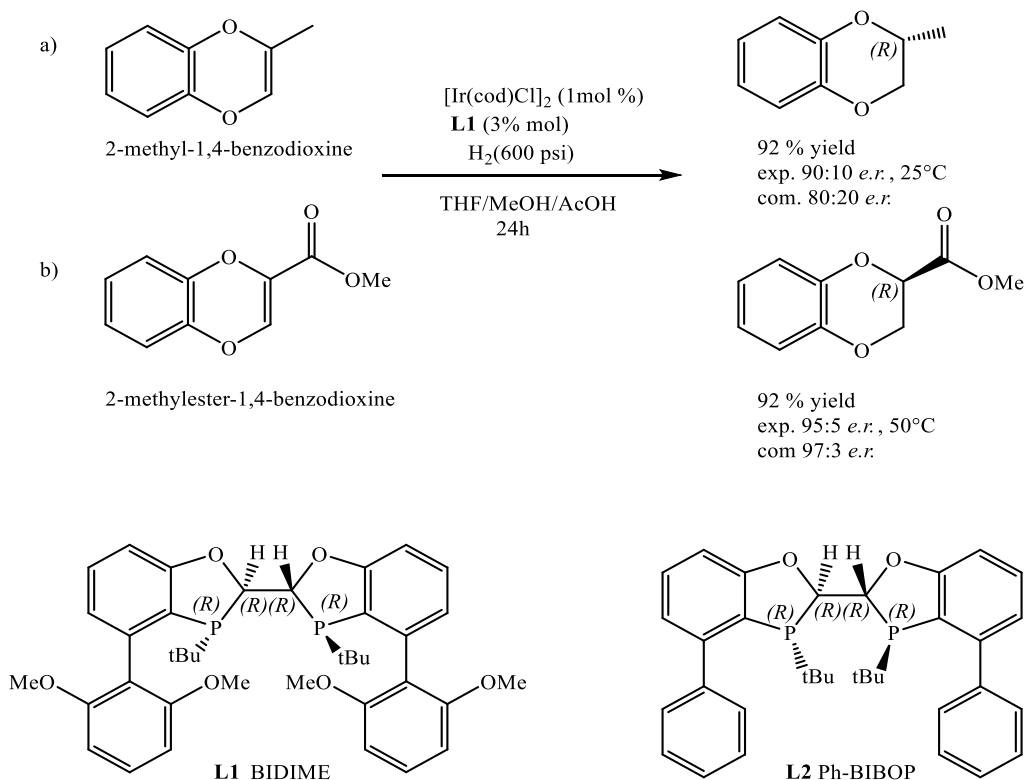


Figure 3.14 Ir-catalyzed hydrogenation of the substrates (a) 2-methyl-1,4-benzodioxine and b) 2-methylester-1,4-benzodioxine. **L1** (BIDIME) dimer is the experimentally used ligand, whereas **L2** (Ph-BIBOP) is the truncated ligand (experimental and computational results by Chong *et al.*, ref ¹³⁸).

The computed enantioselectivities were in good agreement with experiments. For the 2-methyl-1,4-benzodioxine substrate (Figure 3.14, a), the computed enantiomeric ratio *e.r.* of 80:20 (at 298 K) matched the experimentally reported *e.r.* of 90:10. For the second 2-methylester-1,4-benzodioxine (Figure 3.14, b), the obtained *e.r.* of 93:7 (at 323 K) also matched the experimentally reported *e.r.* of 95:5.

3.8 General conclusions

Chapter 3 shows that there are various aspects that have to be considered when modelling homogeneous reactions. This includes basis set considerations, the description of weak interactions such as dispersion forces and the description of the solvent via explicit or implicit

solvent models. In modelling of chemical reactions, the energy profiles are used in order to show the reaction pathways with intermediates and TSs. Finally, with the help of several optimization techniques one can determine and describe stationary points, such as minima or TSs, on the PES.

Chapter 3 also showed some examples of the performances of B3LYP and PBE functionals for geometries, energies and enantioselectivities. It is not possible to say that a "best" computational protocol exists. Some protocol may be superior for the prediction of certain properties, but can fail in the prediction of others. From the described examples, it can be concluded that B3LYP and PBE give good geometries. Regarding to the energies the situation is not so obvious, because there are various types of energies, in which one can be interested in. Herein, the performance of dispersion-corrected B3LYP and PBE functionals for the prediction of reaction barriers and enantioselectivities appears to be acceptable enough to use these functionals for mechanistic studies.

4. Hydrocarboxylation

These days, there is a lot of attention on CO₂ chemistry.^{139,140} Due to the fact that CO₂ is an abundant carbon source, it has a huge potential to be employed in different areas of industry. It can be used as a renewable carbon source in chemical synthesis and also as a solvent in various reactions under supercritical conditions. It is already applied in the food and agricultural industry, in dry-cleaning, in fire extinguishers and in separation processes.¹⁴¹

One primary problem with chemical CO₂ utilization is the thermodynamic stability and kinetic inertness of CO₂.¹⁴² One approach towards overcoming this problem involves the use of transition metals. The CO₂ can be activated via specific interactions with transition metals, either through homogeneous or heterogeneous catalysis. If coupled with high-energy starting materials such as hydrogen, alkene, alkyne, epoxides etc., CO₂ can be converted into energetically stable products: methanol, carboxylic acids, carbamates and carbonates (Figure 4.1). Thus, a number of versatile chemicals and fuels can be obtained from CO₂.¹⁴³

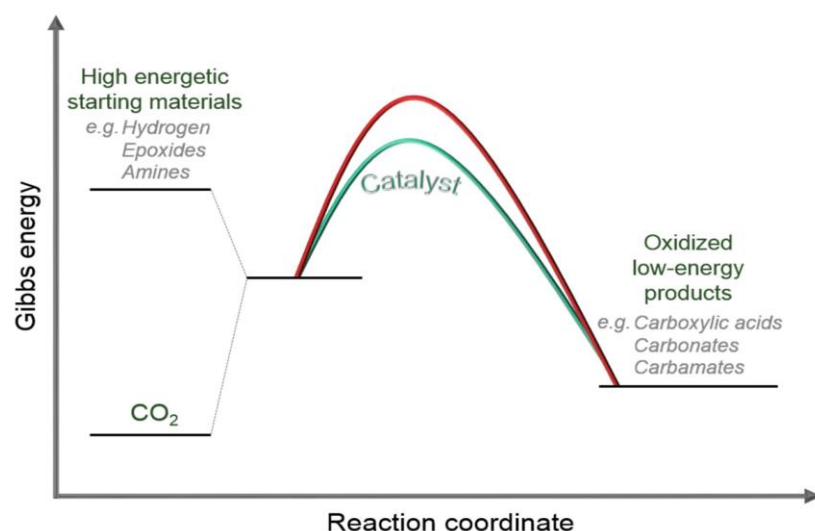


Figure 4.1^k Illustration of the energy levels of carbon dioxide, high-energy reactants and low energy products.¹⁴³ Catalyzed reaction is given with green colour, whereas non-catalyzed reaction is given with the red colour.

^k Adapted with permission from [Calabrese, C.; Giacalone, F.; Aprile, C. Hybrid Catalysts for CO₂ Conversion into Cyclic Carbonates. *Catalysts* **2019**, *9*, 325]. © **2019** by the authors. Licensee MDPI, Basel, Switzerland.

In this chapter, the emphasis is put on the properties of CO₂ and its conversion into carboxylic acids through hydrocarboxylation, employing achiral Rh-COD and several chiral Rh-phosphine catalysts. These results are based on papers **I**, **II** and **III**.

4.1 CO₂ properties

CO₂ is a linear molecule that has an *sp* hybridized C atom linked with two oxygen atoms and has zero dipole moment.¹⁴² It can express ambiphilic character and thus behave either as a Lewis acid on the C atom or as a Lewis base on the oxygen atoms (Figure 4.2). Due to its ambiphilic nature, CO₂ can interact with metals through different binding modes.

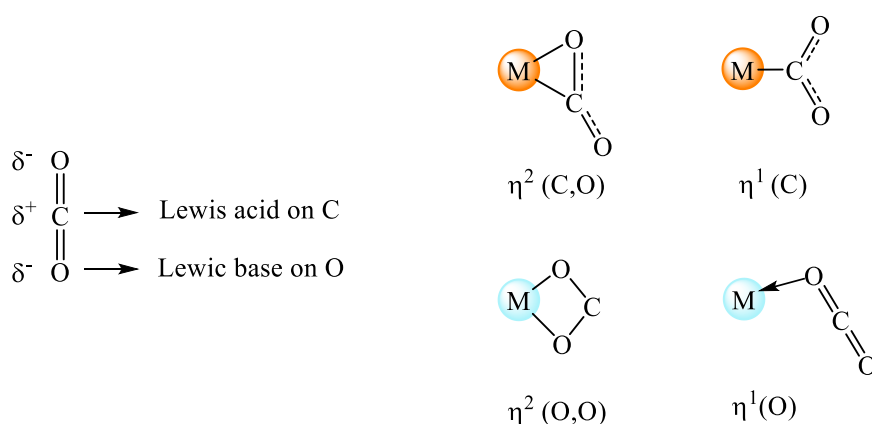


Figure 4.2 Illustration of metal-CO₂ binding modes.

With electron rich metal-complexes, CO₂ can interact via the electrophilic C atom, with two possible binding modes proposed.¹⁴² The first coordination mode occurs via the C=O π bond, which is referred to as an $\eta^2(\text{C},\text{O})$ -binding mode, whereas the second occurs via the C atom, in a $\eta^1(\text{C})$ -fashion. With electron deficient metal-centres, CO₂ interacts through the oxygen atoms.

4.2 Introduction to metal-catalyzed hydrocarboxylations

There are two types of C-CO₂ bond formation with metal-catalyzed reactions and unsaturated substrates, substitution^{144,145} and addition.²⁵ Substitution of alkenes leads to unsaturated carboxylic acids, whereas an addition reaction leads to saturated carboxylic acids (Figure 4.3). A hydrocarboxylation reaction occurs when a hydride and a CO₂ molecule are added to an unsaturated substrate. Metal-catalyzed hydrocarboxylations represent a good strategy for the formation of carboxylic acids, which are important intermediates in the pharmaceutical industry.¹⁴⁶

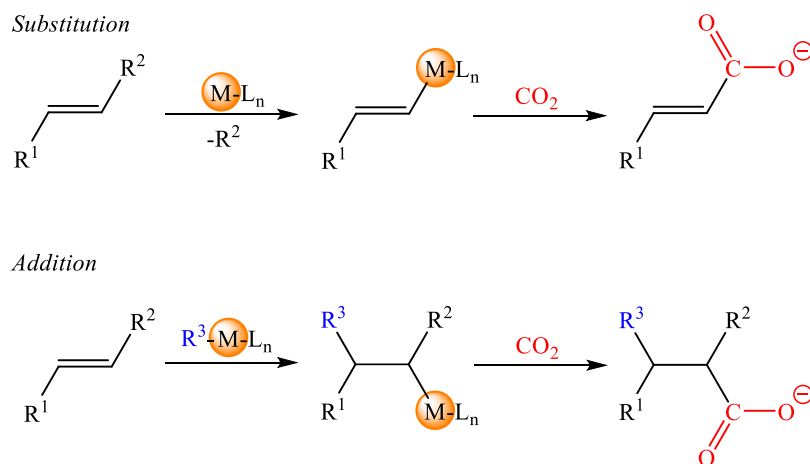


Figure 4.3 Substitution and addition reactions of alkenes with CO_2 .

For carboxylation reactions non-redox and redox mechanisms are possible. For example, a generic non-redox addition mechanism for alkenes is given below (Figure 4.4). First, a metal-hydride species is formed from a precatalyst. This is followed by alkene insertion into the metal-hydride bond to form a metal-alkyl intermediate. This electron-rich species interacts with the electrophilic CO_2 to yield a metal-carboxylate intermediate, which in the presence of a hydride donor liberates the carboxylate and regenerates the active catalyst species, the metal-hydride.

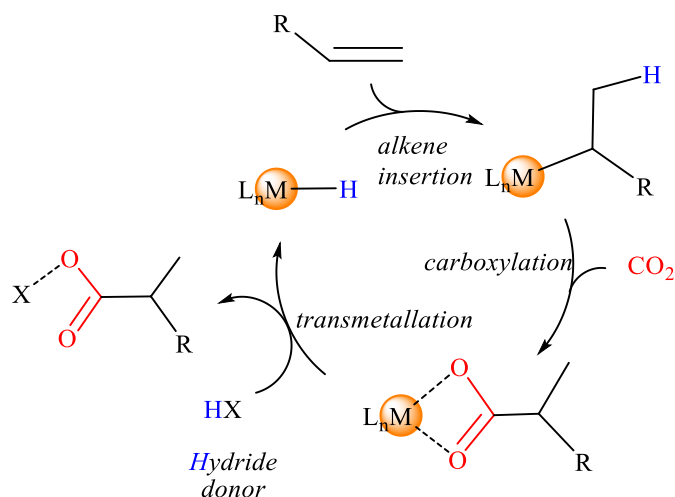


Figure 4.4 A generic metal-catalyzed hydrocarboxylation mechanism.

If terminal alkenes are used as substrates, there are two possibilities for the alkene insertion into the metal-hydride bond (Figure 4.5). In a *1,2* insertion, a metal is bound to the C atom in position 1, whereas a hydride is bound to the C atom in position 2. The opposite situation may also occur and it is referred to as *2,1* insertion. This implies that at least two mechanistic possibilities exist for the migratory insertion step.

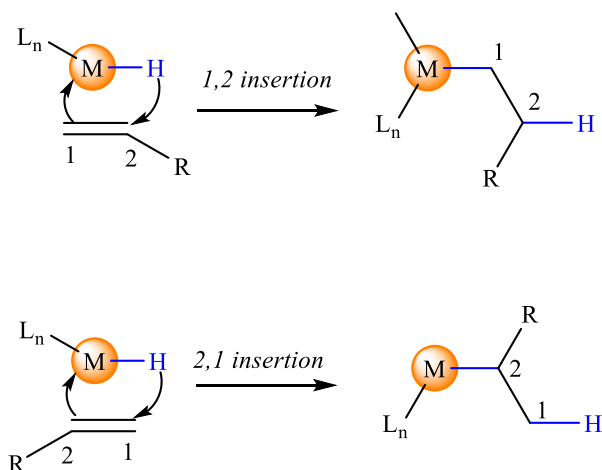


Figure 4.5 1,2 or 2,1 alkene insertion into an M-H bond.

Over the past few decades, numerous studies have been reported, which focus on metal-catalyzed C-CO₂ bond formation with CO₂.^{25,147-155} In 2018, our group reviewed several computational studies including Ni, Rh, Cu and Pd-catalyzed reactions with CO₂ (Paper V).¹⁵¹ For several studies it was shown that Lewis acid additives can enhance the CO₂ insertion activity,^{156,157,160} although the mechanistic basis for this is not fully understood yet.

In my PhD work, I examined Rh-based hydrocarboxylation, thus it will be of special interest to initially outline a few reported computational studies focusing on carboxylations with this precious metal and CO₂.

Examples of computational studies on Rh-mediated carboxylation

In 2006, Iwasawa and co-workers reported an experimental study of Rh(I)-catalyzed carboxylation of aryl and alkenylboronic esters with CO₂ (Figure 4.6).¹⁵⁸ Later, Qin *et al.* conducted a computational investigation, at the PBE0/IEFPCM level of theory.¹⁵⁹ This type of reaction would be a substitution, which involves insertion of CO₂ into a M-C(sp²) bond.

Qin *et al.* also studied two bidentate ligands with different electronic properties, a [dppp (1,3-bis(diphenylphosphino) propane)] and a diene ligand (COD = 1,5-cyclooctadiene). The proposed mechanism included formation of an Rh-aryl species via transmetalation. In this step, an aryl group from an arylboronic ester is transmetalated to the precatalyst to yield the Rh-aryl species. Then, insertion of CO₂ into the Rh-C(sp²) bonds occurs in a η²-fashion, where both C and O atoms coordinate to the metal. This step is found to be rate-limiting. The computed barrier with the dppp ligand was 12.7 kcal/mol and with the COD ligand it was 17.7 kcal/mol.¹⁵⁹ In the last

step, the Rh-carboxylate intermediate undergoes two possible transmetallation paths in order to regenerate the catalyst and liberate the carboxylic acid. Either it undergoes transmetallation with a cesium fluoride or direct transmetallation with an alkylboronic ester takes place. It was proposed that bidentate phosphines are a better choice because of the larger σ -donor/ π -acceptor properties relative to the COD ligand.

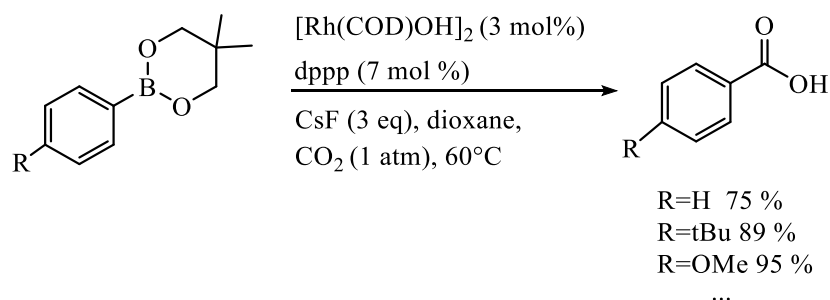


Figure 4.6 Reported experimental $[\text{Rh}(\text{dppp})]$ -catalyzed carboxylation of arylboronic esters (adapted from ref ¹⁵⁸).

In 2011, Ostapowicz *et al.* investigated CO_2 insertion into the Rh-ethyl bond of 38 virtual pincer complexes, at the B97-D level of theory (Figure 4.7).¹⁴⁷ Thirty complexes displayed a three-membered TS, where CO_2 is interacting with the metal through the C atom, in an η^1 -fashion. Only one complex showed a TS with the C=O bond coordinated to the metal.

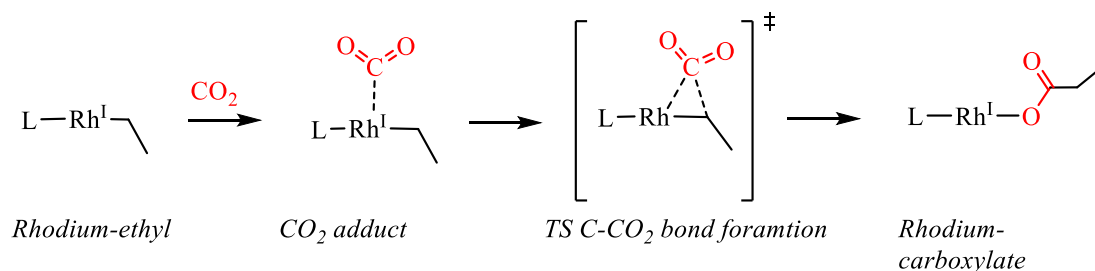


Figure 4.7 Schematic representation of the CO_2 insertion into Rh(I)-pincer-ethyl complexes (adapted from ref ¹⁴⁷).

In seven complexes, Rh- CO_2 interactions were insignificant and greater than 3.2 \AA . The barrier for the CO_2 insertion was computed relative to the CO_2 adduct. The authors noted that CO_2 pre-coordination does not affect the carboxylation barriers. For example, some complexes gave moderate insertion barriers even though CO_2 did not interact with rhodium in the CO_2 -adduct.

A series of recent studies indicated that Lewis acid can activate the CO_2 .^{156,157,160} In 2011, Iwasawa and co-workers reported an experimental study of Rh(I)-catalyzed carboxylation of

arenes via chelation-assisted C-H activation (Figure 4.8).¹⁶⁰ Lv *et al.* studied this reaction computationally, at the B3LYP/SMD level of theory.¹⁵⁶

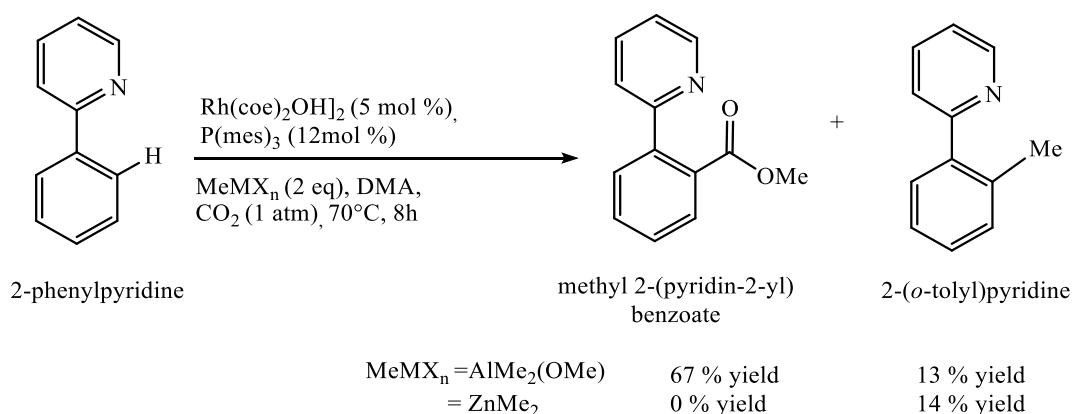


Figure 4.8 Direct Rh(I)-catalyzed carboxylation of 2-phenylpyridine with CO₂ in the presence of AlMe₂(OMe) and ZnMe₂ methylmetallic reagents (adapted from ref ¹⁶⁰).

The proposed mechanism starts with the C-H oxidative addition, followed by CO₂ insertion into the Rh-C(aryl) bond. This step is found to be rate limiting. Next, transmetallation takes place, followed by a methylation reaction. Two Lewis acid additives from the experiments, AlMe₂(OMe) and ZnMe₂, were also tested computationally. During C-CO₂ bond formation step and in the presence of AlMe₂(OMe), the barrier was proposed to decrease by 6.2 kcal/mol compared to the reaction without Lewis acid. On the other hand, the interaction between ZnMe₂ and CO₂ was found to be disfavoured.

Rh-based complexes can accept many different substrates in carboxylation reactions such as alkenes, alkynes, arenes but many aspects of Rh-catalyzed carboxylations are not well understood and more computational works on Rh systems are necessary. For example, to my knowledge no enantioselective Rh-carboxylation has been studied computationally.

In the following section, I am summarizing the results of my work on the Rh-COD-catalyzed hydrocarboxylation of styrene derivatives and α,β -unsaturated carbonyls with CO₂ (Paper I), a reaction originally reported by Mikami and coworkers.²⁵ This is followed by a section where emphasis was put on proposing alternative chiral ligands for the asymmetric Rh-mediated hydrocarboxylation (Paper III), a project that is ongoing in collaboration with the experimental organic chemistry group at UiT.

4.3 Rh-COD-hydrocarboxylation of styrene derivatives and α,β -unsaturated carbonyl compounds with CO_2 (Paper I&II)

In 2016, Mikami and co-workers reported the experimental study of the Rh-COD-mediated hydrocarboxylation of styrene derivatives and α,β -unsaturated carbonyl compounds with CO_2 and ZnEt_2 (Figure 4.9).²⁵ The importance of this study is reflected in the fact that this was the first reported asymmetric hydrocarboxylation of styrenes with CO_2 . However, only moderate enantiomeric excess of 66 % was achieved, indicating that this is a challenging reaction to make enantioselective.

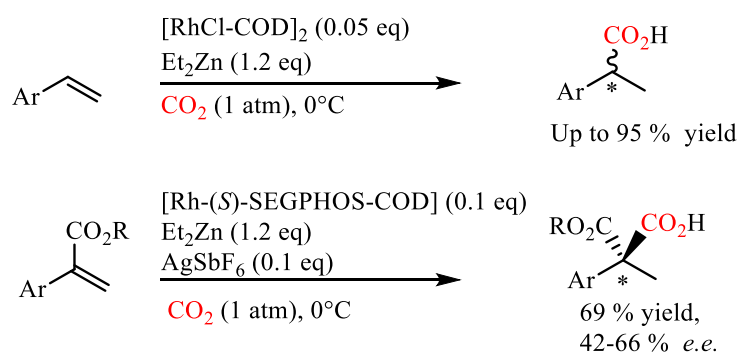


Figure 4.9 Rhodium-catalyzed hydrocarboxylation of alkenes with CO_2 , as reported by Mikami and co-workers (results from Kawashima *et al.*, ref²⁵).

Herein, the reaction mechanism of Rh-COD hydrocarboxylation was studied in detail, at the PBE-D2/IEFPCM level of theory (for additional computational details, see the paper I).¹⁵⁰ Besides the mechanistic investigation, the substrate preferences seen in the experiments was also explored.²⁵ Five functionalized alkenes were studied (Figure 4.10).

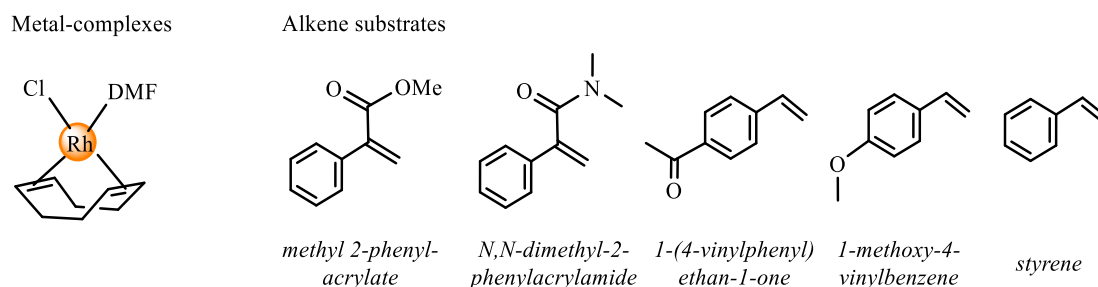


Figure 4.10 Catalyst model and substrates studied in Paper I.¹⁵⁰

Two of them, methyl 2-phenylacrylate and 1-(4-vinylphenyl)ethan-1-one, gave very high yields of 99 % and 89 %, respectively, whereas styrene, 1-methoxy-4-vinylbenzene and *N,N*-dimethyl-

2-phenylacrylamide were inactive substrates. First, the mechanistic details will be summarized, followed by the substrate preferences investigation.

4.4 Results and discussion of Rh-catalyzed hydrocarboxylation

The mechanism proposed by Mikami is given in Figure 4.11, with minor modifications based on our work (Paper I). The active catalyst Rh-Hydride is formed in two steps. First, an ethyl group from Diethylzinc is transmetallated to the precatalyst to yield a Rh-(DMF)-Ethyl intermediate. The coordination of DMF was proposed by me based on my calculations. This is followed by β -hydride elimination to form a Rh-hydride species and liberate ethene.

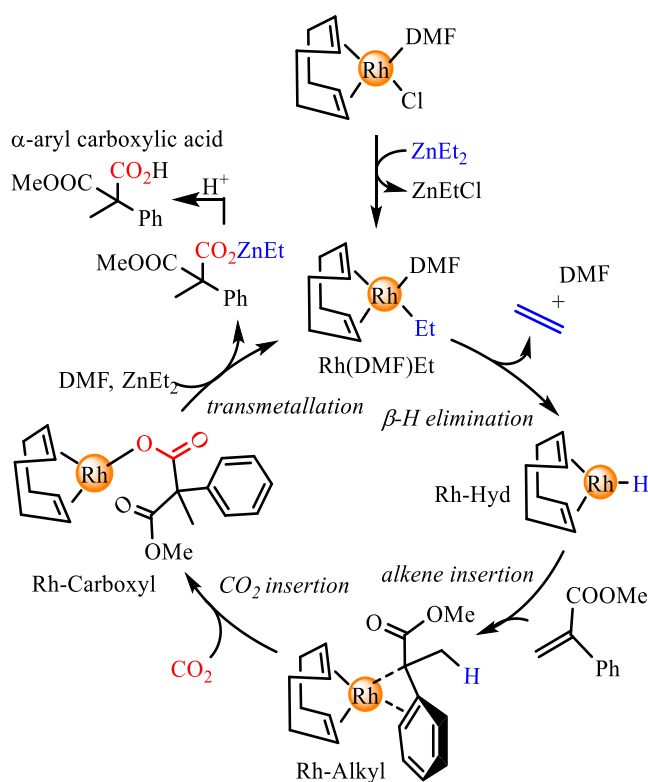


Figure 4.11¹ Proposed mechanism for Rh-COD-catalyzed hydrocarboxylation, based on the previous proposal and computations performed in Paper I.^{25,150}

Then, the alkene substrate inserts into the Rh-Hydride to form a nucleophilic Rh-Alkyl intermediate. Due to the non-symmetric nature of the alkene, two possible alkene insertion pathways exists (*1,2* or *2,1* insertion, Figure 4.5), with hydride transfer to the terminal carbon observed in experiment. In the next step, the C-CO₂ bond formation takes place by CO₂

¹ Adapted with permission from [Pavlovic, Lj.; Vaitla, J.; Bayer, A.; Hopmann, K.H., Rhodium-Catalyzed Hydrocarboxylation: Mechanistic Analysis Reveals Unusual Transition State for Carbon–Carbon Bond Formation. *Organometallics* 2018, 37 (6), 941-948]. Copyright (2018) American Chemical Society.

insertion into the Rh-Alkyl bond. The formed Rh-Carboxylate undergoes one more transmetalation with ZnEt_2 to regenerate the Rh-Ethyl intermediate. Finally, in the presence of acid, the product is liberated as a carboxylic acid.

The substrate methyl 2-phenylacrylate was used to investigate the reaction mechanism. The computed Gibbs free energy profile is given in Figure 4.12. The Rh-DMF-Et species was used as a reference to compute the free energies. The β -hydride elimination occurs via TS β -Hyd with a barrier of only 6.8 kcal/mol. Then, hydride transfer to the terminal C atom takes place to form an energetically stable Rh-alkyl intermediate.

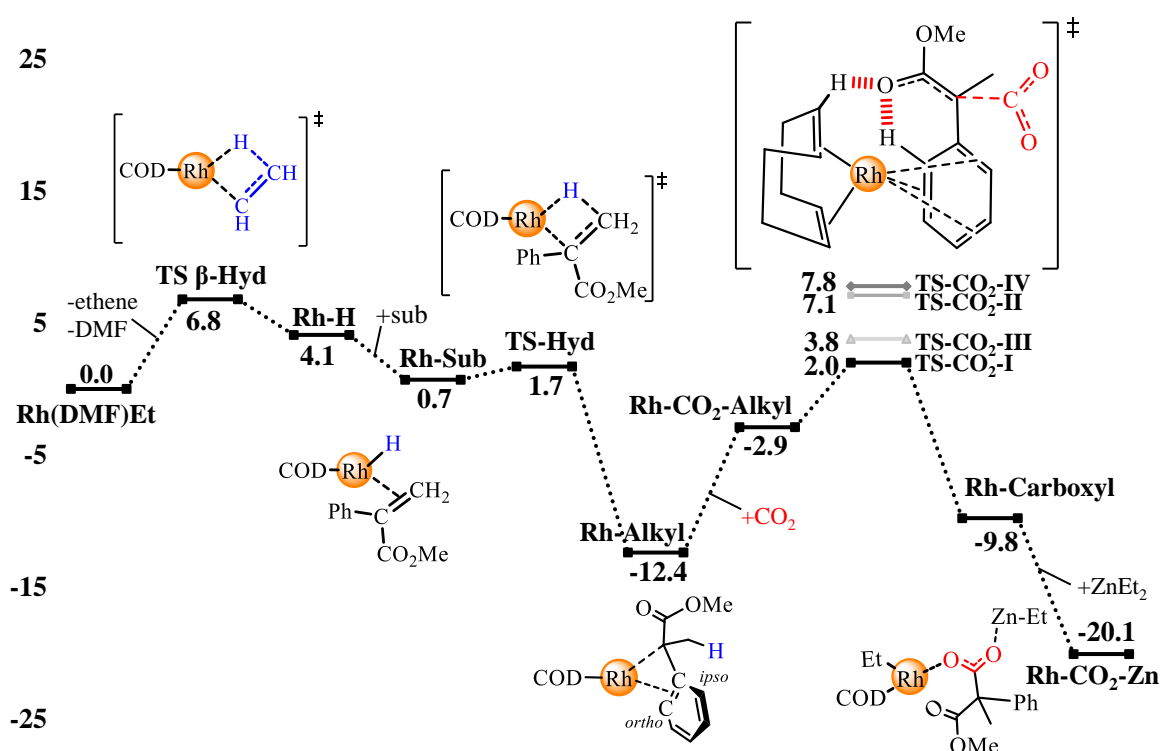


Figure 4.12 Computed free energy profile (kcal/mol, 323 K, PBE-D2/6-311+G(2d,2p) [IEFPCM]/PBE-D2/6-311G(d,p)[IEFPCM] level of theory) for rhodium-COD-catalyzed hydrocarboxylation of methyl 2-phenylacrylate.¹⁵⁰

The alkyl species shows an η^2 coordination mode^m of the phenyl group. After CO_2 insertion, this pathway will lead to the formation of an α -aryl carboxylic acid, which is the experimentally observed product. The alternative hydride transfer forms the β -aryl carboxylic acid and this path was higher in energy (SI of Paper I, Figure S1). The insertion of CO_2 into the alkyl species to form a Rh-carboxyl intermediate via $\text{TS}_{\text{CO}_2\text{-I}}$ appears to be rate-limiting with a barrier of 14.4

^m Proposed resonance structures of the alkyl intermediate are given in the SI of paper I, Figure S2.

kcal/mol. Finally, a transmetalation with ZnEt_2 occurs to form a stable intermediate where both Rh and Zn interact with the oxygen atoms of the carboxylate. Unfortunately, my attempts to find the TS for the transmetalation step failed.

Special attention was devoted to the C-CO₂ bond-forming step. The geometrical analysis of the lowest lying TS showed two important results: First, at the TS, an unusual substrate binding mode is present, where the phenyl ring of the substrate is coordinated to rhodium in an η^6 -fashion (Figure 4.13). The nucleophilic C-atom, which was expected to interact with the rhodium, is in this binding mode placed 3.60 Å away from the metal, indicating that no interaction takes place. This may be explained by the resonance structure of the TS, as outlined in Figure S4, SI of Paper I.

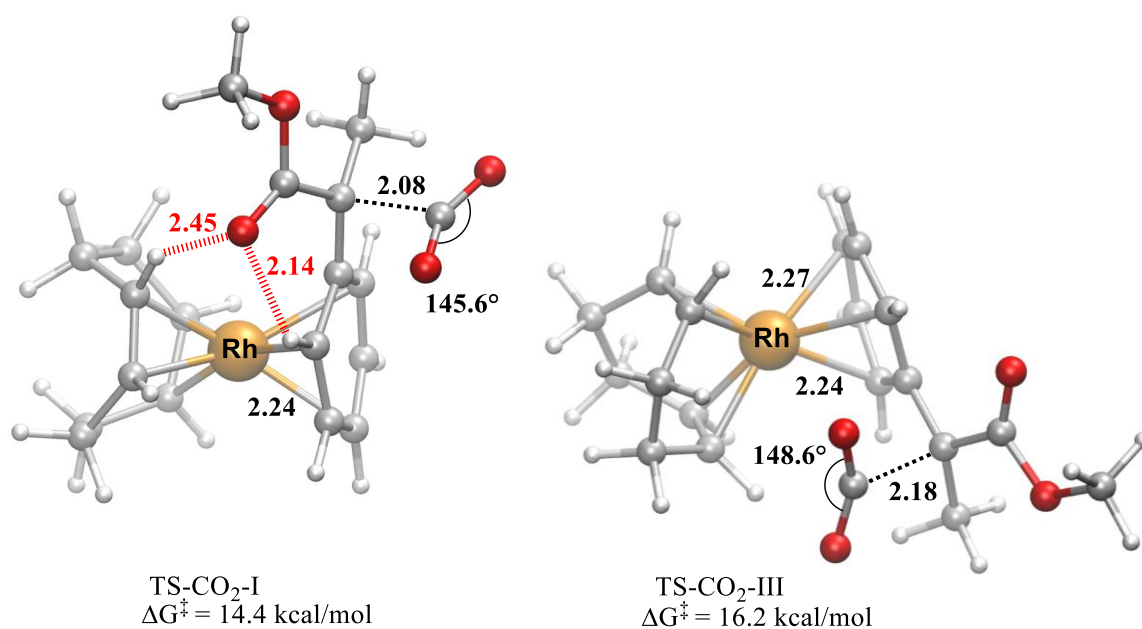


Figure 4.13 Optimized carboxylation TS geometries with methyl 2-phenylacrylate displaying an η^6 -coordination mode: The preferred CO₂ insertion mode with CO₂ far from rhodium (TS_{CO₂-I}, left) and with CO₂ placed closer to rhodium (TS_{CO₂-III}) (distances are in Å).¹⁵⁰

In this binding mode, the negative charge that is formally on the nucleophilic C-atom is delocalized over the ester oxygen, which is stabilized by two CH \cdots O interactions (distances 2.14 Å and 2.45 Å, respectively). The styrene derivatives without ester group will instead exhibit charge delocalization over the phenyl ring. The second important observation made during the analysis of the carboxylation TS is that CO₂ does not seem to interact with the rhodium during C-CO₂ bond formation. This result was unexpected to us due to fact that in many reported

studies, CO₂ interacts with the metal centre.^{148,159,161-163} However, if CO₂ is placed closer to the metal (TS_{CO₂_III}, Figure 4.13, right) the barrier increases by 1.8 kcal/mol.

I also tested alternative TS conformations, where the carbonyl group of ester interacts with the rhodium (TS_{CO₂_II}, CO...Rh distance of 2.16 Å, Figure 4.14) but the energy was higher by 5 kcal/mol relative to the best TS_{CO₂_I}. An alternative TS where the CO₂ is placed closer to rhodium, TS_{CO₂_IV}, had a barrier around 6 kcal/mol higher relative to the best TS_{CO₂_I} (SI of Paper I, Figure S5). Interestingly, the initially expected TS_{CO₂_V}, which shows a Rh-CO₂ interaction, had a barrier of 37.9 kcal/mol, which was higher by 23.5 kcal/mol relative to the best TS_{CO₂_I} (Figure 4.14).

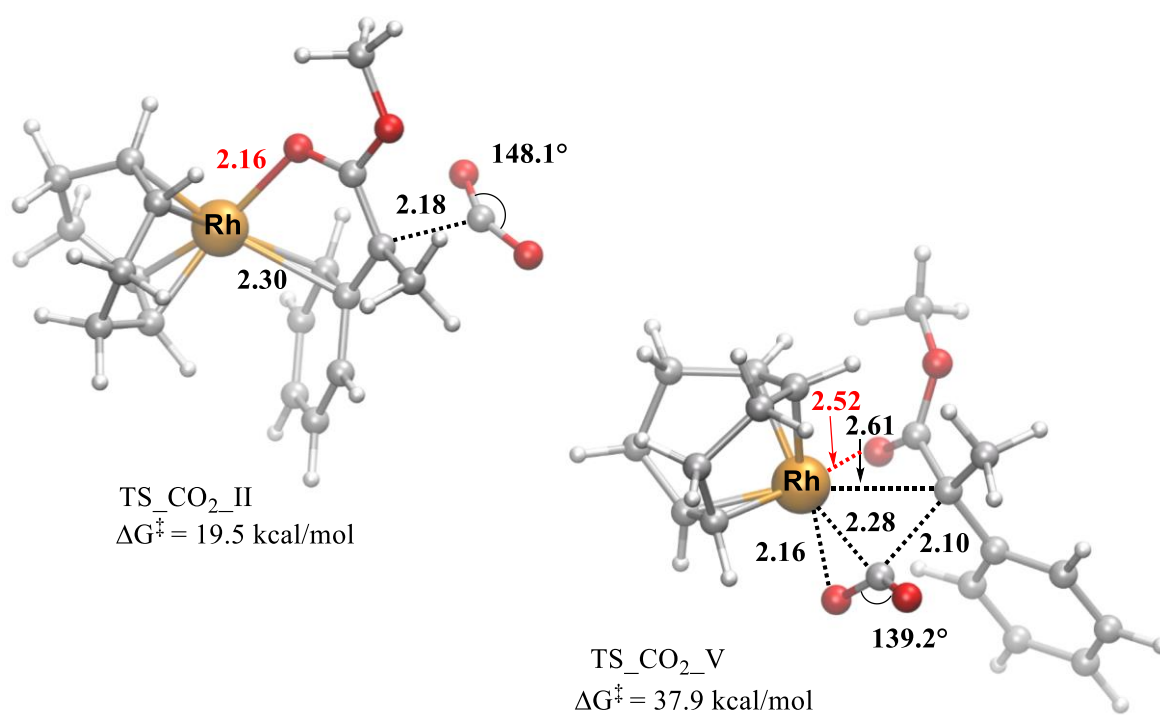


Figure 4.14 Optimized geometries of energetically higher-lying CO₂ insertion TSs displaying a Rh-O_{Ester} interaction (TS_{CO₂_II}) and a Rh-CO₂ interaction (TS_{CO₂_V}) (distances are in Å).¹⁵⁰

The possibility that at the best TS, CO₂ might interact with another species in the reaction mixture, for example with the Lewis acid additive ZnEt₂ or another Rh metal complex was also considered. However, my calculations show that it is not preferable for CO₂ to interact with the additive ZnEt₂ at the TS (Figure 4.15 a). Also a so-called bimetallic insertion mechanism was considered (Paper II),¹⁵⁴ where a second metal complex assist the reaction (Figure 4.15 b). An open coordination site is required in order for another Rh complex to interact with CO₂. Thus, the Rh-Hydride species was employed, which has one open coordinate site, and the effect of

placing this species next to the CO₂ molecule in TS_{CO₂_I} was tested. It was shown that the interaction between the CO₂ and other Rh-complexes increases the insertion barrier from 14.4 to 32.4 kcal/mol, which is not feasible at the reaction temperature of 273 K.

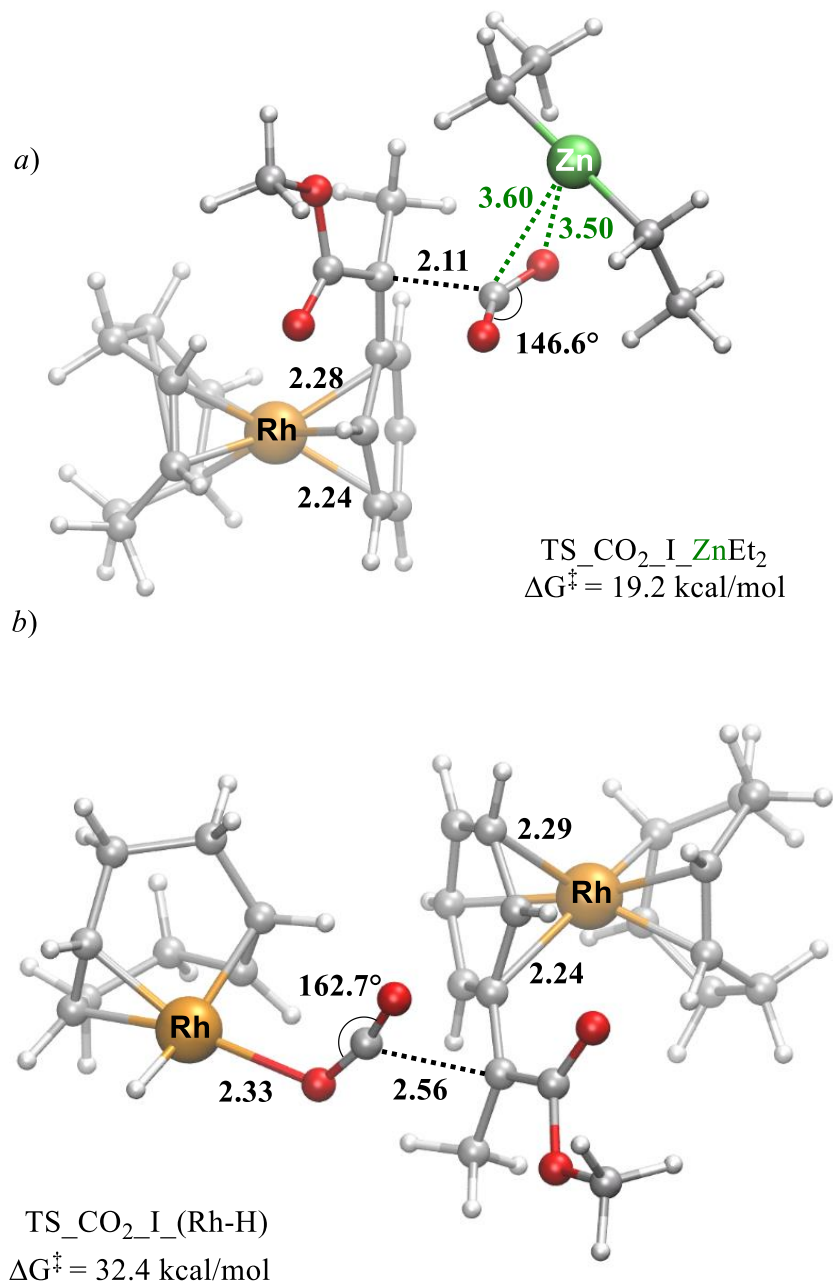


Figure 4.15 Optimized geometries of energetically higher-lying CO₂ insertion TSs with the additive ZnEt₂ (TS_{CO₂_I_ZnEt₂) or with another Rh-COD-H complex present that interacts with CO₂ (TS_{CO₂_I_(Rh-H)) (distances are in Å).^{150,154}}}

4.4.1 Substrate preferences

In order to get deeper insight into the substrate preferences observed in the experiments performed by Mikami,²⁵ I computed five alkenes: an α,β -unsaturated ester and an amide, styrene and two para-substituted styrene-derivatives. In experiments,²⁵ two substrates, the methyl 2-phenylacrylate and the 1-(4-vinylphenyl)ethan-1-one, provided high yields of 99 % and 89 %, respectively. On the other hand, the *N,N*-dimethyl-2-phenylacrylamide, the styrene and 1-methoxy-4-vinylbenzene gave 0 % of yield.

Herein, we envisioned that the lack of reactivity of some substrates may be due to high CO₂ insertion barriers. The barriers for each alkene were computed relative to the corresponding Rh-Alkyl intermediate (Table 4.1).

Table 4.1 Computed CO₂ insertion barriers for different substrates (Gibbs free energies are given in kcal/mol, 273 K) versus experimental yield.²⁵

Substrates	Computed barrier for CO ₂ insertion	Experimental Yield [%] ²⁵
Methyl 2-phenylacrylate	14.4	>99 %
1-methoxy-4-vinylbenzene	16.4	0 %
Styrene	16.7	0 %
1-(4-vinylphenyl)ethan-1-one	18.7	89 %
<i>N,N</i> -dimethyl-2-phenylacrylamide	19.8	0 %

The geometrical analysis of the obtained TSs shows that all structures prefer an η^6 -coordination mode of the substrate, and that CO₂ does not interact with the metal center (Figure 4.16). The lowest computed barrier was found with the methyl 2-phenylacrylate (14.4 kcal/mol), whereas the highest barrier was found for the *N,N*-dimethyl-2-phenylacrylamide substrate (19.8 kcal/mol). Hence, the difference in CO₂ insertion barrier could explain why the ester is active, whereas amide is inactive in this reaction. However, as the barrier of 19.8 kcal/mol should be feasible at the reaction temperature of 273 K, it is possible that the barrier is underestimated, for example due an energetically low-lying species (on- or off-cycle), which I failed to identify. The styrene and 1-methoxy-4-vinylbenzene substrates gave barriers of 16.7 and 16.4 kcal/mol, respectively, which were around 2 kcal/mol higher relative to the lowest barrier obtained with the methyl 2-phenylacrylate. These results match the trend in experiments where styrene and 1-methoxy-4-vinylbenzene substrates were inactive, however, again the overall barriers appear

low. The 1-(4-vinylphenyl)ethan-1-one substrate showed a comparatively high CO₂ insertion barrier of 18.7 kcal/mol, although it should give high yield in experiments.²⁵ It is possible that a lower CO₂ insertion TS exist for this substrate, but I did not manage to locate it, possibly due to the large conformational freedom of the CO₂ insertion TS. However, the correlation between the four other substrates indicates that the CO₂ insertion barriers could explain the experimentally observed substrate preference.²⁵

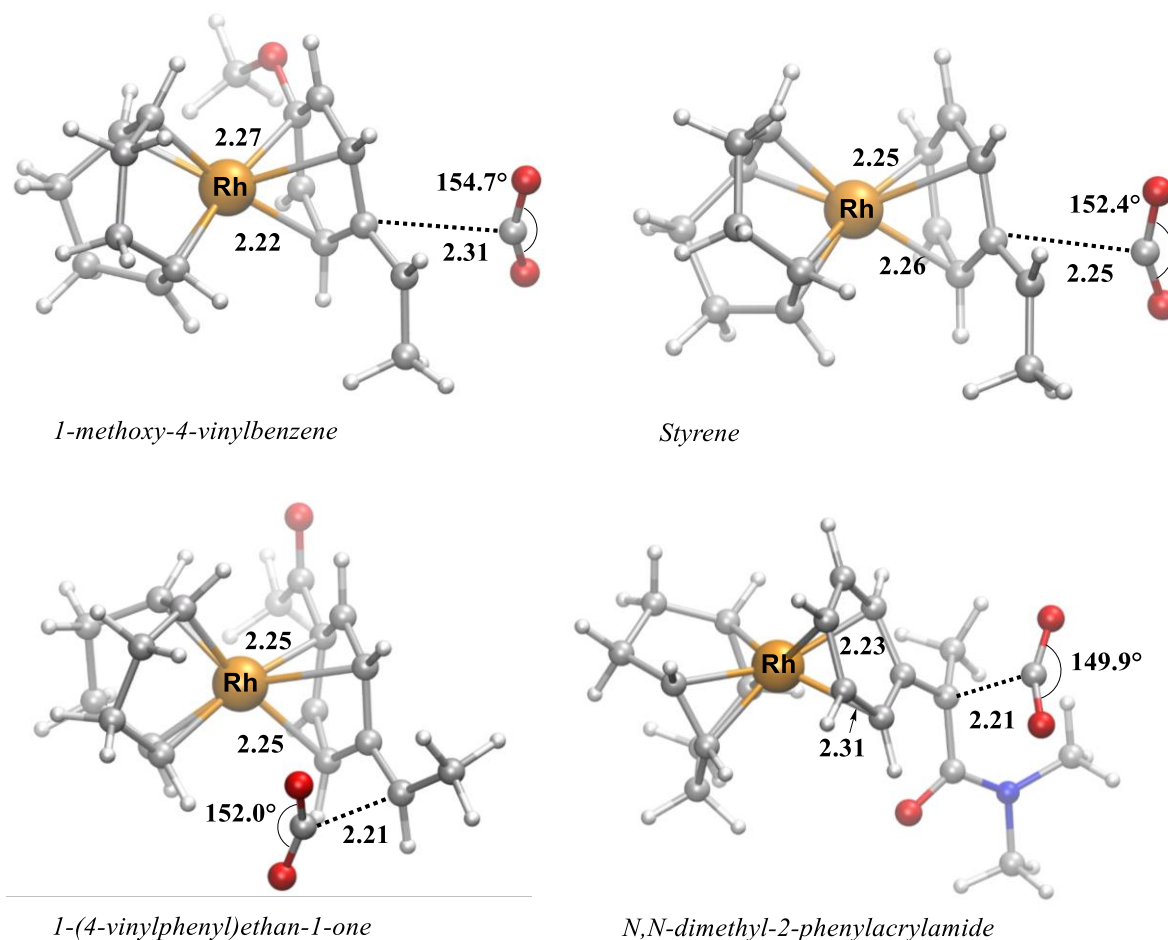


Figure 4.16 The optimized geometries of the lowest lying carboxylation TSs with different substrates (distances are given in Å).¹⁵⁰

4.5 Rh-catalyzed asymmetric hydrocarboxylation with CO₂ (Paper II&III)

The design of enantioselective catalysts, which can afford high *e.e.*'s remains a big challenge in asymmetric metal-based hydrocarboxylation reactions. There is reported only one experimental study, which focus was on asymmetric hydrocarboxylation of styrenes with CO₂.²⁵ On the basis of my results for the Rh-COD-benzyl system,¹⁵⁰ where I showed that during C-CO₂ bond formation, CO₂ does not interact with the metal centre, it is of special interest to understand how CO₂ will behave in the presence of different chiral ligands. Due to the fact that CO₂ is not in a restricted position with respect to the metal during C-CO₂ bond formation, it could be that its position is affected by the repulsive and attractive non-covalent interactions with chiral ligands. A deeper insight into the factors that govern the preferred positions of CO₂ may help to design catalysts with higher enantioselectivities. It is further of high interest to identify more selective catalysts, given that the only known hydrocarboxylation system displayed moderate *e.e.*'s of up to 66 %.²⁵

4.5.1 Potential of various chiral ligands in asymmetric hydrocarboxylation

Our strategy to understand and design complexes for asymmetric hydrocarboxylation was twofold: *i*) Theoretical analysis of the enantioselectivity and the selectivity-determining factors in Rh-catalyzed hydrocarboxylations with different chiral rhodium complexes, where an computational toolkit AARON¹⁶⁴ (An Automated Reaction Optimizer for New catalysts) was used for ligand swapping and then manual DFT optimizations of TSs was performed. *ii*) Experimental testing of several ligands in order to validate the enantioselectivities predicted by the computations. The latter part of our strategy is still ongoing work. Here I will focus on presenting the TS structures predicted with DFT.

Inner versus outer sphere carboxylation with Rh-(S)-SEGPHOS

Our initial analysis focused on the hydrocarboxylation with the Rh-(S)-SEGPHOS catalyst is given in Paper II. Here, I tested the preferred CO₂ insertion path (*inner* versus *outer sphere* insertion (Figure 4.17) and showed that the TS with Rh-CO₂ interactions present (referred to as *inner sphere* CO₂ insertion) is higher in energy by 17 kcal/mol, relative to the best *outer sphere* TS (Paper II, Figure 5, B3LYP-D3).¹⁵⁴ In Paper III we show that our results on the Rh-(S)-SEGPHOS system show the same trend (with a difference between *inner* and *outer sphere*

insertion of >17 kcal/mol), when the PBE-D2 method is used. Therefore, we excluded *inner sphere* TSs in the analysis of other chiral ligands (SI of Paper III, Figure S2).

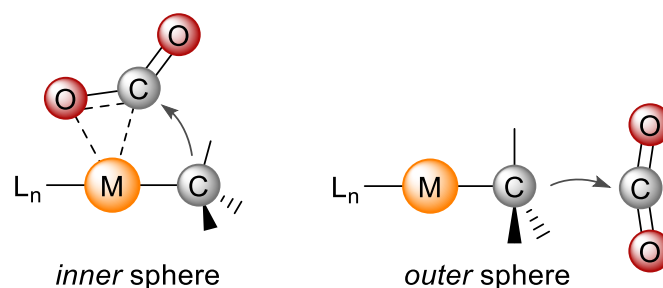


Figure 4.17ⁿ Inner and outer sphere CO₂ insertion paths.¹⁵⁴

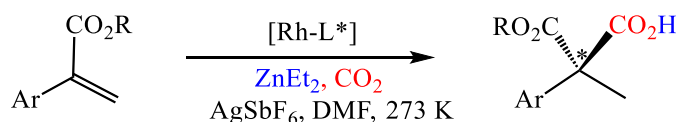
Outer sphere carboxylation with 5 chiral ligands

I proceeded to compare the *outer sphere* carboxylation step with five different Rh complexes with (*S*)-SEGPHOS, (*R,R*)-BDPP, (*R,R*)-tBu-BOX, (*R*)-StackPhos or (*S*)-iPr-PHOX as chiral ligands (Figure 4.18).

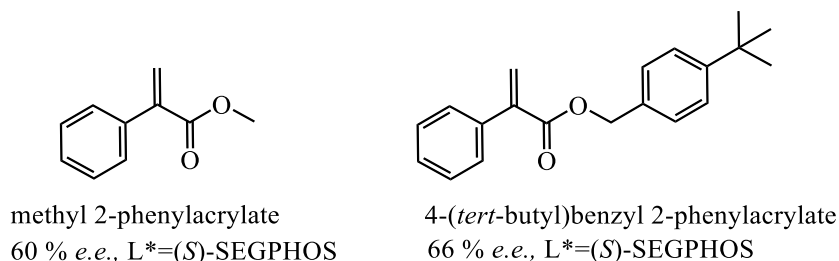
A motivation to include other four chiral ligands, beside (*S*)-SEGPHOS, is based on their successful performances in many metal catalyzed-asymmetric reactions, where high *e.e.*'s and yields were achieved.¹⁶⁵⁻¹⁷⁰ For example, in a (*S,S*)-Ph-BOX-Cu-catalyzed aziridination, several aryl-substituted olefins were converted to the corresponding *N*-tosylaziridines with enantioselectivities of up to 97 % and yields of 76 %.^{165,171} PHOX ligands are found to be excellent choices in Pd-catalyzed allylic substitutions to form dimethyl malonates with the reported *e.e.*'s of up to 98 % and yields of 98 %.^{167,172} In addition, PHOX ligands are found to be efficient in Ir-asymmetric hydrogenations of olefins.¹³² Next, in asymmetric hydrovinylation of 1-vinylcycloalkenes with the [(*S,S*)-2,4-bis-diphenylphosphino-pentane(BDPP)]-CoCl₂ catalyst, the reported *e.e.*'s were more than 99 % and yields of 98 %.¹⁶⁸ A successful application of (*S*)-StackPhos ligand was observed in Cu-catalyzed coupling reactions of aliphatic and aromatic aldehydes with the high *e.e.*'s of up to 95 % and yields of 92 %.^{169,170}

ⁿ Adapted with permission from [García-López, D.; Pavlovic, Lj.; Hopmann, K. H., To Bind or Not to Bind: Mechanistic Insights into C–CO₂ Bond Formation with Late Transition Metals. *Organometallics* **2020**, 39 (8), 1339-1347. <https://pubs.acs.org/doi/10.1021/acs.organomet.0c00090>]. Copyright (2020) American Chemical Society.

A) Computed reaction



B) Computed alkenes



C) Computed chiral ligands (L*)

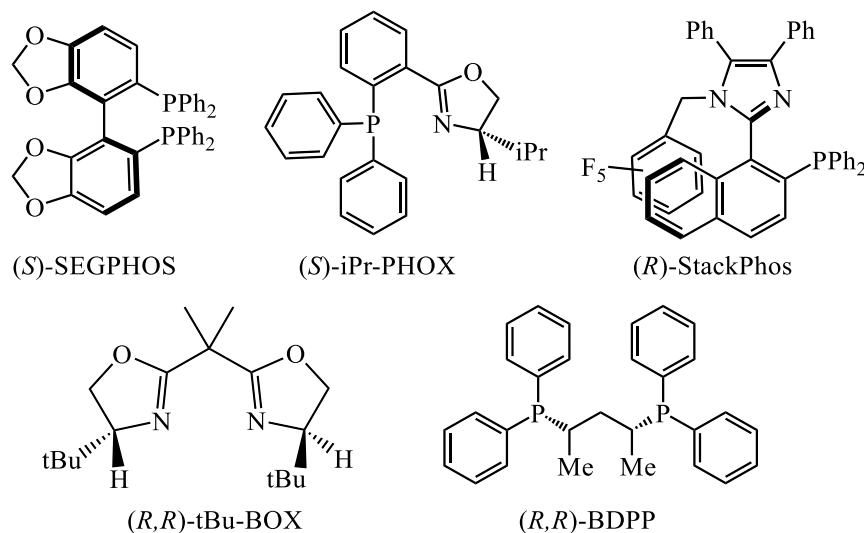


Figure 4.18 Hydrocarboxylation reaction (A) and substrates used in Rh-(*S*)-SEGPHOS-catalyzed hydrocarboxylation (B) by Mikami and coworkers,²⁵ and chiral ligands modelled manually in paper III (C).

For each of these ligands, 10 TSs were built manually with different ligand-substrate orientations (Paper III). Five of them were pro-(*S*)-TSs, whereas the rest of the structures were corresponding pro-(*R*) TSs (Figure 4.19). In two TS geometries, **TS1a** and **TS1b**, the phenyl ring interacts with the Rh-center in an η^6 fashion, where CO₂ is placed far away from the metal (here referred to as *backside insertion*) and the only difference between these two TSs is the orientation of the ester moiety. For **TS2a** and **TS2b**, the CO₂ is positioned closer to metal (here referred to as *frontside insertion*) but still the substrate shows Rh-phenyl interactions. At **TS3**, the oxygen of the carbonyl group of the ester moiety binds to the Rh-center, implying that the phenyl ring of the substrate interacts in an η^2 fashion.

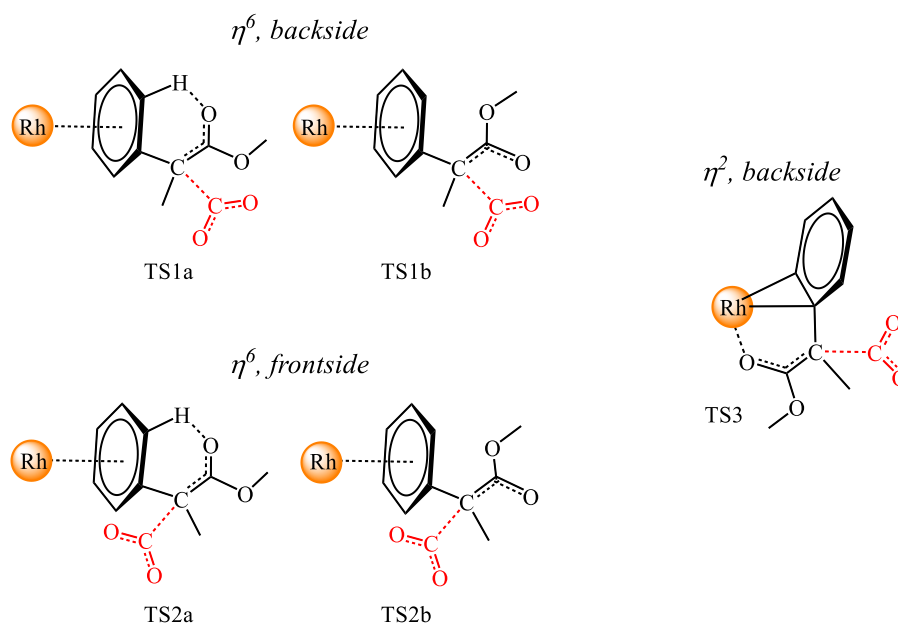


Figure 4.19 Five *outer sphere* TS conformations with different substrate-ligand-CO₂ orientations. For each of these TSs, both pro-(*R*) and pro-(*S*) conformations were included.

Beside the selectivity-determining factors, the aim of this work was to understand what kind of ligands may be advantageous in Rh-catalyzed asymmetric hydrocarboxylation with CO₂. Below, I first modelled the enantioselectivity of the Rh-(*S*)-SEGPHOS complex as a catalyst in the hydrocarboxylation of two experimentally known alkenes,²⁵ methyl 2-phenylacrylate and 4-(*tert*-butyl)benzyl 2-phenylacrylate (Figure 4.18, B). The work was performed at the PBE-D2 level of theory. Next, this study was expanded by employing four more chiral ligands.

4.5.2 Asymmetric Rh-(*S*)-SEGPHOS-catalyzed carboxylation of methyl 2-phenylacrylate.

Herein, I studied the Rh-(*S*)-SEGPHOS mediated C-CO₂ bond formation with methyl 2-phenylacrylate by modelling the 5 TS structures proposed in Figure 4.19. Free energy barriers for CO₂ insertion TSs were computed relative to the Rh-Enolate intermediate (SI of Paper III, Figure S3). At the lowest lying **TS1a_S** ($\Delta G = 12.1$ kcal/mol, 273 K), the Rh-Enolate attacks CO₂ by its *re* face and the experimentally observed (*S*)-product is obtained (Figure 4.20). On the other hand, at the **TS1a_R**, which is higher in energy by 0.7 kcal/mol, CO₂ is attacked by the *si* face of the enolate, yielding the (*R*)-product. The energetic preference for **TS1a_S** would be in agreement with experiment, which showed an *e.e.* of 60 % (*S*).²⁵

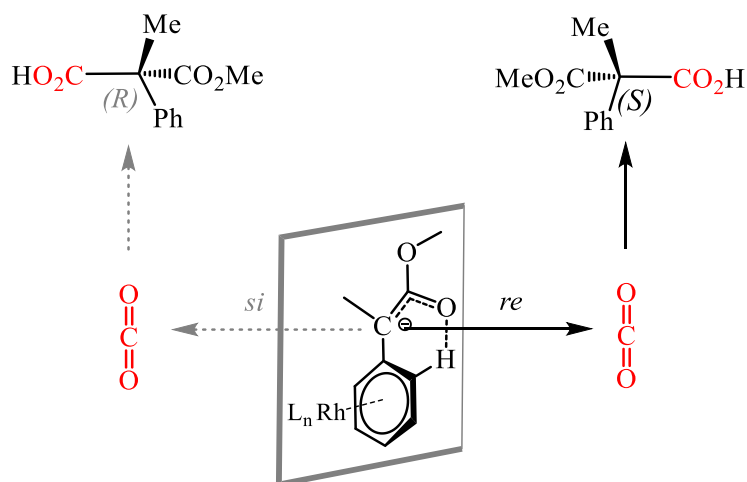


Figure 4.20 Illustration of the enolate attack, showing free CO₂ when (*S*)-SEGPHOS is employed.

In both diastereomeric **TS1a** structures (Figure 4.21), various noncovalent C-H \cdots π interactions between the phenyl rings of the ligand and the substrate are identified. At the lowest lying **TS1a_S** structure, the phenyl rings of the SEGPHOS ligand form two C-H \cdots π interactions with the phenyl ring of the substrate, which is coordinated to the rhodium centre (2.95 Å and 3.10 Å).

η^6 , backside

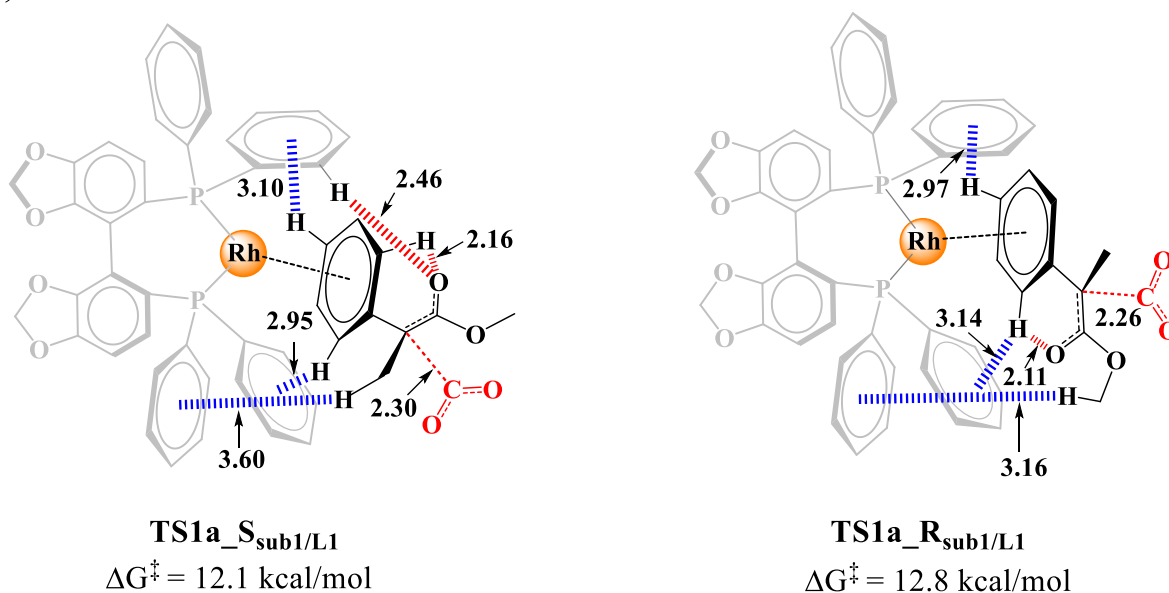


Figure 4.21 Illustration of the noncovalent interactions in the lowest lying pro-(*S*) and pro-(*R*) **TS1a** conformations (backside CO₂ insertion) with Rh-(*S*)-SEGPHOS and methyl 2-phenylacrylate (distances in Å).

There is also a weak C-H \cdots π interaction between the methyl group of the substrate and the phenyl ring of the ligand (3.60 Å). At the energetically higher lying **TS1a_R**, three C-H \cdots π interactions are observed. Two of them are between the phenyl ring of the SEGPHOS ligand and the phenyl of the substrate (2.93 Å and 3.10 Å), whereas one is formed between the phenyl of the ligand and the methyl group of the ester moiety (3.20 Å).

Additionally, in both **TS1a** structures, strong C-H \cdots O interactions *within* the substrate can be seen (TS1a_S: 2.16 Å, TS1a_R: 2.11 Å) but only at the lowest lying **TS1a_S** an additional strong intermolecular C-H \cdots O interaction (2.46 Å) is present, between the oxygen atom of the carbonyl group and the phenyl group of the catalyst (Figure 4.21). This C-H \cdots O distance is significantly larger at the energetically higher **TS1a_R** (3.00 Å).

In the next step, I analyzed the SEGPHOS TSs where CO₂ is placed close to the rhodium centre (referred to as *frontside attack*). Compared to the **TS1a** *backside* conformations, the energy barriers for these two **TS2a** are more than 4 kcal/mol higher (TS2a_S $\Delta G = 18.6$ kcal/mol, TS2a_R $\Delta G = 16.1$ kcal/mol, 273 K). Although favourable C-H \cdots π interactions were identified in both *frontside* TSs structures, the energetically favourable C-H \cdots O interaction between substrate and ligand is now prevented due to a closer position of CO₂ to the metal centre (Figure 4.22). The CO₂ forms C-H \cdots O interactions with the phenyl rings of the SEGPHOS ligand (2.50 Å, 2.90 Å).

η^6 , *frontside*

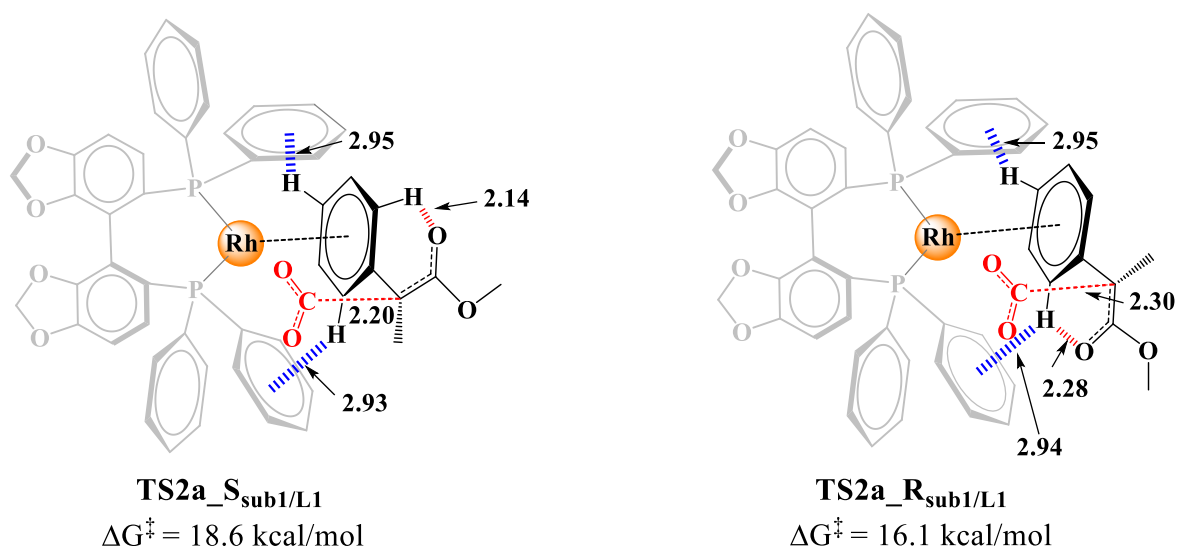


Figure 4.22 Illustration of the noncovalent interactions in pro-(*S*) and pro-(*R*) **TS2a** conformations (*frontside* CO₂ insertion) with Rh-(*S*)-SEGPHOS and methyl 2-phenylacrylate (distances in Å).

Interestingly, the *frontside* CO₂ insertion is not only higher in energy, it would also provide the incorrect enantioselectivity relative to the experiment.²⁵ The **TS2a_R** structure, which leads to the formation of the (*R*)-product, is lower in energy by 2.4 kcal/mol compared to **TS2a_S**, which would afford an *e.e.* of 98 % (*R*), in contrast to the 60 % (*S*) observed in experiment.²⁵ These findings highlight the need to employ experimentally known selectivities as a measure to validate computational mechanisms.

The TS structures, with different orientation of the ester moiety of the substrate, **TS1b** and **TS2b**, were higher in energy by 2 to 3 kcal/mol relative to the best **TS1a_S** (for the obtained energies see Table S1, SI of Paper III). Finally, I analyzed the pro-(*S*) and pro-(*R*) TSs structures where the ester of the carbonyl group interacts with the rhodium and these TSs were higher in energy by 8 kcal/mol. The final enantioselectivity was computed considering all ten TSs structures. The computed *e.e.* of 53.8 % (*S*) is in good agreement with the experimentally reported *e.e.* of 60.0 (*S*) for Rh-(*S*)-SEGPHOS-catalyzed carboxylation of methyl 2-phenylacrylate.²⁵

4.5.3 Asymmetric Rh-(*S*)-SEGPHOS-catalyzed carboxylation of 4-(*tert*-butyl)benzyl 2-phenylacrylate

Further computational investigation was undertaken to evaluate the obtained selectivity with the bulkier substrate 4-(*tert*-butyl)benzyl 2-phenylacrylate (Figure 4.23). This substrate contains two phenyl rings, hence in both TSs many favourable C-H \cdots π interactions can be identified (in the range of 2.90 Å to 3.60 Å, Figure 4.23).

This is a more challenging substrate to model, due to the benzyl ester moiety that expands the conformational search. I tested two TSs structures where CO₂ is placed away from the metal but with Rh-phenyl interactions present. Herein, a similar pattern is seen as in the previous case with the substrate methyl 2-phenylacrylate. At the lowest lying transition state **TS1a_S** ($\Delta G = 12.0$ kcal/mol, 273 K), the Rh-Enolate attacks CO₂ by its *re* face, resulting in formation of the (*S*)-product. The conformation of the substrate and catalyst allows a C-H \cdots O (2.47 Å) interaction to be formed. This interaction lacks at the **TS1a_R** ($\Delta G = 13.0$ kcal/mol), which is higher in energy by 1.0 kcal/mol. The computed *e.e.* of 73 % (*S*) is in a good agreement with the experimental value of 66 % (*S*), reported by Mikami,²⁵ with an error of only 0.2 kcal/mol.

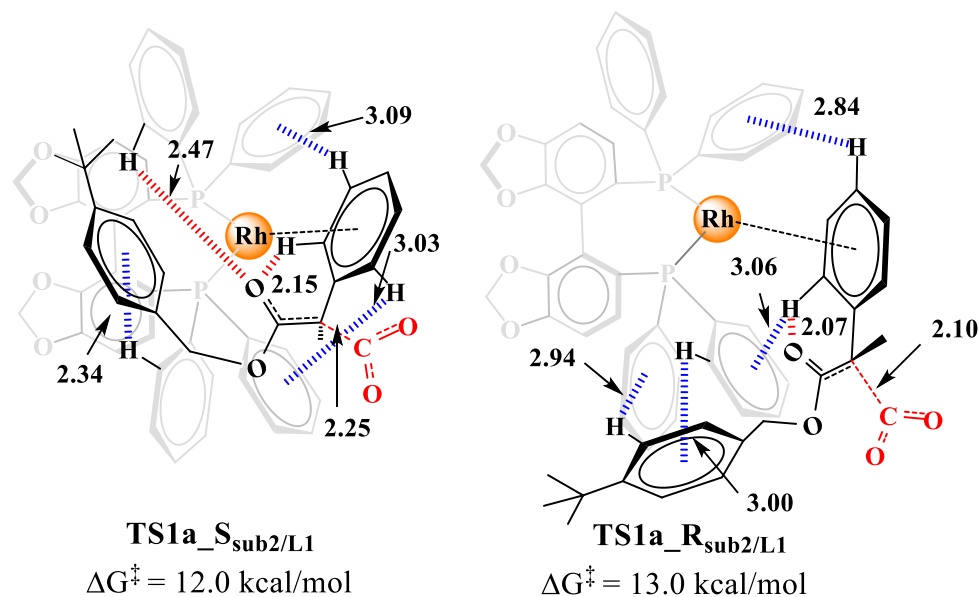


Figure 4.23 Illustration of the noncovalent interactions in the lowest lying pro-(*S*) and pro-(*R*) **TS1a** conformations (backside CO₂ insertion) with Rh-(*S*)-SEGPHOS and the 4-(tert-butyl)benzyl 2-phenylacrylate substrate (distances in Å).

The results indicate that with the chiral (*S*)-SEGPHOS ligand, the enantioselectivity of rhodium-catalyzed hydrocarboxylation appears to be a result of favourable C-H \cdots O interactions between the substrate and the catalyst (Figure 4.21, 4.23). At the preferred TS, the CO₂ molecule is positioned away from the metal center and thus the chiral catalyst is promoting the enantioselectivity only through positioning of the alkene substrate and not through interactions with CO₂.

4.5.4 Asymmetric Rh-(*R*)-StackPhos-catalyzed carboxylation of methyl 2-phenylacrylate.

Our analysis in section 4.5.3 shows that the computational protocol appears to be able to successfully reproduce and rationalize the experimentally reported enantioselectivity of the Rh-(*S*)-SEGPHOS catalysts for two different substrates.²⁵ On basis of this, we speculated that it may be possible to use computational methods to model and predict alternative chiral ligands for Rh-catalyzed hydrocarboxylation. Four ligands were modelled (Figure 4.18), of which the (*R*)-StackPhos gave intriguing results with respect to the observed CO₂ binding mode and will be discussed first.

Originally, the (*R*)-StackPhos ligand was reported by Aponick and co-workers as a promising ligand in Rh-based enantioselective A3-coupling (aldehyde-alkyne-amine) reactions.¹⁷⁰ This chiral *N,P* ligand is based on imidazole, which is linked to the metal through the N atom. Our

calculations show that at the lowest lying **TS2a_S**, the CO₂ prefers *frontside* insertion, where the substrate displays an η^6 -coordination mode (Figure 4.24). The **TS2a_R** conformation is higher in energy by 0.7 kcal/mol. The preference for *frontside* insertion with StackPhos is intriguing as it is different than for the SEGPHOS system, which prefers *backside* insertion (Figure 4.21).

At the lowest lying StackPhos-based **TS2a_S**, several interesting attractive noncovalent interactions are observed (Figure 4.24). In particular, CO₂ is placed above the imidazole ring with an intermolecular distance of around 3.20 Å. This type of imidazole-CO₂ interaction is known as a stacking interaction.¹⁷³⁻¹⁷⁵ There have been reported several computational studies where intermolecular interactions between CO₂ and N-heterocyclic compounds were identified.¹⁷³⁻¹⁷⁵ The ability of a ligand to weakly bind CO₂ is interesting, because in our work, it has been shown in several examples that CO₂ is not in a restricted position during the C-CO₂ bond forming step with rhodium-benzyl complexes (Figures 4.13, 4.16, 4.21, 4.22 and 4.23). This makes the design and study of enantioselective reactions with CO₂ challenging. Therefore, I propose that a promising strategy may be to restrict CO₂ to be in one specific position and thus to decrease its conformational freedom. The results for Rh-(*R*)-StackPhos show that this may be possible through the attractive noncovalent interaction with the imidazole ring. In this way, enantioselectivity will not only be promoted via ligand-alkyl interactions, as with (*S*)-SEGPHOS, but interactions with CO₂ may have an influence as well.

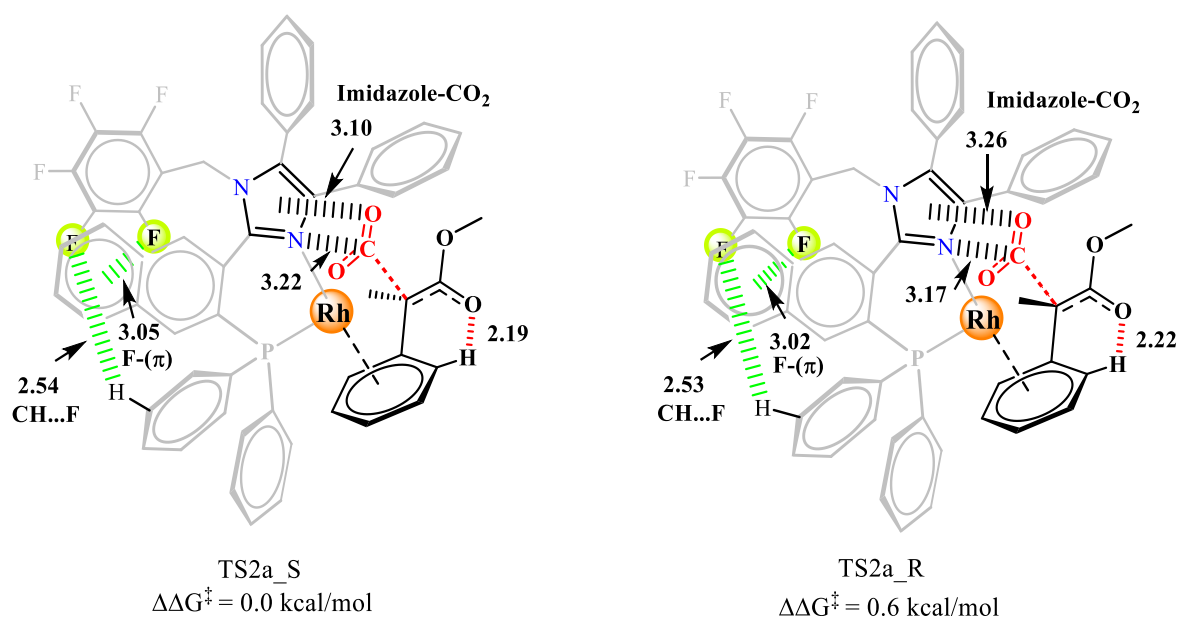


Figure 4.24 Illustration of Imidazole-CO₂ and F- π interactions at the lowest lying pro-(*S*) and pro-(*R*) **TS2a** carboxylation structures with Rh-(*R*)-StackPhos (distances are in Å).

Another interesting non-covalent interactions in the StackPhos system is an F- π interaction (3.05 Å) between the fluoro substituent of the phenyl group and the naphthalene ring, and one C-H \cdots F interaction (2.54 Å, Figure 4.24). Interestingly, the F- π interaction is not observed in the X ray structure of the StackPhos ligand,¹⁷⁰ instead a π - π interaction between the pentafluorophenyl group and the naphthalene ring is seen, with a distance of 3.38 Å. However, in my calculations, the TS with π - π interactions was higher in energy by 2.5 kcal/mol (**TS2a_stack_I**, SI of Paper III, Figure S4).

There is also a possibility that the phenyl substituent from the imidazole ring forms a π - π interaction with the pentafluorophenyl group. This **TS2a_stack_S** was higher in energy by 0.8 kcal/mol relative to best **TS2a_S**. In this structure, one F- π interaction (2.95 Å) between one phenyl group linked to the phosphorus and the pentafluorophenyl group is also identified (SI of Paper III, Figure S5). The corresponding **TS2a_stack_R** was higher in energy by 1.9 kcal/mol relative to best **TS2a_S**. Both of these TS structures, **TS2a_stack_S** and **TS2a_stack_R** structures were also included in the enantioselectivity evaluation due to their low barriers.

Interestingly, the TSs with the *backside* CO₂ insertion (**TS1a** and **TS1b**, SI of Paper III, Table S2.) were higher in energies by 2 to 3 kcal/mol. These TSs show a lack of imidazole-CO₂ interactions. Finally, TS conformations where the carbonyl group of the ester interacts with the rhodium (TS3) provided the highest barriers, with an increase of 10.7 kcal/mol and 15.2 kcal/mol, for the pro-(*S*) and pro-(*R*) TSs, respectively, relative to the best **TS2a_S**.

The enantioselectivity with the StackPhos ligand was evaluated with twelve TSs (SI of Paper III, Table S2), with a computed *e.e.* of 47 % (*S*). Although this is only a moderate *e.e.*, the observed imidazole-CO₂ interaction is intriguing, and further work is planned to explore how this interaction can be exploited to generate more selective ligands.

4.5.5 Asymmetric Rh-(*R,R*)-tBu-BOX-catalyzed carboxylation of methyl 2-phenylacrylate.

The third studied ligand was (*R,R*)-tBu-BOX, which contains two oxazoline rings coordinated to the metal. Our calculations show that at the lowest lying **TS2a_S**, the *frontside* CO₂ insertion is preferred (Figure 4.25). This ligand also displays an intriguing stacking interaction between

CO₂ and the N-heterocyclic ring of the ligand (oxazoline). Formation of the other product enantiomer via **TS2a_R** is higher in energy by only 0.5 kcal/mol.

At the lowest lying **TS2a_S**, several noncovalent interactions can be observed. There is one weak interaction present with a distance of 3.50 Å between the C atom of the CO₂ and the N atom of the oxazoline ring (Figure 4.25). One can also observe a C-H···O interaction between the oxygen atom of the CO₂ and the H atom of the oxazoline ring (2.46 Å). The same type of interactions are recognized at the **TS2a_R** geometry. At this geometry, the C-H···O interaction between the oxygen atom of the CO₂ and the H atom of the oxazoline ring is slightly elongated by 0.14 Å (2.60 Å).

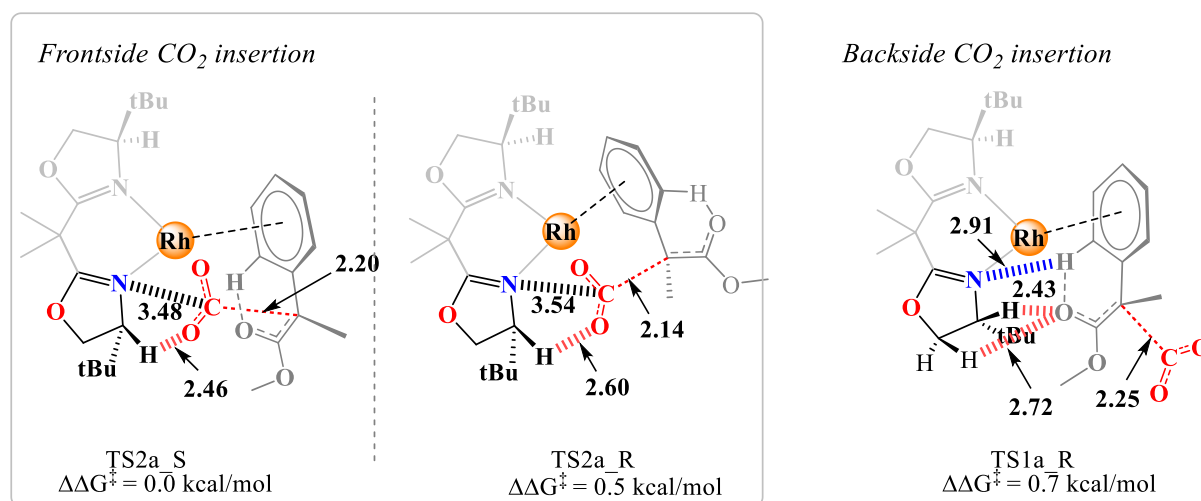


Figure 4.25 Illustration of the noncovalent interactions in the lowest lying pro-(*S*) and pro-(*R*) **TS2a** carboxylation structures alongside **TS1a_R** conformation with Rh-(*R,R*)-tBu-BOX (distances are in Å).

Interestingly, the pro-(*R*) TSs, **TS1a_R** and **TS1b_R** with *backside* insertion, are higher in energy by only 0.7 and 0.8 kcal/mol respectively, relative to the best **TS2a_S** structure (see SI of Paper III, Table S4). At **TS1a_R**, which display a *backside* CO₂ insertion, the oxygen of the carbonyl group of the ester is stabilized through two C-H···O interactions with the ligand (2.43 Å and 2.72 Å). There is one more N···H-π interaction of 2.91 Å between the oxazoline ring and the substrate. This interaction is also present at **TS2a_S** and **TS2a_R**, but it is weaker (3.10 Å and 3.20 Å, respectively).

The pro-(*S*) and pro-(*R*) TSs where the carbonyl group of the ester interacts with the rhodium (TS3) are respectively 3.2 kcal/mol and 5.3 kcal/mol higher in energy than the best **TS2a_S**.

With all ten tested TSs considered, the computed *e.e.* for the Rh-(*R,R*)-tBu-BOX-catalyzed carboxylation of methyl 2-phenylacrylate is only 6.4 % (*S*). It appears that both CO₂ insertion pathways (*frontside* and *backside*) are equally preferred for this ligand, which leads to the very low enantioselectivity.

4.5.6 Asymmetric Rh-(*R,R*)-BDPP-catalyzed carboxylation of methyl 2-phenylacrylate.

The chiral diphosphine ligand (*R,R*)-BDPP was the fourth ligand in my test set. At the lowest lying **TS1a_R**, the CO₂ prefers *backside* insertion (Figure 4.26). **TS1a_S** has a barrier that is only 0.5 kcal/mol higher than **TS1a_R**. Interestingly, for (*R,R*)-BDPP, the TSs with the *frontside* CO₂ insertion are higher in energy by more than 5 kcal/mol (see SI of Paper III, Table S5). This scenario is reminiscent of the diphosphine ligand (*S*)-SEGPHOS. The result may be a consequence of the bulky phenyl groups of the ligand, which restrict CO₂ to prefer insertion via a backside path.

A geometrical analysis of the lowest lying TSs, **TS1a_R** and **TS1a_S** reveals that both TSs contain the CH \cdots O interactions between the carbonyl group of the substrate and a phenyl group of the ligand. At the **TS1a_S**, this interaction appears to be stronger (2.30 Å) than at **TS1a_R** (2.50 Å), although the latter is lower in energy.

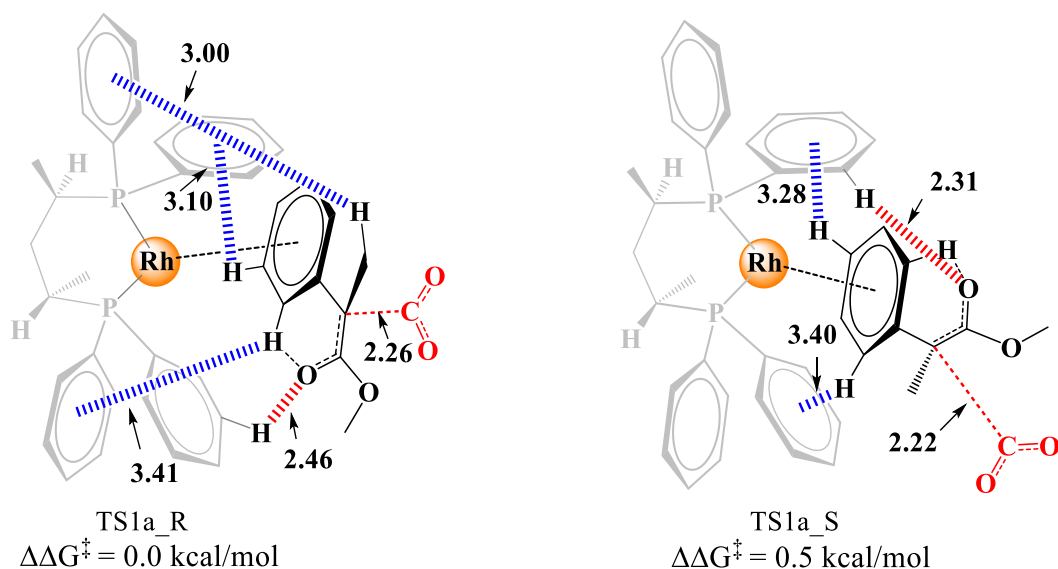


Figure 4.26 Illustration of the noncovalent interactions in the lowest lying pro-(*S*) and pro-(*R*) **TS1a** carboxylation structures with Rh-(*R,R*)-BDPP (distances are in Å).

At both TSs, several C-H \cdots π interactions can be identified between the substrate and the ligand (Figure 4.26), but one of them seems to be only present at **TS1a_R**, a C-H \cdots π interaction of 3.00 Å between the Me group of the substrate and the phenyl ring of the ligand. The TSs where the carbonyl group of the ester interacts with the rhodium (TS3) provide the highest barriers, with the pro-(*S*) and pro-(*R*) TS3 placed 9.7 kcal/mol and 12.1 kcal/mol above the best **TS1a_R** (see SI of Paper III, Table S5).

The computed *e.e.* for the Rh-(*R,R*)-BDPP-catalyzed carboxylation of methyl 2-phenylacrylate, based on all ten TSs, is 24.3 % (*R*). The relatively low *e.e.*'s computed for this and the other studied ligands indicates that the design of more enantioselective hydrocarboxylation reactions is challenging and may explain why this field has not witnessed any significant successes so far.

4.5.7 Asymmetric Rh-(*S*)-iPr-PHOX-catalyzed carboxylation of methyl 2-phenylacrylate.

Chiral phosphino-oxazoline PHOX ligands are being widely used in asymmetric hydrogenation and allylation reactions.¹¹⁷ Therefore, we tested the potential of (*S*)-iPr-PHOX in an asymmetric hydrocarboxylation reaction with CO₂. The lowest lying TSs prefer backside CO₂ insertion (Figure 4.27). Interestingly, the pro-(*R*) and pro-(*S*) TSs have the same energy. The reason for this outcome could be the fact that in the both transition state structures, **TS1a_S** and **TS1a_R**, the same type of noncovalent interactions are present, such as C-H \cdots O and C-H \cdots π , with comparable strength.

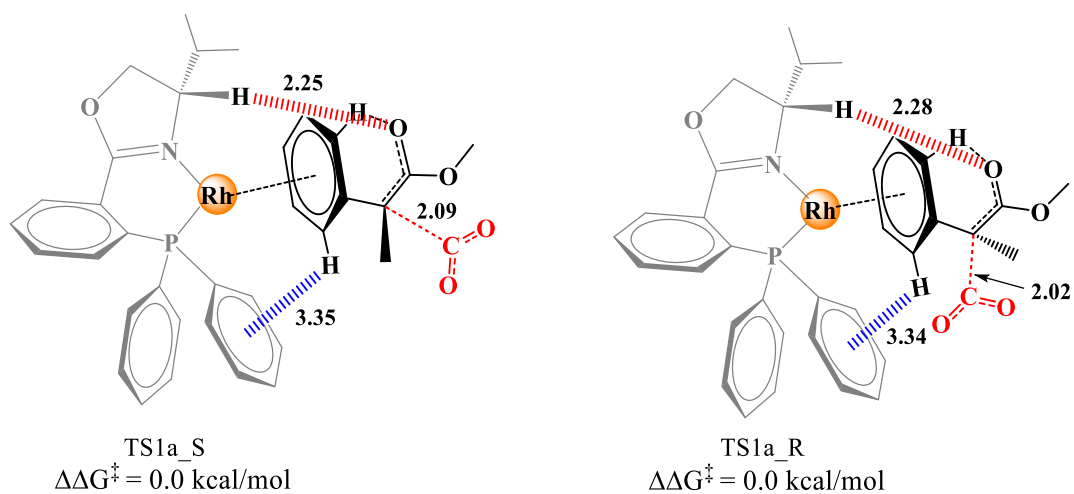


Figure 4.27 Illustration of the noncovalent interactions in the lowest lying pro-(*S*) and pro-(*R*) **TS1a** carboxylation structures with Rh-(*S*)-iPr-PHOX (distances are in Å).

The TSs, which prefer the *frontside* CO₂ insertion, are higher in energy by 1.8 to 3.4 kcal/mol relative to the best TSs, **TS1a_S** and **TS1a_R**. As with the chiral ligands discussed above, TS3 gave the highest barriers, with an energy of 12.3 kcal/mol and 6.5 kcal/mol, for pro-(*S*) and pro-(*R*) TS, respectively, relatively to TS1 (see SI of Paper III, Table S3).

Our computations indicate that there is very low selectivity of 1.8 % for the Rh-(*S*)-iPr-PHOX-catalyzed hydrocarboxylation of methyl 2-phenylacrylate, which is indeed supported by the preliminary experiments of our collaborators (unpublished data).

4.6 General conclusion

In this study, one of the goals was to understand the intimate behaviour of CO₂ in hydrocarboxylation reaction with various Rh-complexes. The initial study of achiral Rh-COD-benzyl complexes (Paper I) showed that CO₂ does not interact with the rhodium during the C-CO₂ bond forming step, which was an unexpected scenario, also given the fact that other Rh-alkyl systems were proposed to have pronounced Rh-CO₂ interactions.¹⁴⁷ We believe that the main difference to other studies is the benzylic nucleophile, which prefers an η^6 -coordination to the rhodium, thus altering the coordination sphere and behaviour of the metal compared to a simpler Csp³ nucleophile such as methyl.

For Rh-COD, the computed substrate preferences seemed to match to the experimentally reported ones for several substrates,²⁵ and for all, the lowest lying TSs showed a lack of Rh-CO₂ interactions (Paper I).

In our study of the asymmetric hydrocarboxylation reactions with CO₂, the preferred TSs geometries observed with the chiral diphosphine ligand SEGPHOS are similar to those observed with Rh-COD, indicating that CO₂ does not interact with the metal (Paper II). As CO₂ is not in a restricted position with respect to the rhodium, we can distinguish two CO₂ insertion paths, *frontside* or *backside*, which both have an η^6 -coordination mode of the substrate. We computed 5 chiral ligands (Paper III), of which one (SEGHOS) was previously used in a hydrocarboxylation reaction by Mikami,²⁵ and the other four (BDDP, tBu-BOX, iPr-PHOX, StackPhos) were proposed by us, based on their use in other metal-catalyzed reactions.

Our results indicate that the nature of the ligand plays an important role for the CO₂ insertion path. Interestingly, less bulky ligands, such as (*R,R*)-tBu-BOX and (*S*)-iPr-PHOX were not able

to restrict the CO₂ in one specific position, thus both insertion paths (*frontside* and *backside*) appear possible. The diphosphine ligands, (*R,R*)-BDPP and (*S*)-SEGPHOS, showed a preference for backside insertion of CO₂. Among all the computed ligands, the previously reported (*S*)-SEGPHOS showed the highest computed enantioselectivity of 73 %, thus no ligand with a predicted higher enantioselectivity could be identified yet. Of the four virtually modelled ligands, (*R*)-StackPhos appears to be the most interesting candidate. This is due to presence of an imidazole-CO₂ interaction, which potentially can restrict the CO₂ position. In this way, enantioselectivity may be promoted via attractive ligand-CO₂ interactions and not only via attractive ligand-substrate interactions. Although a low *e.e.* of 47 % is computed for StackPhos, with a proper further modification of the ligand, higher enantioselectivities may be achievable. On basis of the results obtained in the computations, experimental verification of the StackPhos results and testing of related ligand are currently ongoing in the laboratory of our experimental collaborators.

5. Hydrogenation

In the last few decades, a tremendous diversity of products have been synthesized in metal-catalyzed hydrogenation reactions.^{4,7,17,108,176-181} The search for promising catalysts, which have the potential to be employed in hydrogenation reactions, has a long history. Great attention was given to precious metals such as Rh, Ru and Ir as catalysts.^{3,9,13,132,179,182,183} These metals showed an extraordinary activity and reactivity in various metal-catalyzed hydrogenations. One of the first well-known hydrogenation catalysts was a chloridotris-(triphenylphosphine)-rhodium(I) complex, referred to as the Wilkinson's catalyst (Figure 5.1).⁹ However, it had several disadvantages. For example, functionalized substrates with carbonyl groups were not tolerated, which lead to a limited substrate scope. Later, the cationic Rh and Ir complexes were reported. Representative examples are Schrock-Osborn or Crabtree catalysts,¹⁸⁴ with weakly coordinated anions such as SbF_6 , PF_6 , BF_4 .

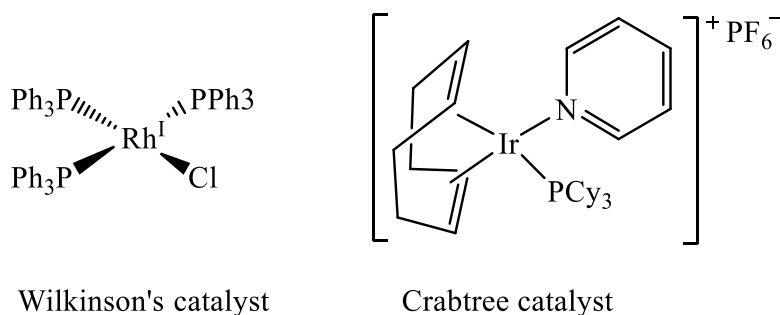


Figure 5.1 The Wilkinson's and Crabtree catalysts.

Although precious metals have been shown to be excellent catalysts, their main limitations are high cost and toxicity. Therefore, there is a need in the science community to swap these noble metals with an inexpensive earth abundant metals, such as Fe, Mn, Ni and Co. However, it is not straightforward to just use a 3d metals instead of a noble metals, because the reactivity of 3d metals is difficult to predict and control, for example, due to close lying oxidation and spin states. It is thus necessary to investigate their reactivity further.

In this Chapter, I will briefly introduce several mechanistic proposals that have been put forward for hydrogenation of alkenes. Then the emphasis will be put on asymmetric Co-catalyzed hydrogenation. Finally, the results presented in paper **IV** are summarized and discussed.

5.1 Mechanistic aspects of metal-catalyzed hydrogenations

Hydrogenation of alkenes can occur through variety of mechanisms. For example, two-electron redox mechanisms are well established for precious metals, such as Rh and Ir.^{9,14,183} A simple M(I)-M(III) redox mechanism is shown in Figure 5.2. It starts with H₂ coordination to the M(I)-complex, which is oxidatively added (OA) to form a M(III)-di-hydride intermediate. This step is referred to as homolytic H₂ cleavage. In the next step, alkene coordination takes place, followed by a hydride transfer to the alkene (migratory insertion step). Finally, proton transfer (reductive elimination) occurs to regenerate the catalyst and liberate the alkane product.

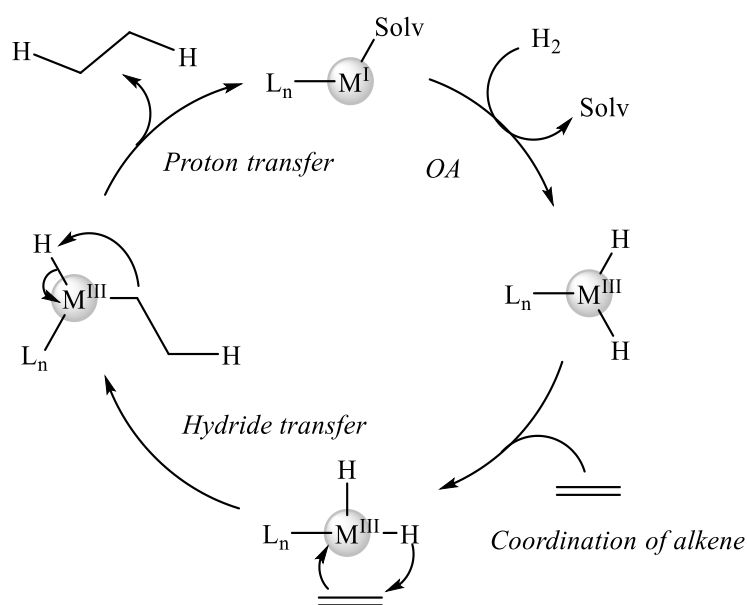


Figure 5.2 Generic redox M(I)-M(III) hydrogenation mechanism.

Another mechanism proposed in the literature is the non-redox σ -bond metathesis mechanism, which can operate in Co-based and Ir-based hydrogenation reactions.^{13,185,186} During this reaction, σ -bonded group to the metal exchanges with a σ -bonded group of a reactant. The σ -bond metathesis step is given in Figure 5.3.

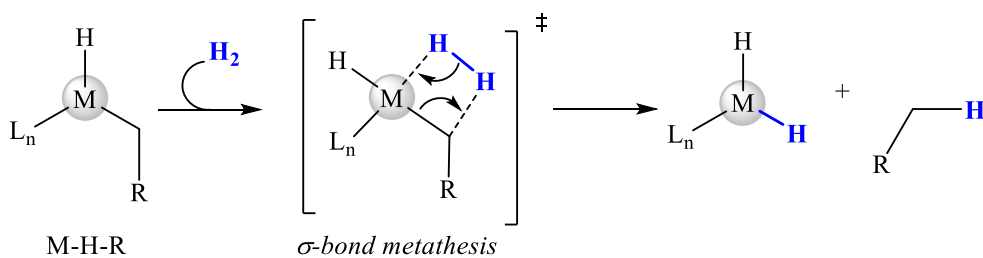


Figure 5.3 A σ -bond metathesis reaction.

The mechanism involves the formation of a metal-hydrogenated species (M-H-R), which is formed after the hydride transfer to the alkene. Then, instead of a direct proton transfer step, as it was proposed for the previously described redox M(I)-M(III) mechanism (Figure 5.2), one more H₂ binds and transfer its proton to the alkyl group of the substrate via a σ -bond metathesis reaction. In this manner, the product is liberated and the catalytic cycle is closed.

5.2 Introduction to asymmetric metal-catalyzed hydrogenation

In this section, I will briefly introduce several examples of well-known chiral ligands. Then I will discuss how the enantioselective conversions can be achieved in enantioselective metal-catalyzed hydrogenations with chiral ligands and certain substrates.

Asymmetric metal-mediated hydrogenation reactions are efficient reactions for the production of fine chemicals in the pharmaceutical industry.³ There are reported numerous studies with different chiral ligands, which are found to be excellent choices for the formation of chiral catalysts.^{4,10-12,15,17,108,117,179,187} Typical chiral ligands used in asymmetric hydrogenation are given in Figure 5.4, where most of them are *P,P* and *P,N* chiral ligands. Among the *P,N* chiral ligands, the phosphino-oxazoline (PHOX) ligands have been successfully used in Ir-based hydrogenation of alkenes.¹¹⁷

It has been shown that C₂-symmetric ligands provide high yields and selectivities because the C₂ symmetry reduces numerous competitive pathways. The first reported C₂-symmetric *P,P*-ligand was the DIOP ligand and it was used in the Rh-asymmetric hydrogenation of alkenes where 71 % of *e.e.* was achieved.¹⁷⁸ Several years later, the DIPAMP and BINAP ligands were synthesized. A Rh-(*R,R*)-DIPAMP catalyst was an extraordinary example because it was employed in the first asymmetric hydrogenation reaction for the industrial production of the L-DOPA drug.¹⁸⁷ For this achievement, Knowles received the Nobel Prize in 2001. The BINAP ligand was synthesized by Noyori who also received the Nobel Prize for his contribution to

asymmetric hydrogenation catalysis.^{10,188} BINAP showed an extraordinary performance in asymmetric Rh-catalyzed hydrogenation of α -(acyl-amino)-acrylic acid compounds, with a reported *e.e.* of more than 90%.¹¹ During the 1990's, the prominent ligands DuPhos and BPE were synthesized by Burk.¹⁸⁹ These ligands provided very high *e.e.*'s in asymmetric hydrogenation of enamides, with cationic Rh(I)-complexes.^{4,190} Several promising attempts have been reported, where Rh-based catalysts have been replaced with cobalt analogues.^{17,191}

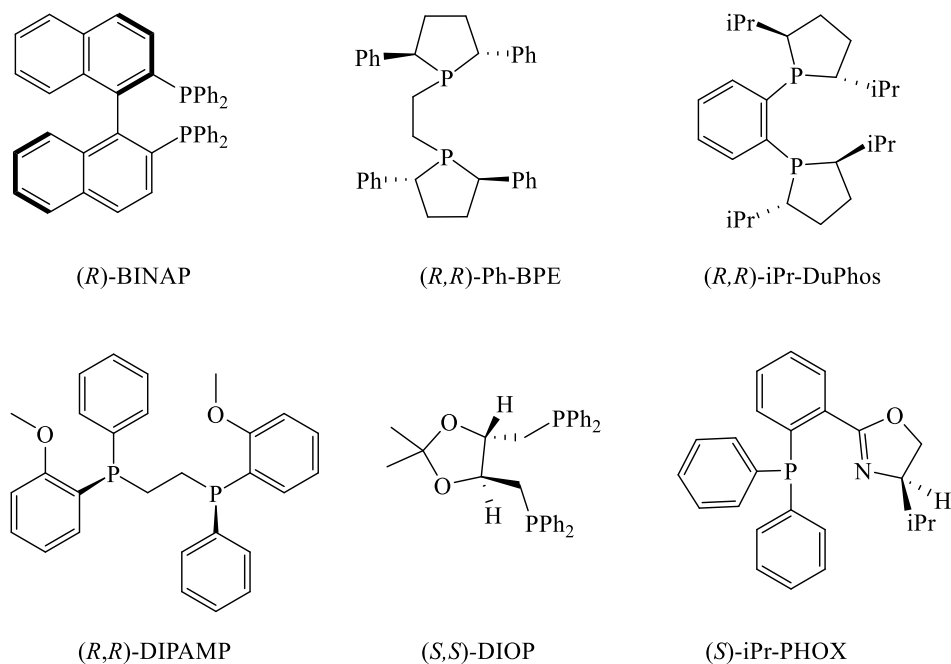


Figure 5.4 Chiral ligands employed in asymmetric metal-catalyzed hydrogenation.

One more aspect of asymmetric hydrogenation is how the enantioselective conversions can be achieved with chiral ligands and certain substrates. A pro-chiral substrate can bind to the metal centre via two faces, *si* and *re* (Figure 5.5). Due to fact that two possible coordination modes of the pro-chiral substrate exist, the subsequent reaction steps will not have the same energy, making it possible to generate (*S*) and (*R*) pathways, which can result in the energetic preference for one pathway and dominant formation of one product enantiomer.

The nature of the coordinated alkene to the metal can have influence on the outcome of the enantioselective reaction. Functionalized alkenes contain various groups such as carbonyl, ester, amine etc., which are linked to the double bond. These groups are often called directing groups because they may help in coordination of the substrate to the metal.

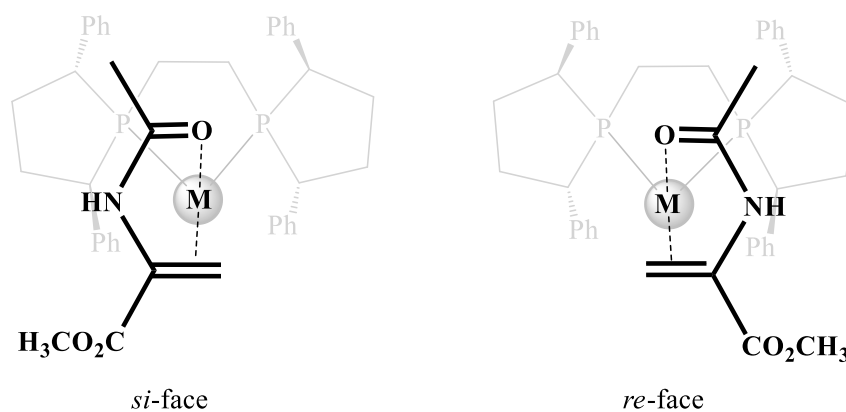


Figure 5.5 Two possible coordination modes of the enamide via *si* or *re* face

Moreover, these functional groups on the unsaturated substrate can interact with the groups of the chiral ligand of the catalyst through different types of non-covalent interactions. It has been reported that non-covalent attractive interactions such as stacking, $\text{CH}\cdots\pi$, $\text{CH}\cdots\text{O}$, etc. and repulsive forces between the substrate and ligand often are responsible for the formation of predominantly one enantiomer.^{192,193}

Regarding the non-precious metal-mediated asymmetric hydrogenation, various first row *3d* metals have been found to be efficient catalysts for a broad scope of unsaturated substrates.¹⁹⁴ For example, Fe can be employed in the asymmetric hydrogenation of ketones^{180,195} and imines^{19,20,82} whereas Co^{15,17,185} has been used for the asymmetric hydrogenation of alkenes while Ni has been used for the asymmetric hydrogenation of α,β -unsaturated compounds¹⁹⁶ and 2-amidoacrylates.¹⁹⁷ Herein, I studied the asymmetric Co-based hydrogenation of enamides, thus it will be of special interest to outline some recent developments and applications of Co-based catalysts.

5.3 Background on Co-mediated asymmetric hydrogenation

One of the promising chiral Co-based catalysts was synthesized by Chirik and co-workers in 2012.¹⁵ It was a C₁-symmetric bis(imino)pyridine-Co complex, which was found to be an efficient catalyst for the asymmetric hydrogenation of 1-alkyl substituted styrenes (Figure 5.6). For example, a high *e.e.* of 90 % was achieved with the (3-methylbut-1-en-2-yl)benzene. Later, our group reported a comprehensive computational study, where alongside mechanistic details, the electronic structure of the catalysts and the origin of the enantioselectivity were investigated.¹⁸⁵

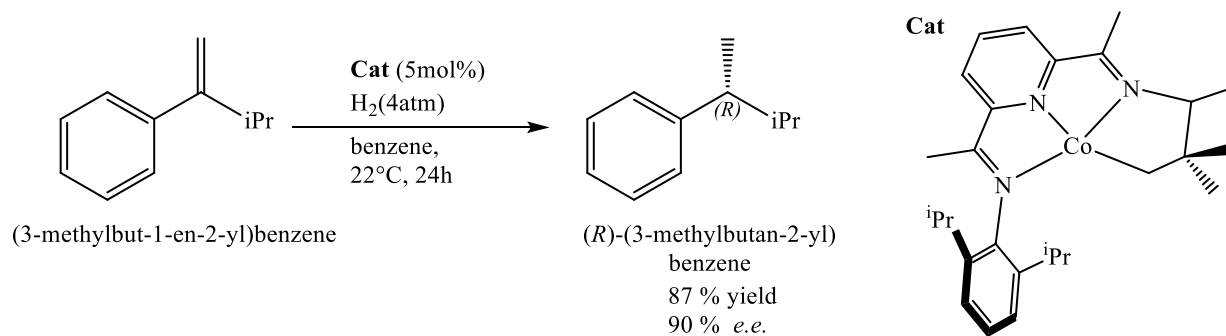


Figure 5.6 Asymmetric hydrogenation of the (3-methylbut-1-en-2-yl)benzene with a bis(imino)pyridine-Co complex (results by Monfette *et al.*, ref ¹⁵).

A few years later, Chirik's team reported an experimental study of the Co-bis(phospine)-catalyzed hydrogenation of terminal and functionalized alkenes (Figure 5.7).¹⁹⁸ The functionalized alkenes contained different functional groups, such as hydroxyl or methoxy groups. The best yields were achieved with hydroxylated and terminal alkenes, whereas unsaturated methyl ether substrates gave less than 5 % of conversion.

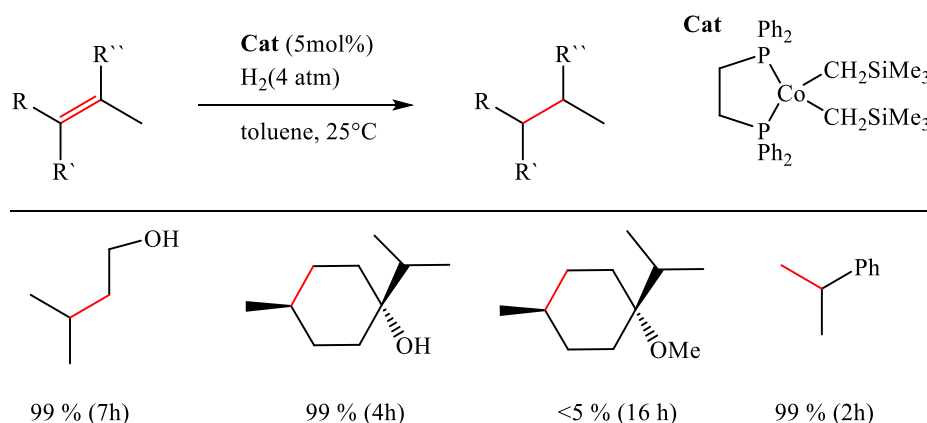


Figure 5.7 Co-bis(phospine)-catalyzed alkene hydrogenation of functionalized alkene (results by Friedfeld *et al.*, ref ¹⁹⁸).

In 2018, Hopmann and Morello reported a detailed mechanistic analysis in order to understand the experimentally observed substrate preference of Co-bis(phospine)-catalyzed hydrogenation of alkenes.²⁸ It was shown that the Co(0)-species can undergo different mechanistic pathways depending on the nature of the substrate. Non-hydroxylated terminal alkenes and alkenes bearing a methoxy group undergo a Co(0)-Co(II) redox pathway. However, a new non-redox metallacycle mechanism was proposed for hydroxylated alkenes. It is worth highlighting that in this mechanism, Co has a +2 oxidation state during the whole catalytic cycle. The proposed pathway is given in Figure 5.8. The active catalyst is proposed to be the Co(II)-monohydride

species, whereas subsequent hydride transfer forms an energetically very stable metallacycle intermediate. In the next step H_2 addition occurs, followed by proton transfer step. Finally, one more substrate inserts, in order to deliver its proton to the oxygen of the alkane. In this manner, the product is released and the active catalyst is regenerated. Interestingly, the active catalyst is not formed through the oxidative addition of the OH group. The obtained barrier for oxidative addition of the alcohol was not feasible at the reaction temperature. It was instead proposed a mechanism²⁸ where the Co(II)-monohydride is formed in the presence of the precatalyst, the substrate and the H_2 pressure. Their results demonstrated that analysis of several substrates is important for the validation of proposed mechanisms.

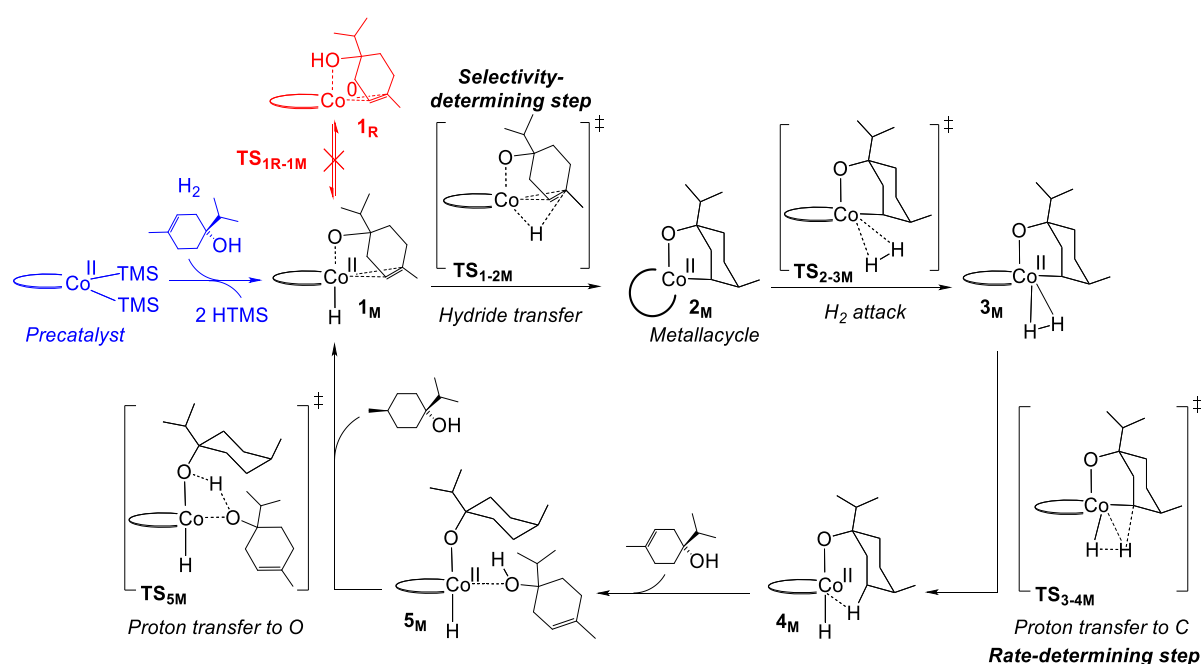


Figure 5.8^o The non-redox metallacycle mechanism for the hydrogenation of hydroxylated alkene (terpinen-4-ol).²⁸

Recently, Chirik and co-workers published several versatile asymmetric Co-based hydrogenation reactions of enamides.^{17,18} In one of them, methyl 2-acetamidoacrylate and *dehydro*-levetiracetam substrates showed very high conversion and enantioselectivities with (*R,R*)-Ph-BPE and (*R,R*)-*i*Pr-DuPhos as chiral ligands.¹⁷

^o Adapted with permission from [Morello, G. R.; Zhong, H.; Chirik, P. J.; Hopmann, K. H. Cobalt-catalysed alkene hydrogenation: A metallacycle can explain the hydroxyl activating effect and the diastereoselectivity, *Chemical Science* **2018**, 9 (22), 4977-4982.] - Published by The Royal Society of Chemistry.

In the next section, my computational results of Co-mediated hydrogenation of alkenes, presented in paper IV, are given.

5.4 Co-catalyzed asymmetric hydrogenation of enamides (Paper IV)

The asymmetric Co-catalyzed hydrogenation study of enamides was reported by Chirik and co-workers in 2018.¹⁷ The optimal reaction conditions were found with CoCl₂ and Zn dust as an activator, in the presence of MeOH at 50 °C. More than 200 chiral ligands were analyzed, with the most promising candidates being (*R,R*)-Ph-BPE and (*R,R*)-iPr-DuPhos. These ligands afforded very high yields and enantioselectivities under optimal reaction conditions.

I have computationally evaluated two of the experimentally studied enamides to establish their preferred mechanistic routes and to obtain insights into how the enantioselectivities of their conversion are controlled (Figure 5.9).

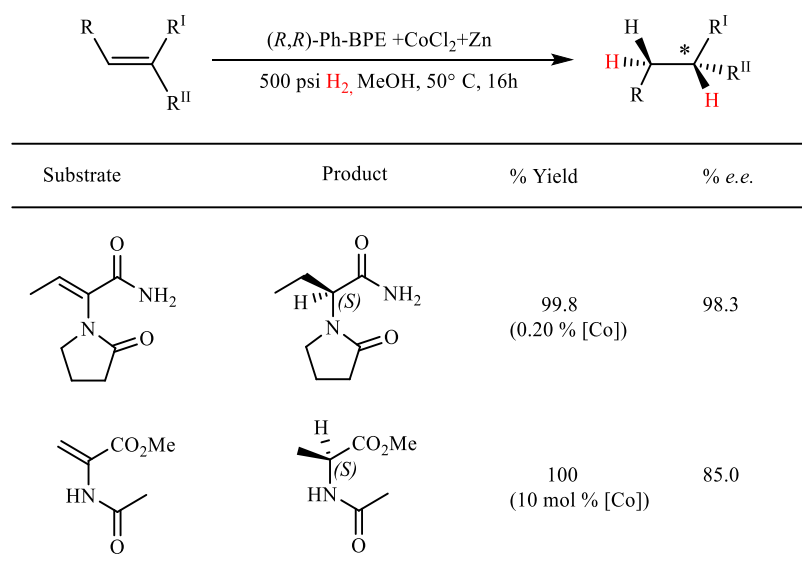
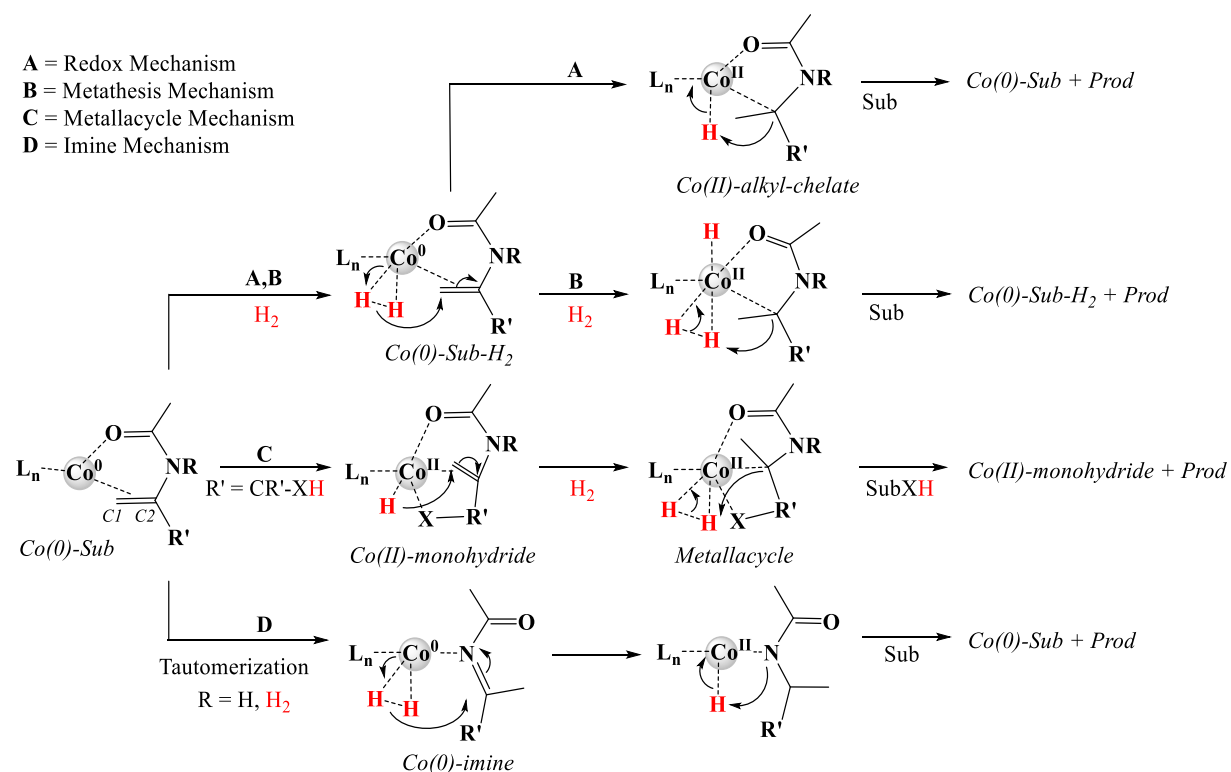


Figure 5.9 Reported examples of (*R,R*)-Ph-BPE-Co-mediated enamide hydrogenation.¹⁷

Several mechanistic possibilities arise for the hydrogenation of the employed enamides, because the studied substrates contain groups that potentially can be deprotonated, such as NH₂ or NH. For all proposed mechanisms, we set out from a Co(0)-enamide complex. This is based on two observations: 1) In experiment,¹⁷ an isolated Co(0)-COD complex is catalytically active. 2) Our computed results show that coordination of the substrate to Co(0) energetically is very favoured and that it comes before a potential H₂ coordination (SI of paper IV, Figure S1). In the Scheme 5.1, the redox Co(0)-Co(II) mechanism is referred to as mechanism **A**, involving

an oxidative hydride transfer from H₂ to the enamide and then reductive elimination of the product. Next, mechanism **B** is a σ -bond metathesis pathway, where after formation of the Co-alkyl chelate, instead of a direct reductive elimination, one more H₂ comes in and transfers a proton to the alkyl. Mechanism **C** is a metallacycle mechanism, previously described in Figure 5.8. Mechanism **D** is proposed as a possibility by us due to fact that some of the enamides potentially could tautomerize to imines. All mechanisms are drawn with initial hydride transfer to C1 of the enamide, but for the mechanisms **A**, **B** and **C**, a hydride transfer to C2 is also possible, increasing the number of mechanistic possibilities. For mechanism **D**, it is also possible that the nitrogen first abstracts a proton, forming an iminium intermediate, and then hydride transfer occurs to the C2 atom.

Additionally, it cannot be excluded that solvent-assisted variants of these pathways are operative, where MeOH can actively participate in the catalytic cycle, serving either as hydrogen bond donor or as a potential proton source.



Scheme 5.1 Possible mechanisms for the hydrogenation of enamides. Mechanism A, B, C are shown with initial hydride transfer to C1, but C2 is also possible. For D, initial transfer to N is also possible.

Below, the mechanistic investigations of two studied enamides are outlined where the enantioselectivities were explored alongside with the potential role of the MeOH solvent.

5.5 Computed results and discussion for enamide hydrogenation

As a catalyst, an open shell, low spin complex Co-(*R,R*)-Ph-BPE was modelled. Two functionalized alkenes were evaluated: methyl 2-acetamidoacrylate (MAA) and *dehydro*-levetiracetam. Herein, only the reaction pathways, which were energetically feasible under the reaction conditions, will be presented and discussed, for each substrate. The final energies are obtained at the B3LYP-D3/6-311++G(2df,2pd)[IEFPCM]//B3LYP-D3//6-311G(d,p)[IEFPCM] level of theory, where the basis set and the pseudopotential LANL2TZ was used on Co. Details of all tested mechanisms can be find in the Supporting Information of the Paper IV.

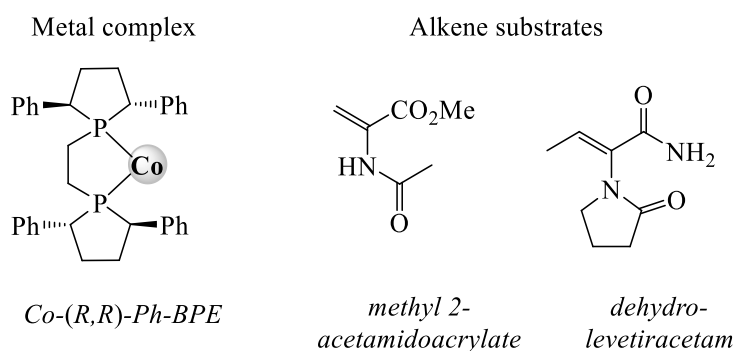


Figure 5.10 Co complex and enamides substrates studied in this thesis.

5.5.1 Hydrogenation of methyl 2-acetamidoacrylate

Chirik and co-workers reported that the Co-mediated hydrogenation of methyl 2-acetamidoacrylate (MAA) was very successful in the presence of the chiral (*R,R*)-Ph-BPE ligand, with a reported yield of 100 % and an observed *e.e.* of 85 %.¹⁷

First, a redox Co(0)-Co(II) mechanism **A** was evaluated (Scheme 5.1, A). This mechanism starts from a substrate-coordinated species (Figure 5.11). MAA is coordinated to the metal through the oxygen of the amide group and the double bond. In the first step, H₂ binds to form a Co(0)-H₂-Sub intermediate, where H₂ is coordinated to Co via its σ -bond, forming a σ -complex. Then, oxidative hydride transfer to the terminal C atom (C1) produces a chelate species with a barrier of 24.3 kcal/mol for the formation of the (*S*)-chelate and 31.1 kcal/mol for the formation of the (*R*)-chelate. The hydride transfer step is both rate- and selectivity-determining.

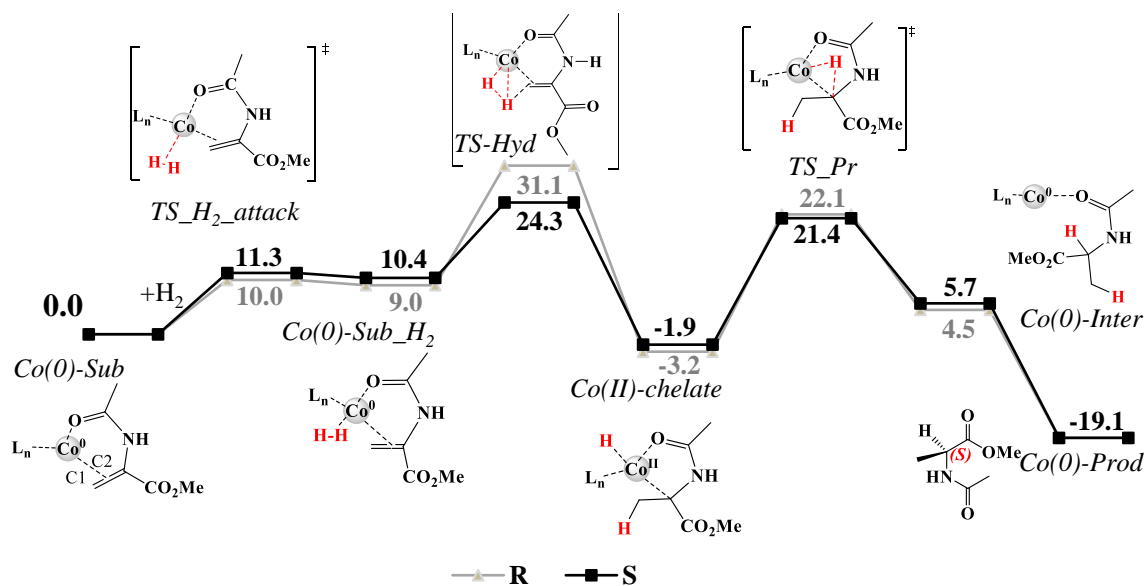


Figure 5.11 Computed Gibbs free energy profile (kcal/mol, 323 K, B3LYP-D3/6-311++G(2df,2pd) [IEFPCM(MeOH)]/B3LYP-D3//6-311G (d,p) [IEFPCM(MeOH)] level of theory) for the hydrogenation of methyl 2-acetamidoacrylate via redox mechanism **A** in the absence of explicit solvent

In the last step, proton transfer to C2 occurs, resulting in the formation of the product and regeneration of the catalyst. The overall barrier of 24.3 kcal/mol for the formation of (*S*)-product is feasible at the reaction temperature of 323 K.¹⁷ An alternative redox mechanism, where hydride transfer occurs to C2 of the MAA is not accessible due to very high barrier of 38.7 kcal/mol (SI of Paper IV, Figure S6).

Then, I tested an alternative non-redox σ -metathesis mechanism **B** (SI of Paper IV, Figure S7). The overall barrier for the formation of the (*R*)-product was 32.7 kcal/mol and 28.6 kcal/mol for the (*S*)-product. For the latter, the barriers are calculated assuming that the chelate intermediates are not in equilibrium, if they are, the (*S*)-barrier increases to 29.9 kcal/mol. The obtained barriers make this mechanism unfavorable.

I proceeded by analyzing a non-redox Co(II) metallacycle mechanism **C**. The proposed mechanism **C** is given in Figure 5.12. The active catalyst Co(II)-monohydride is formed from the Co(0)-Sub species (the mechanistic details of this are discussed below). Then, hydride transfer to C2 takes place, with the low barriers of 18.9 kcal/mol and 20.0 kcal/mol, for both the pro-(*S*) and pro-(*R*) TSs, respectively and in the absence of explicit solvent. This step leads to the formation of a 6-membered Co(II)-metallacycle intermediate, followed by H₂ coordination and subsequent proton transfer step to the C1 atom of the substrate. The Co(II)-

metallacycle and Co(II)-metallacycle-H₂ intermediates can adopt two conformations, where either the oxygen of the amide group or the nitrogen of the amide group can interact with Co. For mechanism **C**, the proton transfer step to C1 is found to be rate-limiting for both (*S*) and (*R*) products, with the barriers of 24.0 kcal/mol and 28.3 kcal/mol, respectively. Finally, one more substrate binds to the Co and transfer its proton to the N atom of the product, via TS_Pr_N. In this manner, the product is liberated and the active catalyst is reformed. The overall barrier for the formation of the (*S*)-product, via metallacycle mechanism **C** (Figure 5.12), is only 0.3 kcal/mol lower than for the redox mechanism **A** (Figure 5.11). Based on these results, both redox **A** and non-redox **C** mechanisms are feasible at the reaction temperature.

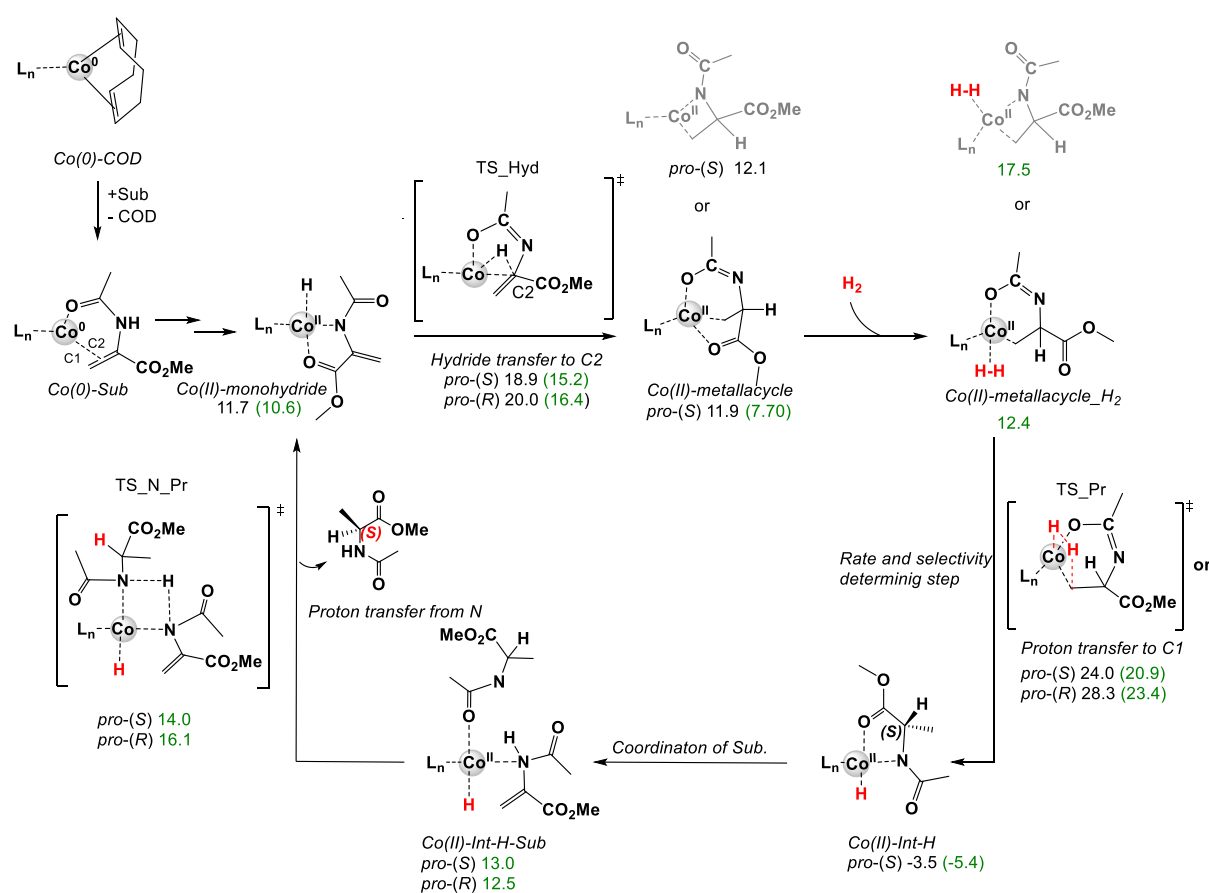


Figure 5.12 The non-redox metallacycle mechanism **C** where hydride transfer occurs to the C2 atom. In parentheses, (green) are given the values obtained with MeOH hydrogen-bonded to MAA (energies are in kcal/mol).

An alternative redox imine mechanism **D** has a barrier of 28.3 kcal/mol (SI of Paper IV, Figure S9), whereas an alternative imine mechanism, proceeding via heterolytic H₂ cleavage gives a barrier of 33.2 kcal/mol (SI of Paper IV, Figure S10). Both of these two **D** mechanisms are excluded due to high barriers. A mechanistic pathway where MeOH can actively participate in

the catalytic cycle coordinated to Co gives also high barrier of 31.4 kcal/mol (SI of Paper IV, Figure S12). Then, an alternative mechanism where coordinated MeOH can behave as a proton source was also tested and this mechanism was excluded due to a very high barrier of 44.5 kcal/mol for the regeneration of the MeOH from the Co-methoxy intermediate (SI of Paper IV, Figure S13). This is in agreement with deuterium labelling studies, where it has been shown a minimal MeOH incorporation.

Thus of all tested mechanisms, our results indicate that for the Co-Ph-BPE-catalyzed hydrogenation of MAA both redox **A** and non-redox **C** pathways compete under reaction conditions.

In the next step, I evaluated the enantioselectivity of MAA hydrogenation by using all four TSs, that correspond to the rate-limiting steps in the redox (**A**) and metallacycle (**C**) mechanisms (SI of Paper IV, Table S2). The computed *e.e.* is 99.8 % (*S*) relative to the experimentally reported *e.e.* of 85 % (*S*) (323 K).¹⁷ Due to the high barriers for formation of the (*R*)-product, only (*S*)-product would be produced, however, the experimentally obtained *e.e.* was 85 %, which implies that some amount of (*R*)-product is formed as well. In order to understand the large barriers for the (*R*) pathway, we first analyzed the optimized geometries of the pro-(*S*) and pro-(*R*) TS-Hyd structures obtained via redox mechanism **A**.

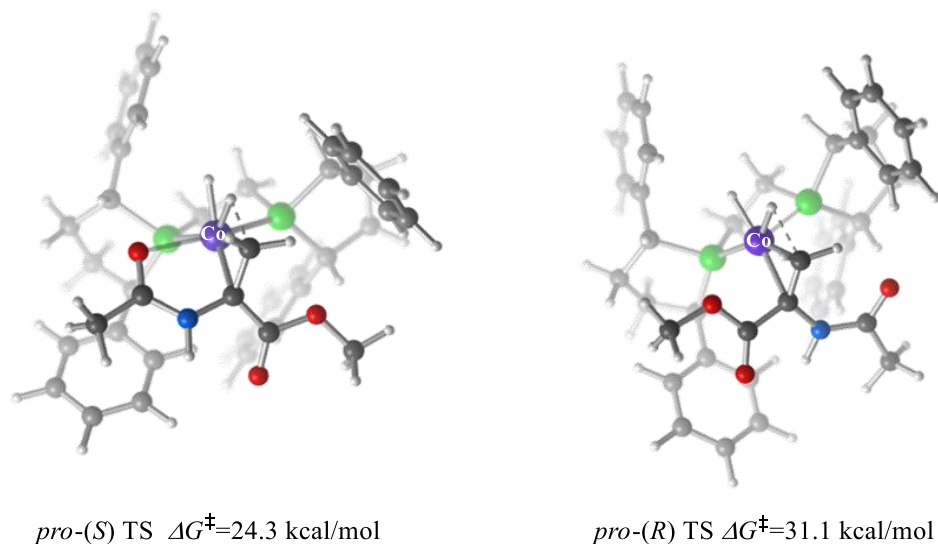


Figure 5.13 The optimized geometries of the pro-(*S*) and pro-(*R*) TS-Hyd with MAA and in the absence of any explicit solvent.

Here we noticed that the *pro*-(*R*) TS-Hyd has less charge stabilization than the *pro*-(*S*) TS, because the oxygen of the amide group at the (*R*)-TS is unable to interact with Co (Figure 5.13).

Effect of explicit solvent on the mechanism and selectivity of MAA hydrogenation

Recently, Chirik and co-workers reported a new hydrogenation study involving cationic bis(phosphine) Co(I) diene and arene compounds.¹⁹⁹ In this paper, they reported the X-ray structure of a Co-(*R,R*)-iPr-DuPhos-MAA complex, where a solvent molecule (dimethyl-ether in this case) is bound to the NH group of the substrate. This crystal structure motivated us to explore two important aspects: the possibility of an explicit solvent hydrogen bonded to the substrate and the influence of this interaction on the barriers and selectivities.

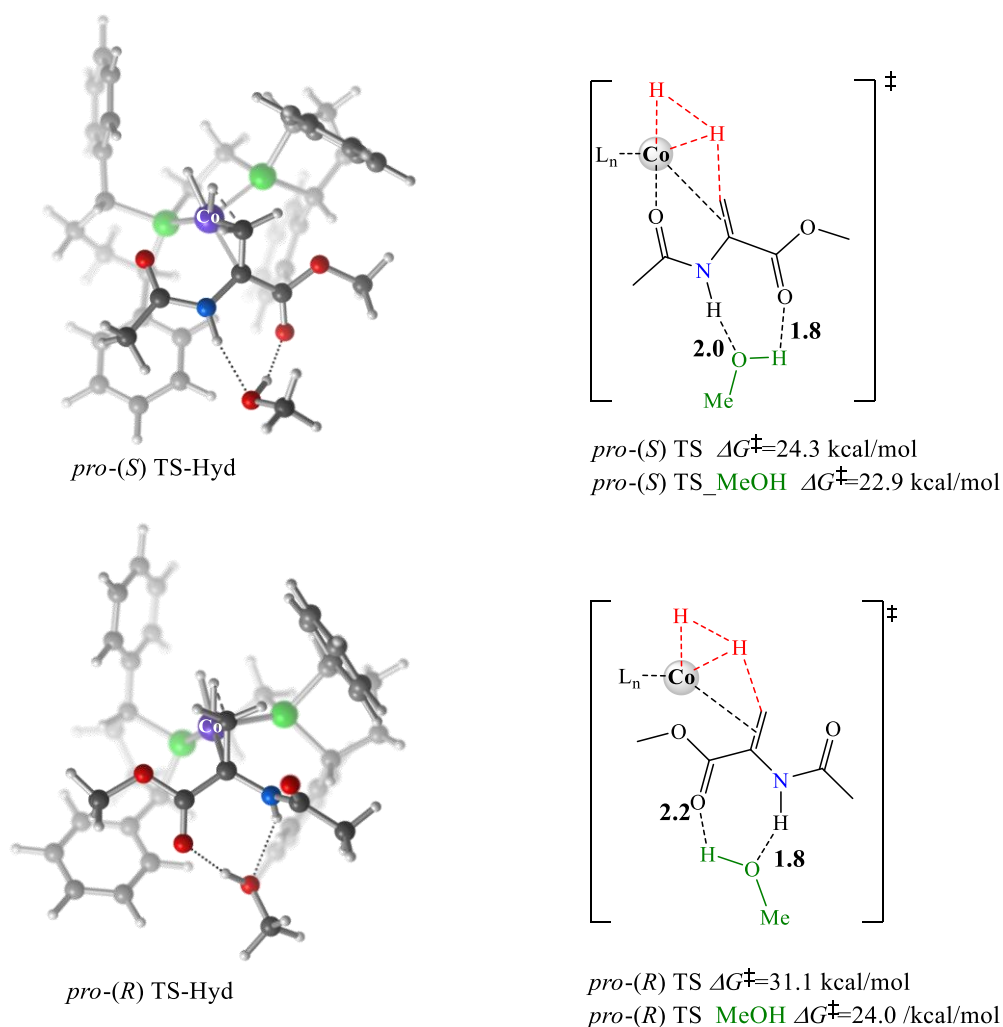


Figure 5.14 On the left side are the optimized *pro*-(*R*) and *pro*-(*S*) TS_Hyd structures with MeOH hydrogen-bonded to the substrate. On the right side are schematic drawing of the TSs and the corresponding barriers with and without MeOH (distances are in Å).

The calculations indicate that MeOH hydrogen-bonded to the substrate decreases the barriers for the redox mechanism **A**. The decrease is slight for the pro-(*S*) TS-Hyd, 1.4 kcal/mol. On the other hand, the decrease for the pro-(*R*) TS-Hyd is significant, 7.1 kcal/mol (Figure 5.14). Based on the finding that hydrogen-bonded solvent can significantly affect the energies of mechanism **A**, we tested the possibility that explicit solvent-substrate interactions can affect the barriers of the mechanism **C**, which is also feasible at reaction temperature of 323 K.¹⁷ A considerable impact was also noted for the metallacycle mechanism **C** where the decrease for the rate-limiting pro-(*S*) TS Pr was 3.1 kcal/mol and for the pro-(*R*) was 4.9 kcal/mol (Figure 5.12, energies with explicit solvent-MAA interactions are given in green). For the other mechanistic pathways **D** and **D-2**, the explicit solvent-MAA interactions did not change the energies significantly (SI of Paper IV, Figures S9 and S10).

With one explicit solvent molecule, the computed *e.e.* (on basis of Mechanisms **A** and **C**) is now 94.7 % (*S*), compared to the experimentally reported *e.e.* of 85 % (*S*).¹⁷

However, due to the conformational freedom of MeOH, the obtained results need to be taken with caution and should be considered as approximate values. The solvent can adopt many different conformations around the catalyst and the substrate, which cannot be tested by the employed static DFT method. It is also not possible with this model to evaluate what effect the additional bulk solvent would have on the enantioselectivity.

Table 5.1 The overall barriers for the Co-Ph-BPE-catalyzed hydrogenation of methyl 2-acetamidoacrylate, without (left) and with (right) explicit MeOH-Substrate interactions, via Mechanisms **A** (Figure 5.11) and **C** (Figure 5.12).

Rate-limiting TS	Mechanism A	Mechanism A (MeOH)
Pro-(<i>S</i>) (Hydride transfer to C1)	24.3	22.9
Pro-(<i>R</i>) (Hydride transfer to C1)	31.1	24.0
TS	Mechanism C (6m)	Mechanism C (6m) (MeOH)
Pro-(<i>S</i>) (Proton transfer to C1)	24.0	20.9
Pro-(<i>R</i>) (Proton transfer to C1)	28.3	23.4
<i>e.e.</i>	99.8 % (<i>S</i>)	94.7 % (<i>S</i>)

Formation of active species in Mechanism C with MAA as substrate

Mechanism **C** is dependent on the initial formation of a Co(II)-monohydride species from the Co(0)-enamide complex (Figure 5.12). This has to occur only once (after which the Co-monohydride is generated in each cycle), but it is nonetheless relevant to search for a

mechanistic pathway, which leads to the formation of the proposed active species Co(II)-monohydride. The oxidative addition of the NH group of the substrate to Co(0) is unlikely, as we computed barriers of >35 kcal/mol for the oxidative addition of OH²⁸ or NH₂ to Co (SI of Paper IV, Fig. S5). A second possible mechanism, which starts from the Co(0)-substrate and occurs via an imine intermediate, gave a very high barrier of 37.2 kcal/mol (SI of the paper IV, Figure S15). Finally, we are considering a path where the precatalyst CoCl₂ under H₂ pressure and in the presence of substrate may form a Co(II)-monohydride, through two σ -bond metathesis steps, each liberating one HCl molecule (SI of paper IV, Fig. S16). A related mechanism was proposed for Co(II)-monohydride formation in our previous computational study.²⁸ This σ -bond pathway is complicated by the fact that the CoCl₂ precursor appears to prefer a different spin state ($S = 3/2$), which is different than the spin surface on which the hydrogenation reaction is expected to occur ($S = 1/2$). This path is still ongoing work.

At this point, the obtained results indicate that both metallacycle **C** and redox mechanism **A**, are close in energy for substrate MAA and both appear to be feasible under the reaction conditions. Currently, our experimental collaborators are trying to perform additional experiments, which can help us understand if both mechanisms are accessible.

5.5.2 Hydrogenation of *dehydro*-levetiracetam

Chirik and co-workers reported that the Co-diphosphine-catalyzed hydrogenation of *dehydro*-levetiracetam leads to the formation of a commercial epilepsy drug *Kepra*, with a yield of 99.8 % and an *e.e.* of 98.3 %.¹⁷ The industrial synthesis of this drug is based on an expensive rhodium catalyst.³ Hence, the reported Co-based system may provide a cheaper synthetic pathway. *Dehydro*-levetiracetam is an interesting substrate, because it possesses an enamide functional group and an ionizable primary amide, making hydrogenation mechanisms **A**, **B** and **C** possible options.

For *dehydro*-levetiracetam, several mechanistic possibilities were explored in detail, with an exclusion of imine mechanism **D**, due to fact that this substrate cannot tautomerize to imine. The redox Co(0)-Co(II) mechanism **A** gives a barrier of 26.5 kcal/mol (SI of paper IV, Figure S2), which can be feasible at the reaction temperature (323 K), whereas the σ -bond metathesis mechanism **B** gives a barrier of 37.7 kcal/mol (SI of paper IV, Figure S3). Calculations indicate that alongside the redox Co(0)-Co(II) mechanism **A**, also the non-redox metallacycle mechanism **C** is the energetically feasible mechanism. Figure 5.15 shows mechanism **C** for

dehydro-levetiracetam, proceeding via a four-membered metallacycle intermediate. These calculations were performed in absence of explicit solvent.

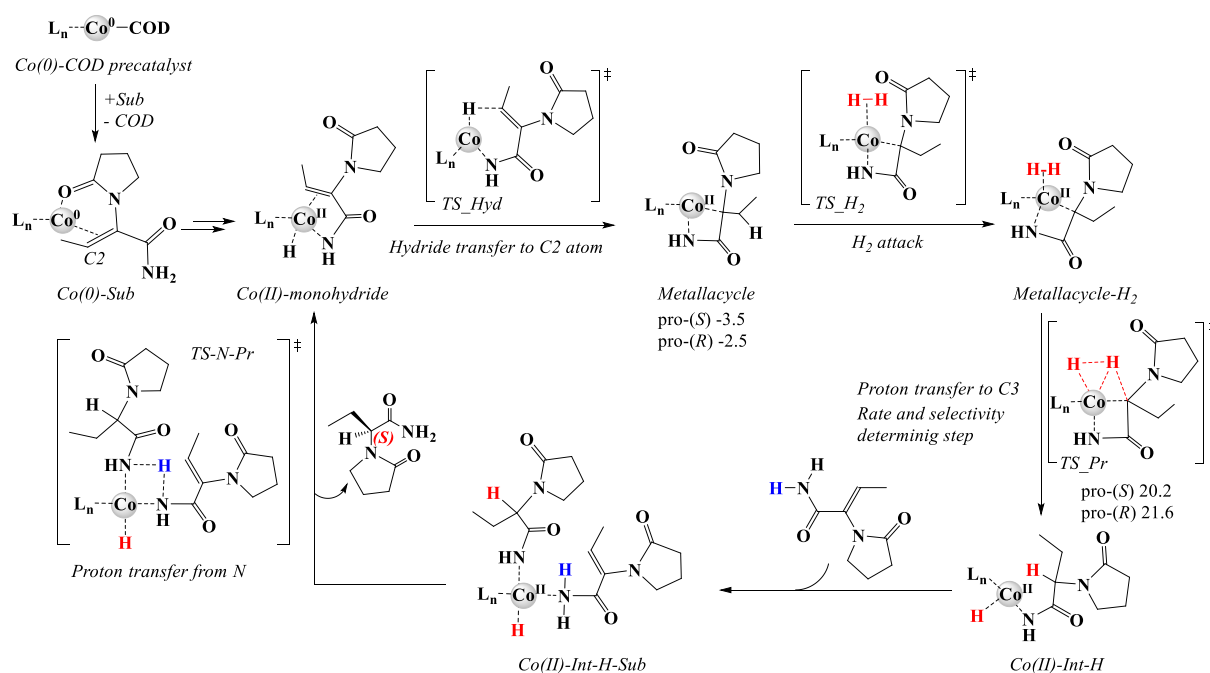


Figure 5.15 The non-redox metallacycle mechanism **C** where hydride transfer occurs to C2 atom (energies are in kcal/mol).

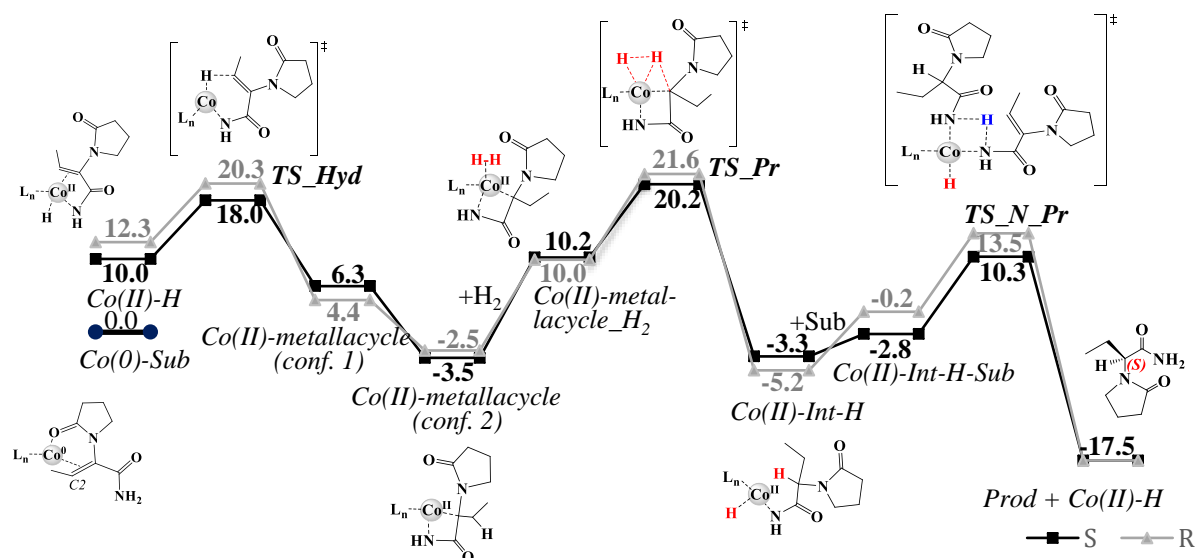


Figure 5.16 Computed energy profile (kcal/mol, 323 K, B3LYP-D3/6-311++G(2df,2pd) [IEFPCM(MeOH)]/B3LYP-D3//6-311G(d,p)[IEFPCM(MeOH)] level of theory) for the hydrogenation of *dehydro*-levetiracetam via metallacycle mechanism **C**. Energies (kcal/mol) are given relative to Co(0)-Sub, which is not part of the cycle, but can be considered an off-cycle thermodynamic sink. The profile is computed in absence of explicit solvent.

On the energy profile, we can distinguish the (*S*) and (*R*) reaction pathways (Figure 5.16). The path with the black colour gives the experimentally observed (*S*)-product. First, the proposed active species Co(II)-monohydride is formed, with an energy of 10 kcal/mol relative to the reference structure Co(0)-Sub (Figure 5.17). The transformation of Co(0)-*dehydro*-levetiracetam to the Co(II)-monohydride only has to occur once and the mechanistic details for how this could occur are discussed in the next section. Once the monohydride is formed, hydride transfer to the C2 atom of the enamide takes place with a low barrier of 18 kcal/mol. The Co-metallacycle conformer 1, which is formed right after hydride transfer, does not have the substrate carbonyl coordinated to Co (Figure 5.16). However, upon recoordination of the carbonyl group, the energetically more favourable Co-metallacycle conformer 2 is formed, which is 3.5 kcal/mol lower in energy relative to the reference Co(0)-Sub intermediate. The formed Co-metallacycle conformer 2 contains an unusual four-membered metallacycle ring, bound to Co through the deprotonated nitrogen and the formally negatively charged carbon. In the next step, H₂ coordination occurs, followed by proton transfer to the C3 atom to yield the Co(II)-Int-H intermediate. This step is found to be rate- and selectivity-determining with a barrier of 23.7 kcal/mol (323 K). Finally, coordination of another substrate takes place, which can transfer its proton to the nitrogen atom (TS-N-Pr), resulting in the formation of the product and regeneration of the active Co(II)-monohydride catalyst. A reaction pathway that leads to the formation of (*R*)-product was also evaluated. The rate- and selectivity-determining step is also the proton transfer, with a barrier of 25.1 kcal/mol.

Another variant of the metallacycle mechanism **C**, where the initial hydride transfer occurs to the C3 atom of the substrate, is also tested (SI of paper IV, Figure S4). The formed intermediate is now a five-membered metallacycle species. The following steps are the same as for the four-membered metallacycle (Figure 5.16), with the only difference that subsequent proton transfer occurs to the C2 atom (the proposed mechanism can be found in the SI of paper IV, Figure S4). Interestingly, the rate-determining step for the formation of the predominant (*S*)-product is the hydride transfer step with a barrier of 23.8 kcal/mol, yet the rate-limiting step for the formation of the (*R*)-product is the proton transfer step with a barrier of 24.0 kcal/mol. The obtained barriers indicate that both variants of the metallacycle mechanism, proceeding through a four or five membered metallacycle, are energetically feasible at the reaction temperature (323 K). Due to fact that redox mechanism is also possible, all three mechanisms may contribute to the final enantioselectivity.

In order to compute the *e.e.*, the Gibbs free energy barriers of all six rate-limiting TSs structures are used in the formula for the determination of the enantiomeric excess. The obtained *e.e.* is 43.3 % (*S*) and this is in disagreement with the observed *e.e.* of 98.3 % (*S*) under catalytic conditions, although the correct major product is predicted.

Effect of explicit solvent on the mechanism and selectivity of dehydro-levetiracetam hydrogenation

The role of the explicit solvent MeOH was explored in order to see if the solvent-substrate interactions could affect the computed energies and selectivities for hydrogenation of *dehydro*-levetiracetam, in analogy to the effects observed for MAA. The results are given in Table 5.2. It can be noted that MeOH hydrogen bonded to *dehydro*-levetiracetam did not improve any of the barriers significantly. Only for the pro-(*S*) TS-Hyd, the barrier decreases by 1.0 kcal/mol. The computed *e.e.* with the inclusion of one explicit solvent molecule is 76.6 % (*S*), which is still somewhat smaller than the experiment which gave 98.3 % (*S*).¹⁷

Table 5.2 The overall barriers for the Co-^{Ph}BPE-catalyzed hydrogenation of *dehydro*-levetiracetam, without (left) and with (right) explicit MeOH-Substrate interactions, via Mechanism A (SI of paper IV, Figure S2) and C (Figure 5.16 and SI of paper IV, Figure S4). The experimentally reported *e.e.* is 98.3 % (*S*) (energies are in kcal/mol).¹⁷

Rate-limiting TS	4-mem. metallacycle	4-mem. metallacycle (MeOH)
Pro-(<i>S</i>) (Proton transfer to C3)	23.7	25.4
Pro-(<i>R</i>) (Proton transfer to C3)	25.1	26.1
TS	5-mem. metallacycle	5-mem. metallacycle (MeOH)
Pro-(<i>S</i>) (Hydride transfer to C3)	23.8	22.8
Pro-(<i>R</i>) (Proton transfer to C2)	24.0	24.1
TS	Redox mechanism	Redox mechanism (MeOH)
Pro-(<i>S</i>) (Hydride transfer to C2)	26.5	25.2
Pro-(<i>R</i>) (Hydride transfer to C2)	32.7	30.0
<i>e.e.</i>	43.3 % (<i>S</i>)	76.6 % (<i>S</i>)

The error of the computed *e.e.* is estimated as 1.7 kcal/mol relative to experiment, implying that one (*S*)-TS would have to be 1.7 kcal/mol lower in energy to reproduce the experimental *e.e.*. This error is larger than is desirable, however, the complex mechanistic picture for *dehydro*-levetiracetam (apparently proceeding through both four- and five-membered metallacycles and

a redox mechanism) and the approximate modelling of the explicit solvent effect imply that there are many possible explanations for the observed deviation.

It should be noted that in the experimental paper¹⁷, the effect of the solvent on the obtained enantiomeric excess was tested and it appears to be significant, altering the *e.e.* of the same substrate from 76 % to 94 % (*S*) in different solvents (MeOH, EtOH, iPrOH, TFE). This observation and my computational results for the two enamides (MAA and *dehydro*-levetiracetam) leads me to the conclusion that explicit solvent-substrate interactions may be crucial for understanding the outcome of the enantioselectivity for Co-catalyzed hydrogenation of enamides. However, with DFT, the effect of the explicit solvent can only be modelled approximately and some deviations between computed and experimental results are therefore not surprising.

It is also interesting to note that there is the possibility that once the Co(II)-mono-hydride active species is formed, it will not be able to revert to the off-cycle Co(0)-Sub complex, implying that the barrier for the hydride transfer step of the five-membered metallacycle mechanism **C** (22.8 kcal/mol for the (*S*)-pathway, SI of Paper IV, Figure S4) is overestimated and the rate-limiting step for the (*S*)-path of this mechanism would instead be the proton transfer (as for the (*R*)-path), with a barrier of 21.1 kcal/mol (SI of Paper IV, Figure S4). In that case, the computed *e.e.* for *dehydro*-levetiracetam would be 98.1 % (*S*), in full agreement with experiment.

Formation of active species in Mechanism C with dehydro-levetiracetam as substrate

We also investigated how the proposed active catalyst of Mechanism **C**, the Co(II)-monohydride, can be formed from Co(0)-*dehydro*-levetiracetam. The direct oxidative addition of the NH₂ group is not feasible at the reaction temperature (323 K, SI of paper IV, Figure S5). The obtained barrier is 42.2 kcal/mol, thus this path was excluded. However, an alternative and apparently feasible pathway can be found (Figure 5.17). First, Co(0)-enamide binds H₂, which is followed by oxidative hydride transfer to the terminal C atom. In this way, the Co-chelate intermediate is formed. Now, the hydride can abstract the proton from the NH₂ group of the enamide in order to form a metallacycle intermediate, which is involved in mechanism **C**. The overall barrier for transformation of Co(0)-*dehydro*-levetiracetam to the metallacycle is 26.5 kcal/mol and it is thus possible to occur at 50° C.

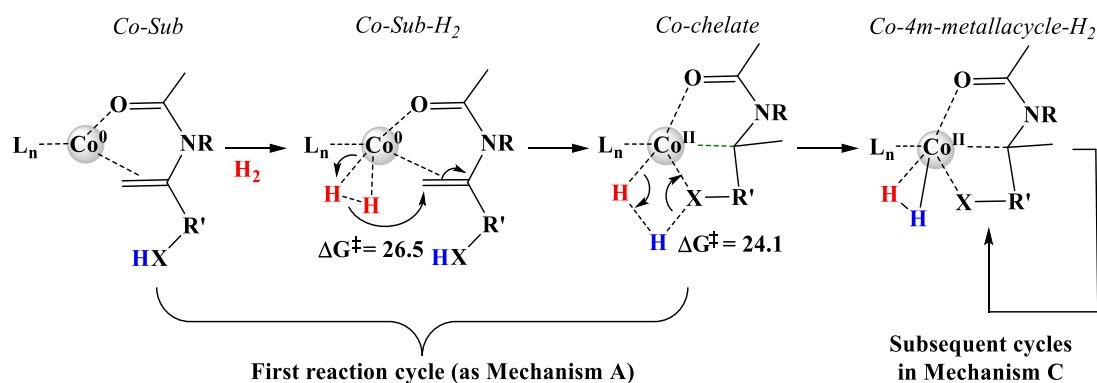


Figure 5.17 Proposed mechanism for the formation of an active catalyst Co(II)-monohydride (energies are in kcal/mol).

In the next cycles, mechanism **C** is proposed to operate with an overall barrier of 23.7 kcal/mol, computed relative to Co(0)-*dehydro*-levetiracetam, as this structure may still act as a thermodynamic sink for the reaction.

5.6 General conclusion

The aim of this study was to get a deeper insight into the mechanistic details of asymmetric Co-catalyzed hydrogenation of functionalized alkenes. In order to validate our computational protocol, the origin of the enantioselectivity was also explored.

The computations showed that both redox **A** and non-redox **C** mechanisms are feasible for two studied enamides, where the non-redox mechanism is slightly preferred for both substrates. The methyl 2-acetamidoacrylate (MAA) substrate forms 6-membered metallacycle intermediates via the Co(II) non-redox mechanism. The computed *e.e.* was 94.7 % relative to the experimentally reported *e.e.* of 85.0 % when explicit solvent-substrate interactions are considered.

The *dehydro*-levetiracetam substrate, with an ionizable NH₂ group can undergo both four- and five membered non-redox metallacycle pathways alongside the redox mechanism. All three mechanisms gave feasible energies. The computed *e.e.* was 76.6 % in presence of explicit solvent, relative to the experimentally reported *e.e.* of 98.3 %.

At this stage of understanding, I believe that the role of the explicit solvent is crucial for the proper estimation of the enantiomeric excess for Co-catalyzed hydrogenation occurring in polar

solvents. In order to model the intimate details about the solvent effect, one should perform molecular dynamic analysis due to the conformational freedom of the solvent.

Finally, this system illustrates the difficulties of modelling experimental reactions that involve complex substrates and catalysts. These neutral cobalt-diphosine systems appear to have various accessible oxidation states (0, I, II),¹⁷ which opens a possibility towards a large number of reaction channels, with and without redox chemistry. The studied substrates are conjugate systems with many polar groups that may interact with solvent or may be deprotonated or isomerized. The combination of these ionisable substrates with redox-active Co-catalysts and protic solvents makes a search for the right mechanism complicated and complex, but the results obtained here may hopefully advance the understanding of Co-catalyzed processes and may also help the experimental group to search and identify some of the computationally proposed intermediates.

6. Conclusions

In the presented thesis, DFT methods were employed in order to determine the preferred hydrogenation and hydrocarboxylation routes of cobalt and rhodium complexes with different substrates. The emphasis was put on the ability of DFT functionals to predict several properties: reaction and activation energies, substrate preferences as well as enantiomeric excesses.

It can be concluded that the PBE functional, combined with empirical dispersion corrections and implicit solvation effects, appears to provide a reasonable description of the reaction and activation energies of Rh-based hydrocarboxylation reactions with styrene-derived substrates. The analysis of TS geometries during the C-CO₂ step, with achiral COD ligand and with other chiral ligands, showed the same conformation, with a preferred outer sphere CO₂ insertion path. In the Rh-(*S*)-SEGPPOS-catalyzed hydrocarboxylation of methyl 2-phenylacrylate, the inner sphere CO₂ insertion path, where Rh-CO₂ interactions are present, was higher in energy by ~17 kcal/mol relative to the best TS, with two tested DFT methods, PBE-D2 and B3LYP-D3. This implies that the PBE and B3LYP functionals were able to predict the same trend. For the prediction of enantiomeric excesses, good agreement between our computations and experimental results was observed, indicating that the computational model and method is able to capture the factors that determine the selectivity in these systems. Based on our work, the enantioselectivity appears to mainly be controlled by weak forces, such as attractive C-H...O interactions.

It can also be concluded that the dispersion corrected B3LYP-D3 functional gave reasonable reaction and activation energies in the Co-based hydrogenation of enamides. However, our mechanistic analysis indicates that Co-diphospine complexes can access many different reaction channels, with and without redox steps and with or without deprotonation of the substrate. The role of explicit solvent on the obtained barriers indicated that solvent interactions with the substrate are crucial for the evaluation of the enantiomeric excess. The barrier reduction of ~7 kcal/mol in presence of explicit solvent relative to the model without solvent-substrate interactions implies that the implicit solvation model may not be good enough to

describe the reactivity of this system. Because of the complexity of the studied reaction pathways, one may have to employ molecular dynamics methods in order to get a better understanding of the solvent effect on the Co-catalyzed hydrogenation.

It is interesting to note that the two studied reactions, Rh-based hydrocarboxylation and Co-based hydrogenation of alkene substrates, are similar in the manner that first a hydride transfer to the substrate occurs and then the nucleophilic substrate carbon attacks an electrophile. In the hydrocarboxylation reaction, the electrophile is CO₂, whereas in the hydrogenation reaction, it is a proton. Thus, the main difference is how the second step occurs. In the hydrocarboxylation study, our results showed an unusual TS geometry for the C-CO₂ bond formation step, where CO₂ does not interact with the metal (*outer sphere CO₂ insertion*) and where the substrate is coordinated to the metal via a phenyl ring instead of the formally nucleophilic C atom. On the other hand, in the hydrogenation reaction, during the second step, the metal-coordinated nucleophilic C atom abstracts a proton from the metal complex (reductive elimination step) or from a metal-coordinated H₂. Therefore, it seems much easier to design and control enantioselective hydrogenation reactions, where the proton transfer step occurs in the vicinity of the chiral ligand than hydrocarboxylation reactions where CO₂ does not interact with the metal center and C-CO₂ bond formation occurs in the outer sphere. In order to improve the enantiomeric excess of such reactions, novel strategies may be necessary, such as designing ligands or additives that can capture CO₂ and restrict its conformational freedom. The computationally observed stacking interactions of CO₂ with N-heterocyclic rings may be an interesting starting point.

In this thesis, I studied reactions with metals, whose reactivity and nature are quite different. The precious metal rhodium has well established oxidation states I and III, with closed shell electronic structures, and thus its behaviour is easier to predict, which may be one of the reasons why rhodium is one of the most used metals in the industry. On the other hand, the non-precious cobalt can access many different oxidation and spin states, which may also involve radical chemistry. This implies that cobalt systems are very complex systems to model and study. The knowledge generated in this thesis on the Co-catalyzed enamide hydrogenation will hopefully be an inspiration towards the design of experiments that can provide more insights into the preferred reaction channels, with the ultimate goal to design Co-based systems where undesirable reaction pathways can be suppressed.

References

- (1) McConathy, J.; Owens, M. J., Stereochemistry in Drug Action. *Prim. Care. Companion. J. Clin. Psychiatry* **2003**, *5* (2), 70-73.
- (2) Blaser, H.-U., Hanreich, R., Schneider, H.-D., Spindler, F. and Steinacher, B. (2004), The Chiral Switch of Metolachlor: The Development of a Large-Scale Enantioselective Catalytic Process. In H.-U. Blaser and E. Schmidt (Eds.) *Asymmetric Catalysis on Industrial Scale: Challenges, Approaches and Solutions*, Weinheim, Germany, Wiley-VCH Verlag GmbH, pp. 55-70.
- (3) Etayo, P.; Vidal-Ferran, A., Rhodium-catalysed asymmetric hydrogenation as a valuable synthetic tool for the preparation of chiral drugs. *Chem. Soc. Rev.* **2013**, *42* (2), 728-754.
- (4) Feldgus, S.; Landis, C. R., Origin of Enantioinversion in the Rhodium-Catalyzed Asymmetric Hydrogenation of Prochiral Enamides and the Effect of the α -Substituent. *Organometallics* **2001**, *20* (11), 2374-2386.
- (5) Aloui, A.; Delbecq, F.; De Bellefon, C.; Sautet, P., Understanding the influence of hydrogen pressure on the enantioselectivity of hydrogenation: A combined theory-experiment approach. *J. Organomet. Chem.* **2017**, 836-837, 90-99.
- (6) Chan, A. S. C.; Pluth, J. J.; Halpern, J., Identification of the enantioselective step in the asymmetric catalytic hydrogenation of a prochiral olefin. *J. Am. Chem. Soc.* **1980**, *102* (18), 5952-5954.
- (7) Halpern, J., Mechanism and Stereoselectivity of Asymmetric Hydrogenation. *Science* **1982**, *217* (4558), 401.
- (8) Halpern, J., Mechanism and stereochemistry of asymmetric catalysis by metal complexes. *Pure Appl. Chem.* **1983**, *55* (1), 99.
- (9) Halpern, J., Mechanistic aspects of homogeneous catalytic hydrogenation and related processes. *Inorg. Chim. Acta* **1981**, *50*, 11-19.
- (10) Kitamura, M.; Ohkuma, T.; Inoue, S.; Sayo, N.; Kumobayashi, H.; Akutagawa, S.; Ohta, T.; Takaya, H.; Noyori, R., Homogeneous asymmetric hydrogenation of functionalized ketones. *J. Am. Chem. Soc.* **1988**, *110* (2), 629-631.
- (11) Kitamura, M.; Tsukamoto, M.; Bessho, Y.; Yoshimura, M.; Kobs, U.; Widhalm, M.; Noyori, R., Mechanism of Asymmetric Hydrogenation of α -(Acylamino)acrylic Esters Catalyzed by BINAP-Ruthenium(II) Diacetate. *J. Am. Chem. Soc.* **2002**, *124* (23), 6649-6667.
- (12) Lu, S.-M.; Bolm, C., Highly Chemo- and Enantioselective Hydrogenation of Linear α,β -Unsaturated Ketones. *Chem. Eur. J.* **2008**, *14* (25), 7513-7516.

- (13) Engel, J.; Mersmann, S.; Norrby, P.-O.; Bolm, C., Mechanistic Insights into the Iridium-Catalyzed Hydrogenations of α,β -Unsaturated Ketones. *Chem. Cat. Chem.* **2016**, *8* (19), 3099-3106.
- (14) Tutkowski, B.; Kerdphon, S.; Limé, E.; Helquist, P.; Andersson, P. G.; Wiest, O.; Norrby, P.-O., Revisiting the Stereodetermining Step in Enantioselective Iridium-Catalyzed Imine Hydrogenation. *Acs Catal.* **2018**, *8* (1), 615-623.
- (15) Monfette, S.; Turner, Z. R.; Semproni, S. P.; Chirik, P. J., Enantiopure C1-Symmetric Bis(imino)pyridine Cobalt Complexes for Asymmetric Alkene Hydrogenation. *J. Am. Chem. Soc.* **2012**, *134* (10), 4561-4564.
- (16) Friedfeld, M. R.; Shevlin, M.; Margulieux, G. W.; Campeau, L.-C.; Chirik, P. J., Cobalt-Catalyzed Enantioselective Hydrogenation of Minimally Functionalized Alkenes: Isotopic Labeling Provides Insight into the Origin of Stereoselectivity and Alkene Insertion Preferences. *J. Am. Chem. Soc.* **2016**, *138* (10), 3314-3324.
- (17) Friedfeld, M. R.; Zhong, H.; Ruck, R. T.; Shevlin, M.; Chirik, P. J., Cobalt-catalyzed asymmetric hydrogenation of enamides enabled by single-electron reduction. *Science* **2018**, *360* (6391), 888-893.
- (18) Zhong, H.; Friedfeld, M. R.; Camacho-Bunquin, J.; Sohn, H.; Yang, C.; Delferro, M.; Chirik, P. J., Exploring the Alcohol Stability of Bis(phosphine) Cobalt Dialkyl Precatalysts in Asymmetric Alkene Hydrogenation. *Organometallics* **2019**, *38* (1), 149-156.
- (19) Zhou, S.; Fleischer, S.; Junge, K.; Das, S.; Addis, D.; Beller, M., Enantioselective Synthesis of Amines: General, Efficient Iron-Catalyzed Asymmetric Transfer Hydrogenation of Imines. *Angew. Chem. Int. Ed.* **2010**, *49* (44), 8121-8125.
- (20) Lagaditis, P. O.; Sues, P. E.; Sonnenberg, J. F.; Wan, K. Y.; Lough, A. J.; Morris, R. H., Iron(II) Complexes Containing Unsymmetrical $P-N-P'$ Pincer Ligands for the Catalytic Asymmetric Hydrogenation of Ketones and Imines *J. Am. Chem. Soc.* **2014**, *136* (4), 1367-1380.
- (21) Sonnenberg, J. F.; Wan, K.Y.; Sues, P. E.; Morris, R. H., Ketone Asymmetric Hydrogenation Catalyzed by $P-NH-P'$ Pincer Iron Catalysts: An Experimental and Computational Study. *Acs Catal.* **2017**, *7* (1), 316-326.
- (22) Smith, S. A. M.; Lagaditis, P. O.; Lüpke, A.; Lough, A. J.; Morris, R. H., Unsymmetrical Iron $P-NH-P'$ Catalysts for the Asymmetric Pressure Hydrogenation of Aryl Ketones. *Chem. Eur. J.* **2017**, *23* (30), 7212-7216.
- (23) Seo, C. S. G.; Morris, R. H., Catalytic Homogeneous Asymmetric Hydrogenation: Successes and Opportunities. *Organometallics* **2019**, *38* (1), 47-65.
- (24) Chirik, P. J.; Wieghardt, K., Radical Ligands Confer Nobility on Base-Metal Catalysts. *Science* **2010**, *327* (5967), 794-795.

- (25) Kawashima, S.; Aikawa, K.; Mikami, K., Rhodium-Catalyzed Hydrocarboxylation of Olefins with Carbon Dioxide. *Eur. J. Org. Chem.* **2016**, (19), 3166-3170.
- (26) Hopmann, K. H., How Accurate is DFT for Iridium-Mediated Chemistry? *Organometallics* **2016**, *35* (22), 3795-3807.
- (27) Weymuth, T.; Couzijn, E. P. A.; Chen, P.; Reiher, M., New Benchmark Set of Transition-Metal Coordination Reactions for the Assessment of Density Functionals. *J. Chem. Theory Comput.* **2014**, *10* (8), 3092-3103.
- (28) Morello, G. R.; Zhong, H.; Chirik, P. J.; Hopmann, K. H., Cobalt-catalysed alkene hydrogenation: a metallacycle can explain the hydroxyl activating effect and the diastereoselectivity. *Chem. Sci.* **2018**, *9* (22), 4977-4982.
- (29) Hazari, N.; Heimann, J. E., Carbon Dioxide Insertion into Group 9 and 10 Metal-Element σ Bonds. *Inorg. Chem.* **2017**, *56* (22), 13655-13678.
- (30) Jensen, F. (2007), *Introduction to Computational Chemistry*. (2nd ed.) Chichester, England, John Wiley & Sons Ltd.
- (31) Peng, Q.; Duarte, F.; Paton, R. S., Computing organic stereoselectivity - from concepts to quantitative calculations and predictions. *Chem. Soc. Rev.* **2016**, *45* (22), 6093-6107.
- (32) Koch, W.; Holthausen, M. C. (2001), *A Chemist's Guide to Density Functional Theory*. (2nd ed.) Weinheim, Germany, Wiley-VCH Verlag GmbH.
- (33) March, N. H., Electron density theory of atoms and molecules. *J. Phys. Chem.* **1982**, *86* (12), 2262-2267.
- (34) Sousa, S. F.; Fernandes, P. A.; Ramos, M. J., General Performance of Density Functionals. *J. Phys. Chem. A* **2007**, *111* (42), 10439-10452.
- (35) Mihail, B.; Leslie, V.-M.; Mark E., T.; Klaus-Robert, M.; Kieron, B., *Density Functionals with Quantum Chemical Accuracy: From Machine Learning to Molecular Dynamics*. *Chem. Rxiv. Preprint*, **2019**.
- (36) Curtiss, L. A.; Raghavachari, K.; Trucks, G.W.; Pople, J. A., Gaussian-2 theory for molecular energies of first- and second-row compounds. *J. Chem. Phys.* **1991**, *94* (11), 7221-7230.
- (37) Curtiss, L. A.; Redfern, P. C.; Raghavachari, K., Assessment of Gaussian-3 and density-functional theories on the G3/05 test set of experimental energies. *J. Chem. Phys.* **2005**, *123* (12), 124107.
- (38) Henry, D. J.; Sullivan, M. B.; Radom, L., G3-RAD and G3X-RAD: Modified Gaussian-3 (G3) and Gaussian-3X (G3X) procedures for radical thermochemistry. *J. Chem. Phys.* **2003**, *118* (11), 4849-4860.

- (39) Curtiss, L. A.; Redfern, P. C.; Rassolov, V.; Kedziora, G.; Pople, J. A., Extension of Gaussian-3 theory to molecules containing third-row atoms K, Ca, Ga-Kr. *J. Chem. Phys.* **2001**, *114* (21), 9287-9295.
- (40) Zheng, J.; Zhao, Y.; Truhlar, D. G., The DBH24/08 Database and Its Use to Assess Electronic Structure Model Chemistries for Chemical Reaction Barrier Heights. *J. Chem. Theory. Comput.* **2009**, *5* (4), 808-821.
- (41) Calbo, J.; Ortí, E.; Sancho-García, J. C.; Aragó, J. (2015), Chapter Two - The Nonlocal Correlation Density Functional VV10: A Successful Attempt to Accurately Capture Non-covalent Interactions. In Dixon, D. A. (Ed.) *Annual Reports in Computational Chemistry*, (1st ed., Vol. 11, pp. 37-102.) Elsevier.
- (42) Zhao G.; L., Bagayoko D.; Williams T. D., Local-density-approximation prediction of electronic properties of GaN, Si, C, and RuO₂, *Phys. Rev. B* (1999) *60*, 1563-1572.
- (43) Kohn, W.; Becke, A. D.; Parr, R. G., Density Functional Theory of Electronic Structure. *J. Phys. Chem.* **1996**, *100* (31), 12974-12980.
- (44) Vosko, S. H.; Wilk, L.; Nusair, M., Accurate spin-dependent electron liquid correlation energies for local spin density calculations: a critical analysis. *Can. J. Phys.* **1980**, *58* (8), 1200-1211.
- (45) Becke, A. D., Density-functional exchange-energy approximation with correct asymptotic behavior. *Phys. Rev. A* **1988**, *38* (6), 3098-3100.
- (46) Proynov, E. I.; Ruiz, E.; Vela, A.; Salahub, D. R., Determining and extending the domain of exchange and correlation functionals. *Int. J. Quantum. Chem.* **1995**, *56* (S29), 61-78.
- (47) Kristyán, S.; Pulay, P., Can (semi)local density functional theory account for the London dispersion forces? *Chem. Phys. Lett.* **1994**, *229* (3), 175-180.
- (48) Ernzerhof, M.; Scuseria, G. E., Assessment of the Perdew-Burke-Ernzerhof exchange-correlation functional. *J. Chem. Phys.* **1999**, *110* (11), 5029-5036.
- (49) Lee, C.; Yang, W.; Parr, R. G., Development of the Colle-Salvetti correlation-energy formula into a functional of the electron density. *Phys. Rev. B* **1988**, *37* (2), 785-789.
- (50) Wang, Y.; Perdew, J. P., Correlation hole of the spin-polarized electron gas, with exact small-wave-vector and high-density scaling. *Phys. Rev. B* **1991**, *44* (24), 13298-13307.
- (51) Kemister, G., Comment on the exchange-energy formula of Ghosh and Parr: A new derivation applicable to molecules. *Phys. Rev. A* **1986**, *34* (5), 4480-4481.
- (52) Perdew, J. P.; Tao, J.; Staroverov, V. N.; Scuseria, G. E., Meta-generalized gradient approximation: Explanation of a realistic nonempirical density functional. *J. Chem. Phys.* **2004**, *120* (15), 6898-6911.

- (53) Tao, J.; Perdew, J. P.; Staroverov, V. N.; Scuseria, G. E., Climbing the Density Functional Ladder: Nonempirical Meta-Generalized Gradient Approximation Designed for Molecules and Solids. *Phys. Rev. Lett.* **2003**, *91* (14), 146401.
- (54) Zhao, Y.; Truhlar, D. G., A new local density functional for main-group thermochemistry, transition metal bonding, thermochemical kinetics, and noncovalent interactions. *J. Chem. Phys.* **2006**, *125* (19), 194101.
- (55) Sparta, M.; Jensen, V. R.; Børve, K. J., Accurate metal-ligand bond energies in the η^2 -C₂H₄ and η^2 -C₆₀ complexes of Pt(PH₃)₂, with application to their Bis-(triphenylphosphine) analogues. *Mol. Phys.* **2013**, *111* (9-11), 1599-1611.
- (56) Tshipis, A.C., DFT flavor of coordination chemistry. *Coord. Chem. Rev.* **2014**, *272*, 1-29.
- (57) Perdew, J.P.; Burke, K.; Ernzerhof, M., Generalized Gradient Approximation Made Simple. *Phys. Rev. Lett.* **1996**, *77* (18), 3865-3868.
- (58) Xin, S.; Harrod, J. F., Enantioselective hydrosilation of ketones in the presence of an S,S-[1,2-bis(tetrahydroindenyl)ethane]-titanium catalyst. *Can. J. Phys.* **1995**, *73* (7), 999-1002.
- (59) Zhou, Q.-L.; Xie, J.-H., (2010) Enantioselective Hydrogenation of Enamines with Monodentate Phosphorus Ligands. In T.C. Nugent (ed.) *Chiral Amine Synthesis*, Weinheim, Germany, Wiley-VCH Verlag GmbH & Co. KGaA, pp. 247-271.
- (60) Fu, Y.; Xie, J.-H.; Hu, A.-G.; Zhou, H.; Wang, L.-X.; Zhou, Q.-L., Novel monodentate spiro phosphorus ligands for rhodium-catalyzed hydrogenation reactions. *Chem. Commun.* **2002**, (5), 480-481.
- (61) Hu, A. G.; Fu, Y.; Xie, J. H.; Zhou, H.; Wang, L. X.; Zhou, Q. L., Monodentate chiral spiro phosphoramidites: efficient ligands for rhodium-catalyzed enantioselective hydrogenation of enamides. *Angew. Chem. Int. Ed. Engl.* **2002**, *41* (13), 2348-50.
- (62) Ditchfield, R.; Hehre, W.J.; Pople, J. A., Self-Consistent Molecular-Orbital Methods. IX. An Extended Gaussian-Type Basis for Molecular-Orbital Studies of Organic Molecules. *J. Chem. Phys.* **1971**, *54*, 724.
- (63) Dunning, Jr., T. H., Gaussian basis sets for use in correlated molecular calculations. The atoms boron through neon and hydrogen. *J. Chem. Phys.* **1989**, *90* (2), 1007-1023.
- (64) Hay, P. J.; Wadt, W. R., Ab initio effective core potentials for molecular calculations. Potentials for K to Au including the outermost core orbitals. *J. Chem. Phys.* **1985**, *82* (1), 299-310.
- (65) Krauss, M.; Stevens, W. J., Effective Potentials in Molecular Quantum Chemistry. *Annu. Rev. Phys. Chem.* **1984**, *35* (1), 357-385.

- (66) Tirado-Rives, J.; Jorgensen, W. L., Performance of B3LYP Density Functional Methods for a Large Set of Organic Molecules. *J. Chem. Theory. Comput.* **2008**, *4* (2), 297-306.
- (67) Skyner, R. E.; McDonagh, J. L.; Groom, C. R.; Van Mourik, T.; Mitchell, J. B. O., A review of methods for the calculation of solution free energies and the modelling of systems in solution. *Phys. Chem. Chem. Phys.* **2015**, *17* (9), 6174-6191.
- (68) C. Cramer, C. J.; Truhlar, D. G., Implicit Solvation Models: Equilibria, Structure, Spectra, and Dynamics. *Chem. Rev.* **1999**, *99* (8), 2161-2200.
- (69) Roux, B. T.; Simonson, T., Implicit solvent models. *Biophys. Chem.* **1999**, *78* (1), 1-20.
- (70) Cancès, E.; Mennucci, B.; Tomasi, J., A new integral equation formalism for the polarizable continuum model: Theoretical background and applications to isotropic and anisotropic dielectrics. *J. Chem. Phys.* **1997**, *107* (8), 3032-3041.
- (71) Tomasi, J.; Mennucci, B.; Cammi, R., Quantum Mechanical Continuum Solvation Models. *Chem. Rev.* **2005**, *105* (8), 2999-3094.
- (72) Tomasi, J.; Mennucci, B.; Cancès, E., The IEF version of the PCM solvation method: an overview of a new method addressed to study molecular solutes at the QM ab initio level. *J. Mol. Struct-Theochem.* **1999**, *464* (1-3), 211-226.
- (73) Grimme, S., Supramolecular Binding Thermodynamics by Dispersion-Corrected Density Functional Theory. *Chem. Eur. J.* **2012**, *18* (32), 9955-9964.
- (74) Burley, S. K.; Petsko, G. A., Aromatic-aromatic interaction: a mechanism of protein structure stabilization. *Science* **1985**, *229* (4708), 23.
- (75) Salonen, L. M.; Ellermann, M.; Diederich, F., Aromatic Rings in Chemical and Biological Recognition: Energetics and Structures. *Angew. Chem. Int. Ed.* **2011**, *50* (21), 4808-4842.
- (76) Sredojević, D.; Bogdanović, G. A.; Tomić, Z. D.; Zarić, S. D., Stacking vs. CH- π interactions between chelate and aryl rings in crystal structures of square-planar transition metal complexes. *Cryst. Eng. Comm.* **2007**, *9* (9), 793-798.
- (77) Veljković, D. Ž.; Janjić, G. V.; Zarić, S. D., Are C-H \cdots O interactions linear? The case of aromatic CH donors. *Cryst. Eng. Comm.* **2011**, *13* (15), 5005-5010.
- (78) Zarić, Snežana D., Metal Ligand Aromatic Cation- π Interactions. *Eur. J. Inorg. Chem.* **2003**, *2003* (12), 2197-2209.
- (79) Malenov, D. P.; Janjić, G. V.; Veljković, D. Ž.; Zarić, S. D., Mutual influence of parallel, CH/O, OH/ π and lone pair/ π interactions in water/benzene/water system. *Comput. Theo. Chem.* **2013**, *1018*, 59-65.

- (80) Bloom, J. W. G.; Wheeler, S. E., Taking the Aromaticity out of Aromatic Interactions. *Angew. Chem. Int. Ed.* **2011**, *50* (34), 7847-7849.
- (81) Hopmann, K.H., Quantum Chemical Studies of Asymmetric Reactions: Historical Aspects and Recent Examples. *Int. J. Quantum Chem.* **2015**, *115* (18), 1232-1249.
- (82) Hopmann, K.H., Iron/Brønsted Acid Catalyzed Asymmetric Hydrogenation: Mechanism and Selectivity-Determining Interactions. *Chem. Eur. J.* **2015**, *21* (28), 10020-10030.
- (83) Wodrich, M. D.; Corminboeuf, C.; Schleyer, P. V. R., Systematic Errors in Computed Alkane Energies Using B3LYP and Other Popular DFT Functionals. *Org. Lett.* **2006**, *8* (17), 3631-3634.
- (84) Zhao, Y.; Schultz, N. E.; Truhlar, D. G., Exchange-correlation functional with broad accuracy for metallic and nonmetallic compounds, kinetics, and noncovalent interactions. *J. Chem. Phys.* **2005**, *123* (16), 161103.
- (85) Zhao, Y.; Schultz, N. E.; Truhlar, D. G., Design of Density Functionals by Combining the Method of Constraint Satisfaction with Parameterization for Thermochemistry, Thermochemical Kinetics, and Noncovalent Interactions. *J. Chem. Theory Comput.* **2006**, *2* (2), 364-382.
- (86) Zhao, Y.; Truhlar, D. G., The M06 suite of density functionals for main group thermochemistry, thermochemical kinetics, noncovalent interactions, excited states, and transition elements: two new functionals and systematic testing of four M06-class functionals and 12 other functionals. *Theor. Chem. Acc.* **2008**, *120* (1), 215-241.
- (87) Zhao, Y.; Truhlar, D. G., Exploring the Limit of Accuracy of the Global Hybrid Meta Density Functional for Main-Group Thermochemistry, Kinetics, and Noncovalent Interactions. *J. Chem. Theory Comput.* **2008**, *4* (11), 1849-1868.
- (88) Grimme, S., Density functional theory with London dispersion corrections. *Wires Comput. Mol. Sci.* **2011**, *1* (2), 211-228.
- (89) Grimme, S., Semiempirical GGA-type density functional constructed with a long-range dispersion correction. *J. Comput. Chem.* **2006**, *27* (15), 1787-1799.
- (90) Grimme, S.; Antony, J.; Ehrlich, S.; Krieg, H., A Consistent and Accurate Ab Initio Parameterization of Density Functional Dispersion Correction (DFT-D) for the 94 Elements H-Pu. *J. Chem. Phys.* **2010**, *132*, 154104.
- (91) Grimme, S.; Ehrlich, S.; Goerigk, L., Effect of the damping function in dispersion corrected density functional theory. *J. Comput. Chem.* **2011**, *32* (7), 1456-1465.
- (92) Rohmann, K.; Hölscher, M.; Leitner, W., Can Contemporary Density Functional Theory Predict Energy Spans in Molecular Catalysis Accurately Enough To Be Applicable for in Silico Catalyst Design? A Computational/Experimental Case

- Study for the Ruthenium-Catalyzed Hydrogenation of Olefins. *J. Am. Chem. Soc.* **2016**, *138* (1), 433-443.
- (93) Sieffert, N.; Bühl, M., Noncovalent Interactions in a Transition-Metal Triphenylphosphine Complex: a Density Functional Case Study. *Inorg. Chem.* **2009**, *48* (11), 4622-4624.
- (94) Kraka, E.; Cremer, D., Computational Analysis of the Mechanism of Chemical Reactions in Terms of Reaction Phases: Hidden Intermediates and Hidden Transition States. *Acc. Chem. Res.* **2010**, *43* (5), 591-601.
- (95) Lewars, E. G. (2016), *Computational Chemistry: Introduction to the Theory and Applications of Molecular and Quantum Mechanics*, (3rd ed.), Springer International Publishing AG Switzerland.
- (96) Koch, W.; Holthausen, M.C. (2001), Chemical Reactivity: Exploring Potential Energy Surfaces. In *A Chemist's Guide to Density Functional Theory*, (2nd ed.), Weinheim, Germany, Wiley-VCH Verlag GmbH, pp. 239-263.
- (97) Jacobsen, R. L.; Johnson, R. D.; Irikura, K. K.; Kacker, R. N., Anharmonic Vibrational Frequency Calculations Are Not Worthwhile for Small Basis Sets. *J. Chem. Theory Comput.* **2013**, *9* (2), 951-954.
- (98) Schlegel, H. B., Optimization Algorithms and Their Applications. *Abstr. Pap. Am. Chem. S* **1986**, *192*, 148-Phys.
- (99) Schlegel, H. B., Geometry optimization. *Wires Comput. Mol. Sci.* **2011**, *1* (5), 790-809.
- (100) Schlegel, H. B., Optimization of Equilibrium Geometries and Transition Structures. *J. Comput. Chem.* **1982**, *3* (2), 214-218.
- (101) Rankin, W. J. (2019), *Chemical Thermodynamics: Theory and Applications*, (1st ed.), United State, CRC Press/Taylor & Francis Group.
- (102) Ryu, H.; Park, J.; Kim, H. K.; Park, J. Y.; Kim, S.-T.; Baik, M.-H., Pitfalls in Computational Modeling of Chemical Reactions and How To Avoid Them. *Organometallics* **2018**, *37* (19), 3228-3239.
- (103) Sokolov, V. I., Chirality in the World of Stereochemistry. *Comp. Math. App.* **1986**, *12* (3, Part 2), 547-563.
- (104) Bringmann, G.; Price Mortimer, A. J.; Keller, P. A.; Gresser, M. J.; Garner, J.; Breuning, M., Atroposelective Synthesis of Axially Chiral Biaryl Compounds. *Angew. Chem. Int. Ed.* **2005**, *44* (34), 5384-5427.
- (105) Christie, G. H.; Kenner, J., LXXI.-The molecular configurations of polynuclear aromatic compounds. Part I. The resolution of γ -6 : 6'-dinitro- and 4 : 6 : 4' : 6'-tetranitro-diphenic acids into optically active components. *J. Chem. Soc., Transactions* **1922**, *121* (0), 614-620.

- (106) Seeman, J. I., Effect of conformational change on reactivity in organic chemistry. Evaluations, applications, and extensions of Curtin-Hammett Winstein-Holness kinetics. *Chem. Rev.* **1983**, *83* (2), 83-134.
- (107) Chakraborty, S.; Saha, C., The Curtin–Hammett Principle. *Resonance* **2016**, *21*, 151–171.
- (108) Gruber, S.; Pfaltz, A., Asymmetric Hydrogenation with Iridium *C,N* and *N,P* Ligand Complexes: Characterization of Dihydride Intermediates with a Coordinated Alkene. *Angew. Chem. Int. Ed.* **2014**, *53* (7), 1896-1900.
- (109) Aloui, A.; Delbecq, F.; Sautet, P.; De Bellefon, C., Further insight in the minor/major concept using hydrogen pressure effect in asymmetric hydrogenation. *J. Mol. Catal. A Chem.* **2012**, *363-364*, 214-222.
- (110) Wang, N. X.; Wilson, A. K., The behavior of density functionals with respect to basis set. I. The correlation consistent basis sets. *J. Chem. Phys.* **2004**, *121* (16), 7632-7646.
- (111) Riley, K. E.; Op't Holt, B. T.; Merz, K. M., Critical Assessment of the Performance of Density Functional Methods for Several Atomic and Molecular Properties. *J. Chem. Theory Comput.* **2007**, *3* (2), 407-433.
- (112) Minenkov, Y.; Singstad, Å.; Occhipinti, G.; Jensen, V. R., The accuracy of DFT-optimized geometries of functional transition metal compounds: a validation study of catalysts for olefin metathesis and other reactions in the homogeneous phase. *Dalton Trans.* **2012**, *41* (18), 5526-5541.
- (113) Grimme, S., Accurate description of van der Waals complexes by density functional theory including empirical corrections. *J. Comput. Chem.* **2004**, *25* (12), 1463-1473.
- (114) Bauschlicher, C. W.; Partridge, H., The sensitivity of B3LYP atomization energies to the basis set and a comparison of basis set requirements for CCSD(T) and B3LYP. *Chem. Phys. Lett.* **1995**, *240* (5), 533-540.
- (115) Zhao, Y.; Truhlar, D. G., Benchmark Energetic Data in a Model System for Grubbs II Metathesis Catalysis and Their Use for the Development, Assessment, and Validation of Electronic Structure Methods. *J. Chem. Theory Comput.* **2009**, *5* (2), 324-333.
- (116) Check, C. E.; Gilbert, T. M., Progressive Systematic Underestimation of Reaction Energies by the B3LYP Model as the Number of C-C Bonds Increases: Why Organic Chemists Should Use Multiple DFT Models for Calculations Involving Polycarbon Hydrocarbons. *J. Org. Chem.* **2005**, *70* (24), 9828-9834.
- (117) Sparta, M.; Riplinger, C.; Neese, F., Mechanism of Olefin Asymmetric Hydrogenation Catalyzed by Iridium Phosphino-Oxazoline: A Pair Natural Orbital Coupled Cluster Study. *J. Chem. Theory Comput.* **2014**, *10* (3), 1099-1108.

- (118) Arnaut, L.; Formosinho, S.; Burrows, H. (2006), 13. Acid-Base Catalysis and Proton-Transfer Reactions. In *Chemical Kinetics*, (1st ed.), Elsevier Science, pp. 321-359.
- (119) Mangiatordi, G. F.; Brémond, E.; Adamo, C., DFT and Proton Transfer Reactions: A Benchmark Study on Structure and Kinetics. *J. Chem. Theory Comput.* **2012**, *8* (9), 3082-3088.
- (120) Patton, D. C.; Porezag, D. V.; Pederson, M. R., Simplified generalized-gradient approximation and anharmonicity: Benchmark calculations on molecules. *Phys. Rev. B* **1997**, *55* (12), 7454-7459.
- (121) Bernskoetter, W. H.; Brookhart, M., Kinetics and Mechanism of Iridium-Catalyzed Dehydrogenation of Primary Amines to Nitriles. *Organometallics* **2008**, *27* (9), 2036-2045.
- (122) Shiekh, B.A., Hierarchy of Commonly Used DFT Methods for Predicting the Thermochemistry of Rh-Mediated Chemical Transformations. *ACS Omega* **2019**, *4* (13), 15435-15443.
- (123) Doherty, M. D.; Grills, D. C.; Huang, K.-W.; Muckerman, J. T.; Polyansky, D. E.; Van Eldik, R.; Fujita, E., Kinetics and Thermodynamics of Small Molecule Binding to Pincer-PCP Rhodium(I) Complexes. *Inorg. Chem.* **2013**, *52* (8), 4160-4172.
- (124) Wilson, A. D.; Miller, A. J. M.; DuBois, D. L.; Labinger, J.A.; Bercaw, J.E., Thermodynamic Studies of $[\text{H}_2\text{Rh}(\text{diphosphine})_2]^+$ and $[\text{HRh}(\text{diphosphine})_2(\text{CH}_3\text{CN})]^{2+}$ Complexes in Acetonitrile. *Inorg. Chem.* **2010**, *49* (8), 3918-3926.
- (125) Besora, M.; Carreón-Macedo, J.-L.; Cimas, Á.; Harvey, J. N. (2009), Spin-state changes and reactivity in transition metal chemistry: Reactivity of iron tetracarbonyl. In Van Eldik, R.; Hubbard, C D. (eds.) *Advances in Inorganic Chemistry*, (Vol. 61, pp. 573-623.) Academic Press.
- (126) Hedström, A.; Lindstedt, E.; Norrby, P.-O., On the oxidation state of iron in iron-mediated C–C couplings. *J. Organomet. Chem.* **2013**, *748*, 51-55.
- (127) Fouqueau, A.; Mer, S.; Casida, M. E.; Daku, L. M. L.; Hauser, A.; Mineva, T.; Neese, F., Comparison of density functionals for energy and structural differences between the high- $[\text{}^5\text{T}^{2g}:(\text{t}_2\text{g})^4(\text{e}_\text{g})^2]$ and low- $[\text{}^1\text{A}_{1g}:(\text{t}_2\text{g})^6(\text{e}_\text{g})^0]$ spin states of the hexaquoferrous cation $[\text{Fe}(\text{H}_2\text{O})_6]^{2+}$. *J. Chem. Phys.* **2004**, *120* (20), 9473-9486.
- (128) Paulsen, H.; Duelund, L.; Winkler, H.; Toftlund, H.; Trautwein, A. X., Free Energy of Spin-Crossover Complexes Calculated with Density Functional Methods. *Inorg. Chem.* **2001**, *40* (9), 2201-2203.
- (129) Salomon, O.; Reiher, M.; Hess, B. A., Assertion and validation of the performance of the B3LYP* functional for the first transition metal row and the G2 test set. *J. Chem. Phys.* **2002**, *117* (10), 4729-4737.

- (130) Kismartoni, L. C.; Weitz, E.; Cedeño, D. L., Density Functional Study of $\text{Fe}(\text{CO})_3$ and $\text{Fe}(\text{CO})_3(\text{L})$ with H_2 and C_2H_4 , where $\text{L}=\text{H}_2$ or C_2H_4 : Reactions Relevant to Olefin Hydro-genation. *Organometallics* **2005**, *24* (20), 4714-4720.
- (131) Lawson Daku, L. M.; Aquilante, F.; Robinson, T. W.; Hauser, A., Accurate Spin-State Energetics of Transition Metal Complexes.1.CCSD(T), CASPT2, and DFT Study of $[\text{M}(\text{NCH})_6]^{2+}$ ($\text{M} = \text{Fe}, \text{Co}$). *J. Chem. Theory Comput.* **2012**, *8* (11), 4216-4231.
- (132) Brandt, P.; Hedberg, C.; Andersson, P. G., New Mechanistic Insights into the Iridium–Phosphanooxazoline-Catalyzed Hydrogenation of Unfunctionalized Olefins: A DFT and Kinetic Study. *Chem. Eur. J.* **2003**, *9* (1), 339-347.
- (133) Lam, Y.-h.; Houk, K. N., Origins of Stereoselectivity in Intramolecular Aldol Reactions Catalyzed by Cinchona Amines. *J. Am. Chem. Soc.* **2015**, *137* (5), 2116-2127.
- (134) Zhou, J.; Wakchaure, V.; Kraft, P.; List, B., Primary-Amine-Catalyzed Enantio-selective Intramolecular Aldolizations. *Angew. Chem. Int. Ed.* **2008**, *47* (40), 7656-7658.
- (135) Schneebeli, S. T.; Hall, M. L.; Breslow, R.; Friesner, R., Quantitative DFT modeling of the enantiomeric excess for dioxirane-catalyzed epoxidations. *J. Am. Chem. Soc.* **2009**, *131* (11), 3965-3973.
- (136) Armstrong, A.; Ahmed, G.; Dominguez-Fernandez, B.; Hayter, B. R.; Wailes, J. S., Enantioselective Epoxidation of Alkenes Catalyzed by 2-Fluoro-N-Carboethoxy-tropinone and Related Tropinone Derivatives. *J. Org. Chem.* **2002**, *67* (24), 8610-8617.
- (137) Wang, Z.-X.; Miller, S. M.; Anderson, O. P.; Shi, Y., Asymmetric Epoxidation by Chiral Ketones Derived from Carbocyclic Analogues of Fructose. *J. Org. Chem.* **2001**, *66* (2), 521-530.
- (138) Chong, E.; Qu, B.; Zhang, Y.; Cannone, Z. P.; Leung, J. C.; Tcyrulnikov, S.; Nguyen, K. D.; Haddad, N.; Biswas, S.; Hou, X.; Kaczanowska, K.; Chwalba, M.; Tracz, A.; Czarnocki, S.; Song, J. J.; Kozlowski, M. C.; Senanayake, C. H., A versatile catalyst system for enantioselective synthesis of 2-substituted 1,4-benzodioxanes. *Chem. Sci.* **2019**, *10* (15), 4339-4345.
- (139) Cokoja, M.; Bruckmeier, C.; Rieger, B.; Herrmann, W.A.; Kuhn, F. E., Transformation of Carbon Dioxide with Homogeneous Transition-Metal Catalysts: A Molecular Solution to a Global Challenge? *Angew. Chem. Int. Ed.* **2011**, *50* (37), 8510-8537.
- (140) Dabral, S.; Schaub, T., The Use of Carbon Dioxide (CO_2) as a Building Block in Organic Synthesis from an Industrial Perspective. *Adv. Synth. Catal.* **2019**, *361* (2), 223-246.

- (141) Alper, E.; Orhan, O. Y., CO₂ utilization: Developments in conversion processes. *Petroleum* **2017**, *3* (1), 109-126.
- (142) Tortajada, A.; Julia-Hernandez, F.; Borjesson, M.; Moragas, T.; Martin, R., Transition-Metal-Catalyzed Carboxylation Reactions with Carbon Dioxide. *Angew. Chem. Int. Ed.* **2018**, *57* (49), 15948-15982.
- (143) Calabrese, C.; Giacalone, F.; Aprile, C., Hybrid catalysts for CO₂ conversion into cyclic carbonates. *Catalysts* **2019**, *9* (4), 325.
- (144) Díaz Velázquez, H.; Wu, Z.-X.; Vandichel, M.; Verpoort, F., Inserting CO₂ into Terminal Alkynes via Bis-(NHC)-Metal Complexes. *Catal. Lett.* **2017**, *147* (2), 463-471.
- (145) Fujihara, T.; Nogi, K.; Xu, T.; Terao, J.; Tsuji, Y., Nickel-Catalyzed Carboxylation of Aryl and Vinyl Chlorides Employing Carbon Dioxide. *J. Am. Chem. Soc.* **2012**, *134* (22), 9106-9109.
- (146) Liu, Y. G.; Chen, Q.; Mou, C. L.; Pan, L. T.; Duan, X. Y.; Chen, X. K.; Chen, H. Z.; Zhao, Y. L.; Lu, Y. P.; Jin, Z. C.; Chi, Y. R., Catalytic asymmetric acetalization of carboxylic acids for access to chiral phthalidyl ester prodrugs. *Nat. Commun.* **2019**, *10*, 1675.
- (147) Ostapowicz, T. G.; Hölscher, M.; Leitner, W., CO₂ Insertion into Metal–Carbon Bonds: A Computational Study of RhI Pincer Complexes. *Chem. Eur. J.* **2011**, *17* (37), 10329-10338.
- (148) Ostapowicz, T. G.; Hölscher, M.; Leitner, W., Catalytic Hydrocarboxylation of Olefins with CO₂ and H₂ - a DFT Computational Analysis. *Eur. J. Inorg. Chem.* **2012**, *2012* (34), 5632-5641.
- (149) Shao, P.; Wang, S.; Chen, C.; Xi, C., Cp₂TiCl₂-Catalyzed Regioselective Hydrocarboxylation of Alkenes with CO₂. *Org. Lett.* **2016**, *18* (9), 2050-2053.
- (150) Pavlovic, Lj.; Vaitla, J.; Bayer, A.; Hopmann, K.H., Rhodium-Catalyzed Hydrocarboxylation: Mechanistic Analysis Reveals Unusual Transition State for Carbon–Carbon Bond Formation. *Organometallics* **2018**, *37* (6), 941-948.
- (151) Obst, M.; Pavlovic, Lj.; Hopmann, K. H., Carbon-carbon bonds with CO₂: Insights from computational studies. *J. Organomet. Chem.* **2018**, *864*, 115-127.
- (152) Obst, M. F.; Gevorgyan, A.; Bayer, A.; Hopmann, K.H., Mechanistic Insights into Copper-Catalyzed Carboxylations. *Organometallics* **2020**, *39*, 9, 1545–1552.
- (153) Gevorgyan, A.; Obst, M. F.; Guttormsen, Y.; Maseras, F.; Hopmann, K. H.; Bayer, A., Caesium fluoride-mediated hydrocarboxylation of alkenes and allenes: scope and mechanistic insights. *Chem. Sci.* **2019**, *10* (43), 10072-10078.

- (154) García-López, D.; Pavlovic, Lj.; Hopmann, K. H., To Bind or Not to Bind: Mechanistic Insights into C-CO₂ Bond Formation with Late Transition Metals. *Organometallics* **2020**, *39* (8), 1339-1347.
- (155) Greenhalgh, M. D.; Thomas, S. P., Iron-catalyzed, highly regioselective synthesis of alpha-aryl carboxylic acids from styrene derivatives and CO₂. *J. Am. Chem. Soc.* **2012**, *134* (29), 11900-11903.
- (156) Lv, X.; Zhang, L.; Sun, B.; Li, Z.; Wu, Y.-B.; Lu, G., Computational studies on the Rh-catalyzed carboxylation of a C(sp²)-H bond using CO₂. *Catal. Sci* **2017**, *7* (16), 3539-3545.
- (157) León, T.; Correa, A.; Martin, R., Ni-Catalyzed Direct Carboxylation of Benzyl Halides with CO₂. *J. Am. Chem. Soc.* **2013**, *135* (4), 1221-1224.
- (158) Ukai, K.; Aoki, M.; Takaya, J.; Iwasawa, N., Rhodium(I)-Catalyzed Carboxylation of Aryl- and Alkenylboronic Esters with CO₂. *J. Am. Chem. Soc.* **2006**, *128* (27), 8706-8707.
- (159) Qin, H.-L.; Han, J.-B.; Hao, J.-H.; Kantchev, E. A. B., Computational and experimental comparison of diphosphane and diene ligands in the Rh-catalysed carboxylation of organoboron compounds with CO₂. *Green Chem.* **2014**, *16* (6), 3224-3229.
- (160) Mizuno, H.; Takaya, J.; Iwasawa, N., Rhodium(I)-Catalyzed Direct Carboxylation of Arenes with CO₂ via Chelation-Assisted C-H Bond Activation. *J. Am. Chem. Soc.* **2011**, *133* (5), 1251-1253.
- (161) Dang, L.; Lin, Z.; Marder, T. B., DFT Studies on the Carboxylation of Arylboronate Esters with CO₂ Catalyzed by Copper(I) Complexes. *Organometallics* **2010**, *29* (4), 917-927.
- (162) Sayyed, F. B.; Tsuji, Y.; Sakaki, S., The crucial role of a Ni(i) intermediate in Ni-catalyzed carboxylation of aryl chloride with CO₂: a theoretical study. *Chem. Commun.* **2013**, *49* (91), 10715-10717.
- (163) Fan, T.; Sheong, F. K.; Lin, Z., DFT Studies on Copper-Catalyzed Hydrocarboxylation of Alkynes Using CO₂ and Hydrosilanes. *Organometallics* **2013**, *32* (18), 5224-5230.
- (164) Guan, Y.; Ingman, V. M.; Rooks, B. J.; Wheeler, S. E., AARON: An Automated Reaction Optimizer for New Catalysts. *J. Chem. Theory Comput.* **2018**, *14* (10), 5249-5261.
- (165) Evans, D. A.; Faul, M. M.; Bilodeau, M. T.; Anderson, B. A.; Barnes, D. M., Bis(oxazoline)-copper complexes as chiral catalysts for the enantioselective aziridination of olefins. *J. Am. Chem. Soc.* **1993**, *115* (12), 5328-5329.

- (166) Magre, M.; Pàmies, O.; Diéguez, M., PHOX-Based Phosphite-Oxazoline Ligands for the Enantioselective Ir-Catalyzed Hydrogenation of Cyclic β -Enamides. *Acs Catal.* **2016**, *6* (8), 5186-5190.
- (167) Trost, B. M.; Van Vranken, D. L., Asymmetric Transition Metal-Catalyzed Allylic Alkylations. *Chem. Rev.* **1996**, *96* (1), 395-422.
- (168) Page, J. P.; RajanBabu, T. V., Asymmetric Hydrovinylation of 1-Vinylcycloalkenes. Reagent Control of Regio- and Stereoselectivity. *J. Am. Chem. Soc.* **2012**, *134* (15), 6556-6559.
- (169) Rokade, B. V.; Guiry, P. J., Axially Chiral *P,N*-Ligands: Some Recent Twists and Turns. *Acs Catal.* **2018**, *8* (1), 624-643.
- (170) Cardoso, F. S. P.; Abboud, K. A.; Aponick, A., Design, Preparation, and Implementation of an Imidazole-Based Chiral Biaryl *P,N*-Ligand for Asymmetric Catalysis. *J. Am. Chem. Soc.* **2013**, *135* (39), 14548-14551.
- (171) D. Desimoni, G.; Faita, G.; Jørgensen, K.A., C₂-Symmetric Chiral Bis(Oxazoline) Ligands in Asymmetric Catalysis. *Chem. Rev.* **2006**, *106* (9), 3561-3651.
- (172) Braunstein, P.; Naud, F.; Rettig, S. J., A new class of anionic phosphinoxazoline ligands in palladium and ruthenium complexes: catalytic properties for the transfer hydro-genation of acetophenone. *New J. Chem.* **2001**, *25* (1), 32-39.
- (173) Prakash, M.; Mathivon, K.; Benoit, D. M.; Chambaud, G.; Hochlaf, M., Carbon dioxide interaction with isolated imidazole or attached on gold clusters and surface: competition between σ H-bond and π stacking interaction. *Phys. Chem. Chem. Phys.* **2014**, *16* (24), 12503-12509.
- (174) Hernández-Marín, E.; Lemus-Santana, A. A., Theoretical Study of the Formation of Complexes Between CO₂ and Nitrogen Heterocycles. *J. Mex. Chem. Soc.* **2015**, *59*, 36-42.
- (175) Lee, H. M.; Youn, I. S.; Saleh, M.; Lee, J. W.; Kim, K. S., Interactions of CO₂ with various functional molecules. *Phys. Chem. Chem. Phys.* **2015**, *17* (16), 10925-10933.
- (176) Casey, C. P.; Guan, H., An Efficient and Chemoselective Iron Catalyst for the Hydrogenation of Ketones. *J. Am. Chem. Soc.* **2007**, *129* (18), 5816-5817.
- (177) Casey, C. P.; Guan, H., Cyclopentadienone Iron Alcohol Complexes: Synthesis, Reactivity, and Implications for the Mechanism of Iron-Catalyzed Hydrogenation of Aldehydes. *J. Am. Chem. Soc.* **2009**, *131* (7), 2499-2507.
- (178) Dang, T. P.; Kagan, H. B., The asymmetric synthesis of hydratropic acid and amino-acids by homogeneous catalytic hydrogenation. *J. Chem. Soc. D: Chem. Comm.* **1971**, (10), 481-481.

- (179) Knowles, W. S.; Sabacky, M. J.; Vineyard, B. D.; Weinkauff, D. J., Asymmetric hydrogenation with a complex of rhodium and a chiral bisphosphine. *J. Am. Chem. Soc.* **1975**, *97* (9), 2567-2568.
- (180) Li, Y.; Yu, S.; Wu, X.; Xiao, J.; Shen, W.; Dong, Z.; Gao, J., Iron Catalyzed Asymmetric Hydrogenation of Ketones. *J. Am. Chem. Soc.* **2014**, *136* (10), 4031-4039.
- (181) Garbe, M.; Junge, K.; Walker, S.; Wei, Z.; Jiao, H.; Spannenberg, A.; Bachmann, S.; Scalone, M.; Beller, M., Manganese(I)-Catalyzed Enantioselective Hydrogenation of Ketones Using a Defined Chiral PNP Pincer Ligand. *Angew. Chem. Int. Ed.* **2017**, *56* (37), 11237-11241.
- (182) Hopmann, K.H.; Bayer, A., On the Mechanism of Iridium-Catalyzed Asymmetric Hydrogenation of Imines and Alkenes: A Theoretical Study. *Organometallics* **2011**, *30* (9), 2483-2497.
- (183) Verdolino, V.; Forbes, A.; Helquist, P.; Norrby, P.-O.; Wiest, O., On the mechanism of the rhodium catalyzed acrylamide hydrogenation. *J. Mol. Catal. A-Chem.* **2010**, *324* (1), 9-14.
- (184) Crabtree, R., Iridium compounds in catalysis. *Acc.Chem. Res.* **1979**, *12* (9), 331-337.
- (185) Hopmann, K.H., Cobalt-Bis(imino)pyridine-Catalyzed Asymmetric Hydrogenation: Electronic Structure, Mechanism, and Stereoselectivity. *Organometallics* **2013**, *32* (21), 6388-6399.
- (186) Knijnenburg, Q.; Horton, A. D.; Heijden, H. v. d.; Kooistra, T. M.; Hetterscheid, D. G. H.; Smits, J. M. M.; Bruin, B. d.; Budzelaar, P. H. M.; Gal, A. W., Olefin hydrogenation using diimine pyridine complexes of Co and Rh. *J. Mol. Catal. A-Chem.* **2005**, *232* (1), 151-159.
- (187) Vineyard, B. D.; Knowles, W. S.; Sabacky, M. J.; Bachman, G. L.; Weinkauff, D. J., Asymmetric hydrogenation. Rhodium chiral bisphosphine catalyst. *J. Am. Chem. Soc.* **1977**, *99* (18), 5946-5952.
- (188) Noyori, R.; Takaya, H., BINAP: an efficient chiral element for asymmetric catalysis. *Acc. Chem. Res.* **1990**, *23* (10), 345-350.
- (189) Burk, M. J.; Feaster, J. E.; Harlow, R. L., New electron-rich chiral phosphines for asymmetric catalysis. *Organometallics* **1990**, *9* (10), 2653-2655.
- (190) Burk, M. J.; Feaster, J. E.; Nugent, W. A.; Harlow, R. L., Preparation and use of C2-symmetric bis(phospholanes): production of alpha-amino acid derivatives via highly enantioselective hydrogenation reactions. *J. Am. Chem. Soc.* **1993**, *115* (22), 10125-10138.

- (191) Hu, Y.; Zhang, Z.; Zhang, J.; Liu, Y.; Gridnev, I. D.; Zhang, W., Cobalt-Catalyzed Asymmetric Hydrogenation of C=N Bonds Enabled by Assisted Coordination and Nonbonding Interactions. *Angew. Chem. Int. Ed.* **2019**, *58* (44), 15767-15771.
- (192) Xu, L.; Hilton, M. J.; Zhang, X.; Norrby, P.-O.; Wu, Y.-D.; Sigman, M. S.; Wiest, O., Mechanism, Reactivity, and Selectivity in Palladium-Catalyzed Redox-Relay Heck Arylations of Alkenyl Alcohols. *J. Am. Chem. Soc.* **2014**, *136* (5), 1960-1967.
- (193) Hopmann, K. H.; Bayer, A., Enantioselective imine hydrogenation with iridium-catalysts: Reactions, mechanisms and stereocontrol. *Coord. Chem. Rev.* **2014**, *268*, 59-82.
- (194) Zhang, Z.; Butt, N. A.; Zhou, M.; Liu, D.; Zhang, W., Asymmetric Transfer and Pressure Hydrogenation with Earth-Abundant Transition Metal Catalysts. *Chin. J. Chem.* **2018**, *36* (5), 443-454.
- (195) Smith, S. A. M.; Prokopchuk, D. E.; Morris, R. H., Asymmetric Transfer Hydrogenation of Ketones Using New Iron(II) (P-NH-N-P') Catalysts: Changing the Steric and Electronic Properties at Phosphorus P'. *Isr. J. Chem.* **2017**, *57* (12), 1204-1215.
- (196) Shevlin, M.; Friedfeld, M. R.; Sheng, H.; Pierson, N. A.; Hoyt, J. M.; Campeau, L.-C.; Chirik, P. J., Nickel-Catalyzed Asymmetric Alkene Hydrogenation of α,β -Unsaturated Esters: High-Throughput Experimentation-Enabled Reaction Discovery, Optimization, and Mechanistic Elucidation. *J. Am. Chem. Soc.* **2016**, *138* (10), 3562-3569.
- (197) Hu, Y.; Chen, J.; Li, B.; Zhang, Z.; Gridnev, I. D.; Zhang, W., Nickel-Catalyzed Asymmetric Hydrogenation of 2-Amidoacrylates. *Angew. Chem. Int. Ed.* **2020**, *59* (13), 5371-5375.
- (198) Friedfeld, M. R.; Margulieux, G. W.; Schaefer, B. A.; Chirik, P. J., Bis(phosphine)-cobalt Dialkyl Complexes for Directed Catalytic Alkene Hydrogenation. *J. Am. Chem. Soc.* **2014**, *136* (38), 13178-13181.
- (199) Zhong, H.; Friedfeld, M. R.; Chirik, P. J., Syntheses and Catalytic Hydrogenation Performance of Cationic Bis(phosphine) Cobalt(I) Diene and Arene Compounds. *Angew. Chem. Int. Ed.* **2019**, *58* (27), 9194-9198.

Paper I

Rhodium-Catalyzed Hydrocarboxylation: Mechanistic Analysis Reveals
Unusual Transition State for Carbon–Carbon Bond Formation

Ljiljana Pavlovic, Janakiram Vaitla, Annette Bayer and Kathrin H. Hopmann

Organometallics, **2018**, 37, 941–948.

Paper II

To bind or not to bind: Mechanistic insights into C–CO₂ bond formation
with late transition metals

Diego García-López, **Ljiljana Pavlovic** and Kathrin H. Hopmann

Organometallics, **2020**, *39*, *8*, 1339-1347.

To Bind or Not to Bind: Mechanistic Insights into C–CO₂ Bond Formation with Late Transition Metals

Diego García-López, Ljiljana Pavlovic, and Kathrin H. Hopmann*

Cite This: *Organometallics* 2020, 39, 1339–1347

Read Online

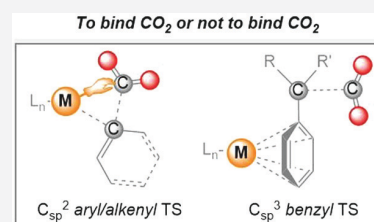
ACCESS |

Metrics & More

Article Recommendations

Supporting Information

ABSTRACT: In transition metal-mediated carboxylation reactions, CO₂ inserts into a metal–nucleophile bond. At the carboxylation transition state (TS), CO₂ may interact with the metal (*inner*-sphere path) or may insert without being activated by the metal (*outer*-sphere path). Currently, there is no consensus as to which path prevails. In order to establish general predictions for the insertion of CO₂ into metal–carbon bonds, we computationally analyze a series of experimentally reported Cu, Rh, and Pd complexes. Our focus is on carboxylation of aromatic substrates, including C_{sp}³ *benzyl* and C_{sp}² *aryl* and *alkenyl* nucleophiles. We observe clear trends, where the nature of the nucleophile determines the preferred path: benzylic C_{sp}³ nucleophiles favor *outer*-sphere and C_{sp}² systems favor *inner*-sphere CO₂ insertion into the metal–carbon bond. An exception are Cu–benzyl bonds, where *inner*- and *outer*-sphere CO₂ insertions are found to be competitive, highlighting the need to include both paths in mechanistic studies and in the rationalization of experimental results. For insertion into Pd–C_{sp}² bonds, we find that the metal–CO₂ interactions at the TS are weak and may be beyond 3 Å for sterically congested ligands. Nonetheless, on the basis of a comparison to other TSs, we argue that the CO₂ insertion into Pd–C_{sp}² bonds should be classified as *inner*-sphere.



INTRODUCTION

Carbon dioxide has the potential to become a versatile building block in organic synthesis.^{1–6} Carboxylation of organic molecules with CO₂ can be catalyzed by transition metals, with good yields for a wide variety of compounds.^{1,2,6} A number of mechanistic studies have been performed on metal-mediated C–CO₂ bond formation,^{7–22} and on the basis of these, the observed mechanisms can be divided into two classes:^{23,24} those that involve metal–CO₂ interactions at the C–C bond formation transition state (TS, *inner*-sphere pathways) and those that do not (*outer*-sphere pathways, Figure 1).

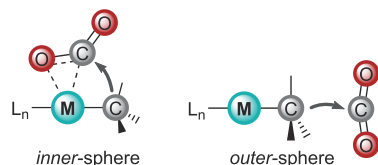


Figure 1. Mechanisms for C–CO₂ bond formation.

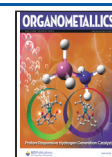
Knowledge about the intimate behavior of CO₂ during C–C bond formation is of importance for at least two reasons. First, as CO₂ is an inert molecule, it may be expected that metal–CO₂ interactions at the TS are needed to polarize and activate CO₂.²⁵ The lack of such interactions would then render CO₂ less active. Interestingly, for some CO₂ hydrogenations, where mechanistic studies predicted an *outer*-sphere path, it has been shown that Lewis acid additives enhance the reaction rate,

possibly by binding and activating the free CO₂ molecule.²⁶ Insights into the intrinsic behavior of CO₂ can thus help to rationalize and predict the effect of additives. Second, in carboxylations involving prochiral nucleophiles, the configuration of the generated chiral center may depend on the mode of CO₂ insertion. Once the diastereomeric metal–nucleophile intermediate is formed, *inner*-sphere CO₂ insertion would retain a given configuration, whereas *outer*-sphere insertion would prompt an inversion. It is relevant to note that there have been relatively few asymmetric C–CO₂ bond formations reported,^{6,27–30} often with low to medium enantiomeric excesses (ee's). It is tempting to speculate that the low ee's in some cases may originate from the inability to restrict the CO₂ molecule to one of the two possible insertion paths. An understanding of how CO₂ behaves could support the design of systems that clearly favor one insertion mode, resulting in better enantioselectivities.

To date, there is no clear consensus as to which pathway, *inner* or *outer*, generally is preferred for C–CO₂ bond formation with late transition metals. For sp² and benzylic sp³ nucleophiles, various complexes based on e.g. Cu, Rh, or Pd have been studied computationally, and it was concluded

Received: February 9, 2020

Published: April 3, 2020



that these systems proceed via *inner*-sphere CO₂ insertion,^{21,23,31–37} but alternative *outer*-sphere paths were not always tested. Actually, for Rh–COD-catalyzed C–C bond formation with benzylic substrates, we recently showed a strong preference for *outer*-sphere insertion.⁷ A review on the behavior of group 9 and 10 metals in CO₂ insertion reactions with a variety of metal–X complexes (X = H, OR, NR₂, CR₃) concluded that systems with low nucleophilicity, including metal–alkyl nucleophiles, prefer *outer*-sphere paths.²⁴ However, only few metal–alkyl examples following this trend were identified, among them Ni and Pd complexes with allylic or nonbenzylic C_{sp}³ nucleophiles.^{9–11} Unfortunately, for many computational studies, it is unclear if both CO₂ insertion modes were evaluated. Further, it is uncertain if the often encountered practice of truncating computational models may have an effect on the mechanistic outcome.

In this work, the prerequisite of a metal–CO₂ interaction for C–CO₂ bond formation is analyzed computationally for a series of experimentally reported examples involving late transition metals: Cu, Rh, and Pd. These metals represent groups 9–11, and they were chosen due to their successful performance in many C–CO₂ bond formations.^{30,38–44} The selected examples also represent a variety of well-known ligands, with monodentate NHC, bidentate phosphine, or tridentate pincer ligands. Our focus is on C–CO₂ bond formation with aromatic substrates, including C_{sp}³ *benzyl* and C_{sp}² *aryl* and *alkenyl* nucleophiles, with all calculations performed on full molecular models.

COMPUTATIONAL DETAILS

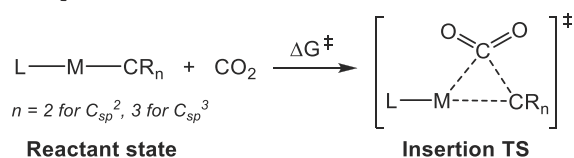
Models. All calculations were carried out employing full molecular models (Table S1), without truncations or symmetry constraints. A closed-shell description of the electronic structure was employed for all systems.

Computational Methods. Quantum mechanical calculations were performed within the framework of density functional theory (DFT)⁴⁵ by employing Gaussian 09, Rev. D01.⁴⁶ Unless specifically indicated otherwise, the B3LYP^{47,48} functional and the Grimme empirical dispersion correction D3^{49,50} and the implicit IEFPCM⁵¹ solvent model were used for geometry optimizations to locate either minima or first-order saddle points (transition states). The nature of the stationary points encountered was characterized by means of harmonic vibrational frequency analysis. All transition metals were described with a Stuttgart/Dresden SDD basis set with the associated pseudopotential,^{52,53} while the rest of the atoms were described with 6-31++G(d,p).^{54–58} This basis set combination is here referred to as BS1.

Energies. Electronic single point energies were computed with basis set BS2, comprising 6-311++G(2d,2p)^{57,59–61} (nonmetal atoms) and SDD(f)⁶² (metal atoms). Temperature corrections (*T*_{corr}) were applied in order to match the experimental reaction conditions. The final Gibbs free energies (1 atm standard state) are computed as

$$G = G_{\text{BS1}} - E_{\text{BS1}} + E_{\text{BS2}} + T_{\text{corr}}$$

Free energy barriers (ΔG^\ddagger) for the CO₂ insertion TSs are calculated relative to a reactant state composed of the metal–alkyl and free CO₂.



For Rh–C_{sp}² systems, a metal–(alkyl)(CO₂) adduct was more stable than the reactant with free CO₂; in this case, barriers are calculated with respect to the adduct.

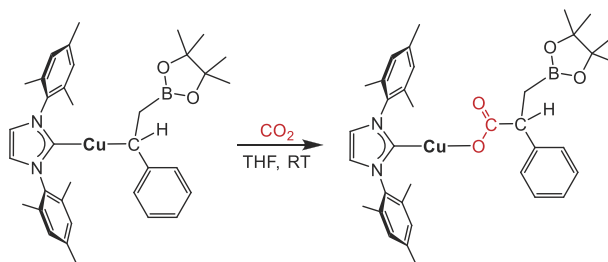
RESULTS AND DISCUSSION

From the literature, we selected Cu, Rh, and Pd complexes that were reported to promote CO₂ insertion into metal–C_{sp}³ or –C_{sp}² bonds. In order to be able to isolate the effect of the carbon nucleophile on the CO₂ insertion path, complexes with similar ligands were chosen for the two kinds of nucleophiles. A compilation of studied reactions is given in the Table S1 in the Supporting Information. The following discussion is structured on the basis of the studied metal, with a subdivision based on the type of nucleophile, *benzyl* or *aryl/alkenyl*.

Copper-Based Benzylic C_{sp}³ Nucleophiles. The coupling of diborane compounds with CO₂ in the presence of Cu can lead to selective boracarboxylation of alkynes,⁶³ alkenes,³⁸ and aldehydes.⁶⁴ The group of Popp and co-workers followed this strategy to functionalize vinylarenes employing NHCs as a Cu ligand to obtain single constitutional isomers.³⁸ The proposed mechanism involves the formation of a borylcuprate species that inserts the vinylarene into the Cu–B bond.⁶⁵ This step was proposed to be rate limiting and to determine the regioselectivity of the following carboxylation of the formed benzylic carbon.^{36,65} In experiments, the NHC ligands IPr and IMes showed different performances, with observed yields of the desired carboxylation product of 17% and 85%, respectively.³⁸ Analysis of the carboxylation barriers with various NHCs pointed to the conclusion that both the electronic and steric natures of the NHC affect the nucleophilicity of the alkyl.⁶⁵ However, only *inner*-sphere CO₂ insertion was considered in the computational evaluations.^{36,65}

Here we studied the *inner*- and *outer*-sphere CO₂ insertion into the Cu–benzyl intermediate formed in the carboxylation of styrene (Scheme 1).³⁸ Our computations include three

Scheme 1. Computed CO₂ Insertion Step in the Cu–NHC-Catalyzed Boracarboxylation of Styrene^a



^aThe experimental reaction was originally reported in ref 38.

different NHCs: the experimentally studied IPr and IMes ligands³⁸ and the *N*-methyl analogue IMe, which has a reduced steric environment (Figures 2 and 3). The results show a substantial preference (2.5 kcal/mol) for *inner*-sphere carboxylation for the smallest IMe ligand, a weaker *inner*-sphere preference (1.3 kcal/mol) for IMes, and a preference for *outer*-sphere insertion (1.6 kcal/mol) for IPr, the largest ligand (Figure 2). The three studied NHCs can be assumed to have small differences in electron donation ability (with the order IMe < IMes ≤ IPr),⁶⁶ and therefore we suggest that the differences in barriers and insertion paths mainly should be

	Cu-IMe	Cu-IMes	Cu-IPr
$\Delta G^\ddagger_{inner}$	16.4	18.8	22.0
$\Delta G^\ddagger_{outer}$	18.9	20.1	20.4

Figure 2. Computed barriers (kcal/mol, 298 K) for carboxylation of NHC–Cu–benzyl complexes.

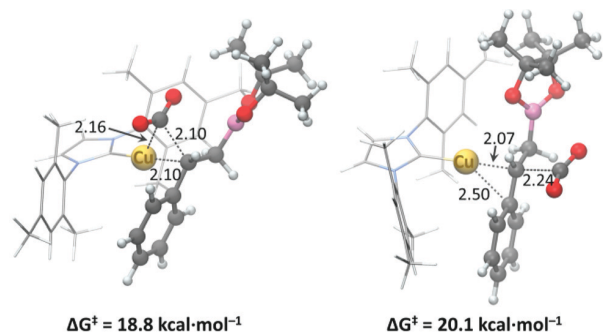


Figure 3. Optimized TSs for *inner*- (left) and *outer*-sphere (right) carboxylations of a benzylic intermediate in the Cu–IMes-catalyzed boracarboxylation (THF, 298 K). Distances are given in Å.

ascribed to sterics. It can be noted that, as the NHC ligand is enlarged, the barriers rise for both the *inner*- and the *outer*-sphere CO_2 insertions. The barrier increase caused by sterics is larger for *inner*-sphere insertion, which intuitively makes sense, eventually leading to preferred *outer*-sphere insertion.

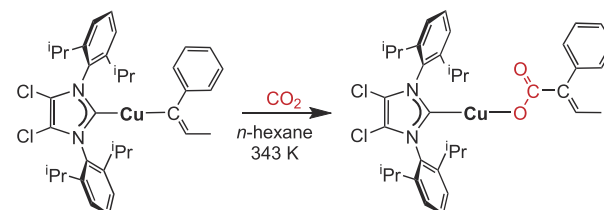
In order to support the preference for *outer*-sphere CO_2 insertion for large NHC ligands, we find it instructive to discuss a related system. Recently, we investigated the Cu–IPr-mediated carboxylation of organoboranes,⁶⁷ a reaction originally reported by Skrydstrup, Nielsen, and co-workers.³⁹ This transformation involves a Cu–benzyl species, which inserts CO_2 (reaction 2 in Table S1 and Figure S1). In our earlier study, a full molecular model was evaluated with DFT (ωB97XD) and DLPNO-CCSD(T), including solvent and temperature (393 K) corrections. Both levels of theory favored an *outer*-sphere path, by respectively 1.8 and 0.3 kcal/mol. Here, we have repeated these calculations with the B3LYP-D3 protocol and again find a small preference for *outer*-sphere CO_2 insertion by 1.0 kcal/mol (393 K). The results obtained for CO_2 insertion into Cu–benzyl bonds are thus consistent across different computational models and methods.

The small differences in barrier for *inner*-sphere versus *outer*-sphere CO_2 insertion for NHC–copper–benzyl species indicate that both pathways are competitive in experiments. This leads to two important conclusions. First, for Cu–NHC complexes, both *inner*- and *outer*-sphere CO_2 insertion should always be evaluated in mechanistic studies. Second, Cu–NHC systems may not be promising for stereoselective carboxylations, because the competing *inner*- and *outer*-sphere TSs would provide opposite configurations. For example, the Cu–NHC-catalyzed bora- and hydrocarboxylations both form products with chiral centers (Scheme 1 and Table S1, reaction 2), making development of an asymmetric version of these reactions desirable.^{38,39} However, even if a chiral NHC ligand may strongly favor one of the two diastereomeric Cu–benzyl intermediates, the subsequent CO_2 insertion would give low

ee's, if both *inner*- and *outer*-sphere insertion takes place. For example, the barrier difference of 1.0 kcal/mol computed for reaction 2 (Table S1) would imply an ee of only 56% (393 K).⁶⁸

Copper-Based Alkenyl and Aryl C_{sp^2} Nucleophiles. Cu–NHC-catalyzed hydrocarboxylation of alkynes to α,β -unsaturated carboxylic acids employing hydrosilane as a mild reducing agent was developed by Tsuji and co-workers (Scheme 2).⁴⁰ The authors reported that symmetric bis-

Scheme 2. Computed CO_2 Insertion Step in the Cu-Catalyzed Hydrocarboxylation of Alkynes^a



^aThe experimental reaction was originally reported in ref 40.

substituted acetylene derivatives afford the corresponding *E* isomers of the carboxylic acid. A proposed mechanism was analyzed computationally by means of DFT, employing a truncated catalyst.³⁴ The four computationally studied substrates all displayed the same regioselectivity, which was stated to be determined after the insertion of the alkyne substrate into the Cu–hydride bond of the active catalyst.³⁴ For the subsequent C– CO_2 bond formation, an *inner*-sphere path was reported.

We studied the carboxylation of the Cu–alkenyl intermediate computationally and succeeded in optimizing both the *inner*- and *outer*-sphere TSs with a full model, using Cl_2IPr as ligand and an alkenyl derived from 1-phenyl-1-propyne (Figure 4).⁶⁹ The angle of the CO_2 molecule at the *outer*-sphere

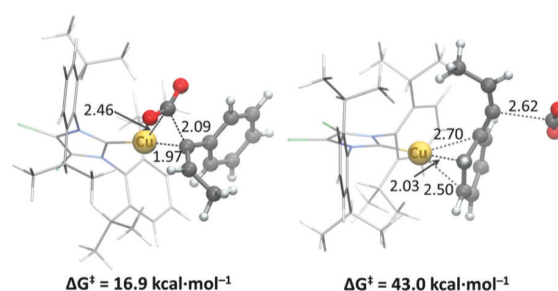


Figure 4. Optimized TS geometries for *inner*- (left) and *outer*-sphere (right) CO_2 insertion into a Cu–alkenyl intermediate (*n*-hexane, 343 K). Distances are given in Å.

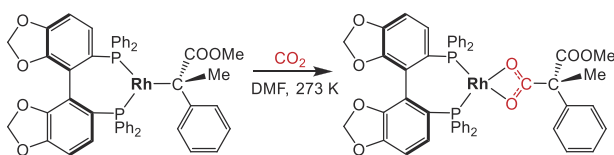
(167°) and *inner*-sphere (144.5°) TS indicates that CO_2 is experiencing considerably more activation in the latter. The computed *outer*-sphere barrier of 43.0 kcal/mol is impossible to overcome at a reaction temperature of 70°C , whereas 16.9 kcal/mol for the *inner*-sphere insertion should be very feasible (up to 29 kcal/mol may be considered viable⁷⁰). It can be noted that the carboxylation barrier does not necessarily represent the overall reaction barrier, as other steps may be rate limiting. However, here we are concerned only with the preferred CO_2 insertion mode, and the results clearly show

that, for this Cu–alkenyl species, the *inner*-sphere path is favored by 26.1 kcal/mol over *outer*-sphere insertion.

A Cu–IPr complex was also used by Hou and co-workers in the catalytic synthesis of arylcarboxylic acids from arylboronic esters (Table S1, reaction 4).⁴¹ Also other organoboronic esters such as vinylic moieties were converted into the corresponding α,β -unsaturated acids. The mechanism was studied computationally by Marder, Lin, and co-workers,³² and an *inner*-sphere TS was reported for a catalyst model, wherein the bulky IPr arms were replaced by Me groups. As shown above (Figure 2), such a truncation may affect the steric constraints and the preferred CO₂ insertion path. Therefore, we studied the full IPr ligand with two experimental substrates, 4-methoxyphenyl and 4-methoxystyrene (Table S1, reactions 4a,b, and Figure S2).⁴¹ As for the truncated catalyst model, our computations on the full model provide the *inner*-sphere CO₂ insertion path for both the *aryl* and the *alkenyl* C_{sp}² nucleophiles, with identical barriers of 15.2 kcal/mol (343 K). All attempts to obtain *outer*-sphere TSs for these systems failed. On the basis of the three examples discussed here, a strong preference for *inner*-sphere CO₂ insertion is apparent for Cu–IPr-mediated carboxylations of C_{sp}² nucleophiles, which is in contrast to the dual pathways observed for benzylic C_{sp}³ nucleophiles.

Rhodium-Based Benzyl C_{sp}³ Nucleophiles. Regioselective rhodium-catalyzed hydrocarboxylation of styrene derivatives and α,β -unsaturated carbonyl compounds was described by the group of Mikami.³⁰ Use of 1,5-cyclooctadiene (COD) as a ligand and ZnEt₂ as an additive afforded α -aryl carboxylic acids in good yields. Moreover, asymmetric induction was successfully achieved in moderate yields with (*S*)-SEGPHOS as a chiral ligand. The proposed catalytic cycle involves transmetalation of an ethyl moiety from ZnEt₂ to Rh, followed by β -hydride elimination. Substrate insertion into the Rh–H bond comprises the next step, and its subsequent coupling to CO₂ renders the carboxylated product (Scheme 3).

Scheme 3. Carboxylation Step in the Rh–(*S*)-SEGPHOS-Catalyzed Hydrocarboxylation of Methyl 2-Phenylacrylate^a



^aThe experimental reaction was originally reported in ref 30.

The Rh–COD-catalyzed hydrocarboxylation was recently investigated by our group.⁷ Computational examination of several substrates supported the proposed mechanism but revealed a strong preference for *outer*-sphere CO₂ insertion. Here we analyzed if these findings also apply if COD is exchanged with the diphosphine ligand (*S*)-SEGPHOS (Table S1, reaction 5). Our results for the substrate methyl 2-phenylacrylate support the preference for an *outer*-sphere CO₂ insertion by a margin of 17.0 kcal/mol ($\Delta G^\ddagger = 15.6$ for *outer*-sphere vs 32.6 kcal/mol for *inner*-sphere insertion; Figure 5). As observed in our previous study,⁷ the *outer*-sphere TS is characterized by an unusual binding mode of the substrate toward the metal center, with η^6 coordination of the phenyl ring (Figure 5, right). It can be noted that the shown *outer*-sphere TS gives the *S* product, whereas the *R* conformer of the

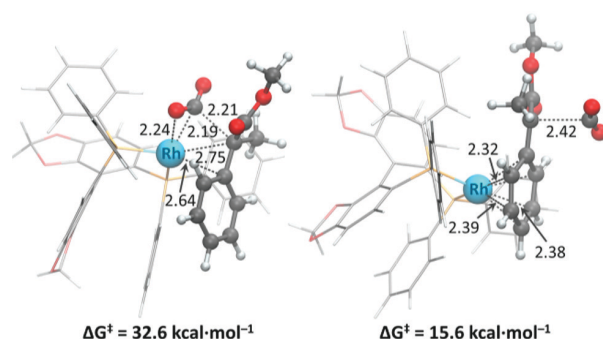


Figure 5. Optimized TSs for *inner*- (left) and *outer*-sphere (right) carboxylation of methyl 2-phenylacrylate with Rh–(*S*)-SEGPHOS (273 K, DMF). Distances are given in Å.

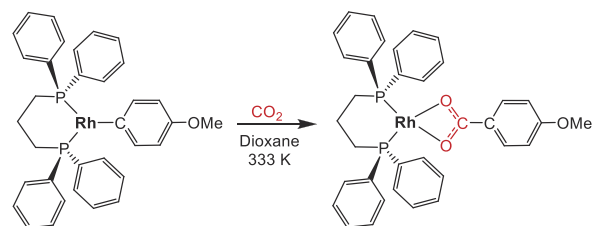
outer-sphere TS is 1.2 kcal/mol higher in energy (Figure S3). The barrier difference corresponds to a computed ee of 80% *S* at 273 K for the studied methyl ester, which is in good agreement with experiments on a related ethyl ester, affording an ee of 60% *S* at 273 K.³⁰ The agreement supports that the *outer*-sphere TS proposed here is operative for Rh–SEGPHOS-catalyzed carboxylations.

A relevant consideration for all *outer*-sphere TSs is whether the CO₂ molecule at the TS may be able to interact with another component in the reaction mixture, for example a Lewis acid additive.²⁶ For the Rh–benzyl system, we have previously shown that CO₂ does not interact with the additive ZnEt₂.⁷ Another possibility may be that CO₂ at the TS interacts with a second Rh complex. We have tested this here for carboxylation of COD–Rh–benzyl. However, the interaction of CO₂ with another Rh complex increases the insertion barrier from 14.4 to 32.4 kcal/mol (273 K, PBE-D2; see the Supporting Information for optimized coordinates and ref 7 for the full computational protocol). This is in line with results indicating that a bimetallic CO₂ insertion mechanism is not beneficial for sterically hindered metal complexes.⁷¹

Rhodium-Based Alkenyl and Aryl C_{sp}² Nucleophiles.

Carboxylation of aryl- and alkenylboronic esters with Rh in the presence of 1,3-bis(diphenylphosphino)propane (dppp) was described by the group of Iwasawa.⁴² The proposed carboxylation mechanism suggests that CO₂ inserts into the rhodium–nucleophile bond (Scheme 4). Kantchev, Qin, and co-workers have studied this reaction using DFT.³³ The results support the suggested mechanism and predict that CO₂ binds to Rh prior to its insertion into the Rh–C bond. With dppp as a ligand, the computed barrier for *inner*-sphere CO₂ insertion was 12.7 kcal/mol (333 K).

Scheme 4. CO₂ Insertion Step in the Rh–dppp-Catalyzed Carboxylation of Arylboronic Esters^a

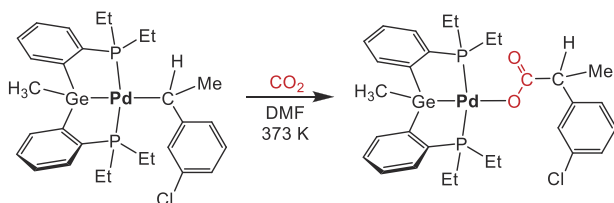


^aThe experimental reaction was originally reported in ref 42.

We have here used 4-methoxyphenyl and 4-methoxystyrene as *aryl* and *alkenyl* C_{sp^2} nucleophiles, respectively, to revisit the carboxylation step (Table S1, reactions 6a,b). These substrates were experimentally studied by Iwasawa and co-workers, with respectively Rh-(dppp) and Rh-(*p*-MeO-dppp) as catalysts.⁴² For both systems, our calculations support that CO₂ coordinates to Rh in a $\eta^2(C,O)$ mode prior to insertion, forming an energetically low lying adduct. The *inner*-sphere barriers with respect to the adducts are 11.2 kcal/mol (4-methoxyphenyl) and 13.3 kcal/mol (4-methoxystyrene, 333 K; Figure S4). As for the Cu- C_{sp^2} systems above, attempts to obtain *outer*-sphere TSs for these Rh complexes failed, possibly due to geometric and orbital constraints that make an *outer*-sphere insertion inaccessible for C_{sp^2} nucleophiles.

Palladium-Based Benzylic C_{sp^3} Nucleophiles. The group of Iwasawa reported regioselective synthesis of α -branched propionic acid derivatives via Pd-pincer(^{Et}PGeP)-catalyzed hydrocarboxylation of styrenes, using a formate salt as both a reductant and a CO₂ source.⁴³ The proposed mechanism suggests that the coordination of formate to the palladium catalyst leads to decarboxylation and generation of a hydride species. Insertion of the styrene into the Pd-H bond produces a Pd-benzyl species, which can react with the released CO₂ to give a palladium-carboxylate complex (Scheme 5).

Scheme 5. Carboxylation of a ^{Et}PGeP-Pd-Benzyl Intermediate in the Hydrocarboxylation of a Substituted Styrene^a



^aThe experimental reaction was originally reported in ref 43.

A DFT study of the Pd-catalyzed carboxylation of unsubstituted styrene has been reported.³⁵ *Inner*-sphere CO₂ insertion into the Pd-benzyl complex was suggested to be rate-determining; however, an *outer*-sphere path was not considered. Here, we performed a computational evaluation of both the *inner*- and *outer*-sphere pathways for this reaction, employing 3-chlorostyrene as substrate, which is experimentally active, in contrast to unsubstituted styrene.⁴³ First, we tried to coordinate CO₂ to the Pd complex. However, the relative energy of the adduct is rather high, 38.6 kcal/mol (Figure S5), indicating that CO₂ coordination will not occur. We then optimized the TSs for insertion of CO₂ into the Pd-benzyl bond. Interestingly, for our model, *outer*-sphere CO₂ insertion is preferred by 7.2 kcal/mol ($\Delta G^\ddagger = 19.8$ kcal/mol for *outer*-sphere vs $\Delta G^\ddagger = 27.0$ kcal/mol for *inner*-sphere, 373 K, Figure 6). The geometry around the Ge-Me moiety in the preferred conformations of the two TSs is worth noting. Whereas the *outer*-sphere insertion TS minimizes the steric hindrance between Ge-Me and 3-chlorostyrene, the *inner*-sphere TS reduces the repulsion between Ge-Me and CO₂ (Figure 6). At the *outer*-sphere TS, the benzylic nucleophile coordinates in an η^2 mode to Pd, in contrast to the η^1 interaction at the *inner*-sphere TS. Indeed, a pattern is seen

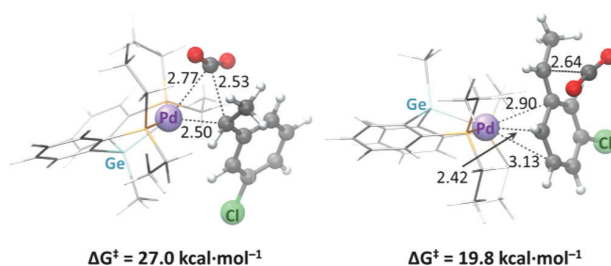


Figure 6. Optimized TSs for *inner*- (left) and *outer*-sphere (right) carboxylation of 3-chlorostyrene with a ^{Et}PGeP-Pd complex (DMF, 373 K). Distances are given in Å.

for all metal-benzyl complexes studied here, where *outer*-sphere TSs show more interactions between the metal and nucleophile (η^2 , η^3 , or η^6 binding) in comparison to *inner*-sphere TSs (η^1 or η^2 , Figures 3, 5, and 6). The stronger substrate coordination may be contributing to lower the energy of the *outer*-sphere TS.

The combined results for the Pd-, Rh-, and Cu-benzyl systems studied here indicate that *outer*-sphere CO₂ insertion in many cases may be preferred for metal-benzyl complexes or, at minimum, may be competitive with *inner*-sphere insertion. This conclusion is in contrast with previous studies reporting *inner*-sphere CO₂ insertion for Pd and Cu with benzylic nucleophiles.^{35,36,65}

Palladium-Based Alkenyl C_{sp^2} Nucleophiles. There appear to be few reported carboxylations of Pd-alkenyl systems; however, the group of Iwasawa has reported one such reaction, involving activation of a vinylic C-H bond of 2-hydroxystyrenes (Table S1, reaction 8).⁴⁴ The isolated X-ray structure of a key Pd-alkenyl intermediate showed that two substrates coordinate to the metal: one of them acts as a neutral ligand, whereas the other has undergone C-H activation to become an alkenyl (Figure 7). The OH groups

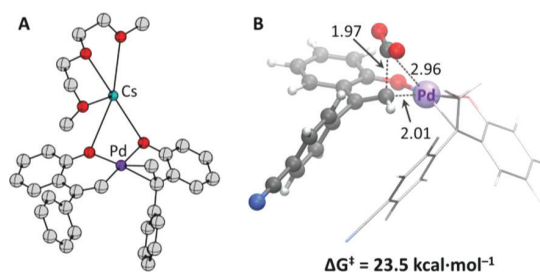


Figure 7. (A) Reported X-ray structure of a Pd-alkenyl complex formed from $H_2C=CRR'$, where R = 2-hydroxyphenyl and R' = phenyl.⁴⁴ Cs is coordinated by diglyme solvent. (B) CO₂ insertion TS computed here for a related Pd-alkenyl species (see main text).

of both substrates are deprotonated and coordinated to Pd, as well as to a Cs counterion present in solution. Here we studied the carboxylation of the Pd-alkenyl complex formed from the substrate that performed best in the reported experiments, $H_2C=CRR'$, where R = 2-hydroxyphenyl and R' = 4-cyanophenyl.⁴⁴ The computations (which were performed without Cs present⁷²) lead to the identification of a single TS, with a barrier of 23.5 kcal/mol (Figure 7). Analysis of the geometry revealed a Pd-C_{CO₂} distance of 2.96 Å, which appears significantly longer than the metal-C_{CO₂} distances found for other C_{sp^2} carboxylation TSs computed here (up to

2.20 Å for Rh–C_{sp}² TSs and up to 2.70 Å for Cu–C_{sp}² TSs, Table S2).

In order to evaluate if the long metal–C_{CO}₂ distance is a general feature of CO₂ insertion into Pd–C_{sp}² bonds, we designed four virtual alkenyl systems on the basis of experimentally known Pd–pincer complexes (for optimized TS geometries see Figures S6–S9). In all cases, the alkenyl nucleophile was derived from 1-phenyl-1-propyne, in analogy to the Cu–C_{sp}² system studied above (Scheme 2). The first virtual Pd–C_{sp}² complex is based on the experimentally known Et^tPGeP ligand (used in the carboxylation of styrene derivatives⁴³), which also was employed in the Pd–C_{sp}³ case above (Scheme 5). The Pd–C_{CO}₂ distance of 2.74 Å at the carboxylation TS is the shortest computed here for a Pd–C_{sp}² complex (Figure 8), which may be due to the flexible Et

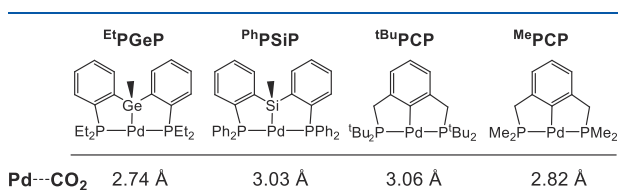


Figure 8. Pd–CO₂ distances at the carboxylation TS of pincer Pd–alkenyl complexes (for optimized geometries see Figures S6–S9).

substituents. The second virtual Pd–C_{sp}² complex features the experimentally known PhPSiP ligand, which has been used in allene carboxylations.⁷³ The congestion caused by the Ph substituents repulses the approaching CO₂, resulting in a metal–C_{CO}₂ distance of 3.03 Å. The third virtual Pd–C_{sp}² complex features the experimentally known tBuPCP ligand (used in carboxylation of Pd–allyl and –methyl groups).¹⁰ The tBu substituents on this complex do not allow a close approach of CO₂, which results in a metal–C_{CO}₂ distance of 3.06 Å, the longest computed here (Figure 8). Out of curiosity, we made a fourth complex, where the tBu groups were truncated to methyl groups to reduce steric hindrance. In comparison to tBuPCP, the metal–C_{CO}₂ distance for the MePCP complex is shorter but remains as much as 2.82 Å (Figure 8).

We did not study an experimental Pd–aryl case here, such as the seminal Pd-catalyzed carboxylation of aryl-bromides reported by Martin and co-workers,⁷⁴ due to the size and complexity of the ligand that was used. However, for comparison to the alkenyl case, we computationally studied a tBuPCP–Pd–phenyl complex (Figure S10). The obtained carboxylation TS shows a Pd–C_{CO}₂ distance of 2.97 Å, similar to those for the Pd–alkenyl systems (Figure 8). However, the computed barrier of 41.7 kcal/mol (298 K) indicates that this complex may not be reactive, in line with results by Wendt and co-workers.⁷⁵

It can be concluded that the six optimized Pd–C_{sp}² TSs show similar geometric features: for example, O=C=O angles of 143–149° and metal–C_{CO}₂ distances of 2.82–3.06 Å (Table 1). However, a question is how these TSs should be classified. Table 1 shows that there is relatively poor similarity to *outer*-sphere TSs computed here but better similarity to other *inner*-sphere TSs. We conclude that the Pd–C_{sp}² TSs may be classified as *inner*-sphere, despite the relatively long metal–C_{CO}₂ distances. It needs to be kept in mind that all Pd–C_{sp}² complexes discussed here have fully saturated coordina-

Table 1. Range of Selected Geometric Parameters for *Inner*- and *Outer*-Sphere CO₂ Insertion TSs in Comparison to Pd–C_{sp}² Systems

	O=C=O (deg)	C _{CO} ₂ –C _{Nu} –M (deg) ^a	M–C _{CO} ₂ (Å) ^a
<i>outer</i> -sphere TSs ^b	147–163	124–146	4.04–5.93
<i>inner</i> -sphere TSs ^c	138–152	51–82	2.16–2.76
Pd–C _{sp} ² TSs ^d	143–149	75–96	2.82–3.06

^aM = metal. ^bBased on 8 *outer*-sphere TSs in Table S2. ^cBased on 11 *inner*-sphere TSs in Table S2, not including Pd–C_{sp}². ^dBased on 6 Pd–C_{sp}² TSs in Table S2.

tion spheres, with four ligands prior to insertion of CO₂, which may explain the low propensity of the metal to interact with CO₂. Therefore, the results for less coordinated Pd species may differ. For example, in the reported geometry for a Pd-catalyzed decarboxylation of aryls, the complex has three ligands in addition to CO₂, which allows for a smaller Pd–C_{CO}₂ distance (2.58 Å) and a pronounced Pd–O_{CO}₂ interaction (2.05 Å),³⁷ not observed in any of the Pd complexes studied here.

CONCLUSIONS

The mechanistic details of transition metal-catalyzed C–CO₂ bond formations were computationally examined for a series of experimentally reported Cu, Rh, and Pd systems involving C_{sp}³ benzyl and C_{sp}² alkenyl or aryl nucleophiles.

For benzylic C_{sp}³ nucleophiles, we show that the studied Pd– and Rh–benzyl complexes strongly favor *outer*-sphere CO₂ insertion. The *outer*-sphere TSs reduce sterics between CO₂ and the metal ligands and allow for stronger coordination of the benzylic substrates to the metal, which may contribute to the observed preference for *outer*-sphere insertion. For four studied Cu–benzyl complexes, our results indicate that large NHC ligands promote a slight preference for *outer*-sphere paths, but as the ligand is reduced, *inner*-sphere insertion becomes equally accessible and eventually favored. Several previous DFT studies reported only *inner*-sphere insertion for carboxylation of Cu– and Pd–benzyl complexes,^{35,36,65} but our study of these complexes shows that *outer*-sphere insertion is equal or lower in barrier. These results highlight that *outer*-sphere pathways need to be included in mechanistic studies of metal–benzyl carboxylations.

For 11 experimental and virtual metal–C_{sp}² complexes based on Cu, Rh, and Pd, our results suggest that CO₂ insertion occurs via an *inner*-sphere pathway, which is in line with previous computational results on Cu– and Rh–C_{sp}² systems.^{21,32–34} For a series of Pd–alkenyl complexes, we show that the CO₂ insertion TSs feature rather weak Pd–CO₂ interactions; however, these TSs should nonetheless be classified as *inner*-sphere.

It has to be kept in mind that our conclusions may be valid only for the studied complexes: e.g., Cu–NHCs, Rh–diphosphine and Rh–dialkenes, and Pd–pincer and Pd–alkoxide complexes. Further studies are needed to show if the mechanistic trends observed here are universal for carboxylation reactions involving late transition metals.

■ ASSOCIATED CONTENT**SI Supporting Information**

The Supporting Information is available free of charge at <https://pubs.acs.org/doi/10.1021/acs.organomet.0c00090>.

Overview of the studied reactions and additional geometrical parameters and figures of computed TSs (PDF)

Optimized coordinates (XYZ)

■ AUTHOR INFORMATION**Corresponding Author**

Kathrin H. Hopmann – Hylleraas Centre for Quantum Molecular Sciences, Department of Chemistry, UiT The Arctic University of Norway, N-9037 Tromsø, Norway; orcid.org/0000-0003-2798-716X; Email: kathrin.hopmann@uit.no

Authors

Diego García-López – Hylleraas Centre for Quantum Molecular Sciences, Department of Chemistry, UiT The Arctic University of Norway, N-9037 Tromsø, Norway

Ljiljana Pavlovic – Hylleraas Centre for Quantum Molecular Sciences, Department of Chemistry, UiT The Arctic University of Norway, N-9037 Tromsø, Norway

Complete contact information is available at: <https://pubs.acs.org/doi/10.1021/acs.organomet.0c00090>

Notes

The authors declare no competing financial interest.

■ ACKNOWLEDGMENTS

This work has been supported by the Research Council of Norway (Centre of Excellence Grant No. 262695), by the Tromsø Research Foundation (Grant No. TFS2016KHH), by NordForsk (Grant No. 85378), and by Notur-The Norwegian Metacenter for Computational Science through grants of computer time (Nos. nn9330k and nn4654k).

■ REFERENCES

- (1) Cokoja, M.; Bruckmeier, C.; Rieger, B.; Herrmann, W. A.; Kühn, F. E. Transformation of Carbon Dioxide with Homogeneous Transition-Metal Catalysts: A Molecular Solution to a Global Challenge? *Angew. Chem., Int. Ed.* **2011**, *50*, 8510–8537.
- (2) Tortajada, A.; Juliá-Hernández, F.; Börjesson, M.; Moragas, T.; Martin, R. Transition-Metal-Catalyzed Carboxylation Reactions with Carbon Dioxide. *Angew. Chem., Int. Ed.* **2018**, *57*, 15948–15982.
- (3) Dabral, S.; Schaub, T. The Use of Carbon Dioxide (CO₂) as a Building Block in Organic Synthesis from an Industrial Perspective. *Adv. Synth. Catal.* **2019**, *361*, 223–246.
- (4) Yang, Y.; Lee, J.-W. Toward Ideal Carbon Dioxide Functionalization. *Chem. Sci.* **2019**, *10*, 3905–3926.
- (5) Darensbourg, D. J. Chemistry of Carbon Dioxide Relevant to Its Utilization: A Personal Perspective. *Inorg. Chem.* **2010**, *49*, 10765–10780.
- (6) Vaitla, J.; Guttormsen, Y.; Mannisto, J. K.; Nova, A.; Repo, T.; Bayer, A.; Hopmann, K. H. Enantioselective Incorporation of CO₂: Status and Potential. *ACS Catal.* **2017**, *7*, 7231–7244.
- (7) Pavlovic, Lj.; Vaitla, J.; Bayer, A.; Hopmann, K. H. Rhodium-Catalyzed Hydrocarboxylation: Mechanistic Analysis Reveals Unusual Transition State for Carbon–Carbon Bond Formation. *Organometallics* **2018**, *37*, 941–948.
- (8) Vummaleti, S. V. C.; Talarico, G.; Nolan, S. P.; Cavallo, L.; Poater, A. How Easy Is CO₂ Fixation by M–C Bond Containing Complexes (M = Cu, Ni, Co, Rh, Ir)? *Org. Chem. Front.* **2016**, *3*, 19–23.

(9) Lau, K.-C.; Petro, B. J.; Bontemps, S.; Jordan, R. F. Comparative Reactivity of Zr– and Pd–Alkyl Complexes with Carbon Dioxide. *Organometallics* **2013**, *32*, 6895–6898.

(10) Johnson, M. T.; Johansson, R.; Kondrashov, M. V.; Steyl, G.; Ahlquist, M. S. G.; Roodt, A.; Wendt, O. F. Mechanisms of the CO₂ Insertion into (PCP) Palladium Allyl and Methyl σ -Bonds. A Kinetic and Computational Study. *Organometallics* **2010**, *29*, 3521–3529.

(11) Schmeier, T. J.; Hazari, N.; Incarvito, C. D.; Raskatov, J. A. Exploring the Reactions of CO₂ with PCP Supported Nickel Complexes. *Chem. Commun.* **2011**, *47*, 1824–1826.

(12) Fan, T.; Chen, X.; Lin, Z. Theoretical Studies of Reactions of Carbon Dioxide Mediated and Catalysed by Transition Metal Complexes. *Chem. Commun.* **2012**, *48*, 10808–10828.

(13) Vummaleti, S. V. C.; Talarico, G.; Nolan, S. P.; Cavallo, L.; Poater, A. Mechanism of CO₂ Fixation by Ir^I–X Bonds (X = OH, OR, N, C). *Eur. J. Inorg. Chem.* **2015**, *2015*, 4653–4657.

(14) Sayyed, F. B.; Tsuji, Y.; Sakaki, S. The Crucial Role of a Ni(I) Intermediate in Ni-Catalyzed Carboxylation of Aryl Chloride with CO₂: A Theoretical Study. *Chem. Commun.* **2013**, *49*, 10715–10717.

(15) Jover, J.; Maseras, F. Computational Characterization of the Mechanism for Coinage-Metal-Catalyzed Carboxylation of Terminal Alkynes. *J. Org. Chem.* **2014**, *79*, 11981–11987.

(16) Yang, L.; Yuan, Y.; Wang, H.; Zhang, N.; Hong, S. Theoretical Insights into Copper(I)–NHC-Catalyzed C–H Carboxylation of Terminal Alkynes with CO₂: The Reaction Mechanisms and the Roles of NHC. *RSC Adv.* **2014**, *4*, 32457–32466.

(17) Yuan, R.; Lin, Z. Mechanism for the Carboxylative Coupling Reaction of a Terminal Alkyne, CO₂, and an Allylic Chloride Catalyzed by the Cu(I) Complex: A DFT Study. *ACS Catal.* **2014**, *4*, 4466–4473.

(18) Ostapowicz, T. G.; Hölscher, M.; Leitner, W. CO₂ Insertion into Metal–Carbon Bonds: A Computational Study of Rh^I Pincer Complexes. *Chem. - Eur. J.* **2011**, *17*, 10329–10338.

(19) Ostapowicz, T. G.; Hölscher, M.; Leitner, W. Catalytic Hydrocarboxylation of Olefins with CO₂ and H₂ – a DFT Computational Analysis. *Eur. J. Inorg. Chem.* **2012**, *2012*, 5632–5641.

(20) Schmeier, T. J.; Nova, A.; Hazari, N.; Maseras, F. Synthesis of PCP-Supported Nickel Complexes and Their Reactivity with Carbon Dioxide. *Chem. - Eur. J.* **2012**, *18*, 6915–6927.

(21) Fan, T.; Sheong, F. K.; Lin, Z. DFT Studies on Copper-Catalyzed Hydrocarboxylation of Alkynes Using CO₂ and Hydrosilanes. *Organometallics* **2013**, *32*, 5224–5230.

(22) Wang, Q.; Guo, C.-H.; Ren, Y.; Wu, H.-S. A Computational Study on the Insertion of CO₂ into (PSiP)Palladium Allyl σ -Bond. *J. Mol. Model.* **2015**, *21*, 122.

(23) Obst, M.; Pavlovic, Lj.; Hopmann, K. H. Carbon–Carbon Bonds with CO₂: Insights from Computational Studies. *J. Organomet. Chem.* **2018**, *864*, 115–127.

(24) Hazari, N.; Heimann, J. E. Carbon Dioxide Insertion into Group 9 and 10 Metal–Element σ Bonds. *Inorg. Chem.* **2017**, *56*, 13655–13678.

(25) Leitner, W. The Coordination Chemistry of Carbon Dioxide and Its Relevance for Catalysis: A Critical Survey. *Coord. Chem. Rev.* **1996**, *153*, 257–284.

(26) Heimann, J. E.; Bernskoetter, W. H.; Hazari, N.; Mayer, J. M. Acceleration of CO₂ Insertion into Metal Hydrides: Ligand, Lewis Acid, and Solvent Effects on Reaction Kinetics. *Chem. Sci.* **2018**, *9*, 6629–6638.

(27) Takimoto, M.; Nakamura, Y.; Kimura, K.; Mori, M. Highly Enantioselective Catalytic Carbon Dioxide Incorporation Reaction: Nickel-Catalyzed Asymmetric Carboxylative Cyclization of Bis-1,3-Dienes. *J. Am. Chem. Soc.* **2004**, *126*, 5956–5957.

(28) Dian, L.; Müller, D. S.; Marek, I. Asymmetric Copper-Catalyzed Carbomagnesiation of Cyclopropenes. *Angew. Chem., Int. Ed.* **2017**, *56*, 6783–6787.

(29) Gui, Y.-Y.; Hu, N.; Chen, X.-W.; Liao, L.; Ju, T.; Ye, J.-H.; Zhang, Z.; Li, J.; Yu, D.-G. Highly Regio- and Enantioselective Copper-Catalyzed Reductive Hydroxymethylation of Styrenes and 1,3-Dienes with CO₂. *J. Am. Chem. Soc.* **2017**, *139*, 17011–17014.

- (30) Kawashima, S.; Aikawa, K.; Mikami, K. Rhodium-Catalyzed Hydrocarboxylation of Olefins with Carbon Dioxide. *Eur. J. Org. Chem.* **2016**, *2016*, 3166–3170.
- (31) Xue, L.; Su, W.; Lin, Z. Mechanism of Silver- and Copper-Catalyzed Decarboxylation Reactions of Aryl Carboxylic Acids. *Dalton Trans.* **2011**, *40*, 11926–11936.
- (32) Dang, L.; Lin, Z.; Marder, T. B. DFT Studies on the Carboxylation of Arylboronate Esters with CO₂ Catalyzed by Copper(I) Complexes. *Organometallics* **2010**, *29*, 917–927.
- (33) Qin, H.-L.; Han, J.-B.; Hao, J.-H.; Kantchev, E. A. B. Computational and Experimental Comparison of Diphosphane and Diene Ligands in the Rh-Catalyzed Carboxylation of Organoboron Compounds with CO₂. *Green Chem.* **2014**, *16*, 3224–3229.
- (34) Wang, Q.; Jia, J.-F.; Guo, C.-H.; Wu, H.-S. Mechanistic Investigation of Cu(I)-Mediated Three-Component Domino Reaction of Asymmetrical Alkynes with Carbon Dioxide: Theoretical Rationale for the Regioselectivity. *J. Organomet. Chem.* **2013**, *748*, 84–88.
- (35) Lv, X.; Huang, F.; Wu, Y.-B.; Lu, G. Origin of Ligand Effects on Reactivities of Pincer-Pd Catalyzed Hydrocarboxylation of Allenes and Alkenes with Formate Salts: A Computational Study. *Catal. Sci. Technol.* **2018**, *8*, 2835–2840.
- (36) Lin, S.; Lin, Z. DFT Studies on the Mechanism of Copper-Catalyzed Boracarboxylation of Alkene with CO₂ and Diboron. *Organometallics* **2019**, *38*, 240–247.
- (37) Xue, L.; Su, W.; Lin, Z. A DFT Study on the Pd-Mediated Decarboxylation Process of Aryl Carboxylic Acids. *Dalton Trans.* **2010**, *39*, 9815–9822.
- (38) Butcher, T. W.; McClain, E. J.; Hamilton, T. G.; Perrone, T. M.; Kroner, K. M.; Donohoe, G. C.; Akhmedov, N. G.; Petersen, J. L.; Popp, B. V. Regioselective Copper-Catalyzed Boracarboxylation of Vinyl Arenes. *Org. Lett.* **2016**, *18*, 6428–6431.
- (39) Juhl, M.; Laursen, S. L. R.; Huang, Y.; Nielsen, D. U.; Daasbjerg, K.; Skrydstrup, T. Copper-Catalyzed Carboxylation of Hydroborated Disubstituted Alkenes and Terminal Alkynes with Cesium Fluoride. *ACS Catal.* **2017**, *7*, 1392–1396.
- (40) Fujihara, T.; Xu, T.; Semba, K.; Terao, J.; Tsuji, Y. Copper-Catalyzed Hydrocarboxylation of Alkynes Using Carbon Dioxide and Hydrosilanes. *Angew. Chem., Int. Ed.* **2011**, *50*, 523–527.
- (41) Ohishi, T.; Nishiura, M.; Hou, Z. Carboxylation of Organoboronic Esters Catalyzed by N-Heterocyclic Carbene Copper(I) Complexes. *Angew. Chem., Int. Ed.* **2008**, *47*, 5792–5795.
- (42) Ukai, K.; Aoki, M.; Takaya, J.; Iwasawa, N. Rhodium(I)-Catalyzed Carboxylation of Aryl- and Alkenylboronic Esters with CO₂. *J. Am. Chem. Soc.* **2006**, *128*, 8706–8707.
- (43) Takaya, J.; Miyama, K.; Zhu, C.; Iwasawa, N. Metallic Reductant-Free Synthesis of α -Substituted Propionic Acid Derivatives through Hydrocarboxylation of Alkenes with a Formate Salt. *Chem. Commun.* **2017**, *53*, 3982–3985.
- (44) Sasano, K.; Takaya, J.; Iwasawa, N. Palladium(II)-Catalyzed Direct Carboxylation of Alkenyl C–H Bonds with CO₂. *J. Am. Chem. Soc.* **2013**, *135*, 10954–10957.
- (45) Parr, R. G.; Yang, W. *Density Functional Theory of Atoms and Molecules*; Oxford University Press: 1989.
- (46) Frisch, M. J.; Trucks, G. W.; Schlegel, H. B.; Scuseria, G. E.; Robb, M. A.; Cheeseman, J. R.; Scalmani, G.; Barone, V.; Mennucci, B.; Petersson, G. A.; Nakatsuji, H.; Caricato, M.; Li, X.; Hratchian, H. P.; Izmaylov, A. F.; Bloino, J.; Zheng, G.; Sonnenberg, J. L.; Hada, M.; Ehara, M.; Toyota, K.; Fukuda, R.; Hasegawa, J.; Ishida, M.; Nakajima, T.; Honda, Y.; Kitao, O.; Nakai, H.; Vreven, T.; Montgomery, J. A., Jr.; Peralta, J. E.; Ogliaro, F.; Bearpark, M.; Heyd, J. J.; Brothers, E.; Kudin, K. N.; Staroverov, V. N.; Kobayashi, R.; Normand, J.; Raghavachari, K.; Rendell, A.; Burant, J. C.; Iyengar, S. S.; Tomasi, J.; Cossi, M.; Rega, N.; Millam, J. M.; Klene, M.; Knox, J. E.; Cross, J. B.; Bakken, V.; Adamo, C.; Jaramillo, J.; Gomperts, R.; Stratmann, R. E.; Yazyev, O.; Austin, A. J.; Cammi, R.; Pomelli, C.; Ochterski, J. W.; Martin, R. L.; Morokuma, K.; Zakrzewski, V. G.; Voth, G. A.; Salvador, P.; Dannenberg, J. J.; Dapprich, S.; Daniels, A. D.; Farkas, O.; Foresman, J. B.; Ortiz, J. V.; Cioslowski, J.; Fox, D. J. *Gaussian 09, rev. D.01*; Gaussian, Inc.: Wallingford, CT, 2013.
- (47) Becke, A. D. Density-functional Thermochemistry. III. The Role of Exact Exchange. *J. Chem. Phys.* **1993**, *98*, 5648–5652.
- (48) Lee, C.; Yang, W.; Parr, R. G. Development of the Colle-Salvetti Correlation-Energy Formula into a Functional of the Electron Density. *Phys. Rev. B: Condens. Matter Mater. Phys.* **1988**, *37*, 785–789.
- (49) Grimme, S.; Antony, J.; Ehrlich, S.; Krieg, H. A Consistent and Accurate Ab Initio Parametrization of Density Functional Dispersion Correction (DFT-D) for the 94 Elements H–Pu. *J. Chem. Phys.* **2010**, *132*, 154104–154119.
- (50) Grimme, S.; Ehrlich, S.; Goerigk, L. Effect of the Damping Function in Dispersion Corrected Density Functional Theory. *J. Comput. Chem.* **2011**, *32*, 1456–1465.
- (51) Scalmani, G.; Frisch, M. J. Continuous Surface Charge Polarizable Continuum Models of Solvation. I. General Formalism. *J. Chem. Phys.* **2010**, *132*, 114110–114115.
- (52) Dolg, M.; Wedig, U.; Stoll, H.; Preuss, H. Energy-adjusted Ab Initio Pseudopotentials for the First Row Transition Elements. *J. Chem. Phys.* **1987**, *86*, 866–872.
- (53) Andrae, D.; Häußermann, U.; Dolg, M.; Stoll, H.; Preuß, H. Energy-adjusted *ab initio* pseudopotentials for the second and third row transition elements. *Theor. Chim. Acta* **1990**, *77*, 123–141.
- (54) Ditchfield, R.; Hehre, W. J.; Pople, J. A. Self-Consistent Molecular-Orbital Methods. IX. An Extended Gaussian-Type Basis for Molecular-Orbital Studies of Organic Molecules. *J. Chem. Phys.* **1971**, *54*, 724–728.
- (55) Hehre, W. J.; Ditchfield, R.; Pople, J. A. Self-Consistent Molecular Orbital Methods. *J. Chem. Phys.* **1972**, *56*, 2257–2261.
- (56) Dill, J. D.; Pople, J. A. Self-consistent Molecular Orbital Methods. XV. Extended Gaussian-type Basis Sets for Lithium, Beryllium, and Boron. *J. Chem. Phys.* **1975**, *62*, 2921–2923.
- (57) Francl, M. M.; Pietro, W. J.; Hehre, W. J.; Binkley, J. S.; Gordon, M. S.; DeFrees, D. J.; Pople, J. A. Self-consistent Molecular Orbital Methods. XXIII. A Polarization-type Basis Set for Second-row Elements. *J. Chem. Phys.* **1982**, *77*, 3654–3665.
- (58) Rassolov, V. A.; Ratner, M. A.; Pople, J. A.; Redfern, P. C.; Curtiss, L. A. 6-31G* Basis Set for Third-Row Atoms. *J. Comput. Chem.* **2001**, *22*, 976–984.
- (59) Spitznagel, G. W.; Clark, T.; von Ragué Schleyer, P.; Hehre, W. J. An Evaluation of the Performance of Diffuse Function-Augmented Basis Sets for Second Row Elements, Na–Cl. *J. Comput. Chem.* **1987**, *8*, 1109–1116.
- (60) Krishnan, R.; Binkley, J. S.; Seeger, R.; Pople, J. A. Self-consistent Molecular Orbital Methods. XX. A Basis Set for Correlated Wave Functions. *J. Chem. Phys.* **1980**, *72*, 650–654.
- (61) McLean, A. D.; Chandler, G. S. Contracted Gaussian Basis Sets for Molecular Calculations. I. Second Row Atoms, Z = 11–18. *J. Chem. Phys.* **1980**, *72*, 5639–5648.
- (62) Ehlers, A. W.; Böhme, M.; Dapprich, S.; Gobbi, A.; Höllwarth, A.; Jonas, V.; Köhler, K. F.; Stegmann, R.; Veldkamp, A.; Frenking, G. A Set of F-Polarization Functions for Pseudo-Potential Basis Sets of the Transition Metals Sc–Cu, Y–Ag and La–Au. *Chem. Phys. Lett.* **1993**, *208*, 111–114.
- (63) Zhang, L.; Cheng, J.; Carry, B.; Hou, Z. Catalytic Boracarboxylation of Alkynes with Diborane and Carbon Dioxide by an N-Heterocyclic Carbene Copper Catalyst. *J. Am. Chem. Soc.* **2012**, *134*, 14314–14317.
- (64) Carry, B.; Zhang, L.; Nishiura, M.; Hou, Z. Synthesis of Lithium Boracarbonate Ion Pairs by Copper-Catalyzed Multi-Component Coupling of Carbon Dioxide, Diboron, and Aldehydes. *Angew. Chem., Int. Ed.* **2016**, *55*, 6257–6260.
- (65) Lv, X.; Wu, Y.-B.; Lu, G. Computational Exploration of Ligand Effects in Copper-Catalyzed Boracarboxylation of Styrene with CO₂. *Catal. Sci. Technol.* **2017**, *7*, 5049–5054.
- (66) Huynh, H. V. Electronic Properties of N-Heterocyclic Carbenes and Their Experimental Determination. *Chem. Rev.* **2018**, *118*, 9457–9492.

(67) Obst, M. F.; Gevorgyan, A.; Bayer, A.; Hopmann, K. H. Mechanistic Insights into Copper-Catalyzed Carboxylations. *Organometallics* **2020**, DOI: 10.1021/acs.organomet.9b00710.

(68) The ee estimate assumes that only one diastereomeric intermediate is formed and that it will react via *inner*- and *outer*-sphere CO₂ insertion (giving opposite configurations) with an energy difference of 1 kcal/mol between the two TSs. However, normally two diastereomeric intermediates are formed in an asymmetric reaction, and each one may react via both *inner*- and *outer*-sphere carboxylation. Thus, the ee for chiral NHCs would be determined by four TSs, not two. Here we have only computed achiral NHCs and can thus only present an estimate based on two TSs.

(69) With Cl₂IPr as ligand, this substrate provided a 75:25 mixture of regioisomers in experiment,⁴⁰ with the major regioisomer exhibiting carboxylation at the phenyl-substituted carbon. The TSs studied here correspond to formation of the major regioisomer.

(70) Ryu, H.; Park, J.; Kim, H. K.; Park, J. Y.; Kim, S.-T.; Baik, M.-H. Pitfalls in Computational Modeling of Chemical Reactions and How To Avoid Them. *Organometallics* **2018**, *37*, 3228–3239.

(71) Arayachukiat, S.; Yingcharoen, P.; Vummaleti, S. V. C.; Cavallo, L.; Poater, A.; Elia, V. D. Cycloaddition of CO₂ to Challenging *N*-Tosyl Aziridines Using a Halogen-Free Niobium Complex: Catalytic Activity and Mechanistic Insights. *Mol. Catal.* **2017**, *443*, 280–285.

(72) Geometry optimizations of a computational model involving Cs and diglyme solvent coordinated to the alkoxide groups (as shown in the X-ray structure, Figure 7) did not converge properly, and Cs and diglyme therefore had to be removed from the model.

(73) Takaya, J.; Iwasawa, N. Hydrocarboxylation of Allenes with CO₂ Catalyzed by Silyl Pincer-Type Palladium Complex. *J. Am. Chem. Soc.* **2008**, *130*, 15254–15255.

(74) Correa, A.; Martín, R. Palladium-catalyzed direct carboxylation of aryl bromides with carbon dioxide. *J. Am. Chem. Soc.* **2009**, *131*, 15974–15975.

(75) Johansson, R.; Jarenmark, M.; Wendt, O. F. Insertion of Carbon Dioxide into (PCP)Pd^{II}–Me Bonds. *Organometallics* **2005**, *24*, 4500–4502.

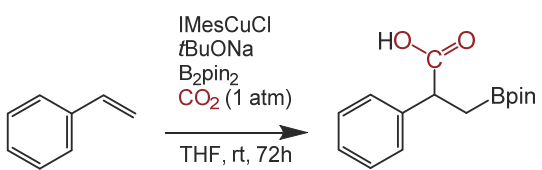
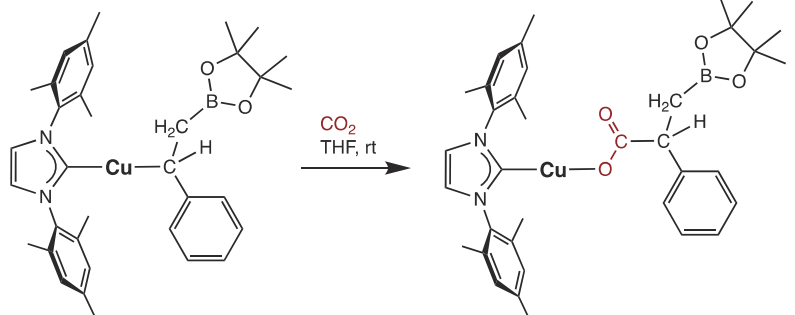
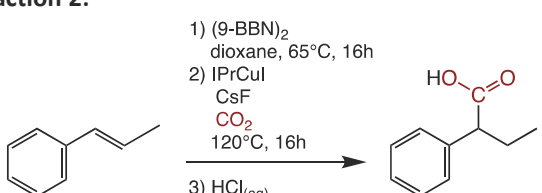
SUPPORTING INFORMATION

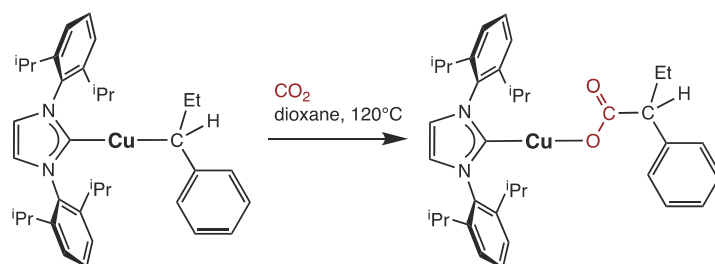
To bind or not to bind: Mechanistic insights into C–CO₂ bond formation with late transition metals

Diego García-López,[†] Ljiljana Pavlovic,[†] Kathrin H. Hopmann*,[†]

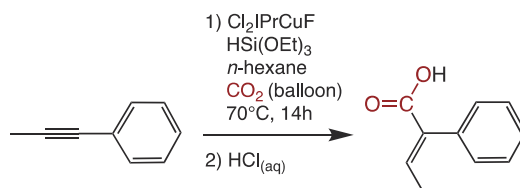
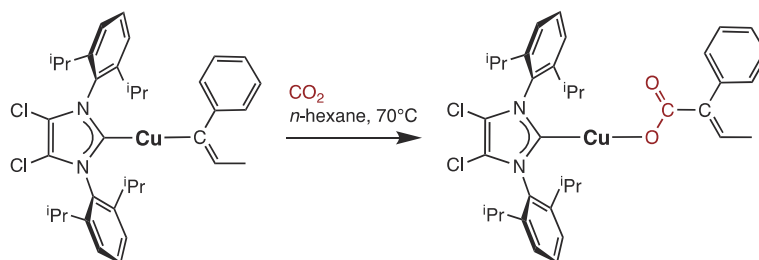
[†]Hylleraas Centre for Quantum Molecular Sciences, Department of Chemistry, UiT The Arctic University of Norway, N9037 Tromsø

Table S1. List of reactions studied computationally here.

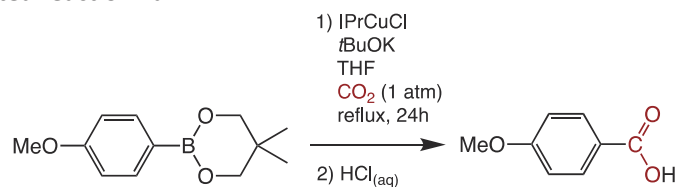
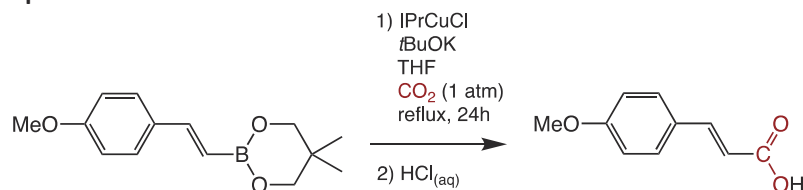
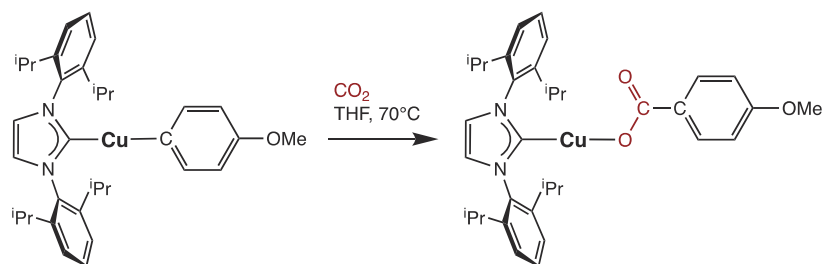
Reaction 1a-c
Experimental reference for reaction 1a-b: Butcher, T. W.; McClain, E. J.; Hamilton, T. G.; Perrone, T. M.; Kroner, K. M.; Donohoe, G. C.; Akhmedov, N. G.; Petersen, J. L.; Popp, B. V., <i>Org. Lett.</i> 2016 , <i>18</i> , 6428.
Experimentally reported reaction 1a:  <p>IMesCuCl tBuONa B₂pin₂ CO₂ (1 atm) THF, rt, 72h</p>
Computed reaction 1a:  <p>CO₂ THF, rt</p>
Computed reaction 1b: As 1a, but with IPr instead of IMes Computed reaction 1c: As 1a, but with IME instead of IMes
Reaction 2
Experimental reference for reaction 2: Juhl, M.; Laursen, S. L. R.; Huang, Y.; Nielsen, D. U.; Daasbjerg, K.; Skrydstrup, T., <i>ACS Catal.</i> 2017 , <i>7</i> , 1392.
Experimentally reported reaction 2:  <p>1) (9-BBN)₂ dioxane, 65°C, 16h 2) IPrCuI CsF CO₂ 120°C, 16h 3) HCl_(aq)</p>

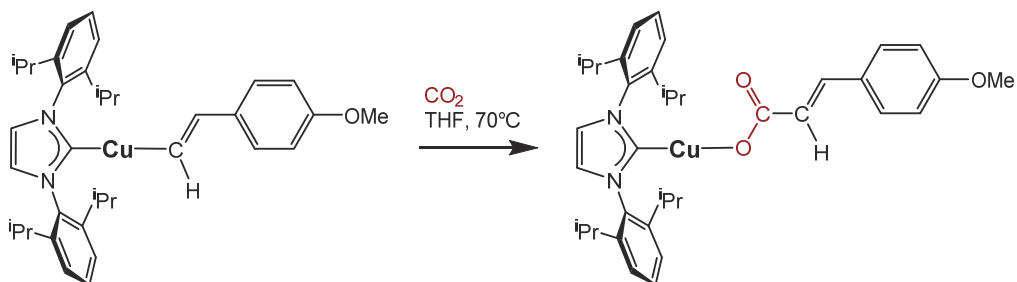
Computed reaction 2:**Reaction 3**

Experimental reference for 3: Fujihara, T.; Xu, T.; Semba, K.; Terao, J.; Tsuji, Y. *Angew. Chemie IE.* **2011**, *50*, 523.

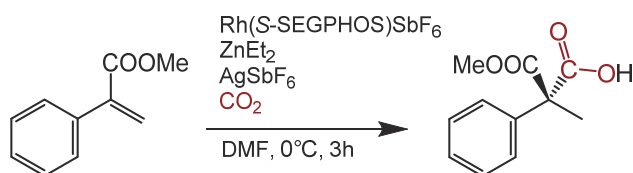
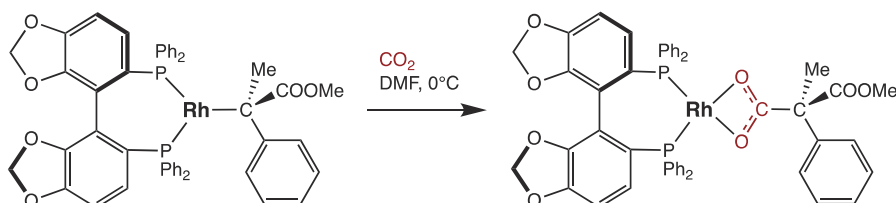
Experimentally reported reaction 3:**Computed reaction 3:****Reactions 4a-b**

Experimental reference reactions 4a-b: Ohishi, T.; Nishiura, M.; Hou, Z., *Angew. Chemie Int. Ed.* **2008**, *47*, 5792.

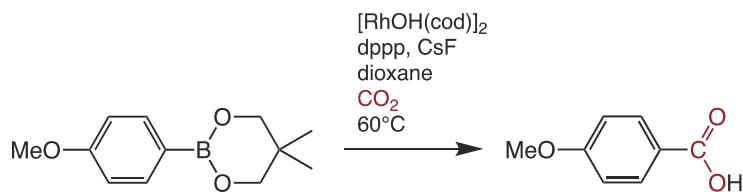
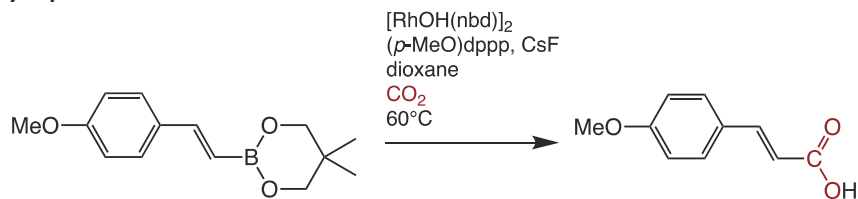
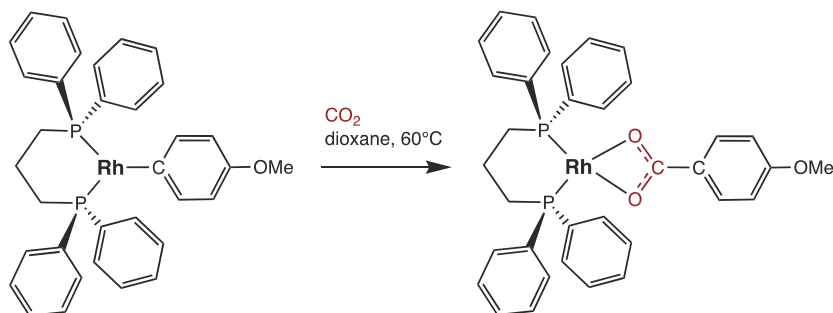
Experimentally reported reaction 4a:**Experimentally reported reaction 4b:****Computed reaction 4a:**

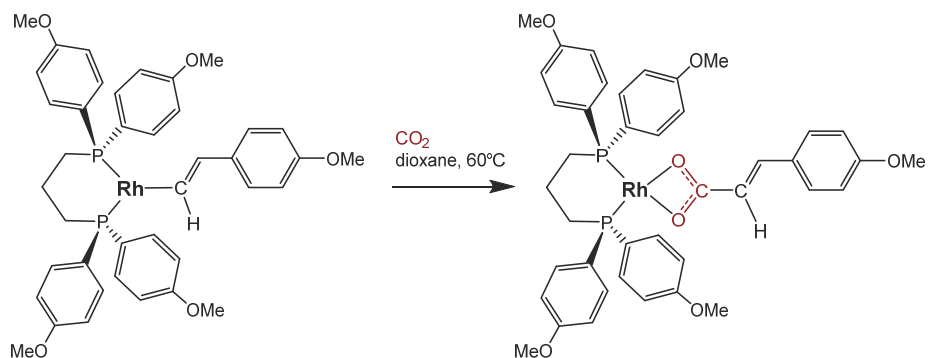
Computed reaction 4b:**Reaction 5**

Experimental reference for reaction 5: Kawashima, S.; Aikawa, K.; Mikami, K., *European J. Org. Chem.* **2016**, 3166.

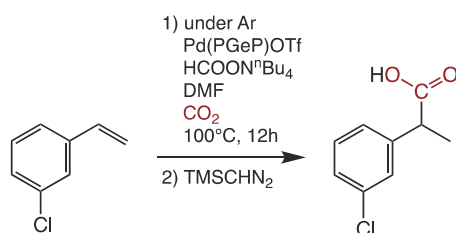
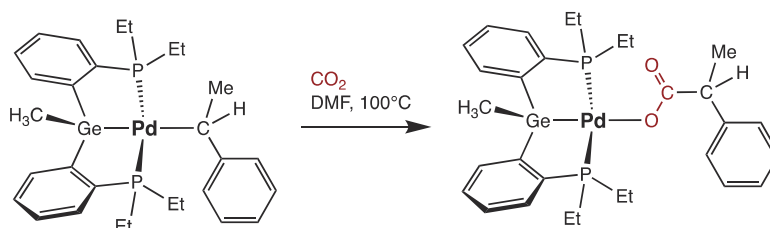
Experimentally reported reaction 5:**Computed reaction 5:****Reactions 6a-b**

Experimental reference for 6a-b: Ukai, K.; Aoki, M.; Takaya, J.; Iwasawa, N., *J. Am. Chem. Soc.* **2006**, 128, 8706.

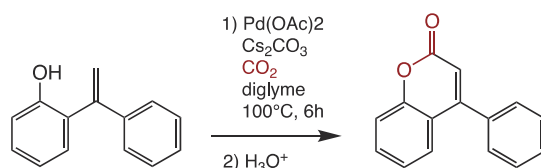
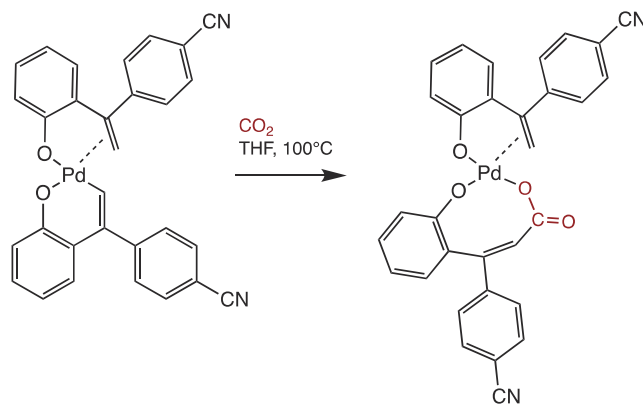
Experimentally reported reaction 6a:**Experimentally reported reaction 6b:****Computed reaction 6a:**

Computed reaction 6b:**Reaction 7**

Experimental reference for 7: Takaya, J.; Miyama, K.; Zhu, C.; Iwasawa, N., *Chem. Commun.* **2017**, 53, 3982.

Experimentally reported reaction 7:**Computed reaction 7:****Reaction 8**

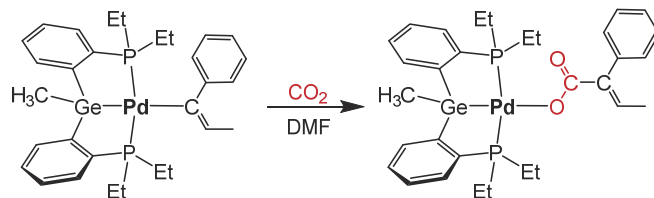
Experimental reference for reaction 8: Sasano, K.; Takaya, J.; Iwasawa, N., *J. Am. Chem. Soc.* **2013**, 135, 10954.

Experimentally reported reaction 8:**Computed reaction 8:**

Reactions 9a-e (virtual reactions)

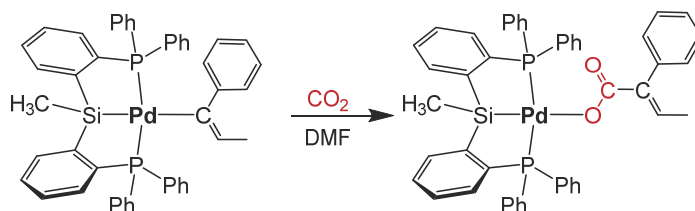
Reference for Pd complex used in 9a: Takaya, J.; Miyama, K.; Zhu, C.; Iwasawa, N. *Chem. Commun.* **2017**, 53, 3982.

Computed reaction 9a:



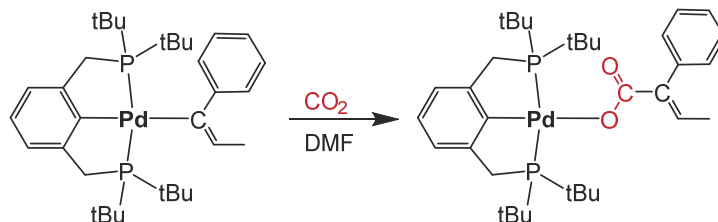
Reference for Pd complex used in 9b: Takaya, J.; Iwasawa, N. *J. Am. Chem. Soc.* **2008**, 130, 15254.

Computed reaction 9b:



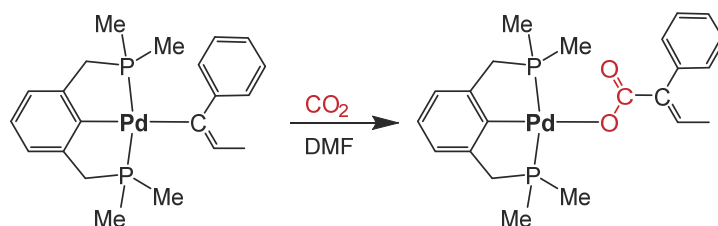
Reference for Pd complex used in 9c: Johnson, M. T.; Johansson, R.; Kondrashov, M. V.; Steyl, G.; Ahlquist, M. S. G.; Roodt, A.; Wendt, O. F. *Organometallics* **2010**, 29, 352.

Computed reaction 9c:



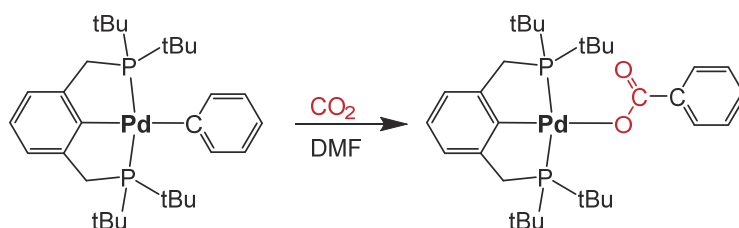
Reference for Pd complex used in 9d: See 9c, but tBu replaced with Me

Computed reaction 9d:



Reference for Pd complex used in 9e: See 9c.

Computed reaction 9e:



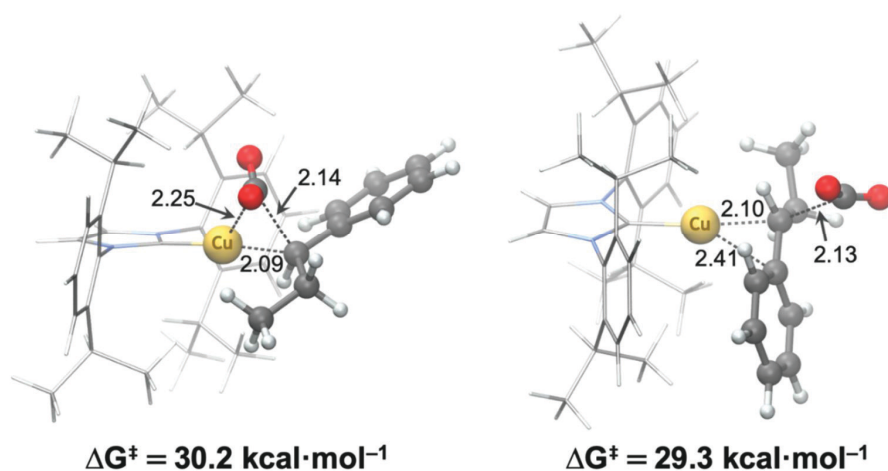


Figure S1. Optimized TS geometries and free energy barriers for *inner* (left) and *outer* (right) sphere CO₂ insertion into a Cu-IPr-benzyl intermediate (393K, 1,4-dioxane). Distances in Å.

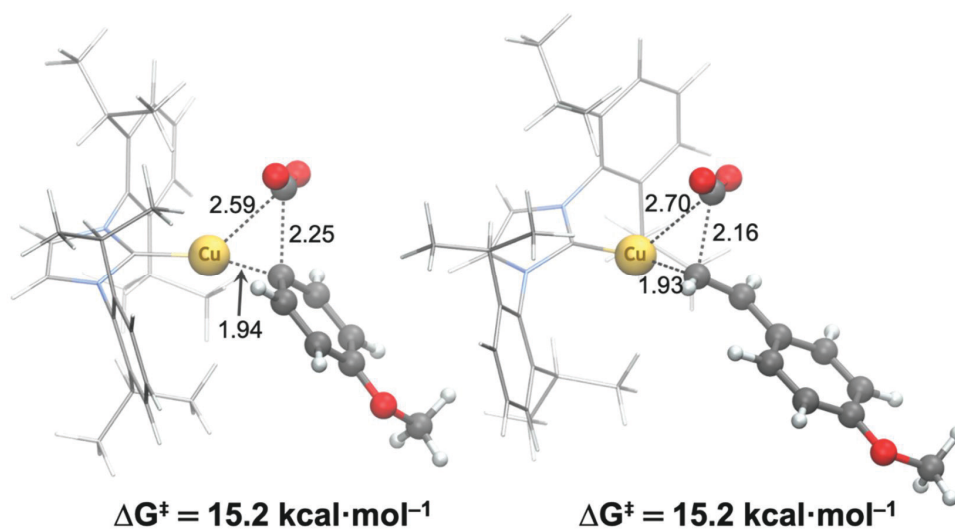


Figure S2. Optimized TS geometries and free energy barriers for *inner* sphere CO₂ insertion into a Cu-IPr-aryl (left) and Cu-IPr-alkenyl (right, 343K, THF). Distances in Å.

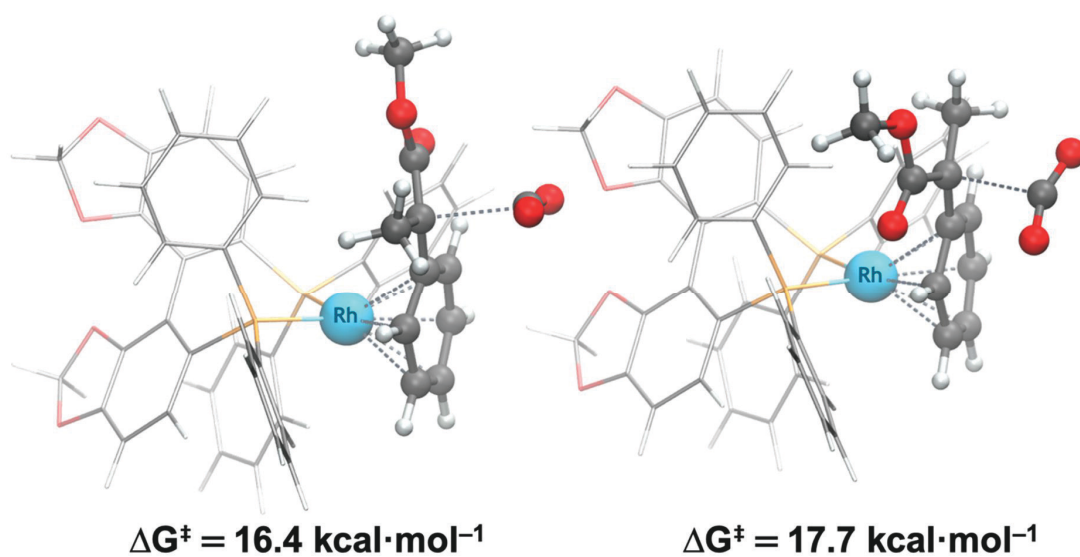


Figure S3. Optimized TS geometries and free energy barriers (DMF, 273 K) for *outer* sphere carboxylations of methyl 2-phenylacrylate with (*S*)-SEGPHOS-Rh leading to formation of the (*S*)-product (left) or the (*R*)-product (right). The barrier difference (including two decimals) is 1.23 kcal/mol, which corresponds to an ee of 80 % (*S*) at 273 K.

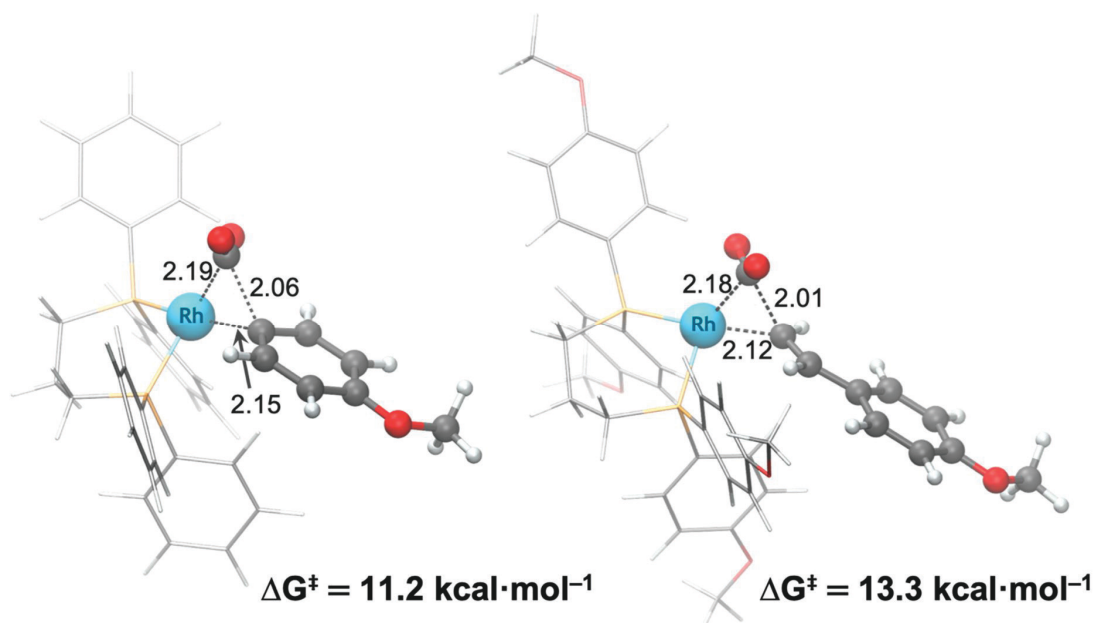


Figure S4. Optimized TS geometries and free energy barriers for *inner* sphere CO₂ insertion into the Rh-C_{sp}² bond formed from 4-methoxyphenyl (left) or 4-methoxystyrene (right, 333K, 1,4-dioxane). Distances in Å.

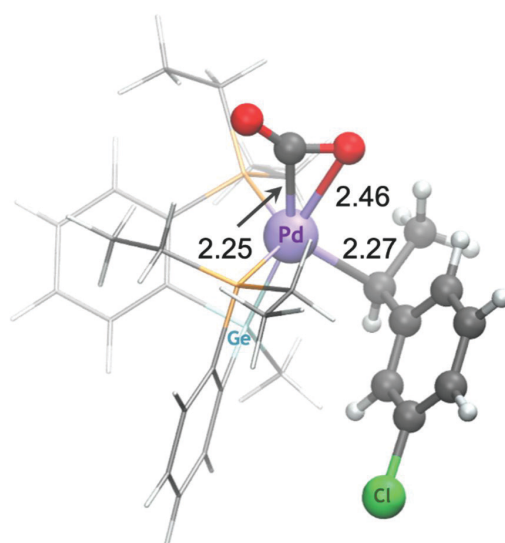


Figure S5. Optimized $\text{EtPGeP-Pd(benzyl)(CO}_2\text{)}$ adduct (DMF).

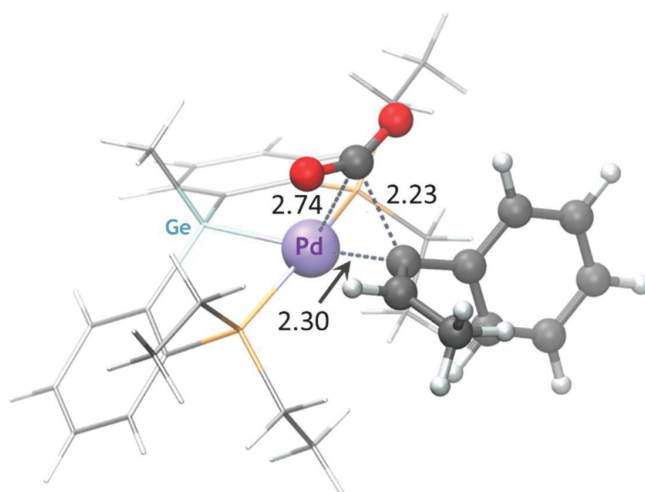


Figure S6. Optimized CO_2 insertion TS for EtPGeP-Pd-alkenyl (DMF). Distances in Å.

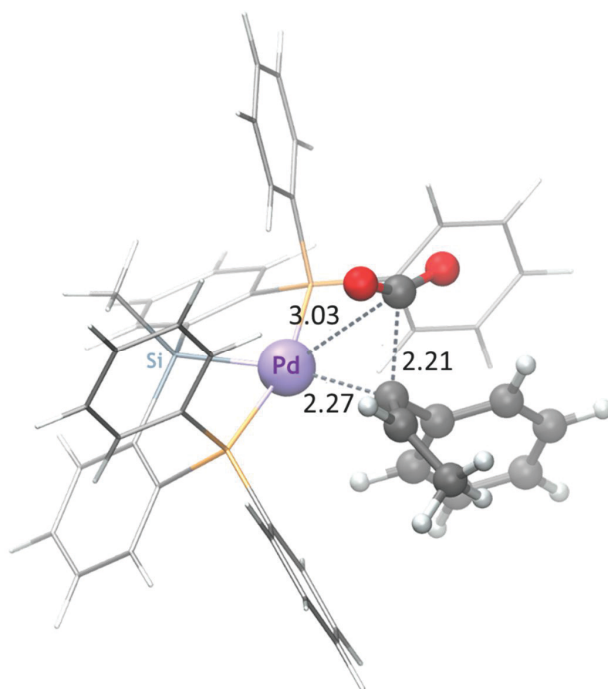


Figure S7. Optimized CO₂ insertion TS for PhPSiP-Pd-alkenyl (DMF). Distances in Å.

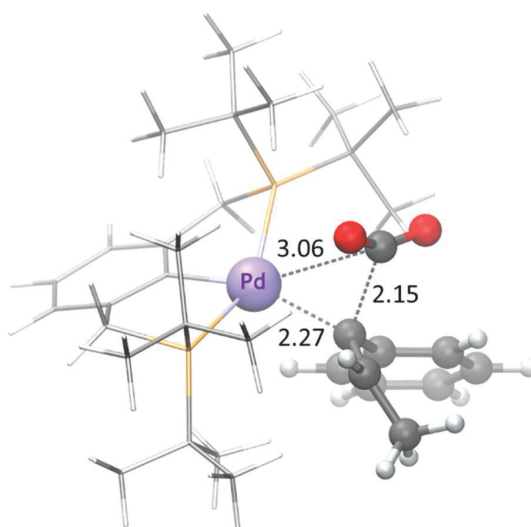


Figure S8. Optimized CO₂ insertion TS for tBuPCP-Pd-alkenyl (DMF). Distances in Å.

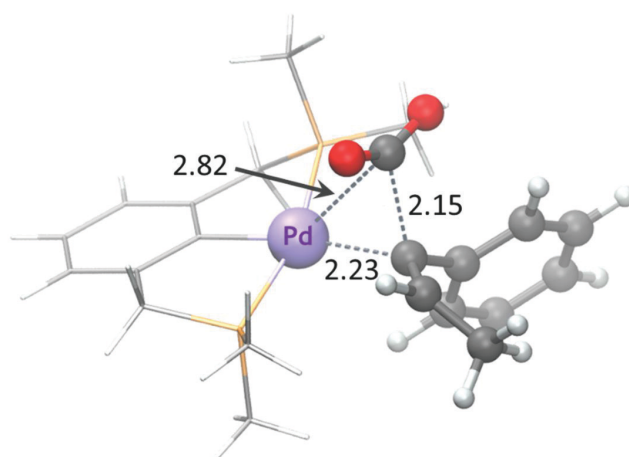
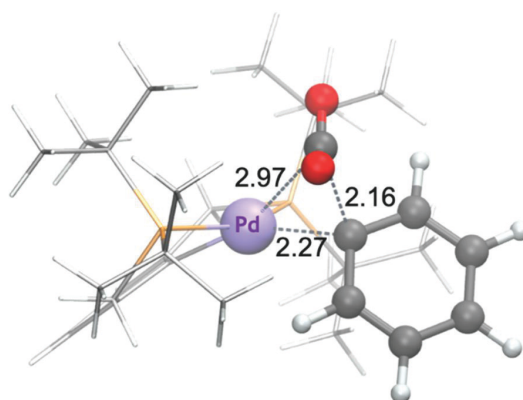


Figure S9. Optimized CO₂ insertion TS for ^{Me}PCP-Pd-alkenyl (DMF). Distances in Å.



$$\Delta G^\ddagger = 41.7 \text{ kcal mol}^{-1}$$

Figure S10. Optimized CO₂ insertion TS for ^{tBu}PCP-Pd-phenyl (DMF, 298 K). Distances in Å.

Table S2. Selected geometric parameters of optimized CO₂ insertion TSs (M = metal, Nu = carbon nucleophile).

Reaction (see Table S1)	Ligand-Metal-Nu	M—C _{Nu} bond	Insertion mode	C _{Nu} —C _{CO2} [Å]	M—C _{Nu} [Å]	M—C _{CO2} [Å]	C _{CO2} —O _{1,CO2} [Å]	C _{CO2} —O _{2,CO2} [Å]	M—O _{1,CO2} [Å]	M—O _{2,CO2} [Å]	O=C=O [°]	C _{CO2} —C _{Nu} —M [°]
1a	IMes-Cu-benzyl	Cu —C _{sp} ³	<i>inner</i>	2.11	2.10	2.16	1.23	1.23	2.67	2.87	138.2	61.7
			<i>outer</i>	2.24	2.07	4.12	1.20	1.20	4.43	4.70	149.3	145.9
1b	IPr-Cu-benzyl	Cu —C _{sp} ³	<i>inner</i>	2.07	2.09	2.17	1.23	1.23	2.68	2.87	138.6	62.9
			<i>outer</i>	2.21	2.08	4.10	1.20	1.20	4.31	4.84	148.8	146.3
1c	IMe-Cu-benzyl	Cu —C _{sp} ³	<i>inner</i>	2.08	2.11	2.16	1.23	1.23	2.70	2.83	137.9	62.0
			<i>outer</i>	2.23	2.08	4.12	1.20	1.20	4.42	4.72	149.4	146.1
2	IPr-Cu-benzyl	Cu —C _{sp} ³	<i>inner</i>	2.14	2.09	2.25	1.23	1.21	2.48	3.08	141.1	64.2
			<i>outer</i>	2.13	2.10	4.04	1.21	1.20	4.22	4.80	147.4	145.7
3	Cl ₂ IPr-Cu-alkenyl	Cu —C _{sp} ²	<i>inner</i>	2.09	1.97	2.46	1.21	1.21	2.80	3.15	144.5	74.7
			<i>outer</i>	2.65	3.67	5.93	1.18	1.18	5.89	6.44	167.0	139.6
4a	IPr-Cu-aryl	Cu —C _{sp} ²	<i>inner</i>	2.25	1.94	2.59	1.20	1.20	3.05	3.09	150.1	75.9
4b	IPr-Cu-alkenyl	Cu —C _{sp} ²	<i>inner</i>	2.16	1.93	2.70	1.20	1.20	3.02	3.33	148.9	82.4
			<i>inner</i>	2.21	2.75	2.19	1.26	1.22	2.24	3.13	138.8	50.9
5	(S)-SEGPHOS-Rh-benzyl	Rh —C _{sp} ³	<i>outer (S)</i>	2.42	3.64	5.46	1.19	1.19	5.44	6.12	156.7	127.9
			<i>outer (R)</i>	2.39	3.70	5.42	1.19	1.19	5.46	6.01	155.6	124.3
6a	dppp-Rh-aryl	Rh —C _{sp} ²	<i>inner</i>	2.06	2.15	2.20	1.25	1.21	2.20	3.20	141.0	62.8
6b	p-OMe-dppp-Rh-alkenyl	Rh —C _{sp} ²	<i>inner</i>	2.01	2.12	2.18	1.26	1.21	2.23	3.17	139.5	63.8
7	^{Et} PGeP-Pd-benzyl	Pd —C _{sp} ³	<i>inner</i>	2.53	2.50	2.77	1.20	1.20	3.06	3.40	151.5	66.8
			<i>outer</i>	2.64	3.35	5.33	1.18	1.18	5.05	6.07	166.1	125.3
8	alkene-Pd-alkenyl	Pd —C _{sp} ²	<i>inner</i>	1.97	2.01	2.96	1.21	1.22	3.31	3.59	143.2	95.9
9a	^{Et} PGeP-Pd-alkenyl	Pd —C _{sp} ²	<i>inner</i>	2.15	2.30	2.74	1.20	1.20	3.04	3.38	147.4	87.3
9b	^{Ph} PSiP-Pd-alkenyl	Pd —C _{sp} ²	<i>inner</i>	2.16	2.27	3.03	1.20	1.20	3.24	3.69	148.7	84.1
9c	^{tBu} PCP-Pd-alkenyl	Pd —C _{sp} ²	<i>inner</i>	2.15	2.27	3.06	1.20	1.20	3.25	3.77	147.5	79.9
9d	^{Me} PCP-Pd-alkenyl	Pd —C _{sp} ²	<i>inner</i>	2.12	2.23	2.82	1.21	1.21	3.13	3.45	146.1	74.5
9e	^{tBu} PCP-Pd-aryl	Pd —C _{sp} ²	<i>inner</i>	2.23	2.27	2.97	1.20	1.20	3.21	3.66	147.6	85.1

Paper III

Computational and experimental insights into asymmetric
Rh-catalyzed hydrocarboxylation with CO₂

Ljiljana Pavlovic, Martin Pettersen, Ashot Gevorgyan, Janakiram Vaitla,
Annette Bayer and Kathrin H. Hopmann (*In preparation*)

Computational and experimental insights into asymmetric Rh-catalyzed hydrocarboxylation with CO₂

Ljiljana Pavlovic,[†] Martin Pettersen,[‡] Ashot Gevorgyan,[‡] Janakiram Vaitla,[‡] Annette Bayer,^{*,‡} and Kathrin H. Hopmann^{*,†}

[†]Hylleraas Centre for Quantum Molecular Sciences, Department of Chemistry, UiT The Arctic University of Norway, N-9037 Tromsø

[‡]Department of Chemistry, UiT The Arctic University of Norway, N-9037 Tromsø, Norway

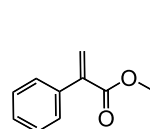
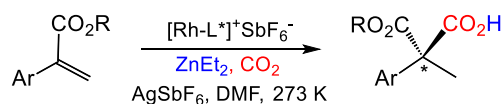
ABSTRACT: The asymmetric Rh-catalyzed hydrocarboxylation of α,β -unsaturated carbonyl compounds was originally developed by Mikami and co-workers (*Eur. J. Org. Chem.* **2016**, 3166), but gives only moderate enantiomeric excesses. In order to understand the factors controlling the enantioselectivity and to propose novel ligands for this reaction, we have used computational and experimental methods to study the Rh-catalyzed hydrocarboxylation with different bidentate *P,P*; *P,N* and *N,N* ligands. The analysis of the C-CO₂ bond formation transition states with DFT methods shows a preference for *outer sphere* CO₂ insertion, where CO₂ can undergo a *backside* or *frontside* reaction with the nucleophile. Of five tested ligands, three prefer the *backside* mode. The two ligands that prefer a *frontside* reaction, StackPhos and ^tBu-BOX, display an intriguing stacking interaction between CO₂ and an N-heterocyclic ring of the ligand (imidazole or oxazoline). Our experimental results support the computationally predicted enantiomeric excesses.

INTRODCUTION

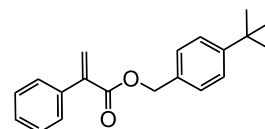
Widespread efforts are currently devoted to the search of catalysts, which can fixate CO₂ into organic molecules.¹⁻⁶ A significant part of this activity is focused on metal-catalyzed carbon-carbon bond formation with CO₂.⁷⁻¹⁶ For metal-catalyzed formation of saturated carboxylic acids, different protocols have been reported. For example, Greenhalgh and Thomas reported an Fe(II)-catalyzed synthesis of α -aryl carboxylic acids from styrene derivatives and CO₂.⁸ Martin and co-workers developed a mild Ni(I)-catalyzed protocol for converting benzyl halides and CO₂ to phenylacetic acids.¹⁵ A Cu(I)/CsF-based protocol for incorporation of CO₂ into disubstituted alkenes was reported by Skrydstrup, Nielsen and co-workers.¹⁶

Interestingly, the protocols mentioned above all involve formation of *chiral* carboxylic acids,^{8,15,16} but as racemic mixtures in all cases. Indeed, the design of enantioselective C-CO₂ bond formation reactions remains a major challenge. This is demonstrated by the fact that only very few studies on asymmetric C-CO₂ bond formation have been reported.^{6,9,17-19} In order to broaden the usefulness of CO₂ as a carbon synthon in the chemical and pharmaceutical industry, it is essential that novel enantioselective carboxylation protocols are developed, for example for the preparation of chiral carboxylic acids, which are important intermediates in many synthetic processes.²⁰

A promising asymmetric C-CO₂ bond formation protocol has been reported by Mikami and co-workers in 2016, involving the first enantioselective hydrocarboxylation of α,β -unsaturated carbonyl compounds (Figure 1).⁹ The rhodium-based reaction involved the use of (*S*)-SEGPHOS as chiral ligand, but only moderate enantiomeric excesses (*e.e.*'s) of up to 66 % could be achieved.⁹ The phosphine-based ligand (*S*)-BINAP gave similar results to (*S*)-SEGPHOS whereas other ligands, such as (*S*)-SynPhos or (*R,R*)-ⁱPR-DuPhos, provided significantly lower *e.e.*'s.⁹



sub1: methyl 2-phenylacrylate
60% (*S*) *e.e.*, L* = (*S*)-SEGPHOS



sub2: 4-(*t*-Bu)benzyl 2-phenylacrylate
66% (*S*) *e.e.*, L* = (*S*)-SEGPHOS

Figure 1. Enantioselective hydrocarboxylation reaction reported by Mikami and coworkers.⁹

A computational analysis of the related non-selective Rh-COD-catalyzed hydrocarboxylation reaction showed that during C-CO₂ bond formation, the CO₂ molecule does not

interact with rhodium.²¹ Moreover, it was shown that benzylic substrates display an unusual η^6 -coordination mode, with the nucleophilic carbon positioned up to 3.6 Å away from rhodium.²¹ The same substrate binding mode and preference for an outer sphere CO₂ insertion was found computationally for the chiral Rh-(*S*)-SEGPHOS catalyst.²² This raises the question how the enantioselectivity is controlled in systems where CO₂ is not constrained through interactions with the metal. Although CO₂ preferably is positioned in the outer sphere, it may still be affected by repulsive and attractive non-bonding interactions with the ligand. A better understanding of the factors that govern the preferred positions and orientations of CO₂ may help to design catalysts with higher enantioselectivities.

Modern computational methods are sufficiently advanced to provide insights into the factors that control the enantioselectivity in metal-catalyzed reactions.²³ For example, the selectivity may be influenced by the presence of specific interactions between the chiral catalyst and the substrate, and in particular nonbonding forces may contribute significantly to the preferred formation of one enantiomer.²⁴⁻²⁷ The identification of the selectivity-determining interactions typically relies on the computational optimization of the involved diastereomeric transition states. Such structures are generally built manually, followed by DFT optimizations, using different optimization algorithms.²⁸⁻³¹ However, approaches to speed-up the computational analysis through automatized techniques have been put forward,^{32,33} with one example being the open-source toolkit AARON (An Automated Reaction Optimizer for New catalysts) designed by Wheeler and co-workers.³² AARON employs TS templates provided by the user, but can automatically swap the ligands to build new geometries.

Herein, we perform a computational analysis of the selectivity-determining factors in the Rh-catalyzed hydrocarboxylation for five chiral rhodium complexes, of which four ligands have not previously been tested in this reaction. Ligand swapping is performed with AARON, followed by DFT optimizations. To validate the enantioselectivities predicted by the computations, an experimental analysis of all systems is performed.

METHODS

Computational models: Calculations were performed with full substrates **sub1** and **sub2** (Figure 1) and with the full ligands (Figure 2). No molecular truncations or symmetry constrains were applied.

For the analysis of the chiral ligands, 10 outer sphere CO₂ insertion TSs were built for each ligand, with different ligand-substrate orientations (Figure 3). Five of them were pro-(*S*)-TSs, and five the corresponding pro-(*R*) TSs. In the conformations **TS1a** and **TS1b**, the phenyl ring of the substrate interacts with the Rh-center in an η^6 fashion, whereas CO₂ is in the outer sphere, leading to a *backside* C-CO₂ bond formation (reminiscent of the S_E2(back) reaction). The difference between **TS1a** and **TS1b** is the orientation of the ester moiety (Fig. 3). At **TS2a** and **TS2b**, the substrate is still bound in an η^6 fashion, but the CO₂ is positioned closer to metal, leading to a *frontside* reaction (reminiscent of the S_E2(front) reaction). At **TS3**, both the phenyl group and the carbonyl oxygen of the substrate interact with the Rh-center. It is important to highlight that for the comparative analysis of the 5 ligands, only *outer sphere* CO₂ insertion was considered,^{21,22} because TS conformations where interactions between Rh and CO₂ take place (referred to as *inner sphere* CO₂ insertion) show very high very high barriers (TS4_S and TS4_R, Supporting Information, Table S1).

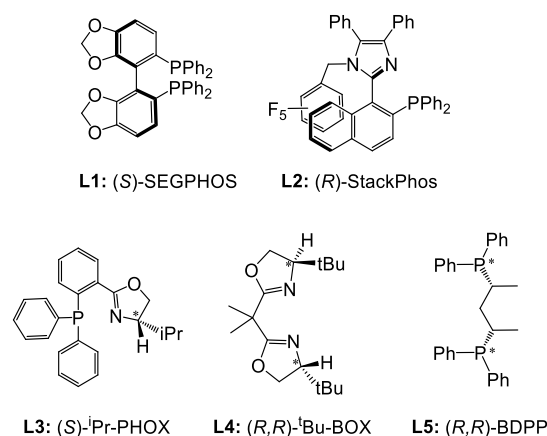


Figure 2. Five chiral ligands studied here in Rh-catalyzed hydrocarboxylation.

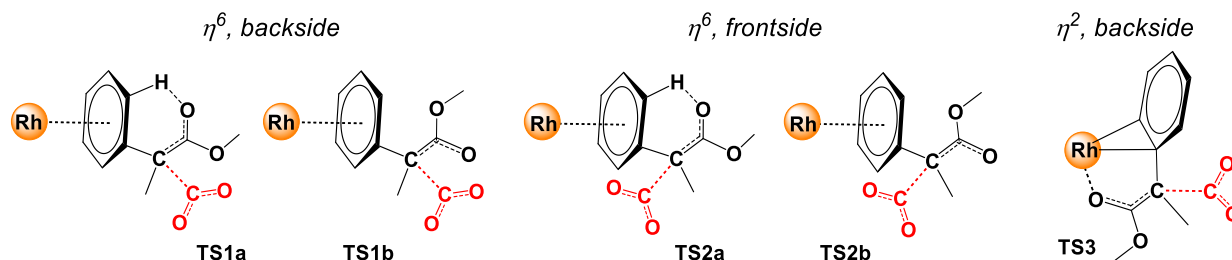


Figure 3. Five TS orientations considered here. For each of these, both pro-(*R*) and pro-(*S*) conformations were included.

Computational methods: All calculations were performed at the DFT level of theory as implemented in Gaussian09 package.³⁴ The DFT functional PBE^{35,36} was employed together with the Grimme empirical dispersion correction (D2³⁷) and the solvation model IEFPCM³⁸⁻⁴⁰ (DMF solvent⁹). The PBE functional has been found to be an adequate choice for rhodium-catalyzed hydrocarboxylation reactions in our previous study,²¹ where it provided a good agreement with experimental results.⁹ The geometries of all intermediates and transition states were fully optimized and frequency calculations were performed in order to confirm the nature of the stationary points, where all transition states structures exhibited only one imaginary frequency.

In geometry optimizations, the BS1 basis set was employed, consisting of 6-311G(d,p) for C, H, O, N, F and P, and the LANL2DZ basis set and pseudopotential for Rh, including an extra f polarization function with exponent 1.35.⁴¹ A larger basis set, BS2, was employed for single point energy calculations, consisting of 6-311+G(2d,2p) on all non-metal atoms and LANL2TZ(f) on rhodium.

In order to convert computed free energies (ΔG° , BS1) at 1 atm into a 1M standard state, a standard state (SS) correction was included. At 273 K, this correction is -1.69 kcal/mol (for a reaction that goes from 2 moles to 1).^{42,43} The final Gibbs free energy was determined with the following expression: $\Delta G^\circ_{1M,273K} = \Delta G^\circ_{1atm,BS1,273K} - \Delta E_{BS1} + \Delta E_{BS2} + SS_{273K}$.

The enantiomeric excess (*e.e.*) was computed using the formula:^{23,44}

$$e.e. (\%) = \frac{\sum_{i=1}^n k_{Ri} - \sum_{i=1}^n k_{Si}}{\sum_{i=1}^n k_{Ri} + \sum_{i=1}^n k_{Si}}$$

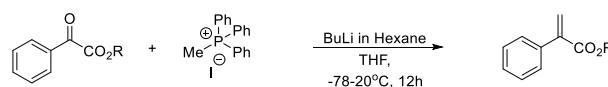
where k_{Ri} are the computed rate constants of TS structures with (*R*) configuration, which are summed from $i = 1$ to $i = n$, where n is equal to the number of TSs within 3 kcal/mol from the best TS. k_{Si} is the equivalent for (*S*)-TSs.

AARON ligand swapping: The TS library used for AARON³² was based on the SEGPHOS structures obtained in the manual DFT analysis. Four ligands present in the AARON ligand library were then specified to be swapped with SEGPHOS. We preoptimized the conformations with the swapped ligands with AARON in two steps, using HF/6-31 in the first step and PBE-D2/BS1_{mod} in the second step, where BS1_{mod} is as BS1 but lacks the additional f polarization function on Rh, as AARON did not allow addition of basis functions. The obtained geometries for all ligands were then used as input for further manual DFT investigations, with the protocol as described above for manual DFT calculations.

General Experimental Details: [Purchase, NMR etc. To be filled in]

Experimental synthesis of methyl and ethyl 2-phenylacrylate: Two strategies for synthesis of acrylates were employed: In the first strategy, paraformaldehyde (0.90 g, 30 mmol, 3.0 equiv), K₂CO₃ (4.15 g, 30 mmol, 3.0 equiv), *n*-Bu₄NI (or *n*-Bu₄NHSO₃) (0.18 g, 0.5 mmol, 0.05 equiv) were added to a

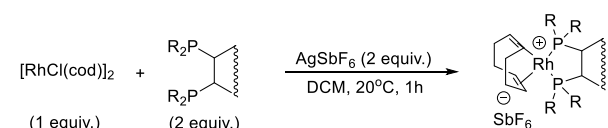
solution of ethyl ester (10 mmol, 1.0 equiv) in toluene (20 mL) at rt. The reaction mixture was heated to 60 °C for 8 h. After cooling to rt, H₂O (10 mL) was added and the aqueous layer was extracted with diethyl ether (20 mL × 3). The combined organic layer was dried over Na₂SO₄, concentrated in vacuo and purified by column chromatography. The corresponding acrylate was obtained as a colorless oil in 64% yield. In the second approach, BuLi in hexane was mixed with the ester and methyltriphenylphosphonium iodide in THF [To be extended]. Ethyl 2-phenylacrylate and methyl 2-phenylacrylate were obtained in 49 % and 56 % yield, respectively.



Experimental preparation of Stackphos: [To be filled in. Based on *J. Am. Chem. Soc.* **2013**, 135, 14548]

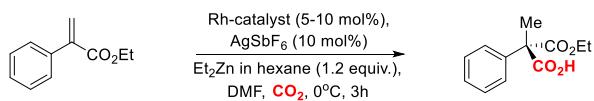
Experimental synthesis of chiral rhodium catalysts:

A Schlenk tube was charged under Ar with [RhCl(cod)]₂ (49.3 mg, 0.10 mmol), and DCM (3.0 mL) was added. Then, a solution of AgSbF₆ (68.8 mg, 0.20 mmol) in DCM (2.0 mL) previously prepared in another Schlenk tube was added via a cannula. After stirring for 30 min, a solution of chiral phosphine ligand (0.20 mmol) in DCM (5.0 mL) was slowly added via a cannula. After stirring for 1 h, AgCl precipitate was removed by filtration under Ar through a bed of Celite. The Rh complex was isolated (quant., air stable orange powder) by concentrating the mixture in vacuo. The following yields were obtained: [Rh(cod)((*S*)-SEGPHOS)]SbF₆ (99%), [Rh(cod)((*S,S*)-BDPP)]SbF₆ (99%), [Rh(cod)((*S,S*)-^tBu-BOX)]SbF₆ (99%), and [Rh(cod)((*rac*)-StackPhos)]SbF₆ (99%). For the PHOX ligand, the counterion used was BarF [to be extended].



Experimental Rh-catalyzed hydrocarboxylation of ethyl 2-phenylacrylate: Rh catalyst (0.05 to 0.01 mmol) and AgSbF₆ (3.4 mg, 0.01 mmol) were weighed into an oven-dried CO₂ pressure tube which was sealed with a septum, evacuated and refilled with CO₂ three times. These solids were dissolved in DMF (0.5 mL). After acrylate (20 μL, 0.10 mmol) was added, ZnEt₂ (120 μL, 0.12 mmol) was added dropwise at 0 °C. After 3 h, the reaction mixture was diluted with Et₂O (5 mL) and quenched with 1N HCl aq. (5 mL). After separation, the aqueous layer was extracted with EtOAc (2 × 5 mL). The combined organic layers were dried over MgSO₄ and evaporated under reduced pressure. The resulting crude product was diluted with Et₂O (10 mL), and then saturated NaHCO₃ aq. (5 mL) was added. After separation, the organic layer was extracted with saturated NaHCO₃ aq. (2 × 5 mL). To the combined aqueous layers, 1N HCl aq. was added until

pH was smaller than 2. The solution was extracted with Et₂O (3 × 10 mL). The combined organic layers were dried over Na₂SO₄ and evaporated under reduced pressure to afford carboxylic acid.



Experimental measurement of enantiomeric excess: [SFC, To be extended]

RESULTS AND DISCUSSION

Our study of the Rh-catalyzed asymmetric hydrocarboxylation reaction consist of three parts. Initially, we validated the computational protocol through analysis of the Rh-(*S*)-SEGPHOS-catalyzed hydrocarboxylation of two experimentally known substrates.⁹ Next, we expanded our computational study to include the CO₂ insertion TSs for four additional chiral ligands, which have not been used in experiments on this reaction before. Finally, we conducted experimental testing of the ligands in the asymmetric Rh-catalyzed hydrocarboxylation.

Computational analysis of Rh-(*S*)-SEGPHOS: The Rh-SEGPHOS-catalyzed hydrocarboxylation was studied computationally with the styrene-type α,β -unsaturated carbonyl substrates **sub1** and **sub2** (Figure 1), which have been studied experimentally by Mikami and co-workers.⁹ The overall hydrocarboxylation mechanism for substrates of this type has been analyzed previously with Rh-COD.²¹ The mechanistic steps include a transmetalation of an ethyl from diethylzinc to the precatalyst, followed by a β -hydride elimination to give an Rh-H intermediate (SI, Figure S1). Insertion of the substrate leads to an energetically low-lying Rh-benzyl species that can attack CO₂.²¹ The CO₂ insertion is rate-determining.²¹ At the carboxylation TS, the benzyl group prefers to coordinate in an η^6 mode to rhodium, with the formally negative charge on the substrate delocalized between the nucleophilic carbon and the ester group, yielding an enolate description (Figure 4). The enolate can attack CO₂ by its *re* or *si* face, and with a chiral ligand, unequal amounts of the (*R*)- and (*S*)-enantiomer of the product can be formed.

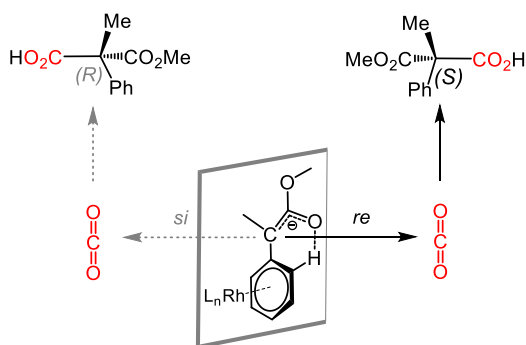


Figure 4. Illustration of the enolate intermediate of **sub1** and its attack on CO₂.

Carboxylation of methyl 2-phenylacrylate: In order to validate our computational protocol and our mechanistic understanding of this reaction, we first analyzed the Rh-(*S*)-SEGPHOS-catalyzed C-CO₂ bond formation with **sub1** (Figure 1). The results support our previous observation that CO₂ prefers to be in the outer sphere during C-CO₂ bond formation,²¹ as the inner and outer sphere TSs with Rh-(*S*)-SEGPHOS show an energy difference of 17.3 kcal/mol in favour of outer sphere insertion (SI, Table S1, Fig. S2).

At the lowest lying outer sphere **TS1a**_{S_{sub1/L1}} ($\Delta G^\ddagger = 12.1$ kcal/mol, computed relative to the Rh-benzyl intermediate, Fig. S3, SI), the η^6 -coordinated enolate attacks CO₂ by its *re* face and the experimentally observed (*S*)-product is obtained. At **TS1a**_{R_{sub1/L1}}, which is higher in energy by 0.7 kcal/mol, CO₂ is attacked by the enolate *si* face, yielding the (*R*)-product (Figure 5). Other outer sphere conformations (Figure 3) were significantly higher in energy (Table 1). On the basis of all TS energies, we evaluated the *e.e.* for the Rh-(*S*)-SEGPHOS-catalyzed hydrocarboxylation of **sub1**, providing a computed *e.e.* of 53.8 % (*S*), in good agreement with the experimentally reported *e.e.* of 60.0 % (*S*).⁹ This indicates that the computational protocol and the included TS conformations provide an adequate description of this reaction.

At the two lowest lying diastereomeric SEGPHOS TSs, **TS1a**_{S_{sub1/L1}} and **TS1a**_{R_{sub1/L1}} (Fig. 5), various noncovalent interactions between SEGPHOS and **sub1** can be identified. At **TS1a**_{S_{sub1/L1}}, the phenyl rings of SEGPHOS form two C-H \cdots π interactions (2.95, 3.10 Å) with the phenyl of the substrate. At the energetically higher lying **TS1a**_{R_{sub1/L1}}, SEGPHOS forms three C-H \cdots π interactions with **sub1**, two with the substrate phenyl (2.97 and 3.10 Å) and one with the methyl group of the ester moiety (3.20 Å, Fig. 5). As the strength of these C-H \cdots π interactions appears similar at the two diastereomeric TSs, they do not seem to determine the selectivity. An analysis of C-H \cdots O attractions at the two TSs shows comparable distances for interactions within the substrate (**TS1a**_{S_{sub1/L1}}: 2.16 Å, **TS1a**_{R_{sub1/L1}}: 2.11 Å), but significant differences in the *intermolecular* C-H \cdots O interaction between the **sub1** carbonyl and the SEGPHOS phenyl (**TS1a**_{S_{sub1/L1}}: 2.46 Å, **TS1a**_{R_{sub1/L1}}: 3.00 Å). We speculate that this C-H \cdots O interaction may be an essential factor in determining the enantioselectivity in the Rh-(*S*)-SEGPHOS-catalyzed hydrocarboxylation of methyl 2-phenylacrylate.

If CO₂ is placed closer to rhodium, here referred to as *frontside* insertion (TS2, Figure 3), the barriers increase by several kcal/mol (Figure 5). Although C-H \cdots π interactions are identified in both TS2 structures, the energetically favourable C-H_{SegPhos} \cdots O_{sub} interaction that is observed in TS1 is prevented in TS2 by the position of CO₂. Interestingly, the *frontside* attack provides an incorrect enantioselectivity, as the **TS2a**_{R_{sub1/L1}} structure is 2.4 kcal/mol lower in energy than **TS2a**_{S_{sub1/L1}}. The experimentally observed (*S*)-selectivity⁹ is thus dominated by the *backside* structures. These findings highlight the need to compare computed results to experimental selectivities to evaluate if adequate TSs conformations were located.

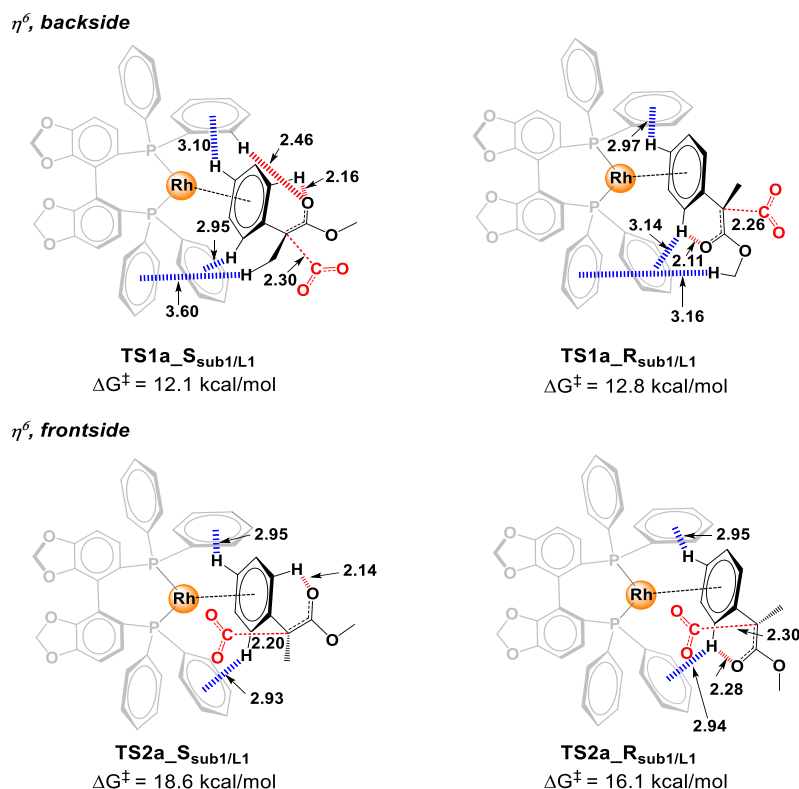


Figure 5. Illustration of the noncovalent interactions at four of the optimized CO₂ insertion TSs for Rh-(*S*)-SEGPPOS-catalyzed hydrocarboxylation of methyl 2-phenylacrylate (**sub1**). Distances in Å.

The TS3 conformations, where the ester of the substrate interacts with rhodium (Figure 3), are ~8 kcal/mol higher in energy than TS1 and are not considered relevant (Table 1).

Carboxylation of 4-(tert-butyl)benzyl 2-phenyl acrylate: Sub2 contains two phenyl rings (Figure 1), leading to several favourable C-H \cdots π interactions during C-CO₂ bond formation (Figure 6). A similar pattern as for **sub1** is observed, where at the lowest lying transition state **TS1a_S_{sub2/L1}** ($\Delta G^\ddagger = 12.0$ kcal/mol), the Rh-enolate (SI, Figure S3) attacks CO₂ by its *re* face, resulting in the (*S*)-product. A favourable C-H \cdots O (2.46 Å) interaction is seen at **TS1a_S_{sub2/L1}**, but lacks at **TS1a_R_{sub2/L1}**, which is higher in energy by 1.1 kcal/mol. The computed *e.e.* of 73% (*S*) is in good agreement with the experimental value of 66% (*S*).⁹

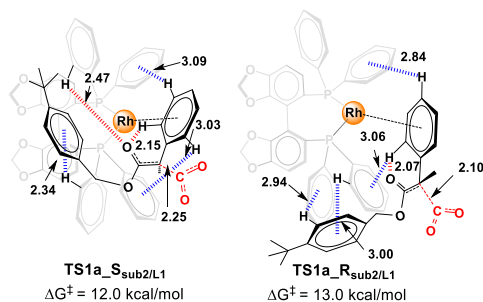


Figure 6. Illustration of the preferred TSs for Rh-(*S*)-SEGPPOS-catalyzed carboxylation of **sub2**. Distances in Å.

The combined results for **sub1** and **sub2** indicate that the enantioselectivity of Rh-(*S*)-SEGPPOS-catalyzed hydrocarboxylation appears to be a result of favourable C-H \cdots O interactions between the substrate and the SEGPPOS ligand. At the preferred TS1a conformations (Figure 5 and 6), the CO₂ molecule is placed away from the metal center (3.60 Å) and thus the chiral catalyst is promoting the enantioselectivity through positioning of the alkene substrate, not through interactions with CO₂.

Potential of other ligands in the Rh-catalyzed asymmetric hydrocarboxylation: From the ligand library of AARON,³² we chose 4 ligands (**L2** to **L5**) with a different ligand scaffold than SEGPPOS and investigated their predicted enantioselectivities with DFT. The selection includes two *P,N* ligands (**L2**: StackPhos, **L3**: PHOX),⁴⁵⁻⁴⁷ an *N,N* ligand (**L4**: 'Bu-BOX)⁴⁸ and a *P,P* ligand (**L5**: BDPP).⁴⁹ These ligands have shown good performance in other reactions (hydrogenations, allylations, aziridination, hydrovinylation),⁵⁰⁻⁵³ and to our knowledge, they have not previously been used in a Rh-catalyzed hydrocarboxylations.

The outer sphere TS conformations depicted in Figure 3 were evaluated for **L2-L5** and **sub1** through manual DFT calculations, with the energies summarized in Table 1 (geometric parameters are shown in Figure 7 and Tables S1-5, SI). For PHOX and BDPP, we see a similar behaviour as for SEGPPOS, with a preference for *backside* insertion (Table 1). However, the StackPhos and 'Bu-BOX ligands show a computed preference for *frontside* insertion. Both

Table 1. Barrier differences ($\Delta\Delta G^\ddagger$, kcal/mol, 273K) for different TS conformations (Figure 3) with computed and experimentally determined *e.e.*'s for Rh-catalyzed hydrocarboxylation of **sub1**

Ligand	η^6 , backside				η^6 , frontside				η^2 , backside		<i>e.e.</i> comp %	<i>e.e.</i> exp %
	TS1a_S	TS1a_R	TS1b_S	TS1b_R	TS2a_S	TS2a_R	TS2b_S	TS2b_R	TS3_S	TS3_R		
L1 (SEGPPOS)	0.0	0.7	3.1	2.0	6.5	4.1	7.3	4.9	8.3	7.9	53.8 (S)	60.0 (S) ^c
L2 (StackPhos)	2.2	2.8	2.1	3.0	0.0^a , 0.8^b	0.6^a , 1.9^b	0.8	1.0	15.2	10.8	47.0 (S)	[on-going] ^d
L3 (ⁱ Pr-PHOX)	0.0	0.0	3.1	1.4	1.8	2.8	2.8	3.4	12.3	6.5	1.8 (R)	(0) ^d
L4 (^t Bu-BOX)	1.9	0.7	3.1	0.8	0.0	0.5	3.6	2.5	3.2	5.3	6.4 (S)	(0) ^d
L5 (BDPP)	0.5	0.0	0.8	1.9	5.8	5.5	8.6	6.4	9.7	12.1	24.3 (R)	(4) ^d

^a TS2a structures as given in Fig. 8 (TS2a_S_{sub1/L2}/TS2a_R_{sub1/L2}), ^b TS2a structures with stacking of pentafluorophenyl and phenyl as given in the SI, Fig. S5 (TS2a_stack_S_{sub1/L2}/TS2a_stack_R_{sub1/L2}), ^c From ref. ⁹, ^d Experimental results obtained here with ethyl 2-phenylacrylate. For BDPP, the (R,R) ligand was computed, but the (S,S) ligand was used in experiments.

ligands display an intriguing stacking interaction between CO₂ and the N-heterocyclic ring of the ligand (imidazole or oxazoline, Figure 7, SI, Figure S7). This interaction is also seen in the energetically higher-lying *frontside* structures of ⁱPr-PHOX (SI, Table S3, TS2a_S).

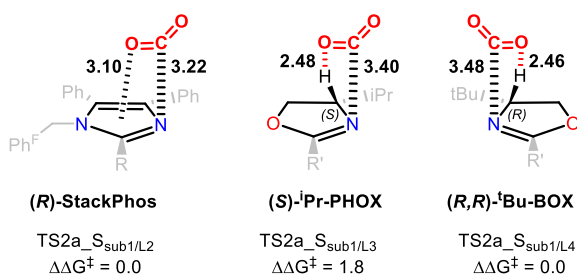


Figure 7. Stacking of CO₂ above the N-heterocyclic ring of L2-L4 at the *frontside* TSs. $\Delta\Delta G^\ddagger$ values (kcal/mol) are relative to the lowest lying TS for each ligand. Distances in Å.

It can be noted that related attractive stacking interactions have been predicted in computational studies focusing on the binding of CO₂ to N-heterocyclic compounds,⁵⁴⁻⁵⁶ and in experimental and computational studies on the solvation of aromatic compounds in supercritical CO₂.⁵⁷ However, to our knowledge, this CO₂ stacking has not been described in the context of an organometallic ligand or a CO₂ insertion reaction.

The heterocycle-CO₂ interaction appears strongest at the

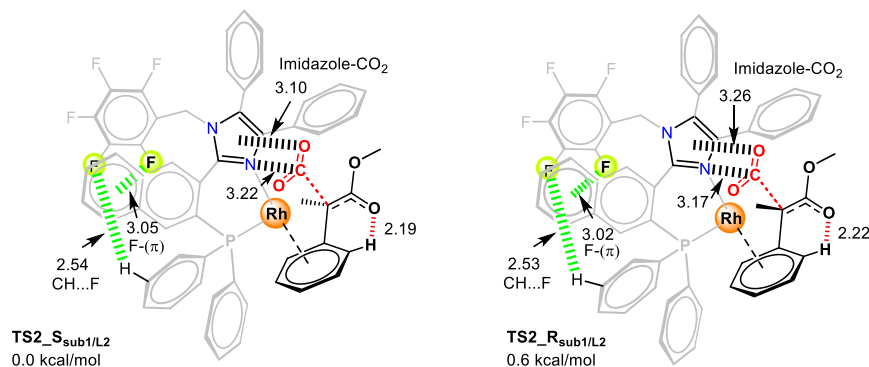


Figure 8. Illustration of the preferred TSs for Rh-(R)-StackPhos-catalyzed carboxylation of **sub1**. Distances in Å.

StackPhos TS geometries, with a nitrogen-CO₂ distance of 3.22 Å (Figure 7). The StackPhos TS geometries with **sub1** are therefore discussed in further detail here. Besides the CO₂-imidazole stacking, the lowest lying TS2a_S_{sub1/L2} also displays an intriguing F- π attraction between a fluoro group of the pentafluoro-phenyl and the naphthalene ring (3.05 Å), alongside a C-H...F interaction (2.53 Å, Figure 8). Interestingly, this F- π interaction is not seen in the X ray structure of the StackPhos ligand,⁴⁵ which instead displays π - π stacking between pentafluorophenyl and naphthalene (3.38 Å). In our computations, this π - π stacking increases the TS energy by 2.5 kcal/mol (SI, Figure S4). A π - π interaction between pentafluorophenyl and another phenyl substituent increases the CO₂ insertion barrier slightly by 0.8 kcal/mol (TS2a_stack_S_{sub1/L2} SI, Figure S5), indicating that this conformation could contribute to the carboxylation. The StackPhos *backside* structures lack imidazole-CO₂ interactions and are higher in energy by 2 to 3 kcal/mol (Table 1). The TS3 structures, where the ester carbonyl interacts with rhodium, are more than 11 kcal/mol above the TS2 structures and therefore not relevant.

The best (R)-pathway obtained for **sub1** with StackPhos proceeds via *frontside* insertion and is 0.6 kcal/mol above the best (S)-structure (Figure 8). TS2a_R_{sub1/L2} also displays stacking of CO₂ above imidazole and an F- π interaction between pentafluorophenyl and the naphthalene ring (Figure 8). The *e.e.* computed on basis of the obtained StackPhos TS structures is 47 % (S) (Table 1), which indicates that this

ligand is not expected to perform significantly better than SEGPHOS despite the intriguing imidazole-CO₂ interaction. [StackPhos experimental study ongoing]

For (*S*)-ⁱPr-PHOX, our DFT analysis indicates essentially no enantioselectivity (1.8 %, Table 1). The lowest lying TSs prefer backside CO₂ insertion, which have almost the same energy for (*R*) and (*S*) pathways (SI, Table S3). At the **TS1a**_{sub1/L4} and **TS1a**_{sub1/L4}, the same type of non-covalent interactions are present, such as C-H...O and C-H...π, with comparable strength (SI, Figure S6). Experimental hydrocarboxylation of ethyl 2-phenyl acrylate (which has an ethyl on the ester, instead of the methyl in **sub1**) showed 0% *e.e.* in our analysis (Table 1), in good agreement with the lack of selectivity in computations.

The other studied ligands are also predicted to give low enantiomeric excesses. Our calculations show that with the (*R,R*)-^tBu-BOX chiral ligand, at the lowest lying **TS2a**_{sub1/L4}, the frontside CO₂ insertion is preferred (SI, Figure S7). Formation of the other product enantiomer via **TS2a**_{sub1/L4} is higher in energy by only 0.5 kcal/mol, with a predicted *e.e.* on basis of all optimized TS conformations of only 6.4 % (Table 1). Experimental hydrocarboxylation of ethyl 2-phenyl acrylate showed 0% *e.e.* in our analysis (Table 1), also here in good agreement with the poor *e.e.* obtained in computations.

With the (*R,R*)-BDPP ligand, at the lowest lying **TS1a**_{sub1/L5}, the CO₂ prefers backside insertion (SI, Figure S8). **TS1a**_{sub1/L5} has a barrier that is only 0.5 kcal/mol higher than **TS1a**_{sub1/L5}. The TSs with the frontside CO₂ insertion are higher in energy by more than 5 kcal/mol (Table S5). This scenario is reminiscent of the biphosphine ligand (*S,S*)-SEGPHOS. The result may be a consequence of the bulky phenyl groups of the ligand, which restrict CO₂ to prefer insertion via a backside path. The overall *e.e.* predicted for this ligand is 24 % (*R*) (Table 1). Our experimental results on ethyl 2-phenyl acrylate showed 4 % *e.e.*, in line with the predicted result.

CONCLUSIONS

We have employed computational and experimental methods to study the potential of bidentate chiral ligands in the asymmetric rhodium-catalyzed hydrocarboxylation.

Our manual DFT analysis of the Rh-(*S*)-SEGPHOS-catalyzed hydrocarboxylation of α,β-unsaturated esters support a preference for outer sphere insertion of CO₂ and an η⁶ coordination of benzylic substrates.²¹ The experimental enantioselectivity of SEGPHOS⁹ is reproduced for two substrates in our calculations and is predicted to arise from the C-H...O interaction between a phenyl group of SEGPHOS and the carbonyl group of the substrate.

An interesting finding in our computational study of other rhodium ligands is an intriguing stacking interaction of CO₂ with N-heterocyclic rings (imidazole or oxazoline) in StackPhos and ^tBu-BOX (Figure 7). However neither these two ligands, nor the other manually studied ligands, ⁱPr-

PHOX and BDPP, are predicted to give a significant enantiomeric excess in this reaction. Our experimental analyses of ^tBu-BOX, PHOX, and BDPP support the computed *e.e.*'s, underpinning the ability of DFT-D to adequately model complex enantioselective reactions.

Our combined results on Rh-catalyzed hydrocarboxylation indicate that the enantioselectivity of this reaction is difficult to control. A possible strategy to be considered is to steer CO₂ into a specific position to decrease its conformational freedom. The noncovalent stacking interactions observed between CO₂ and StackPhos (Figure 8) may be interesting in this sense and variants of this ligand may thus be a relevant starting point for future analysis.

AUTHOR INFORMATION

Corresponding Author: annette.bayer@uit.no,
kathrin.hopmann@uit.no

ACKNOWLEDGMENTS

This work has been supported by a Centre of Excellence Grant (No. 262695), by the Tromsø Research Foundation (No. TFS2016KHH), by Notur - The Norwegian Metacenter for Computational Science through grants of computer time (No. nn9330k and nn4654k), and by NordForsk (No. 85378). We thank Manuel Langer for support with the SFC and Prof. Steven Wheeler, Victoria M. Ingman, Anthony James Schaefer and Stig Rune Jensen for advice and technical assistance in the implementation of AARON.

REFERENCES

1. Cokoja, M.; Bruckmeier, C.; Rieger, B.; Herrmann, W.A.; Kuhn, F.E., Transformation of Carbon Dioxide with Homogeneous Transition-Metal Catalysts: A Molecular Solution to a Global Challenge? *Angew. Chem. Int. Ed.* **2011**, *50* (37), 8510-8537.
2. Dabral, S.; Schaub, T., The Use of Carbon Dioxide (CO₂) as a Building Block in Organic Synthesis from an Industrial Perspective. *Adv. Synth. Catal.* **2019**, *361* (2), 223-246.
3. Tortajada, A.; Julia-Hernandez, F.; Borjesson, M.; Moragas, T.; Martin, R., Transition-Metal-Catalyzed Carboxylation Reactions with Carbon Dioxide. *Angew. Chem. Int. Ed.* **2018**, *57* (49), 15948-15982.
4. Yang, Y.; Lee, J.-W., Toward ideal carbon dioxide functionalization. *Chem. Sci.* **2019**, *10* (14), 3905-3926.
5. Luan, Y.-X.; Ye, M., Transition metal-mediated or catalyzed hydrocarboxylation of olefins with CO₂. *Tetrahedron Lett.* **2018**, *59* (10), 853-861.
6. Vaitla, J.; Guttormsen, Y.; Mannisto, J. K.; Nova, A.; Repo, T.; Bayer, A.; Hopmann, K. H., Enantioselective Incorporation of CO₂: Status and Potential. *Acc. Catal.* **2017**, *7* (10), 7231-7244.
7. Williams, C. M.; Johnson, J. B.; Rovis, T., Nickel-catalyzed reductive carboxylation of styrenes using CO₂. *J. Am. Chem. Soc.* **2008**, *130* (45), 14936-7.
8. Greenhalgh, M. D.; Thomas, S. P., Iron-catalyzed, highly regioselective synthesis of alpha-aryl carboxylic acids from styrene derivatives and CO₂. *J. Am. Chem. Soc.* **2012**, *134* (29), 11900-3.

9. Kawashima, S.; Aikawa, K.; Mikami, K., Rhodium-Catalyzed Hydrocarboxylation of Olefins with Carbon Dioxide. *Eur. J. Org. Chem.* **2016**, (19), 3166-3170.
10. Shao, P.; Wang, S.; Chen, C.; Xi, C., Cp₂TiCl₂-Catalyzed Regioselective Hydrocarboxylation of Alkenes with CO₂. *Org. Lett.* **2016**, 18 (9), 2050-2053.
11. Murata, K.; Numasawa, N.; Shimomaki, K.; Takaya, J.; Iwasawa, N., Construction of a visible light-driven hydrocarboxylation cycle of alkenes by the combined use of Rh(I) and photoredox catalysts. *Chem. Commun.* **2017**, 53 (21), 3098-3101.
12. Fujihara, T.; Nogi, K.; Xu, T.; Terao, J.; Tsuji, Y., Nickel-Catalyzed Carboxylation of Aryl and Vinyl Chlorides Employing Carbon Dioxide. *J. Am. Chem. Soc.* **2012**, 134 (22), 9106-9109.
13. Ukai, K.; Aoki, M.; Takaya, J.; Iwasawa, N., Rhodium(I)-Catalyzed Carboxylation of Aryl- and Alkenylboronic Esters with CO₂. *J. Am. Chem. Soc.* **2006**, 128 (27), 8706-8707.
14. Mizuno, H.; Takaya, J.; Iwasawa, N., Rhodium(I)-Catalyzed Direct Carboxylation of Arenes with CO₂ via Chelation-Assisted C-H Bond Activation. *J. Am. Chem. Soc.* **2011**, 133 (5), 1251-1253.
15. León, T.; Correa, A.; Martin, R., Ni-Catalyzed Direct Carboxylation of Benzyl Halides with CO₂. *J. Am. Chem. Soc.* **2013**, 135 (4), 1221-1224.
16. Juhl, M.; Laursen, S. L. R.; Huang, Y.; Nielsen, D. U.; Daasbjerg, K.; Skrydstrup, T., Copper-Catalyzed Carboxylation of Hydroborated Disubstituted Alkenes and Terminal Alkynes with Cesium Fluoride. *Acc. Catal.* **2017**, 7 (2), 1392-1396.
17. Dian, L.; Müller, D. S.; Marek, I., Asymmetric Copper-Catalyzed Carbomagnesiation of Cyclopropenes. *Angew. Chem. Int. Ed.* **2017**, 56 (24), 6783-6787.
18. Gui, Y.-Y.; Hu, N.; Chen, X.-W.; Liao, L. L.; Ju, T.; Ye, J.-H.; Zhang, Z.; Li, J.; Yu, D.-G., Highly Regio- and Enantioselective Copper-Catalyzed Reductive Hydroxymethylation of Styrenes and 1,3-Dienes with CO₂. *J. Am. Chem. Soc.* **2017**, 139 (47), 17011-17014.
19. Chen, X.-W.; Zhu, L.; Gui, Y.-Y.; Jing, K.; Jiang, Y.-X.; Bo, Z.-Y.; Lan, Y.; Li, J.; Yu, D.-G., Highly Selective and Catalytic Generation of Acyclic Quaternary Carbon Stereocenters via Functionalization of 1,3-Dienes with CO₂. *J. Am. Chem. Soc.* **2019**, 141 (47), 18825-18835.
20. Liu, Y. G.; Chen, Q.; Mou, C. L.; Pan, L. T.; Duan, X. Y.; Chen, X. K.; Chen, H. Z.; Zhao, Y. L.; Lu, Y. P.; Jin, Z. C.; Chi, Y. R., Catalytic asymmetric acetalization of carboxylic acids for access to chiral phthalidyl ester prodrugs. *Nat. Commun.* **2019**, 10.
21. Pavlovic, Lj.; Vaitla, J.; Bayer, A.; Hopmann, K. H., Rhodium-Catalyzed Hydrocarboxylation: Mechanistic Analysis Reveals Unusual Transition State for Carbon-Carbon Bond Formation. *Organometallics* **2018**, 37 (6), 941-948.
22. García-López, D.; Pavlovic, Lj.; Hopmann, K. H., To Bind or Not to Bind: Mechanistic Insights into C-CO₂ Bond Formation with Late Transition Metals. *Organometallics* **2020**, 39 (8), 1339-1347.
23. Peng, Q.; Duarte, F.; Paton, R. S., Computing organic stereoselectivity - from concepts to quantitative calculations and predictions. *Chem. Soc. Rev.* **2016**, 45 (22), 6093-6107.
24. Hopmann, K. H., Quantum Chemical Studies of Asymmetric Reactions: Historical Aspects and Recent Examples. *Int. J. Quantum. Chem.* **2015**, 115 (18), 1232-1249.
25. Hopmann, K. H., Iron/Brønsted Acid Catalyzed Asymmetric Hydrogenation: Mechanism and Selectivity-Determining Interactions. *Chem. Eur. J.* **2015**, 21 (28), 10020-10030.
26. Davis, H. J.; Phipps, R. J., Harnessing non-covalent interactions to exert control over regioselectivity and site-selectivity in catalytic reactions. *Chem. Sci.* **2017**, 8 (2), 864-877.
27. Hopmann, K. H.; Bayer, A., On the Mechanism of Iridium-Catalyzed Asymmetric Hydrogenation of Imines and Alkenes: A Theoretical Study. *Organometallics* **2011**, 30 (9), 2483-2497.
28. Schlegel, H. B., Geometry optimization. *Wires Comput. Mol. Sci.* **2011**, 1 (5), 790-809.
29. Schlegel, H. B., Optimization Algorithms and Their Applications. *Abstr. Pap. Am. Chem. S* **1986**, 192, 148-Phys.
30. Schlegel, H. B., Optimization of Equilibrium Geometries and Transition Structures. *J. Comput. Chem.* **1982**, 3 (2), 214-218.
31. Zheng, J. J.; Frisch, M. J., Efficient Geometry Minimization and Transition Structure Optimization Using Interpolated Potential Energy Surfaces and Iteratively Updated Hessians. *J. Chem. Theory. Comput.* **2017**, 13 (12), 6424-6432.
32. Guan, Y.; Ingman, V. M.; Rooks, B. J.; Wheeler, S. E., AARON: An Automated Reaction Optimizer for New Catalysts. *J. Chem. Theory. Comput.* **2018**, 14 (10), 5249-5261.
33. Rosales, A. R.; Wahlers, J.; Limé, E.; Meadows, R. E.; Leslie, K. W.; Savin, R.; Bell, F.; Hansen, E.; Helquist, P.; Munday, R. H.; Wiest, O.; Norrby, P.-O., Rapid virtual screening of enantioselective catalysts using CatVS. *Nat. Catal.* **2019**, 2 (1), 41-45.
34. Gaussian 09, Revision D.01, Frisch M.J., Trucks G. W., Schlegel H.B., Scuseria G.E., Robb M.A., Cheesman J.R., Scalmani G., Barone V., Menussi B., Petersson G.A., Nakatsuji H., Caricato M., Li X., Hratchain H.P., Izmaylov A.F., Bloino J., Zheng G., Sonnenberg J.L., Hada M., Ehara M., Toyota K., Fukuda R., Hasegawa J., Ishida M., Nakajima T., Honda Y., Kitao O., Nakai H., Vreven T., Montgomery J.A., Jr., Peralta J.E., Ogliaro F., Bearpark M., Heyd J.J., Brothers E., Kudin K.N., Sraroverov V.N., Kobayashi R., Normand J., Raghavachari K., Rendell A., Burant J.C., Iyengar S.S., Tomasi J., Cossi M., Rega N., Millam J.K., Klane M., Knox J.E., Cross J.B., Bakken V., Adamo C., Jaramillo J., Gomperts R., Stratmann R.E., Yazeyev O., Austin A.J., Cammi R., Pomelli C., Ochterski J.W., Martin R.L., Morokuma K., Zakrzewski V.G., Voth G.A., Salvador P., Dannenberg J.J., Dapprich S., Daniels A.D., Farkas Ö, Foresman J.B., Ortiz J.V., Cioslowski J., Fox D.J., Gaussian, Inc., Wallingford CT, **2009**.
35. Becke, A.D., Density-functional exchange-energy approximation with correct asymptotic behavior. *Phys. Rev. A* **1988**, 38 (6), 3098-3100.
36. Lee, C.; Yang, W.; Parr, R. G., Development of the Colle-Salvetti correlation-energy formula into a functional of the electron density. *Phys. Rev. B* **1988**, 37 (2), 785-789.
37. Grimme, S., Semiempirical GGA-type density functional constructed with a long-range dispersion correction. *J. Comput. Chem.* **2006**, 27 (15), 1787-1799.
38. Tomasi, J.; Mennucci, B.; Cammi, R., Quantum Mechanical Continuum Solvation Models. *Chem. Rev.* **2005**, 105 (8), 2999-3094.
39. Tomasi, J.; Mennucci, B.; Cancès, E., The IEF version of the PCM solvation method: an overview of a new method addressed to study molecular solutes at the QM ab initio level. *J. Mol. Struct. Theochem.* **1999**, 464 (1-3), 211-226.
40. Cancès, E.; Mennucci, B.; Tomasi, J., A new integral equation formalism for the polarizable continuum model: Theoretical background and applications to isotropic and anisotropic dielectrics. *J. Chem. Phys.* **1997**, 107 (8), 3032-3041.
41. Ehlers, A. W.; Böhme, M.; Dapprich, S.; Gobbi, A.; Höllwarth, A.; Jonas, V.; Köhler, K. F.; Stegmann, R.; Veldkamp, A.; Frenking, G., A set of f-polarization functions for pseudo-potential basis sets of the transition metals Sc-Cu, Y-Ag and La-Au. *Chem. Phys. Lett.* **1993**, 208 (1), 111-114.

42. Cramer, C. J., *Essentials of computational chemistry : theories and models*. J. Wiley: West Sussex, England; New York, **2002**; p xvii, 542 p.
43. Hopmann, K. H., How Accurate is DFT for Iridium-Mediated Chemistry? *Organometallics* **2016**, *35* (22), 3795-3807.
44. Schneebeli, S. T.; Hall, M. L.; Breslow, R.; Friesner, R., Quantitative DFT modeling of the enantiomeric excess for dioxirane-catalyzed epoxidations. *J. Am. Chem. Soc.* **2009**, *131* (11), 3965-3973.
45. Cardoso, F. S. P.; Abboud, K. A.; Aponick, A., Design, Preparation, and Implementation of an Imidazole-Based Chiral Biaryl P,N-Ligand for Asymmetric Catalysis. *J. Am. Chem. Soc.* **2013**, *135* (39), 14548-14551.
46. Braunstein, P.; Naud, F.; Rettig, S. J., A new class of anionic phosphinooxazoline ligands in palladium and ruthenium complexes: catalytic properties for the transfer hydrogenation of acetophenone. *New J. Chem.* **2001**, *25* (1), 32-39.
47. Rokade, B. V.; Guiry, P. J., Axially Chiral P,N-Ligands: Some Recent Twists and Turns. *Acc. Catal.* **2018**, *8* (1), 624-643.
48. Desimoni, G.; Faita, G.; Jørgensen, K. A., C2-Symmetric Chiral Bis(Oxazoline) Ligands in Asymmetric Catalysis. *Chem. Rev.* **2006**, *106* (9), 3561-3651.
49. Bakos, J.; Orosz, Á.; Cserépi, S.; Tóth, I.; Sinou, D., Chiral sulfonated phosphines. Rhodium(I)-catalyzed asymmetric hydrogenolysis of epoxides. *J. Mol. Catal. A-Chem.* **1997**, *116* (1), 85-97.
50. Sparta, M.; Riplinger, C.; Neese, F., Mechanism of Olefin Asymmetric Hydrogenation Catalyzed by Iridium Phosphino-Oxazoline: A Pair Natural Orbital Coupled Cluster Study. *J. Chem. Theory. Comput.* **2014**, *10* (3), 1099-1108.
51. Trost, B. M.; Van Vranken, D. L., Asymmetric Transition Metal-Catalyzed Allylic Alkylations. *Chem. Rev.* **1996**, *96* (1), 395-422.
52. Evans, D. A.; Faul, M. M.; Bilodeau, M. T.; Anderson, B. A.; Barnes, D. M., Bis(oxazoline)-copper complexes as chiral catalysts for the enantioselective aziridination of olefins. *J. Am. Chem. Soc.* **1993**, *115* (12), 5328-5329.
53. Page, J. P.; RajanBabu, T. V., Asymmetric Hydrovinylation of 1-Vinylcycloalkenes. Reagent Control of Regio- and Stereoselectivity. *J. Am. Chem. Soc.* **2012**, *134* (15), 6556-6559.
54. Lee, H. M.; Youn, I. S.; Saleh, M.; Lee, J. W.; Kim, K. S., Interactions of CO₂ with various functional molecules. *Phys. Chem. Chem. Phys.* **2015**, *17* (16), 10925-10933.
55. Hernández-Marín, E.; Lemus-Santana, A. A., Theoretical Study of the Formation of Complexes Between CO₂ and Nitrogen Heterocycles. *J. Mex. Chem. Soc.* **2015**, *59*, 36-42.
56. Prakash, M.; Mathivon, K.; Benoit, D. M.; Chambaud, G.; Hochlaf, M., Carbon dioxide interaction with isolated imidazole or attached on gold clusters and surface: competition between σ H-bond and π stacking interaction. *Phys. Chem. Chem. Phys.* **2014**, *16* (24), 12503-12509.
57. Kajiya, D.; Saitow, K.-i., Site-Selective Solvation in Supercritical CO₂ Observed by Raman Spectroscopy: Phenyl Group Leads to Greater Attractive Energy than Chloro Group. *J. Phys. Chem. B* **2010**, *114* (50), 16832-16837.

Supporting Information (Draft)

Computational and experimental insights into asymmetric Rh-catalyzed hydrocarboxylation with CO₂

Ljiljana Pavlovic,[†] Martin Pettersen,[‡] Ashot Gevorgyan,[‡] Janakiram Vaitla,[‡] Annette Bayer,^{*,‡} and Kathrin H. Hopmann^{*,†}

[†]Hylleraas Centre for Quantum Molecular Sciences, Department of Chemistry, UiT The Arctic University of Norway, N-9037 Tromsø

[‡]Department of Chemistry, UiT The Arctic University of Norway, N-9037 Tromsø, Norway

Corresponding Author: annette.bayer@uit.no, kathrin.hopmann@uit.no

Contents

1. Proposed mechanism for Rh-catalyzed hydrocarboxylation.....	S2
2. Computational results for Rh-(<i>S</i>)-SEGPPOS	S3
3. The optimized TSs (C-CO ₂) with Rh-CO ₂ interactions	S4
4. The optimized geometries of Rh-enolate intermediates	S4
5. Computational results for with Rh-(<i>R</i>)-StackPhos	S5
6. Computational results for Rh-(<i>S</i>)- ⁱ Pr-PHOX	S7
7. Computational results for Rh-(<i>R,R</i>)- ^t Bu-BOX.....	S8
8. Computational results for Rh-(<i>R,R</i>)-BDPP	S9
9. Selected coordinates of some TSs geometries	S10

1. Proposed mechanism for Rh-catalyzed hydrocarboxylation

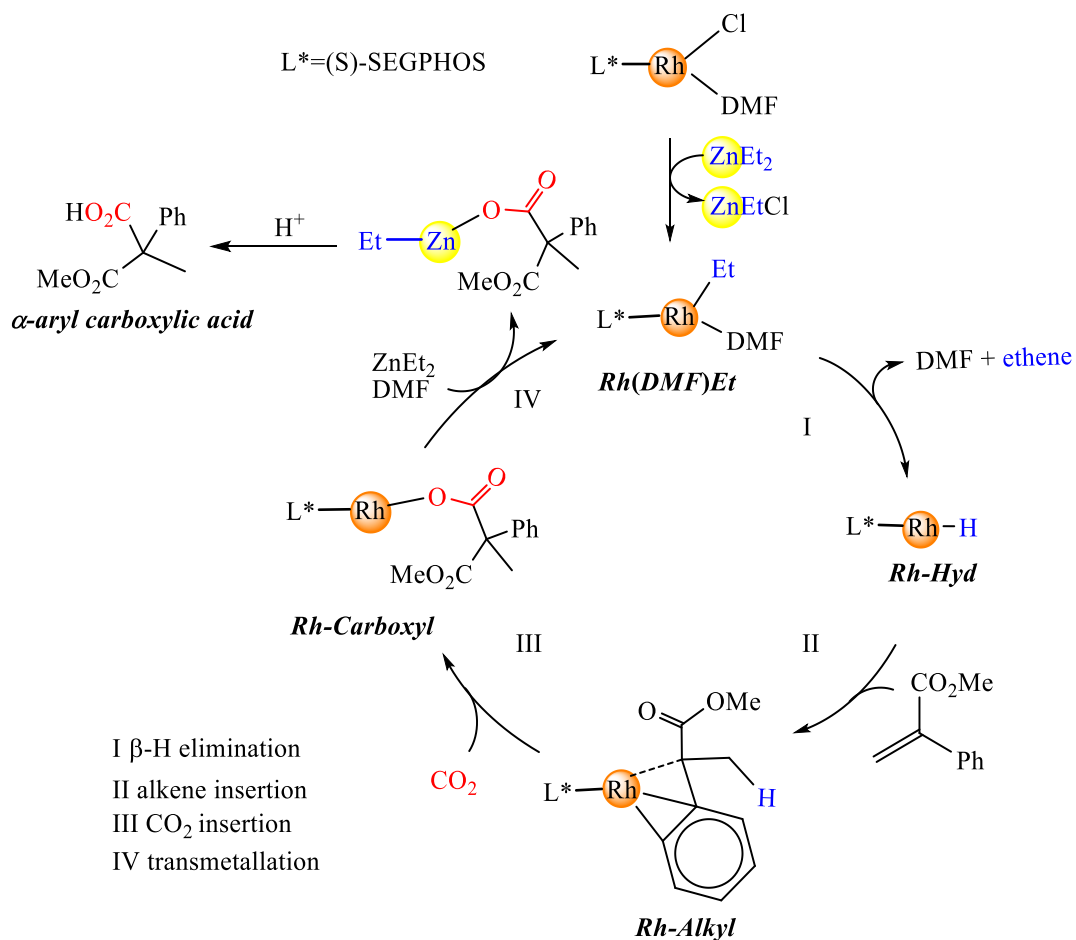


Figure S1. Mechanism for Rh-SEGPHOS-catalyzed hydrocarboxylation, based on the previous experimental proposal,¹ and computations performed in our previous computational study with COD ligand.²

2. Computational results for Rh-(*S*)-SEGPPOS

Table S1. Selected distances (Å) of noncovalent interactions at the TS conformations with Rh-(*S*)-SEGPPOS and methyl 2-phenylacrylate. The energy differences between pro-(*S*) and pro-(*R*) TSs ($\Delta\Delta G^\ddagger$) are given in kcal/mol. The computed *e.e.* is 53.8 % (Table 1, main text).

		TS	Stereo	CH...O (Cat-Sub)	CH... π (Sub-Cat)	C-H...O (within sub)	Rh-C (Nuc)	C-CO ₂	$\Delta\Delta G^\ddagger$	
Outer sphere insertion	Backside CO ₂ insertion	TS1a_S	pro-(<i>S</i>)	2.46	2.95; 3.08;3.60	2.16(Ph)	3.60	2.30	0.0	
		TS1b_S	pro-(<i>S</i>)	2.43	2.85; 3.20	2.40(Me)	3.70	2.20	3.1	
		TS1a_R	pro-(<i>R</i>)	2.97	3.16; 2.97;3.14	2.11(Ph)	3.64	2.26	0.7	
		TS1b_R	pro-(<i>R</i>)	3.32	3.24; 2.94	2.33(Me)	3.67	2.20	2.0	
	Frontside CO ₂ insertion	TS2a_S	pro-(<i>S</i>)	>4.00	2.93;2.95	2.14(Ph)	3.90	2.20	6.5	
		TS2b_S	pro-(<i>S</i>)	>4.00	3.00; 3.24	2.35(Me)	3.90	2.20	7.3	
		TS2a_R	pro-(<i>R</i>)	>4.00	2.95;2.94	2.28(Ph)	3.80	2.32	4.1	
		TS2b_R	pro-(<i>R</i>)	>4.00	2.90; 2.94	2.40(Me)	3.96	2.30	4.9	
	Rh-Ester interaction	TS3_S	pro-(<i>S</i>)	(Rh-Ester)* 2.17	2.71;3.16	2.47(Ph)	3.43	2.45	8.3	
		TS3_R	pro-(<i>R</i>)	2.17	2.64;3.24	2.53(Ph)	3.60	2.30	7.9	
	Inner sphere	Rh-CO ₂ interaction	TS 4_S	pro-(<i>S</i>)	(Rh-CO ₂)* 2.18	2.93; 4.02	2.21(Ph)	2.80	2.23	17.3
			TS 4_R	pro-(<i>R</i>)	2.60	2.82;3.06	2.21(Ph)	2.71	2.07	18.7

3. The optimized TSs (C-CO₂) with Rh-CO₂ interactions

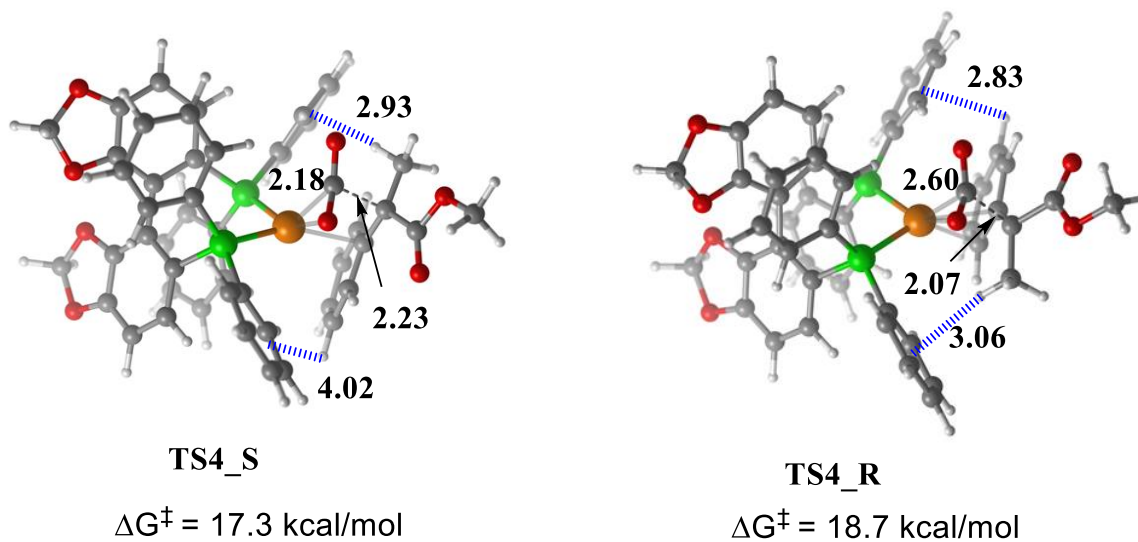


Figure S2. The optimized TSs for C-CO₂ bond formation step with Rh-CO₂ interaction present (inner sphere CO₂ insertion, TS4_S and TS4_R), with methyl 2-phenylacrylate and (*S*)-SEGPHOS (distances in Å).

4. The optimized geometries of Rh-enolate intermediates

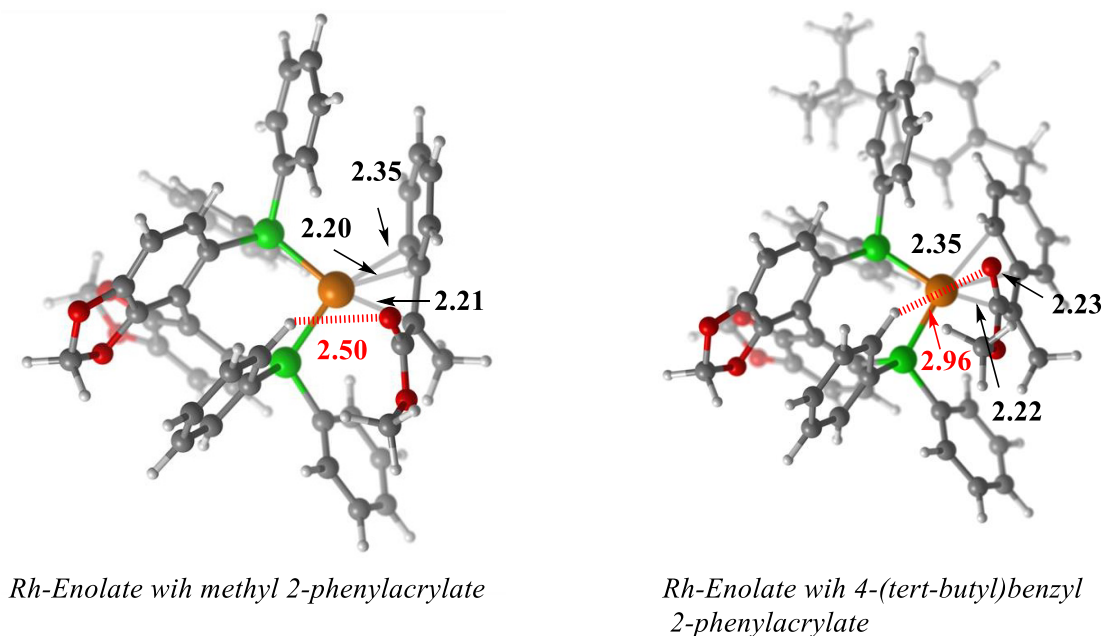


Figure S3. The optimized Rh-Enolate structures. On the left side is given the Rh-Enolate intermediate with methyl 2-phenyl acrylate substrate. On the right side is given Rh-Enolate intermediate with 4-(tert-butyl)benzyl 2-phenylacrylate substrate (distances in Å).

5. Computational results for with Rh-(*R*)-StackPhos

Table S2. Selected distances (Å) of noncovalent interactions at the TS conformations with Rh-(*R*)-StackPhos and methyl 2-phenylacrylate. The energy difference between pro-(*S*) and pro-(*R*) TSs ($\Delta\Delta G^\ddagger$) are given in kcal/mol. The computed e.e. is 47.0 % (Table 1, main text)

	TS	Stereo	C-CO ₂	Rh-C (Nuc)	Imidazole-CO ₂		CH... π (Sub-Cat)	F- π	CH...F	$\Delta\Delta G^\ddagger$
					C _{CO2} -N _{Im}	O _{CO2} -Im.ring				
Backside CO ₂ insertion	TS1a_S	pro-(<i>S</i>)	2.26	3.68	-	-	2.53; 3.16	2.78	2.37 ⁱ	2.2
	TS1b_S	pro-(<i>S</i>)	2.24	3.78	-	-	3.33; 3.32, ⁱⁱ 2.80	2.78	2.37	2.1
	TS1a_R	pro-(<i>R</i>)	2.55	3.48	-	-	2.56; 3.46 ⁱⁱⁱ	2.90	2.45	2.8
	TS1b_R	pro-(<i>R</i>)	2.55	3.52	-	-	2.58; 3.31 ^{iv}	2.94	2.47	3.0
Frontside CO ₂ insertion	TS2a_S	pro-(<i>S</i>)	2.21	3.73	3.22	3.10	2.64;3.28	3.05	2.54	0.0
	TS2b_S	pro-(<i>S</i>)	2.21	3.74	3.26	3.10	2.66; 3.26	3.03	2.53	0.8
	TS2_Stack_2_S	Pro-(<i>S</i>)	2.21	3.73	3.21	3.08	2.66;3.40	2.95	π - π 3.46	0.8
	TS2a_R	pro-(<i>R</i>)	2.23	3.85	3.17	3.26	2.84; 3.18	3.02	2.53 ^v	0.6
	TS2b_R	pro-(<i>R</i>)	2.20	3.85	3.16	3.28	2.73; 3.30	2.96	3.16	1.0
	TS2_Stack_2_R	pro-(<i>R</i>)	2.23	3.83	3.15	3.23	2.82, 3.28	2.91	π - π 3.48	1.9
Rh-Ester interaction	TS3_S	pro-(<i>S</i>)	2.53	2.97	-	-	3.02; 3.50 ^{vi}	2.77	2.31; 2.52	15.2
	TS3_R	pro-(<i>R</i>)	2.32	3.56	-	-	3.07 ^{vii}	2.84	2.40; 2.55	10.8

ⁱ There is one CH...O interaction at 2.54 Å. An intramolecular CH...O interaction is at 2.19 Å.

ⁱⁱ There is one weak CH...O interaction at 3.10 Å

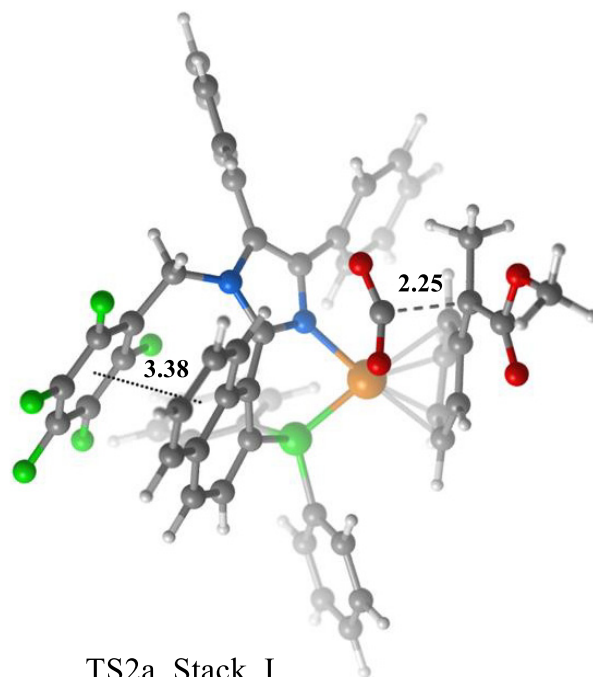
ⁱⁱⁱ There is one CH... π interaction between the Me of the ester and naphthalene ring (2.60 Å). A CH...O interaction is identified at 2.3 Å.

^{iv} There is one CH... π interaction between the Me of the ester and naphthalene ring (2.60 Å).

^v An intramolecular CH...O interaction is at 2.22 Å.

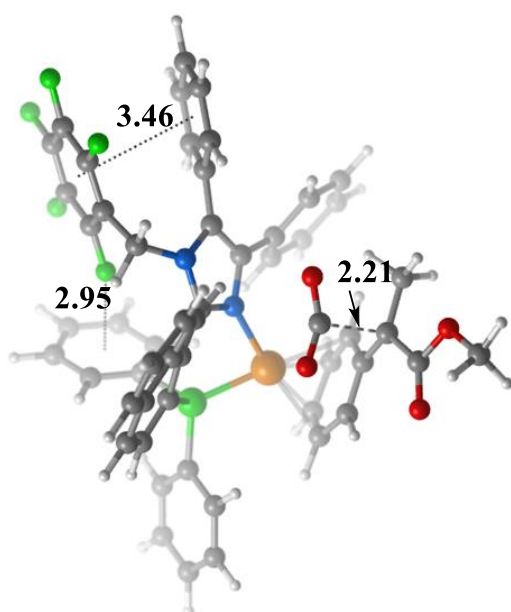
^{vi} A Rh-O=C(ester) interaction is at 2.16 Å.

^{vii} A Rh-O=C(ester) interaction is at 2.26 Å.

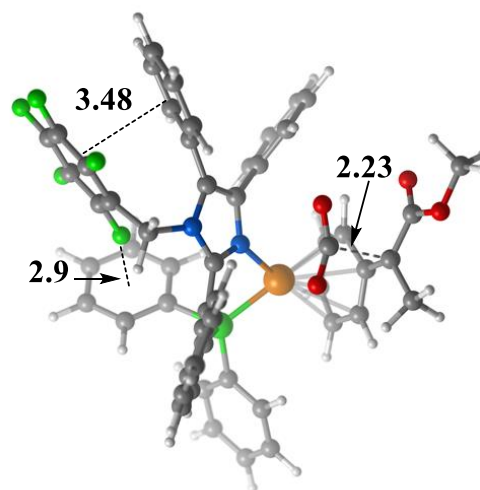


TS2a_Stack_I
 $\Delta G^\ddagger = 2.5$ kcal/mol

Figure S4. Illustration of stacking interaction between the the pentafluorophenyl group and naphthalene ring, at the **TS2a_Stack_I** (distances are in Å).



TS2a_Stack_S
 $\Delta G^\ddagger = 0.8$ kcal/mol



TS2a_Stack_R
 $\Delta G^\ddagger = 1.9$ kcal/mol

Figure S5. Illustration of stacking interaction between the pentafluorophenyl group and the second phenyl group linked to imidazole ring, at the **TS2a_Stack_S** and **TS2a_Stack_R**. The pentafluorophenyl group also forms F- π interaction with the phenyl group, which is attached to the phosphorus (distances in Å).

6. Computational results for Rh-(*S*)-ⁱPr-PHOX

Table S3. Selected distances (Å) of noncovalent interactions at the TS conformations with Rh-(*S*)-ⁱPr-PHOX and methyl 2-phenylacrylate. The energy difference between pro-(*S*) and pro-(*R*) TSs ($\Delta\Delta G^\ddagger$) are given in kcal/mol. The computed *e.e.* is 1.8 (*R*) % (Table 1, main text).

	TS	Stereo	C-CO ₂	CH...O (Sub-Lig)		CH... π (Sub...Lig)		Rh-C (Nuc)	$\Delta\Delta G^\ddagger$
Backside CO ₂ insertion	TS1a_S	pro-(<i>S</i>)	2.09	2.25		3.35		3.77	0.0
	TS1b_S	pro-(<i>S</i>)	2.13	2.64		2.47		3.67	3.1
	TS1a_R	pro-(<i>R</i>)	2.02	2.28		3.34		3.88	0.0
	TS1b_R	pro-(<i>R</i>)	2.04	2.51		3.30		3.88	1.4
Frontside CO ₂ insertion				CH...O	CH... π	N...C* ^{viii}	O...H ^{ix}		
	TS2a_S	pro-(<i>S</i>)	2.23	-	3.65	3.40	2.48	3.82	1.8
	TS2b_S	pro-(<i>S</i>)	2.23	-	3.52	3.44	2.49	3.84	2.8
	TS2a_R	pro-(<i>R</i>)	2.20	2.38	3.36	3.25	2.46	3.74	2.8
	TS2b_R	pro-(<i>R</i>)	2.20	-	3.48	3.28	2.45	3.78	3.4
Rh-Estar	TS3_S	pro-(<i>S</i>)	2.25	Rh-O(Es)	CH... π			3.28	12.3
				2.12	2.53;3.11				
	TS3_R	pro-(<i>R</i>)	2.15	2.09	3.64			3.19	6.5

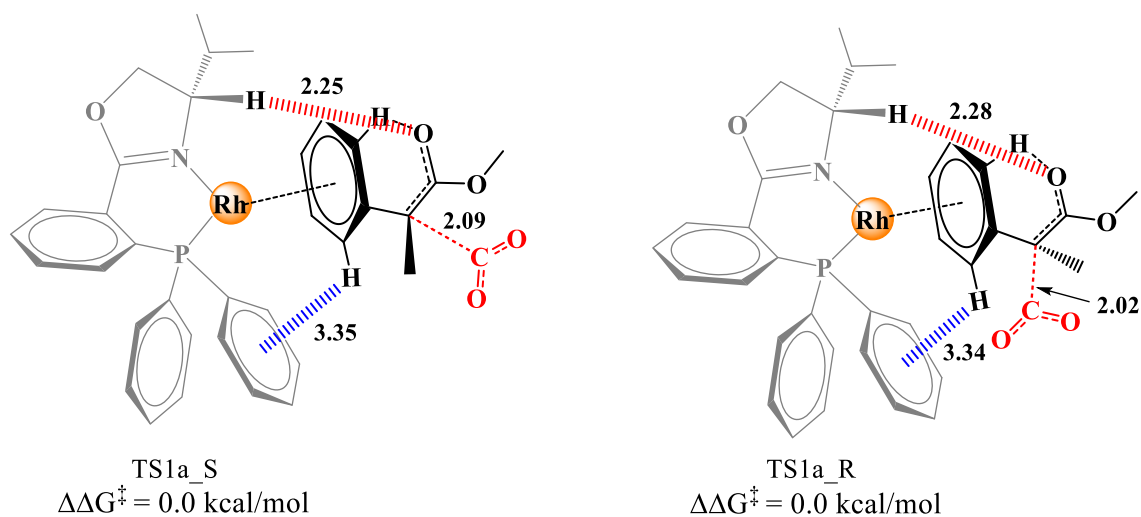


Figure S6. Illustration of the noncovalent interactions in the lowest lying pro-(*S*) and pro-(*R*) TS1a carboxylation structures with Rh-(*S*)-ⁱPr-PHOX (distances are in Å).

^{viii} A N...C interaction is between the N of the oxazoline ring and C of the CO₂

^{ix} A O...H interaction is between the H of the oxazoline ring and O of the CO₂

7. Computational results for Rh-(*R,R*)-^tBu-BOX

Table S4. Selected distances (Å) of noncovalent interactions at the TS conformations with Rh-(*R,R*)-^tBu-BOX and methyl 2-phenylacrylate. The energy difference between pro-(*S*) and pro-(*R*) TSs ($\Delta\Delta G^\ddagger$) are given in kcal/mol. The computed *e.e.* is 6.4 % (*S*) (Table 1, main text).

	TS	Stereo	C-CO ₂	Rh-C (Nuc)	CH...O (Sub-Lig)	N...H(π)	$\Delta\Delta G^\ddagger$
Backside CO ₂ insertion	TS1a_S	pro-(<i>S</i>)	1.98	3.56	2.64	3.34	1.9
	TS1b_S	pro-(<i>S</i>)	2.23	3.90	-	3.40	3.1
	TS1a_R	pro-(<i>R</i>)	2.25	3.76	2.43, 2.72	2.91	0.7
	TS1b_R	pro-(<i>R</i>)	2.26	3.89	3.01	2.92	0.8
Frontside CO ₂ insertion					N(Ox)-C(CO ₂)	H(Ox)-O(CO ₂)	
	TS2a_S	pro-(<i>S</i>)	2.21	4.03	3.48	2.46	0.0
	TS2b_S	pro-(<i>S</i>)	2.26	4.05	3.87	2.35	3.6
	TS2a_R	pro-(<i>R</i>)	2.14	3.96	3.54	2.60	0.5
	TS2b_R	pro-(<i>R</i>)	2.13	3.92	3.61	2.43	2.5
Rh-Estar					Rh-O(Est)	CH- π	
	TS3_S	pro-(<i>S</i>)	2.54	3.06	2.10	2.50	3.2
	TS3_R	pro-(<i>R</i>)	2.39	3.08	2.11	2.53	5.3

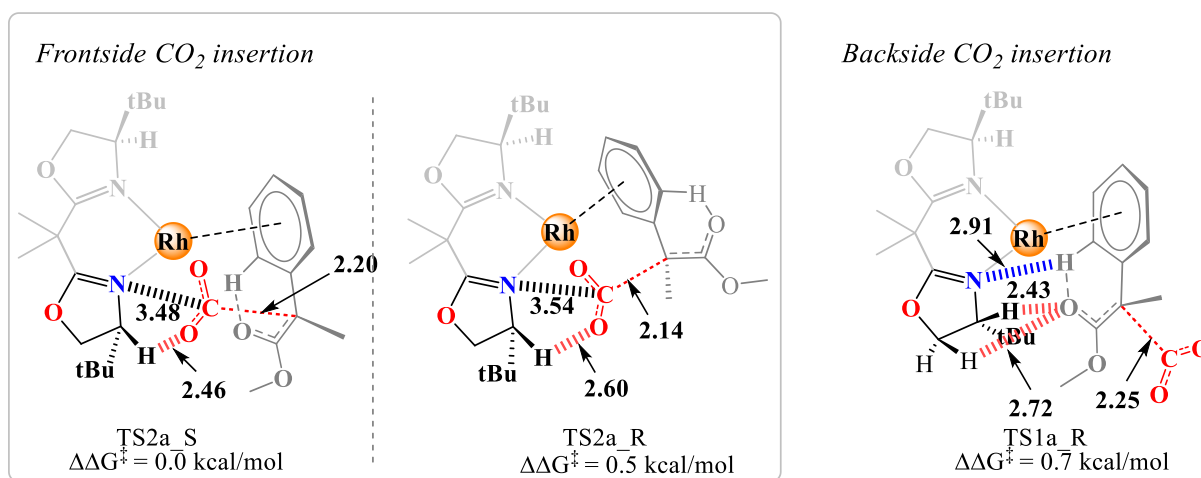


Figure S7. Illustration of the noncovalent interactions at the lowest lying pro-(*S*) and pro-(*R*) TS2a carboxylation structures alongside TS1a_R conformation with Rh-(*R,R*)-^tBu-BOX (distances are in Å).

8. Computational results for Rh-(*R,R*)-BDPP

Table S5. Selected distances (Å) of noncovalent interactions at the TS conformations with Rh-(*R,R*)-BDPP and methyl 2-phenylacrylate. The energy difference between pro-(*S*) and pro-(*R*) TSs ($\Delta\Delta G^\ddagger$) are given in kcal/mol. The computed *e.e.* is 24.3 (*R*) % (Table 1, main text).

	TS	Stereo	C-CO ₂	Rh-C (Nuc)	CH...O (Sub-Lig)	CH... π (Sub-Lig)	$\Delta\Delta G^\ddagger$
Backside CO ₂ insertion	TS1a_S	pro-(<i>S</i>)	2.22	3.64	2.31	3.28; 3.40	0.5
	TS1b_S	pro-(<i>S</i>)	2.22	3.72	3.20	2.83; 3.13; 3.35	0.8
	TS1a_R	pro-(<i>R</i>)	2.21	3.64	2.46	3.00; 3.10; 3.40	0.0
	TS1b_R	pro-(<i>R</i>)	2.18	3.68	2.74	3.11; 3.36	1.9
Frontside CO ₂ insertion	TS2a_S	pro-(<i>S</i>)	2.38	3.82	-	3.38; 3.38	5.8
	TS2b_S	pro-(<i>S</i>)	2.31	3.86	-	3.53; 3.47	8.6
	TS2a_R	pro-(<i>R</i>)	2.45	3.85	-	3.30; 3.47	5.5
	TS2b_R	pro-(<i>R</i>)	2.42	3.82	-	3.36; 3.35	6.4
Rh-Estar	TS3_S	pro-(<i>S</i>)	2.45	3.40	Rh..O(Est) (2.20)	2.52; 3.23	9.7
	TS3_R	pro-(<i>R</i>)	2.28	3.28	Rh..O(Est) (2.22)	2.36; 3.58	12.1

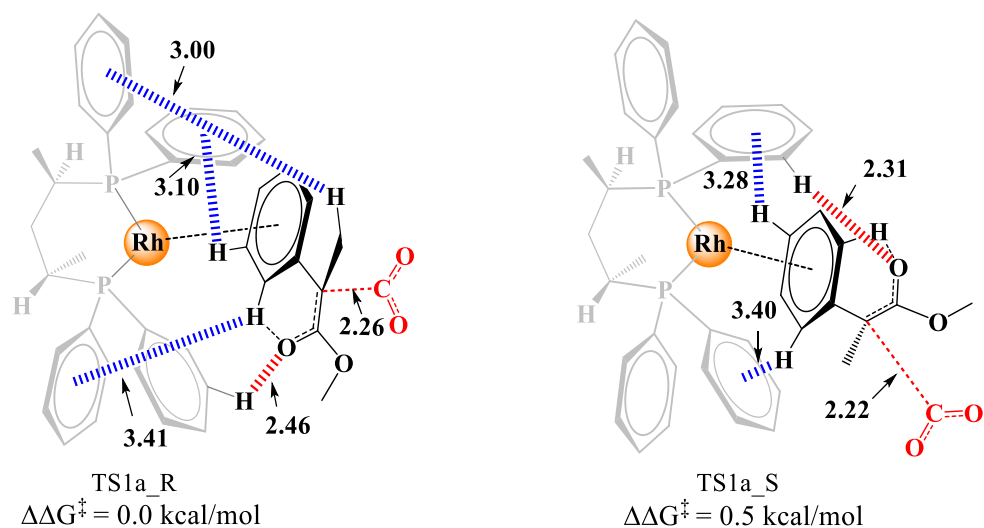


Figure S8. Illustration of the noncovalent interactions in the lowest lying pro-(*S*) and pro-(*R*) TS1a carboxylation structures with Rh-(*R,R*)-BDPP (distances are in Å).

9. Selected coordinates of some TSs geometries

<u>methvl 2-phenylacrylate</u>			
<u>Rh-(S)-SEGPPOS</u>			
TS1a_S			
G298K=-3281.596028			
Img. Freq.=-158.4095			
C	0.244454000	-2.607263000	-3.201689000
C	0.391107000	-2.781934000	-1.811519000
C	1.067553000	-3.913970000	-1.327692000
C	1.584524000	-4.860020000	-2.223746000
C	1.422826000	-4.689124000	-3.603564000
C	0.746909000	-3.561341000	-4.091663000
P	-0.172868000	-1.427418000	-0.698219000
C	0.172485000	-2.036027000	0.999960000
C	1.101509000	-1.338870000	1.785463000
C	1.368771000	-1.768549000	3.090387000
C	0.710364000	-2.891635000	3.608235000
C	-0.216931000	-3.590980000	2.820183000
C	-0.491476000	-3.162514000	1.517457000
P	-0.714477000	1.696556000	-0.216305000
C	-0.083279000	3.391868000	0.123281000
C	-0.710357000	4.539089000	-0.391818000
C	-0.143923000	5.803767000	-0.180192000
C	1.043587000	5.932683000	0.550059000
C	1.672410000	4.789655000	1.064472000
C	1.120372000	3.523459000	0.845521000
C	-2.310000000	1.946179000	-1.096382000
C	-2.449273000	1.465436000	-2.406020000
C	-3.674312000	1.596732000	-3.070552000
C	-4.754819000	2.220168000	-2.431978000
C	-4.611558000	2.714873000	-1.126767000
C	-3.394137000	2.570376000	-0.454018000
C	-1.272736000	1.048992000	1.415414000
C	-2.109500000	-0.109346000	1.425308000
C	-2.372695000	-0.659430000	2.672494000
C	-1.857996000	-0.135115000	3.862859000
C	-1.073284000	1.003948000	3.869912000
C	-0.786889000	1.583046000	2.616978000
O	-2.285326000	-0.884800000	4.927152000
C	-2.948439000	-2.032524000	4.345807000
O	-3.146238000	-1.759061000	2.940733000
C	-2.724571000	-0.732520000	0.222842000
C	-4.099895000	-0.659384000	0.049767000
C	-4.764033000	-1.239716000	-1.036853000
C	-4.083507000	-1.968008000	-1.996472000
C	-2.685299000	-2.061492000	-1.845533000
C	-2.007678000	-1.457521000	-0.777209000
O	-6.110032000	-1.003792000	-0.941329000
C	-6.258865000	-0.077469000	0.161419000
O	-5.003557000	-0.042290000	0.875258000
H	-0.165404000	2.477667000	2.595930000
H	-1.636476000	4.448211000	-0.962663000
H	1.639716000	2.635353000	1.214282000
H	-1.594746000	0.962039000	-2.870107000
H	-3.286427000	2.926015000	0.573753000
H	-0.687325000	1.429317000	4.796788000
H	-0.635505000	6.689346000	-0.589774000
H	2.603245000	4.880186000	1.629438000
H	-3.789775000	1.203869000	-4.083391000
H	-5.452896000	3.203858000	-0.629576000
H	1.481901000	6.919950000	0.713572000
H	-5.712422000	2.317384000	-2.949011000
H	-2.294840000	-2.915468000	4.451202000
H	-3.925536000	-2.169952000	4.828864000
H	-2.123618000	-2.628598000	-2.587419000
H	-4.601371000	-2.441554000	-2.831057000
H	-7.048513000	-0.438469000	0.834245000
H	-6.470393000	0.927715000	-0.241736000
H	1.204640000	-4.052594000	-0.253623000
H	1.582629000	-0.449524000	1.367116000
H	-1.229912000	-3.688698000	0.907169000
H	2.118425000	-5.731355000	-1.837592000
H	0.621524000	-3.417752000	-5.167300000
H	2.087699000	-1.222397000	3.704512000
H	-0.730224000	-4.467053000	3.224327000
H	1.828054000	-5.427703000	-4.298887000
H	0.914861000	-3.222405000	4.629357000
H	-0.248990000	-1.709391000	-3.581563000
Rh	0.866404000	0.473378000	-1.247279000
C	4.053025000	-0.404061000	0.126678000
C	4.995561000	-2.234728000	0.774453000
C	4.270739000	-1.899900000	0.024016000
C	3.328476000	-2.460906000	0.176964000
H	4.671651000	-2.168993000	-0.965751000
C	3.287375000	0.229395000	-0.926090000
C	2.746754000	-0.537666000	-2.029969000
C	2.958843000	1.623883000	-0.962633000
C	2.137962000	0.058299000	-3.177626000
H	2.853478000	-1.621761000	-2.027590000
C	2.225262000	2.188790000	-2.036747000
H	3.265893000	2.248266000	-0.131342000
C	1.872978000	1.441147000	-3.200771000
H	1.832404000	-0.582841000	-4.004797000
H	1.948242000	3.242698000	-1.972471000
H	1.372787000	1.913637000	-4.045383000
C	4.059204000	0.202842000	1.445533000
O	3.638777000	1.322358000	1.779590000
O	4.633086000	-0.625010000	2.402404000
C	4.734086000	-0.042558000	3.712558000
H	3.740378000	0.228292000	4.105030000
H	5.195114000	-0.814187000	4.342466000
H	5.360039000	0.863988000	3.695360000
C	6.124555000	0.430917000	-0.414846000
O	6.788373000	-0.563729000	-0.491225000
O	5.974473000	1.617553000	-0.479327000
TS1a_R			
G298K=-3281.594517			
Img. Freq.=-171.3843			
C	0.986217000	-1.485677000	-3.490255000
C	1.047744000	-2.012115000	-2.185512000
C	1.774907000	-3.188139000	-1.948466000
C	2.420724000	-3.837532000	-3.008715000
C	2.343554000	-3.320960000	-4.307779000
C	1.624052000	-2.141482000	-4.547930000
P	0.191370000	-1.082582000	-0.847153000
C	0.549561000	-1.987512000	0.711282000
C	1.260309000	-1.322943000	1.721162000
C	1.519385000	-1.969380000	2.934075000
C	1.071223000	-3.281535000	3.137770000
C	0.363942000	-3.949078000	2.126349000
C	0.094581000	-3.301497000	0.915670000
P	-1.099170000	1.692671000	0.152110000
C	-0.938403000	3.394541000	0.840339000
C	-1.759531000	4.449737000	0.407469000
C	-1.535817000	5.753288000	0.871946000
C	-0.498147000	6.014573000	1.774462000
C	0.324903000	4.966284000	2.210090000
C	0.112799000	3.667423000	1.738877000
C	-2.625847000	1.760719000	-0.869379000
C	-2.522393000	1.584037000	-2.256054000
C	-3.675399000	1.600195000	-3.049951000
C	-4.929736000	1.801373000	-2.458991000
C	-5.032447000	1.990322000	-1.072342000
C	-3.884066000	1.963645000	-0.274918000
C	-1.608528000	0.632634000	1.571569000
C	-2.131152000	-0.664642000	1.277959000
C	-2.337498000	-1.500450000	2.366836000
C	-2.049802000	-1.124357000	3.683293000
C	-1.575314000	0.139535000	3.984853000
C	-1.356533000	1.010722000	2.897801000
O	-2.358096000	-2.148648000	4.539892000
C	-2.669299000	-3.276449000	3.687610000
O	-2.845798000	-2.773802000	2.344841000
C	-2.509494000	-1.138805000	-0.078693000
C	-3.854175000	-1.312766000	-0.376604000
C	-4.308446000	-1.754140000	-1.623333000
C	-3.426778000	-2.086294000	-2.636445000
C	-2.054339000	-1.922558000	-2.360794000
C	-1.589671000	-1.453060000	-1.123778000
O	-5.676712000	-1.810574000	-1.630487000
C	-6.096677000	-1.249228000	-0.363654000
O	-4.917706000	-1.075380000	0.454259000
H	-0.986349000	2.012307000	3.112601000
H	-2.569929000	4.257223000	-0.297792000
H	0.777255000	2.860630000	2.053746000
H	-1.530599000	1.406182000	-2.684857000
H	-3.962723000	2.081180000	0.808792000
H	-1.376694000	0.447923000	5.011759000
H	-2.177306000	6.565968000	0.523253000
H	1.140733000	5.160739000	2.910084000
H	-3.596870000	1.444563000	-4.128426000
H	-6.010213000	2.152064000	-0.611684000
H	-0.326436000	7.031686000	2.133876000
H	-5.830606000	1.806432000	-3.077066000
H	-1.818040000	-3.979101000	3.698199000
H	-3.605587000	-3.739818000	4.026764000
H	-1.339867000	-2.176403000	-3.143360000
H	-3.775661000	-2.447867000	-3.604228000
H	-6.782499000	-1.949620000	0.134002000
H	-6.558158000	-0.263834000	-0.543631000
H	1.859420000	-3.581695000	-0.935362000
H	1.590014000	-0.295005000	1.539537000
H	-0.480714000	-3.806831000	0.135970000
H	2.993258000	-4.747580000	-2.814372000
H	1.565173000	-1.727973000	-5.557413000
H	2.071399000	-1.448547000	3.719385000
H	0.014635000	-4.972371000	2.285033000
H	2.849426000	-3.830503000	-5.131215000
H	1.269568000	-3.785872000	4.086613000
H	0.442141000	-0.554176000	-3.667141000
Rh	0.822387000	1.062695000	-0.842785000
C	4.047776000	0.532839000	0.750499000

H	4.813662000	0.674750000	2.767271000	Rh	0.907042000	0.878817000	-0.772126000
C	4.101647000	1.191405000	2.113957000	C	4.655806000	0.963678000	0.279522000
H	4.431579000	2.237896000	2.025024000	H	6.094938000	1.731021000	1.708649000
H	3.111315000	1.185453000	2.611590000	C	5.229181000	2.083033000	1.135630000
C	3.237528000	1.191496000	-0.253777000	H	5.546461000	2.942249000	0.515237000
C	2.938804000	0.637749000	-1.561504000	H	4.478588000	2.443110000	1.855225000
C	2.623672000	2.460473000	0.002346000	C	3.535384000	1.330009000	-0.567690000
C	2.315316000	1.392222000	-2.599510000	C	3.008604000	0.512421000	-1.648264000
H	3.283695000	-0.372167000	-1.768787000	C	2.811706000	2.539384000	-0.346783000
C	1.867642000	3.139725000	-0.988607000	C	2.166397000	1.044521000	-2.668994000
H	2.711847000	2.922731000	0.982838000	H	3.413243000	-0.487463000	-1.775180000
C	1.769406000	2.664308000	-2.329366000	C	1.807925000	2.973378000	-1.250087000
H	2.220832000	0.945027000	-3.589226000	H	3.026684000	3.163868000	0.518519000
H	1.366725000	4.068166000	-0.710053000	C	1.552409000	2.303786000	-2.482233000
H	1.247836000	3.239575000	-3.093372000	H	1.966285000	0.455947000	-3.564022000
C	4.228020000	-0.911842000	0.684625000	H	1.259395000	3.888073000	-1.020933000
O	4.031688000	-1.661166000	-0.278083000	H	0.864142000	2.721722000	-3.215983000
O	4.702084000	-1.433179000	1.880374000	C	5.567486000	-0.088022000	-0.173776000
C	4.848136000	-2.863512000	1.890200000	O	5.377402000	-0.933641000	-1.052840000
H	5.494839000	-3.203276000	1.066280000	O	6.737767000	-0.113243000	0.563422000
H	5.301549000	-3.105530000	2.860373000	C	7.626121000	-1.197590000	0.237686000
H	3.862915000	-3.350044000	1.800511000	H	7.139291000	-2.168944000	0.419800000
C	6.014710000	1.108728000	-0.196233000	H	7.936504000	-1.151163000	-0.818038000
O	6.089285000	0.468899000	-1.208088000	H	8.494007000	-1.073832000	0.897885000
O	6.452210000	1.922972000	0.570389000	C	3.574404000	-0.224326000	1.777159000
				O	3.215961000	0.593938000	2.586884000
				O	3.604407000	-1.371146000	1.416538000

TS2a_S

G298K= -3281.587533

Img. Freq.= -240.4899

C	1.562047000	-2.213661000	-2.752985000
C	1.363019000	-2.401350000	-1.370909000
C	2.121189000	-3.372586000	-0.695905000
C	3.049963000	-4.151982000	-1.397667000
C	3.227740000	-3.974693000	-2.774715000
C	2.478721000	-3.002888000	-3.453274000
P	0.252039000	-1.245302000	-0.466581000
C	0.140244000	-1.946183000	1.230596000
C	0.519781000	-1.155327000	2.321773000
C	0.376688000	-1.646783000	3.623415000
C	-0.136561000	-2.933459000	3.834536000
C	-0.505564000	-3.731671000	2.741120000
C	-0.375801000	-3.237357000	1.439035000
P	-1.051646000	1.652731000	0.020352000
C	-0.805857000	3.343210000	0.701126000
C	-1.573908000	4.448436000	0.302509000
C	-1.286099000	5.722157000	0.813246000
C	-0.240684000	5.896723000	1.727788000
C	0.528658000	4.794179000	2.128470000
C	0.255059000	3.524653000	1.611205000
C	-2.389892000	1.795003000	-1.234012000
C	-2.108147000	1.492635000	-2.574816000
C	-3.132256000	1.524687000	-3.528338000
C	-4.435951000	1.869361000	-3.146769000
C	-4.717467000	2.179414000	-1.807889000
C	-3.700131000	2.132183000	-0.849068000
C	-1.894073000	0.735730000	1.368179000
C	-2.466076000	-0.531579000	1.045806000
C	-2.979139000	-1.253758000	2.113899000
C	-2.928472000	-0.797757000	3.435644000
C	-2.396328000	0.438394000	3.756699000
C	-1.874561000	1.198475000	2.690625000
O	-3.485161000	-1.726977000	4.272606000
C	-3.795978000	-2.869462000	3.438629000
O	-3.581762000	-2.482480000	2.063061000
C	-2.559467000	-1.097231000	-0.326126000
C	-3.813324000	-1.230262000	-0.907714000
C	-4.013117000	-1.779519000	-2.178231000
C	-2.956736000	-2.267881000	-2.925694000
C	-1.670740000	-2.146907000	-2.359792000
C	-1.453397000	-1.567725000	-1.101905000
O	-5.349590000	-1.781221000	-2.482697000
C	-5.984743000	-1.033817000	-1.418266000
O	-5.017887000	-0.874631000	-0.357098000
H	-1.442032000	2.174471000	2.912697000
H	-2.388057000	4.320494000	-0.413541000
H	0.880384000	2.671161000	1.888858000
H	-1.088725000	1.197675000	-2.842675000
H	-3.924288000	2.333952000	0.201362000
H	-2.370089000	0.801320000	4.784552000
H	-1.881986000	6.579364000	0.491260000
H	1.351222000	4.925012000	2.835413000
H	-2.915276000	1.269196000	-4.568137000
H	-5.734095000	2.445402000	-1.508104000
H	-0.019300000	6.890763000	2.122991000
H	-5.236234000	1.889128000	-3.890388000
H	-3.109668000	-3.694785000	3.691211000
H	-4.851967000	-3.142616000	3.577126000
H	-0.825944000	-2.533446000	-2.927927000
H	-3.108398000	-2.723000000	-3.904967000
H	-6.846495000	-1.600913000	-1.040638000
H	-6.265820000	-0.036988000	-1.799401000
H	2.006841000	-3.500530000	0.380736000
H	0.899638000	-0.148176000	2.135991000
H	-0.686660000	-3.844281000	0.584910000
H	3.642262000	-4.896169000	-0.860171000
H	2.617545000	-2.849055000	-4.525825000
H	0.657078000	-1.020885000	4.473584000
H	-0.904153000	-4.736081000	2.904498000
H	3.954619000	-4.583610000	-3.317119000
H	-0.254699000	-3.314969000	4.851618000
H	1.008505000	-1.430086000	-3.273341000

TS2a_R

G298K= -3281.590520

Img. Freq.= -219.6442

C	0.707080000	-2.718264000	-2.905922000
C	0.668601000	-2.799602000	-1.499334000
C	1.352932000	-3.845953000	-0.857071000
C	2.050143000	-4.800547000	-1.609873000
C	2.066509000	-4.725146000	-3.007329000
C	1.390107000	-3.681102000	-3.654625000
P	-0.093450000	-1.423581000	-0.538938000
C	-0.111707000	-2.039250000	1.195357000
C	0.540069000	-1.299489000	2.189322000
C	0.481414000	-1.718026000	3.522986000
C	-0.218693000	-2.883196000	3.861282000
C	-0.865319000	-3.630360000	2.864280000
C	-0.821471000	-3.205658000	1.532766000
P	-0.720555000	1.688383000	-0.071812000
C	-0.073661000	3.320690000	0.473517000
C	-0.660942000	4.540222000	0.101292000
C	-0.073615000	5.749513000	0.499469000
C	1.093114000	5.746509000	1.273552000
C	1.681799000	4.528943000	1.645853000
C	1.108364000	3.319640000	1.241462000
C	-2.148097000	2.039093000	-1.177409000
C	-2.086909000	1.622453000	-2.515676000
C	-3.186231000	1.816923000	-3.359625000
C	-4.345022000	2.435329000	-2.870371000
C	-4.405494000	2.857835000	-1.534006000
C	-3.313837000	2.651959000	-0.683776000
C	-1.549321000	1.003018000	1.415281000
C	-2.394479000	-0.133765000	1.238629000
C	-2.887966000	-0.708411000	2.401646000
C	-2.574863000	-0.231697000	3.679094000
C	-1.777870000	0.884484000	3.861060000
C	-1.266760000	1.493606000	2.697449000
O	-3.181746000	-1.007749000	4.629865000
C	-3.805023000	-2.096391000	3.906481000
O	-3.711890000	-1.798603000	2.495745000
C	-2.775858000	-0.719650000	-0.073625000
C	-4.097407000	-0.624377000	-0.488997000
C	-4.566175000	-1.181859000	-1.683147000
C	-3.732686000	-1.906716000	-2.515660000
C	-2.383524000	-2.018199000	-2.120739000
C	-1.894614000	-1.435947000	-0.943105000
O	-5.907511000	-0.935560000	-1.819461000
C	-6.235610000	-0.016949000	-0.750272000
O	-5.128005000	-0.012185000	0.177163000
H	-0.627133000	2.369780000	2.808511000
H	-1.566952000	4.549093000	-0.507763000
H	1.592895000	2.372009000	1.492397000
H	-1.180650000	1.114542000	-2.861421000
H	-3.372396000	2.946680000	0.367018000
H	-1.545370000	1.266152000	4.855634000
H	-0.530326000	6.695511000	0.199302000
H	2.597580000	4.519977000	2.241646000
H	-3.143782000	1.475292000	-4.396497000
H	-5.309687000	3.336772000	-1.150459000
H	1.548650000	6.690930000	1.580201000
H	-5.205698000	2.581893000	-3.527300000
H	-3.251724000	-3.027380000	4.114371000
H	-4.864302000	-2.162620000	4.193244000
H	-1.712701000	-2.591961000	-2.758435000
H	-4.098449000	-2.369355000	-3.432876000
H	-7.138880000	-0.368738000	-0.233871000
H	-6.353750000	0.996239000	-1.171693000
H	1.353828000	-3.908766000	0.232494000
H	1.053125000	-0.377418000	1.905300000
H	-1.346598000	-3.768059000	0.756409000
H	2.584841000	-5.603380000	-1.097058000
H	1.405585000	-3.607257000	-4.744385000
H	0.975085000	-1.128370000	4.298548000
H	-1.413075000	-4.538606000	3.127761000

H	2.611008000	-5.470469000	-3.591381000
H	-0.268716000	-3.207958000	4.903317000
H	0.221614000	-1.883033000	-3.414275000
Rh	0.933427000	0.503608000	-1.029606000
C	4.580485000	-0.309917000	-0.323933000
H	5.519264000	-2.206282000	0.100240000
C	4.828768000	-1.773366000	-0.631929000
H	3.889438000	-2.347176000	-0.579330000
H	5.258697000	-1.920299000	-1.641159000
C	3.544433000	0.363757000	-1.068853000
C	2.790263000	-0.327409000	-2.097526000
C	3.123578000	1.712525000	-0.839636000
C	1.989788000	0.349982000	-3.065717000
H	2.946528000	-1.395452000	-2.241461000
C	2.191752000	2.342013000	-1.700985000
H	3.532664000	2.257958000	0.004512000
C	1.687685000	1.715639000	-2.882478000
H	1.589149000	-0.203877000	-3.914238000
H	1.873177000	3.359004000	-1.466923000
H	1.045589000	2.258399000	-3.575309000
C	5.667615000	0.491543000	0.214760000
O	5.722482000	1.722018000	0.338548000
O	6.731743000	-0.295864000	0.639627000
C	7.812463000	0.437945000	1.240159000
H	8.250271000	1.155135000	0.527506000
H	7.468102000	0.992664000	2.128026000
H	8.556515000	-0.316691000	1.526602000
C	3.647907000	-0.441026000	1.798931000
O	3.320982000	0.678687000	2.070893000
O	3.747966000	-1.610414000	2.027403000

TS4_S

G298K=-3281.572916

Img. Freq.=-210.1447

Rh	1.382292000	0.117695000	0.135730000
P	-0.243735000	1.621483000	0.370153000
P	-0.090920000	-1.462365000	-0.399717000
C	1.189397000	2.598298000	2.553808000
C	0.473934000	2.963491000	1.396399000
C	0.370330000	4.318076000	1.040655000
C	0.966007000	5.297959000	1.845239000
C	1.665658000	4.933579000	3.002654000
C	1.776357000	3.581373000	3.356207000
C	-0.995335000	2.428001000	-1.096300000
C	-0.491652000	2.155936000	-2.376587000
C	-1.123996000	2.704125000	-3.498574000
C	-2.242774000	3.533306000	-3.343442000
C	-2.732352000	3.820762000	-2.060997000
C	-2.118077000	3.260877000	-0.936376000
C	0.666258000	-2.806349000	-1.392027000
C	0.577734000	-4.157659000	-1.016079000
C	1.171903000	-5.143504000	-1.811737000
C	1.845402000	-4.791133000	-2.989779000
C	1.946805000	-3.444082000	-3.358322000
C	1.376761000	-2.449799000	-2.553310000
C	-0.991266000	-2.276838000	0.976382000
C	-0.683879000	-1.907749000	2.292416000
C	-1.424168000	-2.435026000	3.355486000
C	-2.466386000	-3.337327000	3.104419000
C	-2.769122000	-3.714109000	1.787366000
C	-2.039876000	-3.17872000	0.720764000
C	-1.493167000	-0.877825000	-1.453137000
C	-2.539557000	-0.121432000	-0.837621000
C	-3.519578000	0.372964000	-1.687637000
C	-3.497826000	0.179793000	-3.072368000
C	-2.504343000	-0.566764000	-3.679408000
C	-1.502992000	-1.091962000	-2.839106000
O	-4.565454000	0.809001000	-3.650901000
C	-5.250371000	1.495181000	-2.575097000
O	-4.605864000	1.127193000	-1.334783000
C	-2.628403000	0.184263000	0.611647000
C	-3.663050000	-0.336565000	1.374593000
C	-3.790557000	-0.092360000	2.746875000
C	-2.907587000	0.730555000	3.424728000
C	-1.854748000	1.286637000	2.671641000
C	-1.704003000	1.025467000	1.302384000
O	-4.877068000	-0.758874000	3.240849000
C	-5.416697000	-1.516452000	2.130221000
O	-4.671590000	-1.155815000	0.946240000
H	-0.716750000	-1.688835000	-3.298820000
H	0.056647000	-4.438143000	-0.099505000
H	1.516507000	-1.393773000	-2.803330000
H	0.117163000	-1.185201000	2.461936000
H	-2.299044000	-3.440243000	-0.308100000
H	-2.489435000	-0.734383000	-4.756616000
H	1.105824000	-6.191511000	-1.510481000
H	2.493389000	-3.159481000	-4.260341000
H	-1.195576000	-2.130877000	4.379444000
H	-3.584539000	-4.414192000	1.589977000
H	2.301372000	-5.564800000	-3.611679000
H	-3.050477000	-3.742062000	3.934397000
H	-5.150578000	2.582616000	-2.723128000
H	-6.300616000	1.169208000	-2.547767000
H	-1.143861000	1.941262000	3.176250000
H	-3.016198000	0.931188000	4.490847000
H	-6.473851000	-1.247688000	1.988569000
H	-5.278222000	-2.591590000	2.329067000
H	-0.167160000	4.607925000	0.135979000
H	0.370799000	1.494046000	-2.484218000
H	-2.522380000	3.448108000	0.061353000
H	0.884408000	6.349966000	1.562337000

H	2.327296000	3.289731000	4.253257000
H	-0.748364000	2.473239000	-4.498068000
H	-3.602945000	4.469382000	-1.937197000
H	2.129717000	5.701630000	3.625587000
H	-2.738378000	3.952661000	-4.222134000
H	1.294225000	1.541446000	2.812591000
C	4.038877000	-0.500987000	-0.394687000
H	4.700423000	-0.811866000	-2.422765000
C	4.390702000	-1.404040000	-1.555065000
H	5.213350000	-2.093983000	-1.284268000
H	3.530161000	-2.011800000	-1.852824000
C	3.381819000	-1.142215000	0.773554000
C	3.078752000	-0.426676000	1.980911000
C	3.063789000	-2.534332000	0.771033000
C	2.599807000	-1.091122000	3.120509000
H	3.342861000	0.628103000	2.038946000
C	2.568422000	-3.175592000	1.906375000
H	3.233236000	-3.122254000	-0.131003000
C	2.357156000	-2.468637000	3.099936000
H	2.416405000	-0.513528000	4.031077000
H	2.350076000	-4.245640000	1.857639000
H	1.977642000	-2.979289000	3.987555000
C	5.030276000	0.551263000	-0.091881000
O	5.212191000	1.140230000	0.974461000
O	5.791430000	0.862462000	-1.198372000
C	6.716085000	1.948642000	-1.002836000
H	6.177068000	2.874607000	-0.745639000
H	7.430893000	1.718896000	-0.197564000
H	7.239452000	2.062916000	-1.960423000
C	2.709534000	1.007697000	-1.353808000
O	2.706717000	0.821877000	-2.561029000
O	2.687904000	1.959884000	-0.534649000

Rh-(R)-StackPhos

TS2a_S

G298K=-3476.407035

Img. Freq.=-221.2953

C	4.593409000	-0.074311000	0.606824000
H	5.376839000	1.903619000	0.982011000
C	4.997611000	1.312705000	0.141070000
H	5.781304000	1.275747000	-0.638952000
H	4.131184000	1.848264000	-0.272298000
C	3.951192000	-0.946013000	-0.364605000
C	3.534880000	-2.281615000	-0.087337000
C	3.605203000	-0.436383000	-1.686118000
C	2.787111000	-3.003150000	-1.047760000
H	3.730600000	-2.704394000	0.893012000
C	3.078490000	-1.240986000	-2.721178000
H	3.844632000	0.597281000	-1.931313000
C	2.586397000	-2.532605000	-2.389265000
H	2.401663000	-3.989633000	-0.785500000
H	2.960086000	-0.827877000	-3.722388000
H	2.107472000	-3.169612000	-3.133045000
C	5.376668000	-0.685530000	1.680980000
O	5.392396000	-1.867425000	2.038682000
O	6.142405000	0.250838000	2.359972000
C	6.878591000	-0.278951000	3.476572000
H	6.197373000	-0.709009000	4.228302000
H	7.581643000	-1.062057000	3.151262000
H	7.425031000	0.574131000	3.898895000
C	2.861419000	0.347037000	1.920928000
O	2.690265000	1.535680000	1.812136000
O	2.525465000	-0.700091000	2.406298000
Rh	1.451356000	-1.185364000	-1.075714000
N	0.576849000	0.546583000	-0.334610000
N	-0.607414000	1.941871000	0.934508000
C	-0.241755000	0.625630000	0.732820000
C	0.763282000	1.836835000	-0.809214000
C	0.035202000	2.714482000	-0.025397000
C	-0.741417000	-0.491623000	1.531442000
C	-0.847371000	-0.368548000	2.959537000
C	-1.572005000	-1.370396000	3.695767000
C	-2.101225000	-2.490154000	3.004519000
C	-1.834034000	-2.674090000	1.660813000
C	-1.131334000	-1.694240000	0.912866000
C	-0.196639000	0.666708000	3.690951000
C	-0.332858000	0.756651000	5.064624000
C	-1.123544000	-0.181958000	5.776700000
C	-1.717323000	-1.232864000	5.104267000
P	-0.551783000	-2.065293000	-0.803431000
C	-1.909071000	-1.526312000	-1.914314000
C	-0.631365000	-3.897236000	-0.891305000
C	-1.815523000	2.388054000	1.654481000
C	1.609821000	2.175326000	-1.957040000
C	-0.085006000	4.169837000	-0.121825000
H	-2.681728000	-3.230929000	3.560145000
H	-2.167191000	-3.585248000	1.160839000
H	0.450544000	1.367008000	3.158126000
H	0.186481000	1.549266000	5.607985000
H	-1.235162000	-0.087404000	6.859074000
H	-2.293900000	-1.988684000	5.643690000
C	-1.083371000	-1.083386000	-3.205447000
C	-3.256103000	-1.634206000	-1.526859000
C	-3.941026000	-0.861942000	-3.723820000
C	-4.268395000	-1.307095000	-2.435011000
C	-2.599319000	-0.749201000	-4.109757000
H	-0.528031000	-1.014712000	-3.486304000
H	-2.343205000	-0.400435000	-5.112835000
H	-4.735518000	-0.596009000	-4.424459000
H	-5.314742000	-1.383500000	-2.132417000

Table with 3 columns: ID, Value 1, Value 2. Rows include H, C, and Rh labels with numerical values.

TS2a_R

G298K=-3476.406594
Img. Freq.=-232.4419

Table with 3 columns: ID, Value 1, Value 2. Rows include C, H, O, N, P, Rh labels with numerical values.

Table with 3 columns: ID, Value 1, Value 2. Rows include H, C, and Rh labels with numerical values.

Rh-(R-R)-tBu-BOX

TS2a_S

G298K=-1760.049975
Img. Freq.=-233.9518

Table with 3 columns: ID, Value 1, Value 2. Rows include C, H, O, N, Rh labels with numerical values.

C	2.377449000	2.101033000	2.979628000
H	-1.793166000	1.935878000	-0.681750000
H	-0.908288000	4.390735000	0.579840000
H	-1.915199000	3.104248000	1.362197000
H	5.488683000	0.530893000	-0.254084000
H	4.248540000	1.503489000	-1.132247000
H	3.342923000	-0.648086000	-1.760618000
C	-0.080426000	2.073451000	-2.814567000
H	0.308601000	2.584816000	-3.710638000
H	0.601767000	1.253853000	-2.538736000
H	-1.061113000	1.634948000	-3.064412000
C	-1.187099000	4.192277000	-2.116876000
H	-1.278878000	5.000170000	-1.373453000
H	-0.817184000	4.641127000	-3.052615000
H	-2.191429000	3.778067000	-2.307334000
C	1.159070000	3.681402000	-1.341224000
H	1.565787000	4.185209000	-2.232405000
H	1.100838000	4.423770000	-0.528230000
H	1.866056000	2.889863000	-1.043072000
C	4.802832000	-1.779209000	1.210998000
H	5.275337000	-2.732497000	1.496770000
H	5.546973000	-0.978885000	1.347666000
H	3.960915000	-1.599499000	1.899443000
C	3.337805000	-3.053812000	-0.350092000
H	2.910365000	-3.128427000	-1.363106000
H	3.865770000	-3.993893000	-0.122204000
H	2.516548000	-2.926125000	0.368724000
C	5.500301000	-2.107912000	-1.188597000
H	6.014855000	-3.041561000	-0.910466000
H	5.156776000	-2.199440000	-2.232538000
H	6.236837000	-1.289464000	-1.136341000
H	0.616304000	-0.794767000	2.135013000
H	0.331347000	0.301874000	3.513830000
H	1.897422000	-0.566791000	3.377862000
H	2.790289000	2.966534000	2.444282000
H	3.194416000	1.583170000	3.501648000
H	1.647370000	2.453664000	3.720526000

TS2a_R

G298K=-1760.048134
 Img. Freq.=-227.3649

C	-3.613912000	-0.587007000	-0.411909000
H	-5.217036000	0.848537000	-0.662909000
C	-4.268591000	0.579612000	-1.140837000
H	-3.628974000	1.473743000	-1.109644000
H	-4.468648000	0.331684000	-2.198675000
C	-2.357349000	-1.082005000	-0.946638000
C	-1.567656000	-0.219522000	-1.839324000
C	-1.719281000	-2.286140000	-0.590382000
C	-0.521632000	-0.706629000	-2.683154000
H	-1.949693000	0.774420000	-2.068379000
C	-0.438494000	-2.577483000	-1.137415000
H	-2.173463000	-2.952642000	0.136529000
C	0.107506000	-1.919125000	-2.287292000
H	-0.175150000	-0.124620000	-3.537746000
H	0.079595000	-3.464979000	-0.772780000
C	0.965335000	-2.326908000	-2.821909000
C	-4.508707000	-1.534300000	0.272807000
O	-4.251122000	-2.675010000	0.660155000
O	-5.751776000	-0.982925000	0.522885000
C	-6.645096000	-1.835388000	1.263660000
H	-6.834163000	-2.774342000	0.720082000
H	-6.223480000	-2.078647000	2.251865000
H	-7.573900000	-1.261448000	1.373081000
C	-2.839972000	0.306417000	1.374884000
O	-2.471421000	-0.573485000	2.112756000
O	-2.957928000	1.498945000	1.202593000
Rh	0.334225000	-0.415547000	-0.720091000
O	0.443928000	2.877883000	1.923193000
O	3.908662000	0.483807000	1.238692000
N	0.283056000	1.449806000	0.183410000
N	2.239348000	-0.569963000	0.139974000
C	-0.406150000	2.681814000	-0.291364000
C	-0.539165000	3.490569000	1.015640000
C	0.758343000	1.699676000	1.367275000
C	1.648832000	0.765145000	2.159049000
C	2.600525000	0.169827000	1.144278000
C	4.500121000	0.013792000	-0.024263000
C	3.495183000	-1.037003000	-0.519718000
C	0.392141000	3.414045000	-1.409093000
C	3.884735000	-2.490320000	-0.118234000
C	0.774751000	-0.356890000	2.774331000
C	2.401545000	1.518502000	3.268106000
H	-1.399539000	2.405633000	-0.670844000
H	-0.274283000	4.550509000	0.927726000
H	-1.525446000	3.361728000	1.479146000
H	5.496809000	-0.379853000	0.205225000
H	4.575744000	0.886170000	-0.690788000
H	3.356922000	-0.992017000	-1.609377000
C	0.514110000	2.523523000	-2.653738000
H	1.051067000	3.071527000	-3.445590000
H	1.058286000	1.594396000	-2.422468000
H	-0.482695000	2.251755000	-3.039204000
C	-0.390872000	4.681468000	-1.797934000
H	-0.460917000	5.403725000	-0.969039000
H	0.118747000	5.183223000	-2.636002000
C	-1.413177000	4.422956000	-2.121450000
C	1.798168000	3.789735000	-0.914332000
H	2.342754000	4.319748000	-1.711756000
H	1.760106000	4.450648000	-0.033025000
H	2.371380000	2.886226000	-0.650216000

C	4.218805000	-2.596750000	1.379959000
H	4.466184000	-3.642655000	1.621959000
H	5.080855000	-1.971839000	1.661309000
H	3.353887000	-2.303078000	1.996799000
C	2.724367000	-3.443092000	-0.423181000
H	2.417993000	-3.374184000	-1.479129000
H	3.030707000	-4.481077000	-0.215494000
H	1.861601000	-3.195555000	0.210671000
C	5.107997000	-2.893563000	-0.959006000
H	5.397160000	-3.928764000	-0.717105000
H	4.875066000	-2.841431000	-2.035652000
H	5.977788000	-2.246260000	-0.760481000
H	0.247915000	-0.916241000	1.987366000
H	0.027684000	0.087637000	3.447299000
H	1.420002000	-1.040122000	3.347794000
H	3.012186000	2.335131000	2.859865000
H	3.058183000	0.815318000	3.799439000
H	1.675377000	1.935507000	3.978667000

Rh-(R,R)-BDPP

TS1a_R

G298K=-2639.545415
 Img. Freq.=-176.3976

C	2.467899000	-1.727521000	-1.101638000
H	4.493937000	-1.556145000	-0.369313000
C	3.690919000	-0.908327000	-0.738420000
H	4.076171000	-0.371557000	-1.618505000
H	3.453677000	-0.168155000	0.047808000
C	1.362543000	-1.022992000	-1.725958000
C	0.087131000	-1.603713000	-2.023859000
C	1.487435000	0.375504000	-2.090226000
C	-0.917538000	-0.859731000	-2.693639000
H	-0.105951000	-2.626135000	-1.712297000
C	0.535976000	1.070319000	-2.898626000
H	2.384886000	0.919278000	-1.801236000
C	-0.688358000	0.450095000	-3.216429000
H	-1.895083000	-1.321217000	-2.844590000
H	0.746703000	2.094641000	-3.208506000
H	-1.453054000	0.962063000	-3.799386000
C	2.186529000	-2.916881000	-0.303809000
O	1.120877000	-3.538959000	-0.209259000
O	3.309514000	-3.373714000	0.366423000
C	3.117513000	-4.601413000	1.089512000
H	2.804315000	-5.411513000	0.412105000
H	4.091228000	-4.831551000	1.540347000
H	2.352022000	-4.485728000	1.874023000
C	3.095378000	-2.814063000	-2.924014000
O	2.215394000	-3.593300000	-3.181241000
O	4.162182000	-2.328130000	-3.197536000
Rh	-0.412393000	0.477490000	-0.859545000
P	0.512820000	1.749678000	0.731872000
P	-2.304161000	0.245495000	0.323150000
C	0.153143000	3.688667000	2.797110000
C	-0.586996000	2.902604000	1.708797000
H	-0.929048000	3.617508000	0.941509000
C	-1.813986000	2.184042000	2.295604000
H	-2.304036000	2.895610000	2.984376000
H	-1.486790000	1.330004000	2.914665000
C	-2.880868000	1.738200000	1.275970000
H	-3.776843000	1.420540000	1.835187000
C	-3.292362000	2.857434000	0.310067000
C	1.498686000	0.787264000	1.951649000
C	1.696812000	2.932789000	-0.038050000
C	-3.775518000	-0.185690000	-0.702274000
C	-2.246816000	-1.110261000	1.570372000
H	1.057320000	4.179686000	2.404199000
H	-0.518218000	4.468308000	3.193013000
H	0.442008000	3.033314000	3.632869000
H	-2.500434000	3.054231000	-0.432478000
H	-4.207022000	2.588631000	-0.237215000
H	-3.481602000	3.785048000	0.875150000
C	1.362625000	-0.610915000	1.920302000
H	0.702905000	-1.058316000	1.174295000
C	2.074503000	-1.414571000	2.817345000
H	1.956284000	-2.499314000	2.778226000
C	2.940248000	-0.828291000	3.747682000
H	3.501421000	-1.453855000	4.446055000
C	3.096525000	0.565546000	3.775011000
H	3.780819000	1.026771000	4.490963000
C	2.381172000	1.372704000	2.883471000
H	2.525092000	2.453542000	2.903824000
C	3.091611000	2.805419000	0.069496000
H	3.523833000	2.010162000	0.679369000
C	3.935523000	3.692857000	-0.612664000
H	5.018721000	3.581749000	-0.523912000
C	3.394927000	4.713361000	-1.403562000
H	4.054345000	5.404653000	-1.933167000
C	2.002946000	4.839556000	-1.521593000
H	1.573722000	5.627654000	-2.144557000
C	1.159088000	3.949441000	-0.850382000
H	0.075815000	4.030178000	-0.975344000
C	-3.948652000	0.463870000	-1.938288000
H	-3.191772000	1.177234000	-2.274024000
C	-5.071192000	0.192259000	-2.727630000
H	-5.198032000	0.703227000	-3.685010000
C	-6.024754000	-0.739900000	-2.294040000
H	-6.896719000	-0.959358000	-2.914566000
C	-5.854466000	-1.392924000	-1.066632000
H	-6.593081000	-2.122887000	-0.726939000
C	-4.735411000	-1.116922000	-0.269851000

H	-4.605694000	-1.630752000	0.685437000
C	-1.503303000	-2.255183000	1.235774000
H	-0.961519000	-2.291379000	0.287405000
C	-1.404428000	-3.326255000	2.128771000
H	-0.801485000	-4.193930000	1.851862000
C	-2.047783000	-3.262428000	3.372437000
H	-1.963435000	-4.091893000	4.078658000
C	-2.793815000	-2.126279000	3.712748000
H	-3.295836000	-2.069484000	4.681475000
C	-2.899136000	-1.054668000	2.815331000
H	-3.487978000	-0.180681000	3.100151000

C	2.938122000	0.843922000	2.924639000
H	3.383601000	-0.110936000	3.208552000

Rh-(S)-iPr-PHOX

TS1a_S
G298K=-2234.325961

Img. Freq.= -195.3431			
P	2.021072000	0.340768000	0.071300000
O	-0.011801000	-3.284788000	1.701916000
N	-0.284297000	-1.363202000	0.553310000
C	2.428494000	-0.505479000	1.652119000
C	3.557368000	-0.122002000	2.394085000
H	4.166104000	0.714591000	2.045064000
C	3.912872000	-0.799139000	3.566707000
H	4.795441000	-0.483881000	4.127299000
C	3.141882000	-1.881080000	4.009591000
H	3.414273000	-2.415428000	4.921808000
C	2.015713000	-2.275533000	3.286061000
H	1.404566000	-3.110456000	3.630678000
C	1.636989000	-1.593630000	2.111307000
C	0.432030000	-2.037247000	1.413588000
C	-1.320616000	-3.411060000	1.054118000
H	-2.090084000	-3.288116000	1.831309000
H	-1.377704000	-4.416557000	0.617731000
C	-1.331798000	-2.276158000	0.021724000
H	-2.291379000	-1.744224000	0.006680000
C	-0.990315000	-2.702391000	-1.421885000
C	-2.176590000	-3.472141000	-2.014549000
H	-2.328334000	-4.429467000	-1.485287000
H	-1.991582000	-3.705961000	-3.074784000
H	-3.103187000	-2.881988000	-1.933106000
C	0.314968000	-3.498912000	-1.512514000
H	1.162581000	-2.930850000	-1.098894000
H	0.547897000	-3.722649000	-2.565360000
H	0.234662000	-4.459285000	-0.974620000
C	2.936877000	1.925517000	0.144394000
C	2.560034000	2.858333000	1.130134000
H	1.774312000	2.600664000	1.845852000
C	3.186781000	4.106055000	1.189047000
H	2.895489000	4.824234000	1.958771000
C	4.181212000	4.436885000	0.255722000
H	4.664762000	5.415475000	0.297675000
C	4.551696000	3.514243000	-0.729812000
H	5.325212000	3.769963000	-1.457518000
C	3.934658000	2.256768000	-0.786725000
H	4.228930000	1.534762000	-1.551736000
C	2.905021000	-0.655841000	-1.197272000
C	2.326968000	-0.764363000	-2.472901000
H	1.357958000	-0.288891000	-2.653731000
C	2.970764000	-1.500654000	-3.473489000
H	2.517318000	-1.585221000	-4.463823000
C	4.186007000	-2.142371000	-3.197994000
H	4.683002000	-2.727806000	-3.975040000
C	4.760110000	-2.043235000	-1.922577000
H	5.703515000	-2.549553000	-1.705490000
C	4.124819000	-1.298099000	-0.922039000
H	4.570256000	-1.225556000	0.073519000
Rh	-0.137196000	0.512886000	-0.257210000
C	-0.228261000	2.146584000	-1.714671000
C	-1.160068000	1.211153000	-2.251014000
C	-0.486858000	2.710581000	-0.422070000
C	-2.232412000	0.779317000	-1.448407000
H	-1.008658000	0.770210000	-3.240178000
C	-1.656640000	2.387796000	0.308795000
H	0.221966000	3.431337000	-0.011903000
C	-2.554547000	1.382875000	-0.167594000
H	-2.888330000	-0.011432000	-1.803601000
H	-1.831098000	2.883030000	1.261473000
H	0.646010000	2.463464000	-2.284319000
C	-3.765741000	1.058214000	0.589389000
C	-3.818348000	1.596177000	2.010975000
H	-4.746215000	1.293994000	2.508401000
H	-2.962894000	1.228143000	2.606989000
H	-3.791603000	2.695587000	2.003614000
C	-4.463054000	-0.211744000	0.339705000
O	-4.318281000	-0.986844000	-0.612510000
O	-5.420583000	-0.471894000	1.294852000
C	-6.196951000	-1.663751000	1.063244000
H	-5.551669000	-2.556117000	1.051698000
H	-6.907139000	-1.714674000	1.897896000
H	-6.732378000	-1.599896000	0.103289000
H	-0.860946000	-1.757634000	-1.979589000
C	-5.031832000	2.296799000	-0.510806000
O	-5.246344000	1.781688000	-1.586304000
O	-5.241818000	3.267838000	0.183889000

TS1a_R
G298K=-2234.325879

Img. Freq.= -201.3416			
P	-2.078664000	0.278243000	0.012947000
O	-0.255259000	-3.559065000	-1.342888000
N	0.142413000	-1.403098000	-0.812307000
C	-2.855591000	-0.943908000	-1.116244000
C	-4.198102000	-0.800095000	-1.502905000
H	-4.762913000	0.0609774000	-1.161860000
C	-4.821880000	-1.759098000	-2.309471000
H	-5.866939000	-1.626796000	-2.597306000
C	-4.108125000	-2.886740000	-2.733912000
H	-4.588999000	-3.640522000	-3.360304000
C	-2.773677000	-3.047258000	-2.358296000

TS1a_S
G298K=-2639.544319

Img. Freq.= -174.5166			
C	-1.975488000	2.384592000	-0.914865000
H	-2.106449000	4.330858000	0.017987000
C	-1.342366000	3.657661000	-0.386726000
H	-0.612792000	3.445876000	0.417236000
H	-0.823859000	4.197027000	-1.193702000
C	-1.096264000	1.460841000	-1.609980000
C	0.245695000	1.823831000	-1.959084000
C	-1.460340000	0.113600000	-1.992628000
C	1.082792000	0.967443000	-2.727010000
H	0.653204000	2.783979000	-1.647156000
C	-0.658846000	-0.702019000	-2.847161000
H	-2.429216000	-0.255233000	-1.667361000
C	0.620809000	-0.269695000	-3.259714000
H	2.106908000	1.285560000	-2.928196000
H	-1.038584000	-1.682900000	-3.138840000
H	1.254336000	-0.879405000	-3.902804000
C	-3.155612000	1.878917000	-0.222770000
O	-3.709120000	0.781407000	-0.360033000
O	-3.699306000	2.819524000	0.636269000
C	-4.892291000	2.388738000	1.314738000
H	-4.675133000	1.528467000	1.967304000
H	-5.214271000	3.249906000	1.914734000
H	-5.675844000	2.106976000	0.593848000
C	-2.999450000	3.041317000	-2.769025000
O	-2.564281000	4.147871000	-2.957098000
O	-3.699119000	2.128346000	-3.119318000
Rh	0.486497000	-0.320045000	-0.879247000
P	-0.501929000	-1.682222000	0.925490000
P	2.375260000	-0.263880000	0.329826000
C	-0.279610000	-3.723124000	2.561975000
C	0.530880000	-2.922945000	1.536113000
H	0.879387000	-3.615721000	0.753186000
C	1.761503000	-2.276262000	2.192037000
H	2.207342000	-3.033989000	2.861500000
H	1.442939000	-1.439970000	2.839177000
C	2.868825000	-1.822778000	1.219290000
H	3.763329000	-1.565790000	1.811132000
C	3.264593000	-2.907230000	0.207885000
C	-1.458326000	-0.759009000	1.864233000
C	-1.731507000	-2.761237000	-0.251399000
C	3.874450000	0.126849000	-0.669739000
C	2.400622000	1.036140000	1.639989000
H	-1.176877000	-4.172845000	2.109295000
H	0.350855000	-4.534504000	2.961105000
H	-0.592666000	-3.086801000	3.404048000
H	2.487053000	-3.039527000	-0.563339000
H	4.202065000	-2.644186000	-0.302292000
H	3.406762000	-3.867715000	0.730191000
C	-1.165677000	0.604392000	2.033845000
H	-0.417397000	1.064470000	1.383671000
C	-1.838945000	1.359217000	3.000960000
H	-1.603682000	2.419275000	3.119612000
C	-2.822107000	0.758093000	3.796351000
C	-3.355165000	1.346256000	4.547313000
C	-3.135645000	-0.597604000	3.617520000
C	-3.913512000	-1.064927000	4.226018000
C	-2.458094000	-1.355909000	2.656256000
H	-2.720089000	-2.404798000	2.509501000
C	-3.084280000	-2.387317000	-0.336745000
H	-3.423206000	-1.461328000	0.130776000
C	-3.987349000	-3.178454000	-1.058998000
H	-5.035581000	-2.876317000	-1.122035000
C	-3.551954000	-4.344637000	-1.700327000
H	-4.258914000	-4.960145000	-2.261440000
C	-2.201803000	-4.714965000	-1.626523000
H	-1.851516000	-5.619233000	-2.129666000
C	-1.294329000	-3.925420000	-0.911830000
H	-0.242866000	-4.220551000	-0.881668000
C	3.991079000	-0.443635000	-1.950499000
C	3.172585000	-1.060485000	-2.331701000
C	5.134164000	-0.213847000	-2.723467000
H	5.217748000	-0.662190000	-3.716301000
C	6.163995000	0.598514000	-2.227615000
H	7.052398000	0.786743000	-2.834946000
C	6.049855000	1.172918000	-0.954973000
H	6.848772000	1.809557000	-0.567471000
C	4.910668000	0.936780000	-0.174139000
H	4.824623000	1.387432000	0.817565000
C	1.842921000	2.285443000	1.314977000
H	1.402736000	2.425835000	0.325252000
C	1.816282000	3.322970000	2.250464000
H	1.373829000	4.284947000	1.980374000
C	2.341692000	3.120290000	3.534662000
H	2.312269000	3.924420000	4.273407000
C	2.900664000	1.880849000	3.867873000
H	3.311181000	1.714873000	4.866542000

C	-2.683632000	-0.812667000	1.710501000	H	-1.466370000	0.179144000	-3.895522000
C	-3.702088000	-0.765261000	2.671909000	H	-1.921330000	-3.800565000	-2.269326000
C	-3.432833000	-0.308032000	3.966686000	H	-4.230673000	-0.270931000	4.712283000
C	-2.138634000	0.116383000	4.302414000	H	-2.110441000	-2.216383000	-4.186662000
P	-0.020365000	-0.358858000	0.812486000	H	-0.121042000	0.442319000	3.589911000
C	-0.771438000	-0.964045000	-0.753410000	Rh	0.951915000	1.661326000	0.708508000
C	-0.891101000	-0.070372000	-1.826232000	C	-1.924333000	3.545510000	-0.609715000
C	-1.384030000	-0.517084000	-3.057385000	H	-2.573528000	3.761395000	-2.665828000
C	-1.746400000	-1.860946000	-3.219882000	C	-1.640801000	3.721562000	-2.092261000
C	-1.636252000	-2.753406000	-2.143857000	H	-1.102047000	4.665250000	-2.265125000
C	-1.156594000	-2.307000000	-0.908659000	H	-1.023224000	2.893556000	-2.486820000
P	2.771601000	0.770061000	-0.271752000	C	-0.748604000	3.414300000	0.250312000
C	3.710181000	2.089564000	-1.148511000	C	-0.770040000	2.883129000	1.596168000
C	5.033995000	2.414923000	-0.810849000	C	0.536101000	3.847260000	-0.203386000
C	5.672829000	3.496002000	-1.434740000	C	0.320801000	3.020855000	2.504214000
C	5.000403000	4.252158000	-2.401765000	H	-1.697697000	2.435476000	1.943557000
C	3.677696000	3.932197000	-2.741299000	C	1.658855000	3.859905000	0.666874000
C	3.032148000	2.864852000	-2.110872000	H	0.674130000	4.182205000	-1.228751000
C	3.991795000	-0.025629000	0.848291000	C	1.555915000	3.523767000	2.049132000
C	3.781343000	0.032815000	2.233377000	H	0.198614000	2.693259000	3.536820000
C	4.670206000	-0.611758000	3.101672000	H	2.627977000	4.153157000	0.261172000
C	5.774523000	-1.303867000	2.586602000	H	2.419471000	3.605500000	2.708480000
C	5.991697000	-1.352688000	1.201173000	C	-3.167793000	2.868318000	-0.225698000
C	5.097850000	-0.722306000	0.329761000	O	-3.483453000	2.442211000	0.885029000
C	2.491287000	-0.535900000	-1.537439000	O	-4.082219000	2.827972000	-1.271012000
C	2.098079000	-1.830386000	-1.082031000	C	-5.397539000	2.359590000	-0.903444000
C	1.783616000	-2.752694000	-2.071219000	H	-6.031573000	2.672731000	-1.748133000
C	1.806962000	-2.445506000	-3.435424000	H	-5.736046000	2.877126000	0.008536000
C	2.205260000	-1.201010000	-3.890053000	C	-2.384365000	5.468751000	0.082064000
C	2.551094000	-0.250745000	-2.908857000	O	-2.981391000	5.381504000	1.132223000
O	1.362912000	-3.517534000	-4.162904000	O	-1.908421000	6.237534000	-0.726421000
C	1.221519000	-4.597821000	-3.211560000	C	-5.479856000	0.863761000	-0.701751000
O	1.335783000	-4.033785000	-1.886153000	C	-4.674161000	-0.019747000	-1.428959000
C	2.024651000	-2.247410000	0.342398000	C	-6.405876000	0.329428000	0.208140000
C	2.914290000	-3.207201000	0.807777000	C	-4.781846000	-1.404067000	-1.241570000
C	2.914719000	-3.673193000	2.127052000	H	-3.930771000	0.373570000	-2.126534000
C	1.987905000	-3.225237000	3.051374000	C	-6.513991000	-1.051647000	0.387944000
C	1.069585000	-2.253465000	2.606138000	H	-7.035392000	1.005270000	0.794913000
C	1.076358000	-1.759935000	1.293789000	C	-5.698363000	-1.950973000	-0.327679000
O	3.901811000	-4.609051000	2.291777000	H	-4.122646000	-2.055314000	-1.815049000
C	4.668691000	-4.573240000	1.064809000	H	-7.236120000	-1.438529000	1.111913000
O	3.899327000	-3.835388000	0.089910000	C	-5.827327000	-3.458414000	-0.079701000
H	2.882882000	0.732194000	-3.241269000	C	-5.528121000	-3.760607000	1.405355000
H	5.564360000	1.832203000	-0.055302000	H	-5.628904000	-4.842687000	1.593298000
H	1.988670000	2.642470000	-2.345323000	H	-4.502682000	-3.452951000	1.666572000
H	2.895241000	0.559158000	2.603689000	H	-6.227625000	-3.229648000	2.070671000
H	5.245062000	-0.784535000	-0.751305000	C	-4.853506000	-4.277168000	-0.942441000
H	2.239064000	-0.962218000	-4.953399000	H	-3.806284000	-4.013412000	-0.723945000
H	6.700167000	3.745796000	-1.159744000	H	-4.992193000	-5.349137000	-0.729088000
H	3.143066000	4.522238000	-3.489161000	H	-5.033335000	-4.114102000	-2.017781000
H	4.495217000	-0.584159000	4.179643000	C	-7.268298000	-3.908634000	-0.404756000
H	6.853291000	-1.891588000	0.799461000	H	-8.002622000	-3.376197000	0.220179000
H	5.501226000	5.093777000	-2.885450000	H	-7.506646000	-3.713076000	-1.462957000
H	6.464937000	-1.812228000	3.263816000	H	-7.374492000	-4.990165000	-0.216398000
H	0.227172000	-5.051257000	-3.326589000				
H	2.035617000	-5.327029000	-3.365517000				
H	0.329309000	-1.884090000	3.315824000				
H	1.971355000	-3.600100000	4.075183000				
H	4.823572000	-5.598790000	0.703432000				
H	5.616688000	-4.039775000	1.250613000				
H	-2.919338000	-1.150129000	0.699609000				
H	-0.558982000	0.962531000	-1.680759000				
H	-1.043736000	-3.007000000	-0.077194000				
H	-4.710043000	-1.073614000	2.388251000				
H	-1.921921000	0.482264000	5.308744000				

References

1. Kawashima, S.; Aikawa, K.; Mikami, K., Rhodium-Catalyzed Hydrocarboxylation of Olefins with Carbon Dioxide. *Eur J Org Chem* **2016**, (19), 3166-3170.
2. Pavlovic, Lj.; Vaitla, J.; Bayer, A.; Hopmann, K. H., Rhodium-Catalyzed Hydrocarboxylation: Mechanistic Analysis Reveals Unusual Transition State for Carbon–Carbon Bond Formation. *Organometallics* **2018**, *37* (6), 941-948.

Paper IV

Mechanistic study of asymmetric Co-catalyzed
hydrogenation of enamides

Ljiljana Pavlovic, Hongyu Zhong, Paul J. Chirik and Kathrin H. Hopmann
(*In preparation*)

